UNIVERSIDAD AUTONOMA DE MADRID

Departamento de Fisica de la Materia Condensada, Nanociencia y Biofisica

QUANTUM TRANSPORT AND TOPOLOGICAL FEATURES IN TWO-DIMENSIONAL MATERIALS

TESIS DOCTORAL PRESENTADA POR

Francesca Finocchiaro

DIRECTORES:

Prof. Francisco Guinea López

Prof. Pablo San-Jose

TUTOR:

Prof. Guillermo Gómez Santos

Madrid, Mayo de 2018

' Son of man
You cannot say, or guess, for you know only
A heap of broken images'

T. S. Eliot

Ai miei fratelli e ai miei genitori
(to say nothing of the cats)

Acknowledgments

Working on this thesis has been a great challenge, and as some newborn wrinkles testify, it signified a personal before than scientific growth. If this was possibile, it was above all because of the great people that accompanied me along the way.

I first of all want to express my appreciation to my supervisors. Paco, thanks to his vast experience in the field and his physical intuition, guided me during these four years and gave me the important possibility of working with him on a number of high-impact projects. Also, I am deeply grateful to Pablo, that has been my cosupervisor for the last three years of thesis. I owe him a lot. Not only because of his sharp mind, his good ideas and his natural talent for communicating them, but also, and perhaps more importantly, for his constant resolute encouragements and positive feedbacks, deriving from a steady confidence in my capacities. Our meetings are always refreshing and motivating, and invariably leave me with a constructive self-reliance and a clarity of mind that seems impossible just a few hours before.

My deep gratefulness goes right after to Joaquin Fernandez-Rossier. It is quite obvious that none of this would have happened without the SPINOGRAPH network. However, there is much more to this. His precious guidance in Alicante put me back on track when my motivation was going through a rough patch. He was able to dig up my sleeping potential and make me feel part of his group, providing me with a nice project that finally took shape in what is now the skyrmions paper. I've learnt a lot from him, from the right amount of pragmatism to how to take care firsthand of my works and projects at the same time as knowing that someone is watching your back, in my view the perfect pedagogical strategy. I cannot go on but mentioning the other person that took special care of me in the Alicante period (and ever since), that is Jose Lado. I cannot thank him enough for his infinite wisdom, for the passion for physics that he is effortlessly able to imprint into others, his patience, his constant availability and down-to-earthiness, and, not last, his friendship. I've learnt so much from him during my short stay that it is hard to summarize it in a few words. Last but not least, I close the part dedicated to the Alicante team with Noel, who was always there for me, long before Alicante and up to these days. He was there for profession-related issues (I owe him most of the python technicalities that I've learnt there) but, more importantly, he was there for all the rest. I cherish all the fun we had at the many conferences that we attended together, plus the scattered weekends that we sometimes tried to attach to them (a special mention goes to the UK road trip with a perpetually sleeping Jose in the back of the car with us trying to survive by driving in the correct lane) and finally for his hospitality during my first week in Alicante in his amazing house by the sea. On passing, I have to thank the rest of the Alicante crew that made my stay there one of the best period spent in Spain, and with no trace of doubt the one that I remember as being the most carefree: Miguel, Taner and Bernat.

As for the Madrid group, I want first of all to express the immense gratitude that I owe my brothers in arms, aka the papis: José Angel, el Vene and Gelito (or, as he is also known, Anguel). Moving together from ICMM to IMDEA marked a crucial moment in my Madrid both professional and personal life such that, looking back, I cannot imagine myself right now without that turning point. Our relationship goes beyond that between

just colleagues and that between just friends. It is a bond that formed in the most natural form as family relationships do: by virtue of an intense shared experience that marked us with recognizable and shared traits. During these last years, they have been a sort of replacement family and my personal certitude of soft-landing in the adversities because I could always count on them. Though a specific and special mention is deserved by each of them, I skip it because I'm sure they perfectly know how they helped me keep my mental sanity during our journey together.

Then, there is Laura. She's meant so much to me during these years and in so many ways that it is difficult to shape them into a brief account. She's the first person who's taken care of me in Madrid, someone that I could always blindly count on, during thesis-related crisis when we would hide in some ICMM corners to cry, laugh and talk about physics all at the same time, down to the many physics-unrelated moments that we shared, among which I'll always treasure the many 'sleepovers' first at her house in Opera and then at my house when she moved out of Madrid (a moment that I recall with enormous sadness). During the years she's been a great friend and an inspiration for the determination and hard work that she's able to devote to literally everything.

Of course, I cannot forget the rest of the group. First of all, those who where there the whole time: Maria, Belen, Rafa, Alberto and Nacho. Maria, for her determination to keep the group together no matter what, and for giving us all a sense of being looked after by a tireless big brother that leaves nothing to chance. I've learnt much from the self-organized courses on QFT and topology, and much more from the strict moral code that she relentlessly applies to our profession, pushing us to constantly question our work, our motivation, our knowledge and our performance. Among the others, I wish to thank Alberto in particular for his relentless support during these years. I have always taken his passion and hard work as a master example of all that is good and worthy in the academic world. I truly admire him for his consistence with his principles all the way to what it takes to survive head-on without getting one's hands dirty. Of course, the laughters shared at lunch and the 'español callejero' learnt from him during the years are also a crucial part of the package. A though goes also to Ramon, Leni and Pilar, who have always been very nice and sincerely interested in my work.

Beyond who's always been there, there is also who was there for just a while. Among them, a special thank goes to Mauricio, one of the most amazing person I got to know as I was newly arrived. His unmistakable argentinian accent together with his wisdom and some invaluable conversations that we shared in the cafeteria during the first months of my stay are amongst the best memories I guard of that period. I want to bring up as well Andreas Bill, Yago, Bruno, Vincenzo and Hector. To Hector, even though this is no proper thank you, I owe much in terms of personal growth, since dealing with him when I just got to Madrid was a though challenge. Facing his rough basque personality taught me a lesson that, at the end of the day, made me stronger (sink or swim, some say). Also, I owe him my exposure to group theory. A special person that I want to thank is Fernando. His time spent in IMDEA marked another important moment in my PhD experience, as I had the chance to share a few valuable months with one of the brightest minds, at the same time as one of the humblest persons, I have ever met. Talking physics with him always felt inspiring and natural and, what's more important, completely free of any judgmental attitude. Finally, I feel like expressing my gratitude to those who arrived last, the niños: Raquel, Vicente, Oscar and Alfonso. It's been such a pleasure and such a fresh take eating with them during these last months, and such fun to organize with them the Wednesday meetings (that we have been able to carry forward against all odds). In a few months, we naturally generated a friendly, humble and stimulating environment to discuss physics that I really regard as priceless.

I close this physics-related account with a special thank to my SPINOGRAPH fellows,

especially Denis, Pep, Sowmya, Mario, Weinjin, Regina and the French guy. We had so much fun together and I have always felt very lucky for sharing this experience with such wonderful persons. Thanks to them, attending the SPINOGRAPH conferences has always been something that I enthusiastically looked forward to do.

This list would be incomplete without mentioning all the work-unrelated people who stood by me during these four years, the close ones as well as those geographically far apart. One of the persons that has been a constant and a certainty in Madrid has been Fede, a great friend on top of being an almost flat-mate for a long time. He was always there, to share our physics-related anxieties and self-doubts, and to help me get my self together in many occasions. I also cannot forget Marco, who has been literally the first friendly face that I've seen in Madrid when he made space for me and my intrusive immigrant bags as I was newly arrived. I also have to mention Matteo 'il Mori', Angelica, Paul, Elena and Riccardo. Finally, I have a hard time imagining my life hadn't I got into afro-contemporary dance classes two years ago. Therefore, first of all and to my own surprise, I guess I have to thank Lucyanna for making it happen (and Luca for pushing me to do it, of course). However, the rest kind of happened by itself, in some magical and mysterious way that still amazes me. I couldn't feel more privileged for meeting my beloved dancing soul mates, Ines, Luli, Clara and Ana. The amazingly strong bond we have built in such a short time, the deep reciprocal understanding and fellow feelings about virtually everything are simply incredible. I am grateful for all I've learnt from them, their integrity, their maturity, their amazing view of the world, all of it so new to me.

Taking this thesis to an end and, at the same time, leading a pseudo-normal Madrid life, with its ups and downs and my hundreds of personal idiosyncrasies, wouldn't have been an easy task without the omnipresent backbone of my hometown people. Knowing that I could count on their unconditional and ubiquitous support is what really kept me going. First of all, nothing would be the same without Sara, Roberta, Giulia and Cesca. They are my second family and they have been somehow present in every single moment of our long time spent far away. I feel especially lucky for the incredible sequence of life-coincidences, both personal and professional, that kept me and Roberta interlaced during these years as two perfectly matched twins who could always understand what was going on with the other; for Sara's moving efforts to keep up with my so asbtract physics-related world and academic professional life and her being a pillar, The Pillar, of our old cherished Rome life; for the overlapping PhD experience that we lived with Cesca and her many trips to Madrid, that played such an important role in my final capitulation, swollen with love, to this city; for Giulia's empathic understanding of all the incertitudes that accompanied me during these years, and still do, with her typical touch of sweetness. Also, it's impossible to imagine a Spain-related experience without having a fellow soul such as Simone to share all my thoughts and irreverent feelings with. His constant visits and our neverending jokes about Spain (that spanish people hate, for being openly mocked, but other italians hate as much, for not really understanding what's funny about it, making us unpopular virtually everywhere) are really invaluable. I also feel the deepest happiness for having Silvia and Vale as friends. The shared experience of being women physicists in such a manly world is possibly what initially made us come closer, but there's much more to it. We have supported each other unrestingly during these years and I've looked to them as a sort of admirable elder sisters for having been through what I went through, just some time before I did. Finally, even though we kind of loosened the intense bond that sustained our long-term friendships for years, I cannot omit Matteo, Mipa and Corinne. This thesis is on them, too.

There's no more appropriate dedicatory than the one to this thesis (cats included). I really owe everything to my family. My parents' support has been unconditional during

these years, and, though I sometimes think it is a product of some big ancestral misunderstanding, their blind faith in my abilities and my potential is what made me withstand every difficulty head-on and with growing strength and confidence each day. Thank you for the person I am. It's all on you. My brothers are the two persons I've missed more during these years away from home. I feel so lucky to have them, and look to them in so many ways they have no idea of. I am proud, so intensely, of who they are, who they were and of the adults they are growing into. I admire the integrity they put into their work, their patience, their infinite wisdom, their consistency with their principles. They are a constant inspiration for everything I do and for the person I want to be.

'La storia non si fa coi se e coi ma'. Nevertheless, it is quite safe to say that this thesis wouldn't be here at all *if* it wasn't for Luca, for so many reasons I won't even try to give an account of them. So I will just say that he's everywhere in these pages, and I'm afraid it's impossible to find the right words to thank him for standing right next to me during these years.

This list cannot end without an ode to Madrid, the city that so innocently welcomed me, and that in return received such a bipolar mixture of love and hate from my side. I came here being presumptuous and convinced to know a lot about everything, I see that so clearly now, and leave it (?) way stronger and humbler. Being pushed to question everything you've always taken for granted is, at the end of the day, the most enriching experience that one can ever live.

Thank you all, so much, for everything.

Abstract

This thesis starts by providing an overview of some amongst the essential aspects of low-dimensional topologically nontrivial electronic phases (first chapter), and follows by presenting four theoretical studies on novel phenomena that arise in two-dimensional materials. In three of these four chapters, we put forward innovative routes for tailoring the emergent topological properties of graphene (second and third chapters) and semiconducting quantum wells proximitized with superconductors (fourth chapter). The fifth chapter deals instead with the rich spin and valley-dependend low-energy description of semiconducting two-dimensional transition metal dichalcogenides.

In graphene, we propose two schemes for engineering two independent topological phases of matter, both relying on the unconventional relativistic-like low-energy properties of this material. Specifically, in the second chapter we consider a graphene Hall bar on top of a magnetic insulator as a possible detector for skyrmions, using as a working priciple the anomalous Hall signal produced by these magnetic whirls. We demonstrate that the linear semimetallic dispersion of graphene, which places it on the brink of becoming topological, is able to enhance the Hall signal. In addition, graphene's one-atom thickness make it especially suitable for extrinsic engineering through proximity with a vast range of materials. We therefore suggest that these two properties combined render the detection of skyrmions by means of graphene especially effective. In the third chapter we focus on a special time reversal-broken quantum spin Hall phase that can be hosted by samples of twisted bilayers of graphene in the quantum Hall state. We show that, in the regime of large twisting angles where the two layers are virtually decoupled, the interplay between electronic interactions and an applied electric field drives the system into the targeted phase by lifting the eightfold degeneracy of the zero Landau level in a nontrivial fashion. To implement this phase, crucially, no spin-orbit interactions nor Zeeman fields are needed, which constitutes a rather novel and attractive feature of the proposal.

In the fourth chapter we focus on a different platform based on a two-dimensional electron gas with strong spin-orbit coupling in the quantum Hall regime. We study the topological properties of this system when it is proximitized with a narrow superconducting strip and a Zeeman field is applied parallel to the strip direction, revealing unconventional features that provide for a novel implementation of a topological π Josephson junction. We exploit this finding to propose a protected route towards quantum computational operations with Majorana zero modes at the junction.

Finally, in the last chapter we derive a $\mathbf{k} \cdot \mathbf{p}$ low-energy description for transition metal dichalcogenides based on rigorous symmetry-rooted group theoretical arguments. We then allow for all possible symmetry breaking terms that preserve time reversal invariance, and classify them according to the microscopic properties of different kinds of interactions and defects. The resulting characterization is particularly interesting because of the unconventional coupled spin and valley physics.

Resumen

Esta tesis empieza ofreciendo una perspectiva general sobre algunos de los aspectos esenciales de las fases electrónicas de baja dimensionalidad topológicamente no triviales (primer capítulo), y sigue con la presentación de cuatro estudios teóricos sobre fenómenos novedosos en materiales bidimensionales. En tres de los cuatro capítulos, proponemos rutas innovadoras para modelar las propiedades topológicas emergentes de grafeno (segundo y tercer capítulo) y pozos cuánticos semiconductores proximizados con superconductores (cuarto capítulo). Por otro lado, el quinto capítulo está centrado en la descripción de baja energía de monocapas bidimensionales de dicalcogenuros de metales de transición.

En grafeno, proponemos dos esquemas para realizar dos fases topológicas independientes, ambas basadas en las propriedades relativistas de baja energía de este material. Concretamente, en el segundo capítulo consideramos un sensor de efecto Hall de grafeno acoplado a un aislante magnético como un posible detector de skyrmiones, utilizando como principio de funcionamiento la señal Hall anómala producida por estos remolinos magnéticos. Demostramos que la dispersión semimetalica lineal de grafeno, una propiedad que le coloca en el borde de hacerse topológico, es capaz de magnificar la señal Hall. Además, su grosor de tan solo un átomo hace que este material sea especialmente apto para ser manipulado extrínsecamente a través de efecto proximidad con una amplia gama de materiales. Proponemos por lo tanto que la combinación de estas dos propiedades hace que la detección de skyrmiones a través de grafeno sea especialmente eficaz. En el tercer capítulo nos centramos en una fase Hall cuántica de espín con ruptura de simetría de inversión temporal, que puede darse en muestras de bicapas de grafeno rotadas en el estado Hall cuántico. Demostramos que, en el régimen de ángulos de rotación grandes en el cual las dos capas están prácticamente desacopladas, las interacciones electronicas junto a un campo électrico aplicado fuerzan al sistema en la fase deseada levantando de forma no trivial la degeneración de grado ocho del nivel cero de Landau. Para implementar esta fase, crucialmente, no se necesitan ni interacción espín-órbita ni campos Zeeman, lo cual constituye una característica novedosa y atractiva de la propuesta.

En el cuarto capítulo, nos enfocamos en una plataforma diferente basada en un gas electrónico bidimensional con fuerte interacción espín-órbita en el régimen Hall cuántico. Estudiamos las propiedades topológicas de este sistema cuando está acoplado a una tira superconductora estrecha y se aplica un campo Zeeman en la dirección de la tira, revelando caracteristicas no convencionales que permiten una realización novedosa de una unión Josephson topológica con una diferencia de fase π. Explotamos este hallazgo para proponer una ruta protegida hacia operaciones computacionales cuánticas con los modos cero de Majorana de la unión.

Finalmente, en el último capítulo derivamos una descripción $\mathbf{k} \cdot \mathbf{p}$ de baja energía para dicalcogenuros de metales de transición a través de argumentos rigurosos de teoría de grupos basados en simetría. A continuación, admitimos todos los términos que rompen las simetrias del sistema excepto la invariancia bajo inversión temporal, y los clasificamos según las propiedades microscopicas de diferentes tipos de interacciones y defectos. La

caracterización resultante es especialmente interesante debido a la física no convencionál generada por el acoplo entre espín y valle.

Contents

1 Introduction **1**
1.1 Hexagonal 2D platforms . . . 2
1.1.1 Graphene . . . 2
1.1.2 Transition metal dichalcogenides (TMDCs) . . . 5
1.2 Topology in physics . . . 6
1.2.1 Berry phase and Berry curvature . . . 7
1.2.2 Celebrated topological phases . . . 10
1.2.3 The quantum Hall effect . . . 12
1.3 Organization of the thesis . . . 16

2 Electrical detection of skyrmions in graphene devices **19**
2.1 Introduction . . . 19
2.2 Theoretical background . . . 23
2.2.1 Mathematical properties of skyrmions . . . 23
2.2.2 The anomalous Hall effect . . . 25
2.3 Continuum approach . . . 26
2.4 Tight binding quantum transport approach . . . 28
2.4.1 Landauer's formalism for transport . . . 29
2.4.2 Calculation of the Hall response in a three-terminal geometry . . . 30
2.5 Results . . . 32
2.5.1 Hall response in the ideal case . . . 33
2.5.2 Deviations from ideality . . . 37
2.6 Conclusions . . . 43

3 Quantum Spin Hall Effect in Twisted Bilayer Graphene **45**
3.1 Introduction . . . 45
3.2 Twisted bilayer graphene . . . 47
3.2.1 Geometric properties . . . 47
3.2.2 Band structure . . . 51
3.3 Theory of the quantum Hall effect in twisted bilayer graphene . . . 53
3.3.1 Quantum Hall effect in monolayer graphene . . . 54
3.3.2 Quantum Hall effect in twisted bilayer graphene . . . 63
3.4 Quantum spin Hall effect in Twisted bilayer graphene . . . 72
3.4.1 Twisted bilayer graphene in an electric field . . . 72
3.4.2 Experimental evidence . . . 75
3.4.3 Rescaling of the parameters . . . 78
3.4.4 Effects of intersite repulsion . . . 78
3.4.5 Discussion . . . 81
3.5 Conclusions . . . 82

4 Topological π-junctions from crossed Andreev reflection in the quantum Hall regime **85**
4.1 Introduction . . . 85
4.2 Majorana zero modes . . . 89
4.2.1 Elements of quantum computation . . . 90
4.2.2 Non-Abelian statistics and braiding . . . 92
4.2.3 Platforms that support Majoranas . . . 96
4.3 The Crossed Andreev reflection (CAR) mechanism in quantum Hall systems 100
4.3.1 Andreev reflection processes in normal platforms . . . 100
4.3.2 Andreev reflection processes in quantum Hall systems . . . 101
4.3.3 Induced pairing . . . 103
4.3.4 Induced gap . . . 107
4.4 Numerical calculations . . . 109
4.4.1 Tight binding model . . . 110
4.4.2 Spectra of systems with PBC . . . 111
4.4.3 Spectra of finite-size systems . . . 115
4.4.4 Topological π junctions . . . 116
4.4.5 Stability of CAR-induced topological π junctions . . . 118
4.5 Tunnel-Braid operations . . . 120
4.5.1 Conventional topological π junctions . . . 120
4.5.2 CAR-induced topological π junctions . . . 125
4.6 Conclusions . . . 127

5 Disorder in Transition Metal Dichalcogenides **129**
5.1 Introduction . . . 129
5.2 Symmetry analysis . . . 130
5.3 Classification of the Bands at $\mathbf{K}_{\pm}$ . . . 134
5.4 Classification of the operators . . . 141
5.4.1 Spinless system . . . 141
5.4.2 Spinful system . . . 143
5.5 Hamiltonian of Pristine TMDC's . . . 144
5.6 Disorder Potential . . . 148
5.6.1 Disorder Corrections to the Conduction Band . . . 150
5.6.2 Disorder Corrections to the Valence Band . . . 151
5.7 Discussion and Conclusions . . . 153

Conclusions **155**

Conclusiones **157**

Appendix A Time reversal symmetry **159**

Appendix B Elements of Group Theory **163**
B.1 Groups and their Properties . . . 163
B.1.1 Conjugacy and Classes . . . 164
B.1.2 Direct Product Group . . . 165
B.2 Theory of Group Representations . . . 165
B.2.1 Representations and their Properties . . . 165
B.2.2 Great Orthogonality Theorem . . . 166
B.2.3 Characters . . . 166
B.2.4 Decomposition of Reducible Representations . . . 168
B.2.5 Representations in Quantum Mechanics . . . 168

B.2.6 Basis Functions for Irreps 171
B.2.7 Direct Products and Representations 172
B.3 Crystallographic Symmetries 173
B.3.1 Point Groups and Space Groups 173

List of Publications **175**

Bibliography **177**

Chapter 1

Introduction

This thesis is mainly concerned with investigating the quantum transport properties of two-dimensional (2D) systems, with a specific interest in their symmetries and emergent topological properties. On a priviledged footing, three out of four chapters are dedicated to hexagonal-lattice 2D systems, specifically graphene and semiconducting monolayers of transition metal dichalcogenides (TMDCs) [1–4]. The remaining chapter deals instead with a generic two-dimensional electron gas (2DEG), that serves as a paradigm for a broad class of systems such as semiconducting quantum wells. However, while the former systems present an intrinsic interest rooted in their geometrical properties, the latter merely serves as a building block to engineer a platform where non-trivial physical ingredients are combined to test the onset of exotic phenomena.

The interest in two-dimensional systems has witnessed a huge boost ever since the discovery of graphene in 2004 [5] by the Manchester group of Professors Geim and Novoselov, who were afterwards awarded a Nobel prize for having succeded for the first time to isolate a single layer of graphite by mechanical exfoliation. This discovery gave rise to a flourishing advancement of this field of research on both the theoretical [1,6–12] and experimental side [13–20]. Many phenomena well-known in conventional materials were predicted and discovered in graphene, often presenting anomalous features ascribable to its relativistic-like low-energy dispersion [13,21–28]. Also, composite structures such as graphene bilayers and trilayers, with a variety of stacking orders ranging from higly ordered structures to compounds with misalignment faults were investigated, usually presenting far from standard low-energy features [29–37].

During the following years, a richer collection of 2D materials has been progressively uncovered, starting from the family of single-layer TMDCs. Specifically, in this thesis we are interested on semiconducting monolayers with general formula MX_2, with M=Mo, W and X=S, Se [4,38–43]. These systems have a geometry very similar to that of graphene, and they are characterized by akin low-energy properties [38,43–46]. However, additional effects stemming from the lack of inversion symmetry (due to the presence of two different constituent elements rather than only one, as in graphene) and from a large spin-orbit interaction inherited from the heavy transition metal atoms, further expand the already diverse playground offered by graphene.

Along with these novel compounds, nowadays technologies are allowing an ever improved ability to grow thin layers of a variety of materials. The experimental workability of these platforms in a number of configurations has been well demonstrated, in particular for the class of 2D semiconducting quantum wells proximitized with superconductors relevant to this thesis [47–53].

The reason to devote special attention to 2D materials is to be sought in at least two key aspects: (i) their improved experimental flexibility and versatility as compared with three-dimensional (3D) systems for a variety of applications, such as proximity effects, response to external applied fields, exceptional suitability for gating and contacting; (ii) the extended variety of physical phenomena that they can host owing to their reduced

dimensionality, ranging from the celebrated quantum Hall effect (a topic which will be tackled to a great extent in the course of this introductory chapter) to manifestations of exotic non-Abelian statistics of particles that is forbidden in three dimensions, a subject that we will study in detail in the fourth chapter.

This introductory chapter is divided into three sections. In the first section, we give an account of the geometrical and electronic properties of honeycomb lattice systems, namely graphene and TMDCs. In the second section we review the basic concepts underlying the thriving field of topology in physics, a leitmotive that recurs troughout the first chapters of the thesis, providing the reader with some key concepts that will prove useful in the reading of these chapters. We defer instead a detailed account of the tools needed for the fifth chapter, namely, symmetries and their role in condensed matter, to appendices A and B. Finally, in the last section we briefly discuss the organization of the rest of the thesis into chapters.

1.1 Hexagonal 2D platforms

In this section, we review the basic geometrical and electronic properties of systems with honeycomb lattices: graphene and TMDCs.

1.1.1 Graphene

A graphene monolayer is composed of two interpenetrating sublattices of Carbon atoms, that we label A and B for convenience, where the atoms pertaining to each individual sublattice form a triangular Bravais lattice with lattice parameter $a = 2.46$ Å [1]. Sites A occupy the positions

$$\mathbf{r}^A_{n,m} = n\mathbf{a}_1 + m\mathbf{a}_2 \tag{1.1}$$

with

$$\mathbf{a}_1 = a\left(\frac{1}{2}, \frac{\sqrt{3}}{2}\right) \quad \text{and} \quad \mathbf{a}_2 = a\left(-\frac{1}{2}, \frac{\sqrt{3}}{2}\right) \tag{1.2}$$

whereas the B atoms are displaced by a vector

$$\boldsymbol{\delta} = \frac{1}{3}(\mathbf{a}_1 + \mathbf{a}_2) = a(0, 1/\sqrt{3}) = a_0(0, 1) \tag{1.3}$$

where we have defined the Carbon-Carbon distance $a_0 = a/\sqrt{3} = 1.42$ Å. Therefore, sites B occupy the positions

$$\mathbf{r}^B_{n,m} = \mathbf{r}^A_{n,m} + \boldsymbol{\delta}. \tag{1.4}$$

The hexagonal lattice of graphene is depicted in Fig. 1.1a, where the primitive vectors $\mathbf{a}_{1,2}$ are explicitly shown. It is straightforward to see that the lattice has a basis of two atomic sites per unit cell. The reciprocal vectors for this lattice are

$$\mathbf{b}_1 = \frac{2\pi}{a_0}\left(\frac{1}{\sqrt{3}}, \frac{1}{3}\right) \quad \text{and} \quad \mathbf{b}_2 = \frac{2\pi}{a_0}\left(-\frac{1}{\sqrt{3}}, \frac{1}{3}\right)$$

The graphene Brillouin zone (BZ) is the parallelogram formed by these two vectors, even though it is common practice to refer to the BZ as the equivalent hexagon with corners

$$\mathbf{K} = \frac{4\pi}{3a}(1, 0) \quad \text{and} \quad \mathbf{K}' = \frac{4\pi}{3a}(-1, 0) \tag{1.5}$$

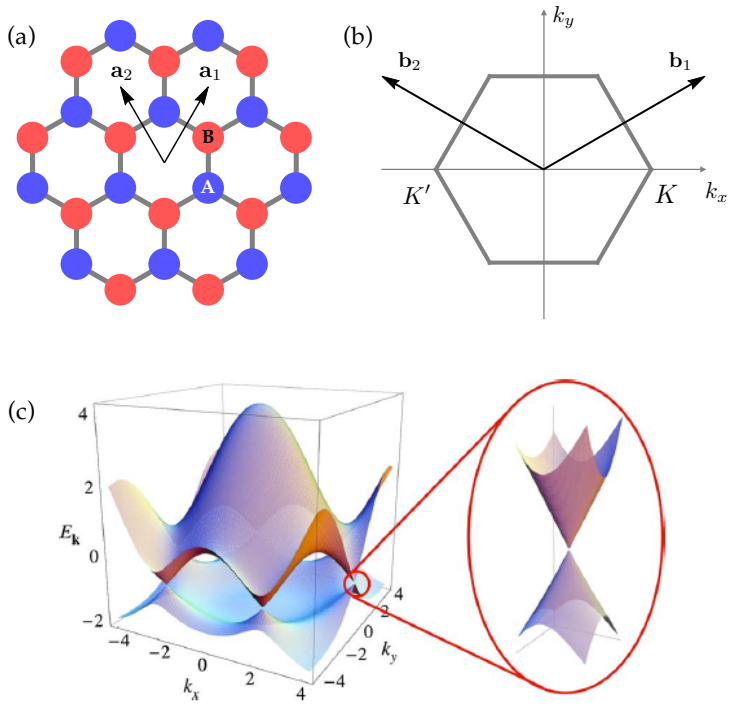

FIGURE 1.1: (a) Hexagonal graphene lattice where the A and B sublattices are colored in blue and red, respectively, and the primitive vectors $\mathbf{a}_{1,2}$ are explicitly shown. (b) Brillouin zone of the graphene lattice where the reciprocal lattice vectors $\mathbf{b}_{1,2}$ and the two inequivalent valleys $\mathbf{K}$ and $\mathbf{K}'$ are explicitly shown. (c) Graphene band structure in the BZ. The zoomed region shows the Dirac cone-like low-energy dispersion around one of the BZ corners. [Adapted with permission from Ref. [1]]

also called valleys. The hexagonal BZ is shown in Fig. 1.1 along with the reciprocal vectors $\mathbf{b}_{1,2}$. The simplest tight-binding Hamiltonian for graphene considers p_z-orbitals electrons that hop only between nearest neighboring sites with amplitude $t \approx 2.7$ eV, that is, between atoms on different sublattices separated by a distance a_0, and can be written as

$$H = -t \sum_{<i,j>} \left[c^\dagger_{i,A} c_{j,B} + \text{H. c.} \right] \tag{1.6}$$

where the sum is limited to atoms within the same unit cell or within nearest neighboring unit cells, where, as mentioned above, each cell contains two atomic sites, each belonging to a different sublattice, that we have labeled A and B. The operators $c^\dagger_{i,s}$ and $c_{i,s}$, with $s = A, B$ therefore respectively create and annihilate an electron on the sublattice s of the i-th unit cell, whose position $\mathbf{R}_i$ is taken to be coincident with the position of the A atom within the cell. By taking the Fourier transform of the creation and annihilation operators as

$$c_{i,A} = \frac{1}{\sqrt{N}} \sum_{\mathbf{k}} c_{\mathbf{k},A} e^{i\mathbf{k}\cdot\mathbf{R}_i} \quad \text{and} \quad c_{i,B} = \frac{1}{\sqrt{N}} \sum_{\mathbf{k}} c_{\mathbf{k},B} e^{i\mathbf{k}\cdot(\mathbf{R}_i+\delta)} \tag{1.7}$$

with N the number of unit cells, Hamiltonian (1.6) can be rewritten as

$$H = -t \sum_{\mathbf{k}} \left[c^\dagger_{\mathbf{k},A} c_{\mathbf{k},B} \sum_{i=1}^{3} e^{i\mathbf{k}\cdot\delta_j} + \text{H. c.} \right] \tag{1.8}$$

since each atom has three nearest neighbors belonging to the opposite sublattice that are displaced by the three vectors

$$\boldsymbol{\delta}_1 = \boldsymbol{\delta} = a_0(0,1) \quad \boldsymbol{\delta}_2 = \frac{a_0}{2}(-\sqrt{3},-1) \quad \boldsymbol{\delta}_2 = \frac{a_0}{2}(\sqrt{3},-1) \tag{1.9}$$

By defining the annihilation and creation spinorial operators in sublattice space as

$$c_{\mathbf{k}} = (c_{\mathbf{k},A}, c_{\mathbf{k},B})^T \quad \text{and} \quad c^\dagger_{\mathbf{k}} = (c^\dagger_{\mathbf{k},A}, c^\dagger_{\mathbf{k},B}) \tag{1.10}$$

Eq. (1.8) can be rewritten in matricial form as

$$H = \sum_{\mathbf{k}} c^\dagger_{\mathbf{k}} H_{\mathbf{k}} c_{\mathbf{k}} \tag{1.11}$$

with

$$H_{\mathbf{k}} = -t \begin{pmatrix} 0 & \sum_{i=1}^3 e^{i\mathbf{k}\cdot\boldsymbol{\delta}_j} \\ \sum_{i=1}^3 e^{-i\mathbf{k}\cdot\boldsymbol{\delta}_j} & 0 \end{pmatrix} \tag{1.12}$$

Upon explicitly expanding the sum around the $\mathbf{K}, \mathbf{K}'$ valleys up to first order in momentum, one is left with the following Hamiltonian

$$H^K_{\mathbf{k}} = \frac{3ta_0}{2} \begin{pmatrix} 0 & k_x - ik_y \\ k_x + ik_y & 0 \end{pmatrix} \tag{1.13}$$

and

$$H^{K'}_{\mathbf{k}} = \frac{3ta_0}{2} \begin{pmatrix} 0 & -k_x - ik_y \\ -k_x + ik_y & 0 \end{pmatrix} \tag{1.14}$$

that is, by introducing the Pauli matrices $\boldsymbol{\sigma} = (\sigma_x, \sigma_y, \sigma_z)$ acting in sublattice space, and defyining the Fermi velocity for graphene as $v_F = 3ta_0/2$

$$H^\tau_{\mathbf{k}} = v_F(\tau k_x \sigma_x + k_y \sigma_y) \tag{1.15}$$

where $\tau = 1$ at $\mathbf{K}$ and $\tau = -1$ at $\mathbf{K}'$ and $\sigma_{x,y}$ are Pauli matrices acting in sublattice space. Note that the low-energy Hamiltonians at $\mathbf{K}$ and $\mathbf{K}'$ are related by time-reversal symmetry, that in a spinless system is implemented by the complex conjugation operator. Diagonalization of this Hamiltonian yields, for both valleys, the linear dispersion

$$E_{\mathbf{k},\pm} = \pm v_F |\mathbf{k}| \tag{1.16}$$

associated to the valley-dependent eigenspinors

$$\psi^\tau_{\mathbf{k},\pm} = \frac{1}{\sqrt{2}} \begin{pmatrix} e^{-\tau i\theta_{\mathbf{k}}/2} \\ \pm e^{\tau i\theta_{\mathbf{k}}/2} \end{pmatrix} \tag{1.17}$$

where $\theta_{\mathbf{k}} = \arctan(k_x/k_y)$. One then sees that the low-energy dispersion of graphene is a relativistic one characterized by a velocity $v_F \approx 10^6$ m/s, and its carriers are Dirac-like fermions in 2D. From this very peculiar dispersion relation, shown in Fig. 1.1c, stem all the unconventional properties that differentiate graphene from conventional systems with standard parabolic dispersion. We will discuss one of these 'anomalies' in the next section, where we will explicitly compute the unconventional Landau levels sequence of graphene in the quantum Hall regime.

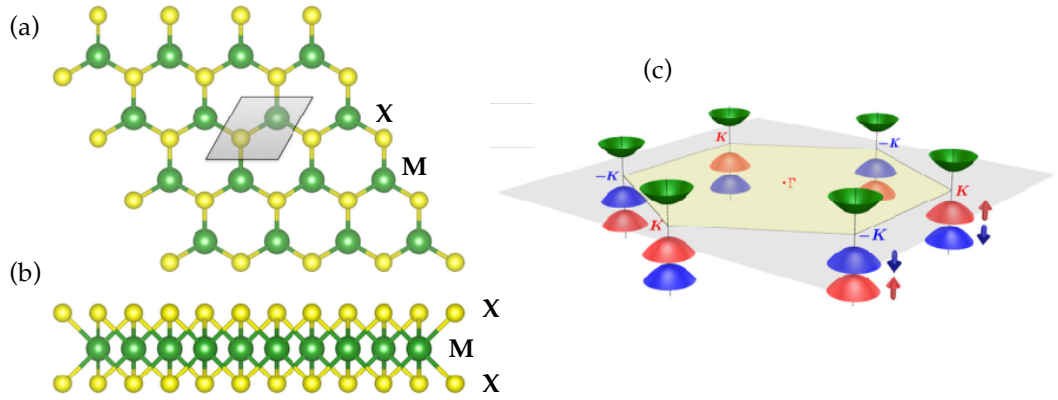

FIGURE 1.2: Structure of a typical TMDC lattice with formula MX_2 (a) seen from the top; (b) seen from the side. Green and yellow atoms correspond respectively to the transition metal (M) atoms and to the chalcogen (X) atoms. (c) Sketch of the low-energy dispersion of TMDCs around the inequivalent corners of the BZ. Notice that the green colour represent spin unpolarized bands, whereas blue and red colors represent oppositely spin-polarized states along the out-of-plane quantization axis.

1.1.2 Transition metal dichalcogenides (TMDCs)

Transition metal dichalcogenides are Van der Waals layered materials with general formula MX_2, with each individual layer composed of three atomic planes, namely a one-atom-thick plane of transition metal atoms (M) sandwiched between two layers of chalcogen atoms (X), all arranged in triangular arrays. The outer planes are rotated with respect to the central one in such a way that the overall planar structure of the system realizes a staggered honeycomb lattice equivalent to that of graphene, as shown in Fig. 1.2a, with the A and B sublattices corresponding to the triangular lattice of transition metal atoms M and to the two sublattices of chalcogen atoms X, respectively [3,4,43,46,54]. The structure as seen from the top and from the side is shown in Fig. 1.2a and b, respectively. The lateral view is shown instead in Fig. 1.2b. The BZ zone is hexagonal as shown in Fig. 1.2c. However, building a tight binding model is a much more complicated task in these systems than in graphene because of the many atomic orbitals involved [43,46,55]. Several models for capturing the low-energy features of the spectrum by fitting it to the DFT bands have been proposed with a number of involved orbitals ranging from three [46] to eleven [43]. A different approach to derive a continuum model for the dispersion around the high-symmetry points rests on a group theoretical approach based on symmetry considerations [54,56]. We will deal with such a derivation in great detail in the fifth chapter. At this level, it suffices to say that both approaches, as well as experimental confirmations, reveal that monolayer samples of TMDCs are semiconductors with a direct band gap located at the two inequivalent corners of the Brillouin zone K and K' [43,54]. This endows the spectrum of these systems with the same appealing multivalley structure as graphene. However, at odds with graphene, TMDCs lack inversion symmetry because the two interpenetrating sublattices are composed of different atomic species. Due to the simultaneous presence of the heavy transition metal atoms, endowed with a large atomic spin-orbit coupling (SOC), and to the lack of inversion symmetry, breaking of spin degeneracy is allowed. However, since the $z \to -z$ symmetry is preserved, the out-of-plane spin polarization is protected against any type of mirror-preserving perturbation. This enables the formation of a large spin splitting that affects the valence band more severly than the conduction band due to their different orbital composition [54,56–58]. Also, due

to the time reversal symmetry connecting the two valleys, this spin splitting is opposite at $\mathbf{K}$ and $\mathbf{K}'$. A minimal two-bands Hamiltonian that takes care of all these properties is given by Eq. (1.15) with the addition of a mass term Δ and a valley-dependent spin-splitting term in the valence band sector [58]

$$H^{\tau}_{\mathbf{k}} = v_F(\tau k_x \sigma_x + k_y \sigma_y) + \Delta\sigma_z + \frac{\lambda}{2}\tau s_z(1-\sigma_z) \tag{1.18}$$

where $\sigma_{x,y,z}$ are now Pauli matrices acting in the space spanned by the conduction and valence bands (that do not coincide with sublattices, as was the case for graphene) and s_z is a Pauli matrix acting in spin space. All these features are sketched in Fig. 1.2c.

1.2 Topology in physics

Up to very recently, the underlying principle beyond the classification of quantum phases of matter has been that of spontaneous symmetry-breaking. Specifically, phase transitions from a given quantum state to a lower symmetry state where one or more symmetries have been broken are the object of the Ginzburg-Landau theory [59], that has been the paradigm for explaining (almost) all of the exotic quantum phases discovered during last century, among which superconductivity, ferromagnetism, Bose-Einstein condensation and many more. In this theory, the microscopic details of the system under analysis are disregarded and quantum states are characterized by a *local* order parameter that assumes a nonzero value only in the highly ordered symmetry-broken phase. However, during the last decades its has become overwhelmingly clear that there are a number of phases of matter that are not captured by this model, characterized by a higly *non-local* order parameter, for which a Landau-Ginzurg theory cannot be developed in the standard way. These phases are said to be topologically ordered, and their classification required elaborating a novel paradigm that rests on concepts borrowed from the mathematical notion of topology [60–62].

The mathematical concept of topological invariance is introduced to classify different geometrical objects into broad classes distinguished by their shapes in spite of their microscopic properties [63]. This leads to a crucial criterion underpinning topological classes: according to this criterion, objects from a given class can be continuously deformed into one another, whereas objects from different classes require an abrupt and discontinuous action to transform into each other. A well-known example is that of 2D surfaces, classifiable according to the number of holes they contain. In this sense, objects with the same number of holes, or genus - e. g. zero as in the case of a sphere or an ellipsoid, or one as in the case of a donut or a teacup - belong to distinct topology classes that can be labeled by their genus.

The concept of topological classification in physics is equivalent, and applies to gapped Hamiltonians (either insulating or superconducting) of many-particle systems [64]. In this context, the idea of a continuous deformation that preserves the topological character of an Hamiltonian is that of a change that doesn't close the gap. Therefore, for two systems to be in the same class, they have to be described by Hamiltonians whose low-energy spectra can be deformed one into the other without closing the gap. In turn, if in order to deform one Hamiltonian into another the gap needs to close at some point, this indicates that the two Hamiltonians belong to different topological classes. In the same way in which 2D mathematical surfaces can be characterized by the genus, distinct physical classes of topologically inequivalent Hamiltonians can be characterized by a topological index playing the same role as the order parameter in Ginzburg-Landau theories [60,61,64]. The topological index for a given system is

determined by its dimensionality and the discrete symmetries of the Bloch Hamiltonian, and it can be either a $\mathbb{Z}$ invariant, which can take on any integer value, or a $\mathbb{Z}_2$ invariant, which can only be either 0 or 1. It has been shown that in every spatial dimension there exist precisely five distinct classes of topological insulators or superconductors, and within each class the different topological sectors can be distinguished by the topological invariant [65,66]. The theory encompassing the topological classification of solid-state gapped systems goes under the name of *ten-fold* way [66,67]. Here we will not go into further details since a full treatment of the topic is beyond the scope of this thesis and in the following we will concentrate only on the cases relevant to the topics covered in it, that are 2D systems in the presence or absence of given symmetries, such as time reversal invariance and charge conjugation.

1.2.1 Berry phase and Berry curvature

In this subsection, we present the idea of topological order as naturally emerging in the context of the evolution of quantum systems with a parametric dependence [68–70].

Basic definitions Under an adiabatic evolution of a set of 'slow' degrees of freedom $\mathbf{R} = (R_1, R_2, ...)$ that perform a closed path $\mathcal{C}$ in the parameter space, a *non-degenerate* eigenstate of an Hamiltonian that depends on these parameters picks up a geometrical phase. Two key requirements are that the state vectors $|n(\mathbf{R})\rangle$ (i) all reside in the same Hilbert space, (ii) are single-valued throughout the whole evolution. The phase thus acquired is called *Berry phase* by virtue of the physicist who first introduced it [68] and it is given by

$$\gamma_n = \oint_{\mathcal{C}} d\mathbf{R} \cdot \mathcal{A}_n(\mathbf{R}) \tag{1.19}$$

where $\mathcal{A}_n(\mathbf{R})$ is a vector called Berry connection, defined as

$$\mathcal{A}_n(\mathbf{R}) = i\langle n(\mathbf{R})|\nabla_{\mathbf{R}}|n(\mathbf{R})\rangle \tag{1.20}$$

It is easy to see that, because the eigenvector $|n(\mathbf{R})\rangle$ is gauge-dependent, $\mathcal{A}_n(\mathbf{R})$ is gauge-dependent as well. On the contrary, $\gamma_n(\mathbf{R})$ is a gauge-independent quantity and only depends on the geometric aspect of the closed path $\mathcal{C}$ on which the integration in Eq. (1.19) is performed. By drawing an analogy with electrodynamics, one can think of the Berry connection as a vector potential that, as in electromagnetism, is characterized by an intrinsic degree of arbitrariness (in other words, an intrinsic gauge-dependence) stemming from its lack of physical meaning. Following these premises, a gauge-field tensor can be derived from $\mathcal{A}_n(\mathbf{R})$ as

$$\Omega^n_{\mu\nu}(\mathbf{R}) = \frac{\partial \mathcal{A}^n_\nu}{\partial R^\mu} - \frac{\partial \mathcal{A}^n_\mu}{\partial R^\nu} = i\left[\left\langle \frac{\partial n}{\partial R^\mu}\middle|\frac{\partial n}{\partial R^\nu}\right\rangle - \left\langle \frac{\partial n}{\partial R^\nu}\middle|\frac{\partial n}{\partial R^\mu}\right\rangle\right] \tag{1.21}$$

called Berry curvature. In three and two dimensions, Eq. (1.21) can be recast in the more compact form

$$\mathbf{\Omega}_n(\mathbf{R}) = \nabla_{\mathbf{R}} \times \mathcal{A}_n(\mathbf{R}) \tag{1.22}$$

whence it is clearer that, within the previously drawn electromagnetic analogy, the Berry curvature plays the role of a magnetic field. The Berry curvature is gauge-invariant, and therefore observable, and it is a local manifestation of the geometric properties of the wavefunction in the parameter space. Because of Stoke's theorem, we have that it can be rewritten as

$$\gamma_n = \oint_{\mathcal{C}} d\mathbf{R} \cdot \mathcal{A}_n(\mathbf{R}) = \int_{\mathcal{S}} d\mathbf{S} \cdot \mathbf{\Omega}_n(\mathbf{R}) \tag{1.23}$$

where $\mathcal{S}$ is any surface enclosed by the curve $\mathcal{C}$.

The Berry phase is somewhat special in that it is a potentially observable quantity that nonetheless cannot be expressed in the usual form for observable physical quantities, that is, expectation values of Hermitian operators. This peculiarity stems from the assumption made at the very beginning that the Hamiltonian depends on a set of parameters, what in general implies that the system it describes is not isolated. In fact, a parametric dependence of the Hamiltonian always encodes a coupling with degrees of freedom that are not included in the Hilbert space, and is due to the fact that the system under analysis is not truly isolated but rather part of a larger system. The consequence of this projection is that some observable quantities manifest as gauge-invariant phases rather than expectation values of operators.

Berry phase effects on crystalline solids In crystalline solids, by performing an opportune unitary tranformation one can cast the original problem into one characterized by a $\mathbf{k}$-dependent Hamiltonian $H(\mathbf{k})$ ($\mathbf{k}$ being the crystal momentum) with eigenstates $|u_n(\mathbf{k})\rangle$ all living in the same Hilbert space [69,70]. This space is nothing but the Brillouin zone, that can be considered as the parameter space for the transformed Hamiltonian $H(\mathbf{k})$. We therefore identify the Bloch momentum $\mathbf{k}$ with the parameter $\mathbf{R}$. Since the $\mathbf{k}$-dependence of the eigenstates is inherent to the Bloch problem, as this parameter is moved through a closed path in the Brillouin zone, the Bloch states will inevitably pick up a Berry phase given by

$$\gamma_n = i \oint_{\mathcal{C}} d\mathbf{k} \cdot \langle u_n(\mathbf{k}) | \nabla_{\mathbf{k}} | u_n(\mathbf{k}) \rangle \tag{1.24}$$

with the Berry curvature now defined as

$$\mathbf{\Omega}_n(\mathbf{k}) = \nabla_{\mathbf{k}} \times i \langle u_n(\mathbf{k}) | \nabla_{\mathbf{k}} | u_n(\mathbf{k}) \rangle \tag{1.25}$$

Notice that the Berry curvature is an intrinsic property of the band structure since it only depends on the wavefunction.

Anomalous velocity A fundamental consequence of the Berry phase effects on the properties of Bloch electrons is that the group velocity of electrons subject to an external electric field acquires an additional term, called the anomalous velocity, that is proportional to the Berry curvature and to the applied field, namely

$$\mathbf{v}_n(\mathbf{k}) = \nabla_{\mathbf{k}} \varepsilon_n(\mathbf{k}) \rightarrow \mathbf{v}_n(\mathbf{k}) = \nabla_{\mathbf{k}} \varepsilon_n(\mathbf{k}) - \frac{e}{\hbar} \mathbf{E} \times \mathbf{\Omega}_n(\mathbf{k}) \tag{1.26}$$

where $\varepsilon_n(\mathbf{k})$ is the dispersion of the n-th non degenerate crystalline band [70,71]. It is easy to see that since this additional term is always perpendicular to the direction of the applied field, it will give rise to a transverse, or Hall, component in the velocity. This phenomenon is at the basis of virtually every unquantized *intrinsic* Hall phenomena occuring in metals, from the well-known Hall effect to more exotic ones such as the intrinsic anomalous or the valley Hall effects.

Given that the group velocity must be invariant under the symmetries of the system, one can obtain valuable information from Eq. (1.26). In fact, in the presence of time reversal (TR) symmetry, imposing that $\mathbf{v}_n$ and $\mathbf{k}$ change sign under TR whereas $\mathbf{E}$ does not, results in the following condition for the Berry curvature:

$$\mathbf{\Omega}_n(-\mathbf{k}) = -\mathbf{\Omega}_n(\mathbf{k}) \tag{1.27}$$

Instead, in the presence of inversion symmetry, imposing that $\mathbf{v}_n$, $\mathbf{k}$ and $\mathbf{E}$ all change sign under inversion results in the following condition on the Berry curvature:

$$\mathbf{\Omega}_n(-\mathbf{k}) = \mathbf{\Omega}_n(\mathbf{k}) \tag{1.28}$$

Of course, this implies that when both symmetries are present the Berry curvature has to vanish identically throughout the whole Brillouin zone. However, in systems where either symmetry is broken or both are, the Berry curvature can be non-zero and in this case the anomalous group velocity will be finite as well, thus originating a Hall current in metals or, as we will see below, allowing for topological invariants such as the Chern number to be nonzero.

Chern number In a 2D insulating system, the integral of the Berry curvature over the full BZ, a closed manifold that has the topology of a torus, is quantized in the units of 2π and is nothing but the Chern number of the filled bands, where the Chern number of the n-th band is defined as

$$C_n = \frac{1}{2\pi} \int_{BZ} dk_x dk_y \, \mathbf{\Omega}_n(\mathbf{k}). \tag{1.29}$$

This number is a $\mathbb{Z}$ topological invariant [66] that equals to the net number of monopoles inside the BZ, that are degeneracy points in the parameter space. Notice that, because of Eq. (1.27), the Chern number is identically zero if time reversal invariance holds. In turn, it can be shown that the Chern number of 2D insulators is connected with the Hall conductance as

$$\sigma_{xy} = \frac{e^2}{h} \sum_{n \in \text{filled bands}} C_n. \tag{1.30}$$

The Chern number stays exactly quantized even in the presence of many-body interactions and disorder. The reason is to be sought in the fact that it must be an integer, so it can only be varied in a discontinuous way. Therefore, small perturbations (that result in small changes of topologically trivial physical quantities) cannot change it [70]. This, in turn, is physically reflected in the robustness of the Hall conductance against perturbations.

We notice that the Chern number is a special case of a $\mathbb{Z}$ topological invariant characterizing 2D systems with no TR symmetry. However, systems with different symmetries and in different dimensions will be characterized by invariants (either $\mathbb{Z}$ or $\mathbb{Z}_2$) other than the Chern number [66]. Importantly, since the protection discussed above is a general outcome of topological invariance, it holds for any system characterized by any other finite invariant.

Bulk-boundary correspondence The result of obtaining a nonzero conductance when the Fermi level lies within a gap may at first sight seem puzzling. This apparent contradiction is clarified by the mathematical argumentations given above, stating that the gap closure between two topologically distinct phases is unavoidable. This gap closure is the key to understand the nonzero conductance: edge states must appear at the boundary between systems belonging to different topological classes. In particular, since the vacuum can be considered as a trivial insulator, it is to be expected that any system with a non-zero topological invariant presents edge modes at the boundary with vacuum. These modes are responsible for carrying the protected quantized currents predicted by theory in the form of an integer Hall conductance in the units of e^2/h (cfr Eq. (3.22)), and are therefore a robust property as long as the symmetries of the system are preserved. This is true of course if the system size is larger than the typical extension of the edge states, that

are exponentially localized on a distance given by the inverse of the gap, so that they do not couple through the bulk. These ideas are part of a more general paradigm, known as the bulk-edge correspondence, stating that at the boundary between two systems characterized by different topological indexes will arise a number of edge modes equal to the difference in topological indexes of the two systems [71].

1.2.2 Celebrated topological phases

In this subsection we encompass some of the topological phases relevant to this thesis.

Quantum Hall effect The paradigm example of the phenomenology described so far is the integer quantum Hall effect (QHE), discovered by Klitzing *et al.* in 1980 [72], who found that in a strong magnetic field the Hall conductance is exactly quantized in units of e^2/h. The origin of this quantized transverse conductivity must be sought not in the mere formation of Landau levels but rather in their nontrivial topological character or, stated more rigorously, in the fact that the Chern number of the bands is nonzero. In turn, this is possible because the presence of a magnetic field breaks time reversal invariance, an ingredient that is necessary to have a net nonzero Berry curvature in the magnetic BZ, as made clear by Eq. (1.27). As seen above, the Chern number of the system corresponds to the number of conductance channels emerging at the boundaries with vacuum, that in the case of the QHE is also referred to as the filling factor ν. These channels are chiral, meaning that they carry charge unidirectionally, and they are protected from backscattering by the spatial separation of the counterpropagating channels, that are found at the opposite edge of the sample. The physics of the QHE will be studied in detail in the next subsection, and it will be a crucial ingredient of the phenomena discussed in the third and fourth chapters of the thesis.

Topological insulators and quantum spin Hall effect A distinct topological class is that of time reversal invariant systems with strong spin-orbit coupling. These systems are also called topological insulators (TIs), and they can be either two-dimensional or three-dimensional. One of the first theoretical poposal for 2D TIs, also called quantum spin Hall (QSH) insulators, was cast by Bernevig, Hughes and Zhang in 2006 [73]. Specifically, they predicted a thickness-dependent SOC-driven gap inversion in HgTe/CdTe quantum wells associated with a topological quantum phase transition, a prediction that was experimentally confirmed for the first time by Koning *et al.* in 2007 [74]. This phase is characterized by two oppositely spin-polarized counterpropagating edge states. Because of SOC, the spin polarization is bound to be perpendicular to the direction of motion, and because of this spin-momentum locking these states are also referred to as helical and they are protected from backscattering by time reversal symmetry. However, these systems have a zero Chern number in the BZ because of TR invariance. However, nonzero quantized responses are still possible. By defining a Chern number for each spin polarization, C_σ with $\sigma = \uparrow, \downarrow$, one can define a 'spin Chern number' as $C_s = C_\uparrow - C_\downarrow$, indicating that there is a net spin current circulating along the edges of the system. This quantity is a $\mathbb{Z}_2$ topological invariant, fundamentally different from $\mathbb{Z}$ invariants as the Chern number, which characterizes the topological nature of TR invariant bands of 2D systems with well-defined spin polarization. When spin is not well defined C_s loses its meaning, although a $\mathbb{Z}_2$ topological invariant can always be defined for time-reversal symmetric 2D systems [66,67]. Remarkably, QSH phases are also possible in systems with no TRS. Discussing a concrete realization of this possibility is the subject of chapter three.

Analogously to 2D TIs, 3D TIs are characterized by a bulk gap and gapless surface states. Specifically, special compounds such as Bi_2Te_3, Sb_2Te_3 and Bi_2Se_3 exhibit surface states consisting of a single Dirac cone [75–78].

Quantum anomalous Hall effect A state of matter that is closely related with the QSH insulator but that exists in the absence of TR symmetry is the so-called quantum anomalous Hall (QAH) insulator, that is a band insulator characterized by chiral quantized edge conductance without an orbital magnetic field [64]. The simplest way of realizing this phase is by introducing magnetic dopants into a TI, which has the effect of breaking TR symmetry. Loosely speaking, doping the system with spin-polarized impurities changes the spin-dependent chemical potentials of the two conducting spin species of the QSH insulator, in turn modifying in opposite fashions the sizes of their bulk gaps. At a critical density of dopants, one of the two spin species is completely depleted, thus leaving the system with only the edge states associated with the opposite spin polarization to conduct. The original helical system (two oppositely spin-flavoured counterpropagating states) is therefore converted into a chiral one (only one spin-polarized species conducting), corresponding to the evolution from a QSH phase to a QAH phase, or, equivalently, from a system characterized by a $\mathbb{Z}_2$ to one characterized by a $\mathbb{Z}$ topological invariant. Other possibilities exist, such as coupling 2D systems to non-trivial magnetic textures [79,80], decorating a honeycomb lattice with alternate positive and negative magnetic fluxes that sum to a net zero flux [81], or combining Rashba SOC and exchange in graphene [11].

Anomalous Hall effect Analogously to the standard quantum Hall effect, also the anomalous one presents an unquantized version, the anomalous Hall effect (AHE), a phenomenon observed in conducting ferromagnets when spin-orbit interactions are important [82]. This effect refers to the onset of a finite transverse Hall conductance induced by the momentum-space Berry curvature-related anomalous contribution to the group velocity. This is possible because, even though no magnetic field is needed for this effect to occur, TR symmetry is broken by the ferromagnetic ordering of the system. As we will see in chapter two, this physics can also arise in the presence of non-coplanar spin structures (known as skyrmions) with associated spin-chirality and real-space Berry curvature [82–84].

Topological supeconductors Insulating states such as those reviewed above are not the only ones to which the idea of a topological order can be attached. Among other, an additional topological phase of matter that is relevant to this thesis and specifically to chapter four, is that of topological superconductivity [64,67,71,85]. There is a direct analogy between superconductors (SCs) and insulators because the Bogoliubov-de Gennes Hamiltonian for the quasiexcitations of a superconducting condensate is analogous to that of an insulator, in that they both have a gapped spectrum. Therefore, it is natural to expect that the concepts borrowed from topology can be extended from the insulating to the superconducting state. In 2D, the classification of topological SCs is similar to that of topological insulators. TR breaking SCs are classified according to an integer $\mathcal{N}$ ($\mathbb{Z}$ invariant), similarly to how the Chern number classifies TR breaking topological phases, whereas TR invariant SCs are classified by a $\mathbb{Z}_2$ invariant. TR breaking topological SCs in 1D and 2D are specially interesting because of their relation with non-Abelian statistics and their potential application in the field of topological quantum computation [64,86]. The simplest model of a topological SC is that of the $\mathcal{N} = 1$ $p_x + ip_y$ pairing state for spinless fermions in 2D, characterized by one Majorana zero mode bound to each of

its vortices (giving rise to exotic non-Abelian statistics when the vortices are moved one around the other), plus a chiral Majorana edge state circulating along the boundary [86]. However, many more platforms have been proposed for engineering topological superconductivity. We postpone a more exhaustive discussion about this topic to chapter four, that is entirely dedicated to exploring this phase of matter.

1.2.3 The quantum Hall effect

As mentioned above, the quantum Hall effect was the first phenomenon to be associated with the existence of topological pahses of matter. Before its discovery in the eighties, only the classical version of this effect was known, and it had been discovered a century earlier by Edwin Hall [87]. This effect consists in the generation of a voltage difference (the Hall voltage) across an electrical conductor, transverse to an applied electric current and to a magnetic field perpendicular to the current. This phenomenon can be classically explained by the transverse accumulation of charges driven by the Lorentz force that acts on the carriers by deflecting their trajectory. The accumulated charges, in turn, give rise to an induced electric field that explains the measured Hall voltage. An hand-waving explanation of the QHE is that for large applied magnetic field, the cyclotron orbits traced by the charges decrease in radius so that they tend to effectively localize. In this situation, the only electrons that can contribute to transport are those at the boundaries of the sample that follow a path of skipping orbits through which thay can propagate across the edges of the sample. A more rigurous quantum-mechanical account of this phenomenon, though not involving topological concepts, is provided by the calculation of the spectrum of a 2D system in an out-of-plane magnetic field. Given the importance of this effect for large part of this thesis, we review below the calculation of the QH spectrum for two different platforms, namely standard 2DEGs (relevant for chapter four) and graphene (relevant for chapter three).

The quantum Hall effect in 2DEGs

The Hamiltonian for nearly-free electrons reads:

$$H = \frac{p^2}{2m}$$

where m is the effective mass near the conduction band edge. When an electromagnetic field is present, described by a vector potential $\mathbf{A}$, by performing the minimal coupling the Hamiltonian results in:

$$H = \frac{(\mathbf{p} - q\mathbf{A})^2}{2m}$$

in the case of electrons $q = -e$, therefore:

$$H = \frac{(\mathbf{p} + e\mathbf{A})^2}{2m} \tag{1.31}$$

By choosing the Gauge $\mathbf{A} = B(0, x, 0)$ one gets

$$H = \frac{(p_x, p_y + eBx, 0)^2}{2m} = \frac{p_x^2 + (p_y + eBx)^2}{2m}$$

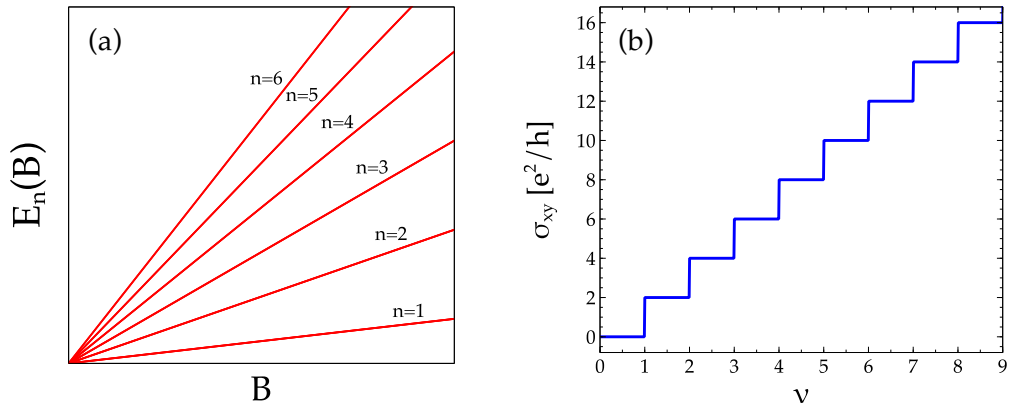

FIGURE 1.3: (a) Dispersion of the first six Landau levels of a 2DEG as a function of the magnetic field. (b) Hall conductance σ_{xy} as a function of the filling factor ν for a 2DEG.

By considering a trial solution of the kind $\psi(x,y) = e^{ik_y y}\phi(x)$ the Schroedinger equation associated with this Hamiltonian reads

$$\left[\frac{p_x^2 + (p_y + eBx)^2}{2m}\right] e^{ik_y y}\phi(x) = \epsilon e^{ik_y y}\phi(x)$$

By applying the derivative contained in the y component of the momentum operator, this reduces to

$$\left[\frac{p_x^2 + (k_y + eBx)^2}{2m}\right] \phi(x) = \epsilon\phi(x)$$

We define:

$$H_{k_y}(x, p_x) = \frac{p_x^2}{2m} + \frac{e^2B^2}{2m}\left(x + \frac{ky}{eB}\right)^2 = \frac{p_x^2}{2m} + \frac{e^2B^2}{2m}\left(x + \ell_B^2 k_y\right)^2$$

with $\ell_B = \sqrt{1/eB}$ the magnetic length. By further defining the cyclotron frequency as $\omega_c = eB/m$, the Hamiltonian becomes

$$H_{k_y}(x, p_x) = \frac{p_x^2}{2m} + \frac{1}{2}m\omega_c^2\left(x + \ell_B^2 k_y\right)^2$$

This is nothing other than the Hamiltonian of a quantum harmonic oscillator with frequency given by the cyclotron frequency and centered around the guiding center coordinate $x^* = -\ell_B^2 k_y$. This entails that the position along the x direction and the momentum along the y become correlated in such a way that the wavefunctions of electrons with opposite momenta k_y and $-k_y$ are centered around opposite positions along the x direction, x^* and $-x^*$. Secondly, the energy levels are given by

$$\epsilon_n = \omega_c\left(n + \frac{1}{2}\right) \quad n = 0, 1, 2, ... \tag{1.32}$$

that is, they are independent of k_y and therefore they do not disperse. This result indicates that the spectrum is organized in evenly spaced non-dispersing harmonic oscillator levels, that are called Landau levels (LLs), whose energy grows linearly with the magnetic field (see Fig. 1.3a). Due to the lack of dependence of the energy on k_y, the degeneracy

of each level is enormous. The total number of states in each Landau level can be calculated to be $N = \Phi/\Phi_0$ where $\Phi = BS$ is the flux of the magnetic field and $\Phi_0 = h/e$ the flux quantum. Therefore, the degeneracy of each LL is given by the number of flux quanta penetrating the sample. To these eigenenergies correspond the harmonic oscillators eigenfunctions

$$\psi_{n,k_y}(x,y) = \frac{e^{ik_y y}}{\sqrt{L_y}}\varphi_n(x + \ell_B^2 k_y) \tag{1.33}$$

where

$$\varphi_n(x) = \frac{1}{\sqrt{2^n n! \pi^{1/2} \ell_B}} H_n\left(\frac{x}{\ell_B}\right) e^{-x^2/2\ell_B^2}$$

and $H_n(x)$ is a Hermite polynomial of order n. The Hall conductance associated with the dispersion in Eq. (1.32) is

$$\sigma_{xy}^{\text{2DEG}} = \frac{2e}{h} n \quad n = 0, 1, 2, ... \tag{1.34}$$

and it is shown in see Fig. 1.3b.

The quantum Hall effect in graphene

We now provide the same derivation in graphene. By using the gauge as before, $\mathbf{A} = B(-y, 0, 0)$, we perform the minimal coupling substitution into graphene's Hamiltonian

$$H = v_F \left[\tau p_x \sigma_x + p_y \sigma_y\right] \rightarrow v_F \left[\tau(p_x + eA_x)\sigma_x + (p_y + eA_y)\sigma_y\right] =$$
$$v_F \left[\tau(p_x - eBy)\sigma_x + p_y \sigma_y\right] \tag{1.35}$$

The generic solution for the associated Dirac equation

$$v_F \left[\tau(-i\partial_x - eBy)\sigma_x - i\partial_y \sigma_y\right] \psi(x,y) = \epsilon \psi(x,y) \tag{1.36}$$

has the form $\psi(x,y) = e^{ik_x x}\phi(y)$. Substituting into Eq. (1.36) we arrive at

$$v_F \left[\tau(k_x - eBy)\sigma_x - i\partial_y \sigma_y\right] \phi(y) = \epsilon \phi(y) \tag{1.37}$$

that in matrix form reads

$$v_F \begin{pmatrix} 0 & \tau(k_x - eBy) - \partial_y \\ \tau(k_x - eBy) + \partial_y & 0 \end{pmatrix} \phi(y) = \epsilon \phi(y) \tag{1.38}$$

By defining the variable $\xi = \ell_B k_x - y/\ell_B$, with ℓ_B the previously introduced magnetic length, this equation can be rewritten as

$$\frac{v_F}{\ell_B} \begin{pmatrix} 0 & \tau\xi - \partial_\xi \\ \tau\xi + \partial_\xi & 0 \end{pmatrix} \phi(\xi) = \epsilon \phi(\xi) \tag{1.39}$$

In valley $\mathbf{K}$, where $\tau = 1$, we have

$$\frac{v_F}{\ell_B} \begin{pmatrix} 0 & -\partial_\xi + \xi \\ \partial_\xi + \xi & 0 \end{pmatrix} \phi(\xi) = \omega_c \begin{pmatrix} 0 & a^\dagger \\ a & 0 \end{pmatrix} \phi(\xi) = \epsilon \phi(\xi) \tag{1.40}$$

where $\omega_c = \sqrt{2}v_F/\ell_B$ is the cyclotron frequency of graphene and a, $a^\dagger$ are the standard annihilation and creation harmonic oscillator operators, defined as

$$a = \frac{1}{\sqrt{2}}(\partial_\xi + \xi) \quad \text{and} \quad a^\dagger = \frac{1}{\sqrt{2}}(-\partial_\xi + \xi) \tag{1.41}$$

Eq. (1.40) admits the solutions

$$\phi_n^{\mathbf{K}}(\xi) = \begin{pmatrix} \Psi_n(\xi) \\ \pm\Psi_{n-1}(\xi) \end{pmatrix} \tag{1.42}$$

associated to the eigenenergies $\epsilon_n = \pm\omega_c\sqrt{n}$, where the $\Psi_n(\xi)$ are the solutions of the quantum harmonic oscillators already encountered in Eq. (1.33). On the other hand, in valley $\mathbf{K}'$, where $\tau = -1$, we have

$$\frac{v_F}{\ell_B}\begin{pmatrix} 0 & -\partial_\xi - \xi \\ \partial_\xi - \xi & 0 \end{pmatrix}\phi(\xi) = -\omega_c\begin{pmatrix} 0 & a \\ a^\dagger & 0 \end{pmatrix}\phi(\xi) = \epsilon\phi(\xi) \tag{1.43}$$

Eq. (1.43) admits the solutions

$$\phi_n^{\mathbf{K}'}(\xi) = \begin{pmatrix} \Psi_{n-1}(\xi) \\ \mp\Psi_n(\xi) \end{pmatrix} \tag{1.44}$$

associated to the eigenenergies $\epsilon_n = \pm\omega_c\sqrt{n}$. The Landau levels at the opposite Dirac points $\mathbf{K}$ and $\mathbf{K}'$ have exactly the same spectrum and hence each Landau level is doubly degenerate. Considering the spin degeneracy as well, the total degeneracy of each LL is 4. Notice also that the cyclotron frequency, that sets the scale of the separation between LLs, is now proportional to $\sqrt{B}$ in contrast with the nonrelativistic problem where the cyclotron energy is linear in B, compare Fig. 2.3a with Fig. 1.3a. This implies that the energy scale associated with the Dirac fermions is rather different from the one found in ordinary 2DEGs, and it can be up to two orders of magnitude larger than the latter for fields of the order of ≈ 10 T. The $\sqrt{n}$ dependence of the LLs dispersion relation has two important consequences: (i) LLs in graphene are not evenly spaced as they are in standard 2DEGs; (ii) a LL of zero energy associated with $n = 0$ exists. This last property, together with the additional valley degeneracy characteristic of graphene, is responsible for the non conventional sequence of plateaus of the transverse conductivity in the QHE regime

$$\sigma_{xy} = \pm\frac{4e}{h}\left(n + \frac{1}{2}\right) \quad n = 0, 1, 2... \tag{1.45}$$

shown in Fig. 2.3b, where we notice in particular the absence of a plateau at $n = 0$. The eigenfunctions for the anomalous 'zero' Landau level (ZLL) are

$$\phi_0^{\mathbf{K}}(\xi) = \begin{pmatrix} \Psi_0(\xi) \\ 0 \end{pmatrix} \tag{1.46}$$

in valley $\mathbf{K}$ and

$$\phi_0^{\mathbf{K}'}(\xi) = \begin{pmatrix} 0 \\ \Psi_0(\xi) \end{pmatrix} \tag{1.47}$$

in valley $\mathbf{K}'$. This result is crucial. It entails that the ZLL at each valley is completely sublattice polarized, and that the sublattice polarization at different valleys is opposite. As we will see in the third chapter, the valley-sublattice locking of the ZLL together with its fourfold degeneracy allow for interactions to split it nontrivially at high magnetic

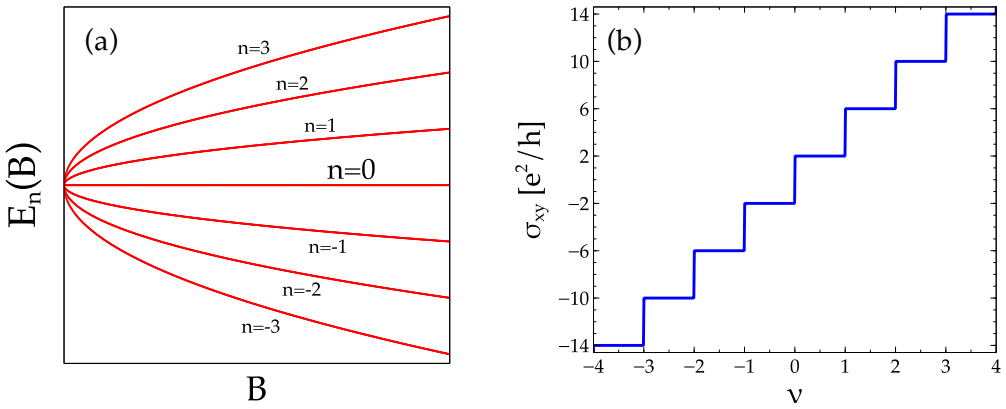

FIGURE 1.4: (a) Dispersion of the first seven Landau levels ($n \in [-3:3]$) of graphene as a function of the magnetic field. (b) Hall conductance σ_{xy} as a function of the filling factor ν for monolayer graphene.

fields, with appealing consequences.

1.3 Organization of the thesis

The thesis is organized as follows.

In the second chapter we investigate the Hall response that non-coplanar spin structures are able to induce in graphene via proximization of the latter with a magnetic insulating system. In particular, by calculating the Hall conductance of a graphene flake placed on top of a magnetic material, we demonstrate that this device can be a powerful detector of skyrmions, using as a working principle the anomalous Hall effect produced by the exchange interaction of the graphene electrons with the noncoplanar magnetization of these objects. The tool employed to calculate the conductance of a multiterminal graphene quantum dot is that of Landauer-Buttiker formalism for quantum transport on the lattice [88]. We show that for realistic exchange interactions a single skyrmion yields Hall voltages well within reach of the experimental state of the art, and fairly stronger than those that standard 2DEGs would develop in an analogous configuration. This result is quite robust against a number of contingent effects that may condition the measurement, among which the presence of random disorder in a dirty sample and the periodic potential associated with the mismatch between the graphene sample and the insulator underneath.

In the third chapter we study the possibility of stabilising a quantum spin Hall phase in twisted graphene bilayer in the QH regime. Previous proposals to engineer such a phase in graphene rested on either the intrinsic spin-orbit coupling of graphene [6] or on interaction-induced broken-symmetry states of graphene monolayers in the presence of a large Zeeman field [89]. However, the SOC strength in graphene is quite weak so that the expected QSH gap is inadequately small for any practical purpose [7,90]. On the other hand, the excessively strong Zeeman fields needed for the second implementation are incompatible with the realistic objective of engineering Majorana physics in graphene by proximity to a superconductor. The alternative set-up that we put forward, by contrast, doesn't rest on either of these two interactions, with the QSH phase being induced instead by a combination of electronic interactions and gating. We notice that the proposed phase is fundamentally different from the one extensively described in section 1.2 since

in the present system TR symmetry is broken by the presence of a magnetic field. We analyze how magnetic flux, electric field, interlayer rotation angle and interactions, treated at a mean field level, combine to produce the targeted QSH phase. We compare our results with an experimental realization of this very scheme [91] and find, in particular, that purely local electronic interactions are not sufficient to account for the experimental observations, which demand at least nearest-neighbour interactions to be included.

In the fourth chapter we consider a 2DEG in the QH regime in the presence of a Zeeman field, with the Fermi level tuned to filling factor $\nu = 1$. We show that, in the presence of spin-orbit coupling, contacting the 2DEG with a narrow strip of an s-wave superconductor produces a topological superconducting gap along the contact as a result of crossed Andreev reflection processes across the strip. Remarkably, the sign of this topological gap is found to depend periodically on the ratio between the strip width and the Fermi wavelength. An interface between two halves of a long strip with topological gaps of opposite sign implements a novel kind of π junction, hosting a pair of Majorana zero modes that do not split despite their overlap. We show that this junction is robust and less sensitive to small perturbations if compared with standard Josephson π junctions. We finally propose that such a finding can be exploited to perform protected non-Abelian *tunnel-braid* operations [92] that generalize standard braiding of Majorana bound states. The superiority of executing this kind of operations in the proposed platform is that they do not require any fine tuning of the parameters.

In the fifth chapter we use group theoretical arguments for classifying Bloch bands and electronic operators relevant for the low-energy dispersion of 2D TMDCs at the inequivalent corners of the BZ, where we choose to triple the unit cell in such a way that the valleys become equivalent and can be treated on equal footing. A $\mathbf{k} \cdot \mathbf{p}$ theory-based approach then allows us to derive a low-energy effective Hamiltonian for describing the lowest conduction and valence bands. This model captures several important features, namely the trigonal warping of the bands, electron-hole symmetry breaking, and the appearence of a quadratically dispersing mass term. Starting from this model, we deduce the most general form of disorder potential that break all the symmetries of the system with the exception of time reversal.

Chapter 2

Electrical detection of skyrmions in graphene devices

2.1 Introduction

The interest in magnetic skyrmions, noncoplanar spin textures endowed with nontrivial real-space topolgical features, has witnessed a momentous increase in recent years owing to the improved ability to experimentally detect and manipulate them [93–95]. Skyrmions are predicted to occur in noncentrosymmetric magnetic crystals with chiral interactions, and they have been observed forming lattices in a variety of materials ranging from metallic and semiconducting [96–100] to insulating such as the chiral-lattice magnet Cu_2OSeO_3 [101–104] and the scandium-doped hexagonal barium ferrite $BaFe_{12-x-0.05}Sc_xMg_{0.05}O_{19}$ with $x = 0.16$ [105]. To date, they are detected by means of neutron scattering [96], tunneling electron microscopy (TEM) [97] and even individually, with atomic scale resolution, by means of spin-polarized scanning tunneling microscopy (SP-STM) [93,106,107] and atomic size sensors [108].

A variety of interactions can assist noncollinear arrangements, and sometimes more than one contribute simultaneously [83]. These include: (i) long-ranged magnetic dipolar interactions [109,110]; (ii) the relativistic Dzyaloshinskii-Moryia interaction [111,112] in non-centrosymmetic magnets; (iii) frustrated exchange interactions [113] or (iv) four-spin exchange interactions [107], and the size of an individual skyrmion can range from 1 nm to 1 μm depending on which specific mechanism is involved. The common physical phenomenon underlying all of these interactions is the competition felt by the spins between aligning with their neighbors and being perpendicular to them, which favors chiral ordering. In most cases, this happens in systems where inversion symmetry breaking combined with spin-active interactions stabilize a frustration-induced spin spiral (or helical) ground state at zero field. A skyrmion lattice phase is then favored as a result of applying a magnetic field, since, in contrast to the spin spiral state which is magnetically compensated, the skyrmion lattice exhibits a net magnetization and is, therefore, favored by the Zeeman energy [83]. By further increasing the magnetic field, the parallel alignment of the magnetic moments becomes energetically more and more favorable, until the skyrmion phase is eventually saturated to a conventional ferromagnetic phase [83,93,98]. It is therefore the competition between the energy scales set by the external field and the internal spin degrees of freedom what controls the phase space of these systems, and specifically the extension (and therefore the stability) of the skyrmionic phase, that is attained for only a finite range of external fields and temperatures. An example of the transition through these phases can be nicely observed in Fig. 2.2a, where a sequence of SP-STM images of a PbFe bilayer on Ir(111) is shown as the magnetic field is ramped up [93], and in Fig. 2.1a, that shows a series of Lorentz TEM images of a thin film of FeGe as a function of both the magnetic field and the temperature [98]. Moreover, in thin films the physics described above acquires an additional twist since the skyrmion lattice phase

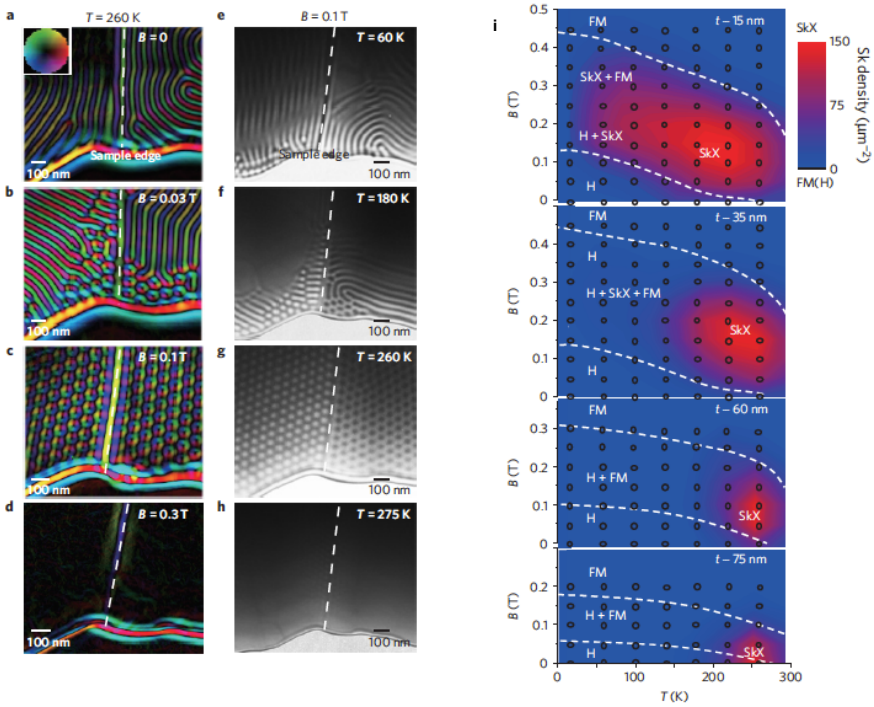

FIGURE 2.1: External magnetic field and temperature dependence of the skyrmion lattice in FeGe. (a) to (d) Changes in the lateral magnetization distribution under magnetic fields applied normal to the sample plane at a temperature $T = 260$ K. (e) to (h) Temperature dependence of the magnetic domain configuration (under-focused Lorentz transmission electron microscopy images) at a constant magnetic field of $B = 0.1$ T. (i) Thin-plate thickness dependence of the phase diagrams in the (T, B) plane. H, SkX and FM stand for the helical, skyrmion lattice and ferromagnetic phases, respectively. The colour bar indicates the skyrmion density per square micrometre. [Adapted with permission from Ref. [98]]

space has been demonstrated to increase as the thickness of the sample is decreased [98]. This behaviour is shown in Fig. 2.1b, where the phase diagram of FeGe thin films is shown at room temperature and for different thicknesses. As the sequence evidences, for thickesses $\lesssim 35$ nm the skyrmionic phase extends over a fairly wide window in the (T, B) plane, demonstrating the stabilization of a robust skyrmion lattice. These compounds are especially appealing as the diameter of the skyrmions can exceed the film thickness, which may be favorable for controlled skyrmion manipulation by surface techniques. At the ultimate limit, a single atomic layer of Fe on Ir(111) exhibits a skyrmion lattice even in the *absence* of an external field [93,107].

The topological nature of skyrmions combined with their particle-like nature and high insensitivity to roughness has motivated proposals to use them as elementary units to store classical digital information [114–116], inspired by the magnetic domain-wall racetrack memories [117]. Such a perspective has become increasingly attractive since the possibility of manipulating two-dimensional magnetic lattices by creating and destroying individual skyrmions by means of spin-polarized currents in STM devices has been experimentally proved [95] in an ultrathin film of a PbFe bilayer on Ir(111). This is shown with vivid clarity in Fig. 2.2b, where the sequence of the individual writing and deleting processes at four atomic defects is framed in a series of constant-current images. The above possibility, along with the finding [114,118] of skyrmion motion driven by ultralow current densities on the order of 10^{-6} A m^{-2}, considerably smaller than those needed for domain-wall motion in ferromagnets, makes skyrmions potentially optimal

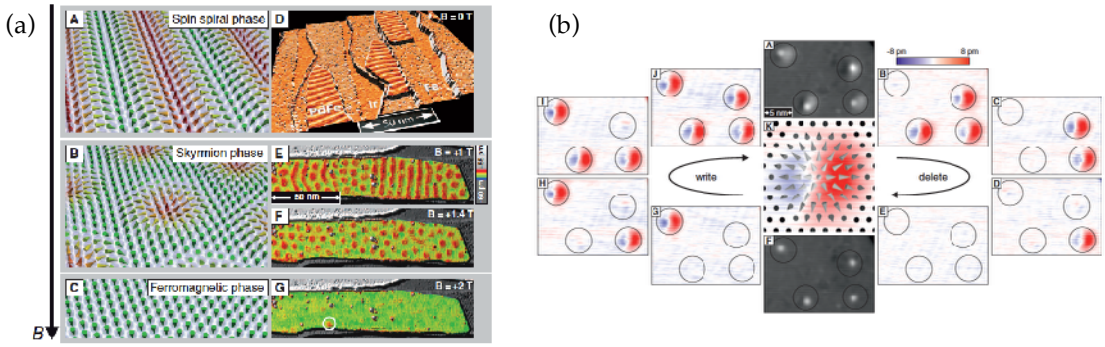

FIGURE 2.2: PbFe bilayer on Ir(111). (a) (A)-(C) Perspective sketches of different magnetic phases as the external field B is ramped up. (D) Overview SP-STM image of the sample at $B = 0$ T. (E)-(G) PdFe bilayer at different finite magnetic fields (magnetically out-of-plane sensitive tip). (E) Coexistence of spin spiral and skyrmion phase. (F) Pure skyrmion phase. (G) Ferromagnetic phase. (b) Creation and annihilation of single skyrmions. (A) Constant current image of a sample region with four defects, each hosting a skyrmion marked by a circle (magnetically in-plane sensitive tip). (B)-(E) Sequence of difference SP-STM images showing the selective erasing of all four skyrmions using local voltage sweeps. (F) The sample area without skyrmions (constant-current image) and (G) to (J) their successive rewriting (difference images). (K) Schematic spin configuration. Note that the asymmetric appearance of the skyrmions results from a canted SP-STM tip magnetization. [Adapted with permission from Ref. [93]]

candidates for the next generation of magnetoelectronic readout devices.

Because of their real-space nontrivial topology, skyrmions are able to give rise to anomalous Hall currents of intrinsic nature in the magnetic conductors that host them, what has been shown to be ascribable to an emergent gauge field that couples with the electrons' spins [82,83,119–121]. Applying external currents to skyrmionic systems can also induce the so-called skyrmion Hall effect, in which skyrmions drift through the material hosting them with a transverse velocity component arising from current-induced spin-orbit torque effects, much alike charged particles in the conventional Hall effect [83,122–124]. Interestingly, the experimental demonstration of this possibility, remained elusive for years, has been recently reported [125,126].

While many theoretical works on this topic are mainly concerned with skyrmion transportation and related effects [116,122,124], here we concentrate on the low current regime where the skyrmions stay frozen (below the critical or depinning current that is able to drag them), and suggest that their topology can be instrumental to their very detection, by using as a working principle the anomalous Hall current that they are able to induce in the itinerant electrons to whose spins they couple [83,127]. Specifically, we put forward the idea that this can be done in an exceptionally efficient way by coupling graphene Hall probes to magnetic systems. Indeed, we believe that graphene unique properties are ideal to implement such a device. First of all, being atomically thin maximizes proximity effects, making it an optimal material to grow on top of magnetic materials. To give a concrete example, the possibility of growing a graphene flake on top of a single atomic layer of Fe on a Ir(111) substrate (a system known to host a skyrmion lattice) has recently been demonstrated [80,94]. The controlled manipulation of the magnetic state of the hybrid graphene/Fe/Ir(111) islands (represented by red/green/grey areas) achieved in Ref. [94] is shown in Fig. 2.3. Furthermore, the fabrication of high-quality graphene electronic devices both at the micron and nanometer scale is absolutely well established [128–130] and its use as a magnetic sensor for magnetic adsorbates has

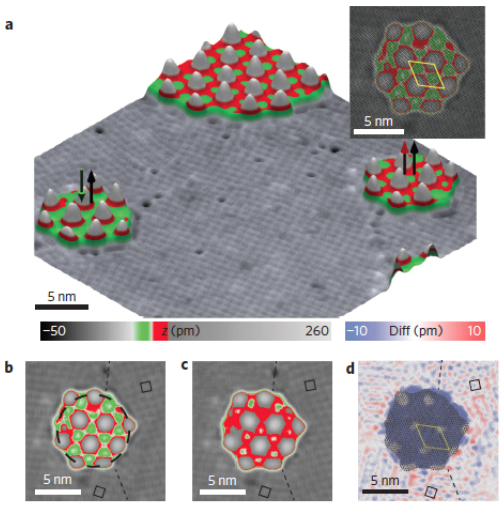

FIGURE 2.3: (a) Pseudo-three-dimensional representation of graphene islands in a monolayer of Fe on Ir(111): the skyrmion lattice is depicted in light grey, whereas graphene/Fe/Ir islands (Gr-FM units) are shown in green-red-grey. The magnetization directions (parallel or antiparallel, indicated respectively as $\uparrow\uparrow$ and $\downarrow\uparrow$) of two representative Gr-FM units with respect to the tip's magnetization direction (black arrows) are indicated by green and red arrows, respectively. (b), (c) SP-STM images of a Gr-FM unit in the $\downarrow\uparrow$ and the $\uparrow\uparrow$ states, respectively. (d) Change in magnetization visualized in a difference image: blue/red areas indicate a switch of magnetization from $\downarrow\uparrow/\uparrow\uparrow$ to $\uparrow\uparrow/\downarrow\uparrow$. [Adapted with permission from Ref. [94]]

been already tested experimentally [131,132] and studied theoretically [133]. Last but not least, it has been theoretically demonstrated [79] that coupling the Dirac electrons of graphene with a skyrmion lattice drives graphene into a quantum anomalous Hall phase characterized by a Chern number $C = 2N$ for $N = \pm 1$ already at very weak couplings, whereas in standard 2DEGs one has to go the strong coupling regime in order to attain an analogue phase [80,83,134]. All this hints at graphene as a material very sensitive to magnetic stimulii, able to generate estremely high responses if compared to non-relativistic materials. To prove our point, we compute the skewness of the scattering and the associated Hall signal induced in a graphene island coupled to a single skyrmion in a multi terminal geometry by making use of Landauer's formalism for conductance [88]. We study the magnitude of the effect as a function of the exchange interaction, skyrmion size, and device dimensions, as well as comparing it with the one that would be generated in a 2DEG under comparable circumstances [127].

The chapter is organized as follows. In the second section we introduce the mathematical properties of skyrmions and then we briefly review the possible mechanisms generating the anomalous Hall effect. In the third section we approach the problem analytically by discussing the 2D Dirac equation in the continuum coupled to a nonuniform spin texture and, performing a standard rotation in spin space, we unveil two types of influence on the Dirac electrons. In the fourth section we introduce the Landauer's formalism tool employed throughout the rest of the chapter to study the conductance in a multiterminal Hall bar geometry and describe the setup of the proposed Hall experiment. Finally, in the fifth section, we discuss the results obtained by applying Landauer's formula to a graphene flake coupled to a single skyrmion, characterizing the Hall conductance as a function of several parameters and comparing the effectiveness of graphene with that of a standard two-dimensional electron gas. Also, in this section we contrast the ideal case of a perfectly clean sample working in the balistic limit with a more realistic situation where a variety of deviations from ideality are taken into account, namely

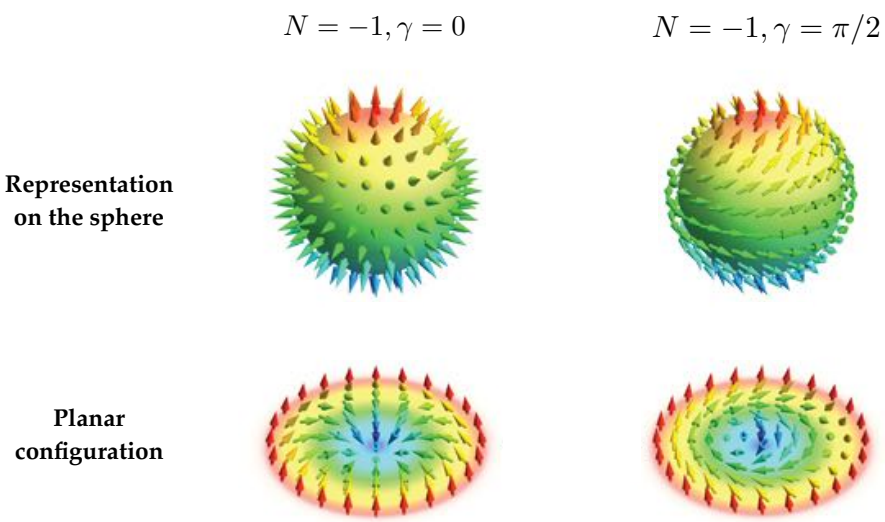

FIGURE 2.4: Planar and spherical representation of two skyrmions corresponding to the same winding number $N = -1$ and different helicities $\gamma = 0, \pi/2$.

the role of disorder, the effect of a periodic moiré potential induced by a mismatched substrate, and the possibility of non-local exchange interactions.

2.2 Theoretical background

2.2.1 Mathematical properties of skyrmions

Mathematically, skyrmions are 2D topological objects that can be characterized by an index, the winding number N, defined as

$$N = \frac{1}{4\pi} \int_{\mathcal{S}} \mathbf{n}(x,y) \cdot \left(\frac{\partial \mathbf{n}(x,y)}{\partial x} \times \frac{\partial \mathbf{n}(x,y)}{\partial y} \right) dx\, dy \tag{2.1}$$

where $\mathbf{n}(x,y) : \mathbb{R}^2 \to \mathbb{R}^3$ is a map from the 2D real space manifold to the unit sphere S_2 describing a classical unitary magnetization field, and the two-dimensional integral is performed over the overall area $\mathcal{S}$ occupied by the skyrmion [83]. The winding number N (also called topological charge) is an integer that counts how many times the spin configuration $\mathbf{n}(x,y)$ wraps around the unit sphere S_2. The configurations described by the field $\mathbf{n}(x,y)$ can be classified according to their winding number: configurations that can be smoothly deformed into each other have the same topological charge N, whereas those that need an abrupt or discontinuous change to go from one to the other belong to topological classes characterized by different winding numbers. This is the same as saying that this parameter cannot be changed by local fluctuations, since it is a global property, whereas the latter are purely local, and in this sense systems characterized by an integer value of N are said to be topologically protected phases of matter.

A skyrmion is characterized by exhibiting an integer nonzero N. To mathematically define it, one can express the magnetization field $\mathbf{n}(x,y)$ as a mapping from the polar plane coordinates $\mathbf{r} = (r, \phi)$ to the unit sphere coordinates (Φ, Θ),

$$\mathbf{n}(\mathbf{r}) = (\cos\Phi(\phi)\sin\Theta(r), \sin\Phi(\phi)\sin\Theta(r), \cos\Theta(r)) \tag{2.2}$$

provided the spin configuration at $r = \infty$ is ϕ-independent so that it can be mapped to a single point on the sphere. The integral in Eq. (2.1) can be then calculated by making use of the following transformation rules

$$\partial_x = \cos\phi\partial_r - \frac{1}{r}\sin\phi\partial_\phi \qquad \partial_y = \sin\phi\partial_r + \frac{1}{r}\cos\phi\partial_\phi \tag{2.3}$$

and by evaluating the vector product, that yields

$$\frac{\partial \mathbf{n}}{\partial x} \times \frac{\partial \mathbf{n}}{\partial y} = \frac{\partial_r\Theta\partial_\phi\Phi}{r}\sin\Theta\left(\cos\Phi\sin\Theta, \sin\Phi\sin\Theta, \cos\Theta\right) \tag{2.4}$$

so that, finally,

$$\frac{1}{4\pi}\int_{\mathcal{S}} \mathbf{n}\cdot\left(\frac{\partial \mathbf{n}}{\partial x}\times\frac{\partial \mathbf{n}}{\partial y}\right)dx\,dy = \frac{1}{4\pi}\int_0^\infty dr\sin\Theta\partial_r\Theta\int_0^{2\pi} d\phi\partial_\phi\Phi =$$

$$\frac{1}{4\pi}\left[\Phi(2\pi)-\Phi(0)\right]\left[\cos\Theta(0)-\cos\Theta(\infty)\right] \tag{2.5}$$

Since $\Phi(\phi)$ must be a single-valued function of ϕ, the difference $\Phi(2\pi) - \Phi(0)$ is an integer multiple of 2π,

$$\Phi(2\pi) - \Phi(0) = 2\pi\nu \tag{2.6}$$

On the other hand, the second factor within square brackets in Eq. (2.5) can only be nonzero if $\Theta(0) \neq \Theta(\infty)$. Specifically, it will be equal to ± 2 if

$$\cos\Theta(0) = -\cos\Theta(\infty) \tag{2.7}$$

In fact, in this case

$$N = \frac{1}{4\pi}\int_{\mathcal{S}} \mathbf{n}\cdot\left(\frac{\partial \mathbf{n}}{\partial x}\times\frac{\partial \mathbf{n}}{\partial y}\right)dx\,dy = \frac{1}{4\pi}\times(2\pi\nu)\times(\pm 2) = \pm\nu \tag{2.8}$$

Condition (2.7) is satisfied if $\Theta(0) = 0$ and $\Theta(\infty) = \pi$ or viceversa. This means that a necessary condition for the winding number to be a finite integer is that the spin polarizations picked up at $r = 0$ and $r = \infty$ must be out of plane and antiparallel. For the mapping described above we adopt the following model [83]

$$\Phi(\phi) = N\phi + \gamma \tag{2.9}$$

where N is the winding number and γ is a phase called helicity that can be gauged away by rotation around the z axis, and

$$\Theta(r) = \begin{cases} \pi & \text{for } r = 0 \\ f(r) = \pi\left(1 - r/R\right) & \text{for } 0 < r \leq R \\ 0 & \text{for } r > R \end{cases} \tag{2.10}$$

where $f(r) = \pi\left(1 - r/R\right)$ is a function of the radial coordinate that describes a smooth radial profile inside of the skyrmion radius R. Such a texture describes a magnetic configuration where the spins are all aligned perpendicular to the film plane with the exception of those comprised within the radius R that progressively align along the antiparallel direction, which is picked up exactly at $r = 0$. Two typical skyrmion configurations can be seen in Fig. 2.4, both in a planar configuration (bottom line) and wrapped around

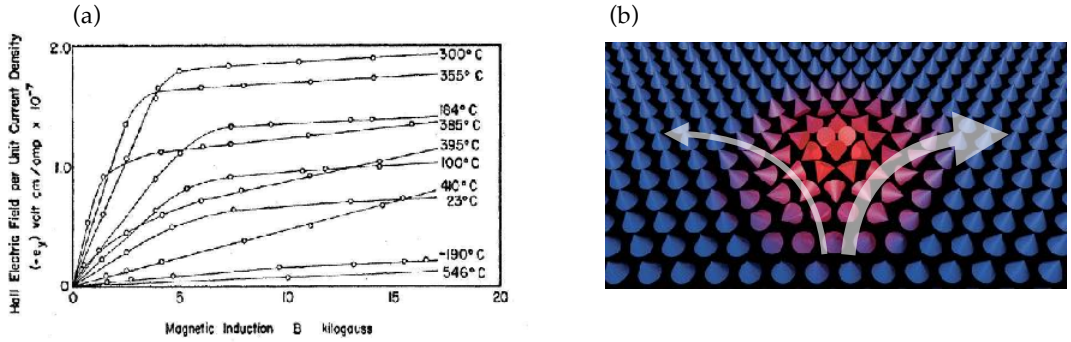

FIGURE 2.5: (a) The Hall effect in Ni. At temperatures $T \gtrsim 400^\circ$ (paramagnetic phase), the Hall response varies linearly with the field, as expected from the standard Hall effect. At temperatures $T \lesssim 400^\circ$ C the curves saturate as a function of the field, indicating the presence of an anomalous component in the Hall response. [Data from Ref. [136]] [Figure adapted with permission from Ref. [137]] (b) Schematics of the current deflection experienced by a particle surfing a magnetic skyrmion.

a sphere (top line) to make the mapping described by Eq. (4.44) more evident, corresponding both to a winding number $N = -1$ and to helicities respectively of $\gamma = 0$ and $\gamma = \pi/2$. In the following we will forget about the helicity and set $\gamma = 0$ since, being a gauge-dependent quantity, it has no physical meaning and therefore no physically observable effects.

2.2.2 The anomalous Hall effect

The so-called anomalous Hall effect (AHE) refers to the onset of large Hall currents in magnetic systems without the need of an applied magnetic field [82]. It was first detected as an additional, or 'anomalous', component in the Hall conductance summing up to the standard Hall response when a planar ferromagnetic conductor in spite of a nonmagnetic material is subject to an external magnetic field [135]. As seen in the introductory chapter of the thesis, the conventional Hall effect refers to the emergence of a voltage tranverse to an applied electric field in the presence of a perpendicular magnetic field [87]. This effect was discovered in 1879 by Edwin Hall who, already at the time, noticed that the tranverse response generated by magnetic materials was significantly higher than in nonmagnetic compounds. Remarkably, the dependence of this response on the external field is qualitatively different for the two kinds of compounds. An example of this behaviour can be seen in Fig. 2.5a, where the Hall voltage of nichel is plotted as a function of the magnetic field at different temperatures. It is clear that the standard linear dispersion is obtained only at very high temperatures ($T \gtrsim 400^\circ$ C), when the system is paramagnetic, whereas at lower temperatures ($T \lesssim 400^\circ$ C), when the system is a ferromagnetic phase, the curves saturate as a function of the field. While this phenomenon remained largely uncomprehended for roughly a century, nowadays considerable progresses have been made and light has been shed on the phenomenon to a great extent. Surveying the present understanding of the AHE, we can group the sources of the anomalous Hall currents into three broad classes: (i) skew-scattering contribution; (ii) side-jump contribution; (iii) intrinsic contribution. As for the definition of these three contributions, on which there is somewhat of a discrepancy in the literature, we refer to the quite comprehensive review presented in Ref. [82]. The skew-scattering mechanism (i) yields a Hall conductance $\sigma_{xy} = \sigma_{\mathrm{H}}$ that is proportional to the quasiparticle transport lifetime τ, and it can be ascribed to the chiral features of the disorder-induced

scattering off defects in spin-orbit coupled ferromagnets. It is therefore related to scattering, and the associated Hall resistance ρ_{H} is proportional to the longitudinal resistivity $\rho_{\mathrm{H}} \sim \rho$. The other two contributions (ii) and (iii) are both scattering-independent, and therefore the Hall conductivity does not depend on τ. Accordingly, the Hall resistivity is proportional to the square of the longitudinal resistivity, $\rho_{\mathrm{H}} \sim \rho^2$ [82]. Notice that it is this qualitative behaviour that allows discriminating between the possible causes of the observed anomalous response: the skew scattering dominates in very clean samples (since τ can be very large in this case), whereas the remnant mechanisms are expected to become important in dirty samples and at high temperatures. Among them, the side-jump mechanism is merely identified as the contribution to the scattering-independent Hall response that remains once the intrinsic contribution, for which a well-established predictive theory exists, is subtracted to it. This intrinsic contribution is the one that we have referred to in the introduction to the thesis when discussing topological features of crystalline solids. Like all the topological properties that we have covered therein, the intrinsic contribution to the anomalous Hall effect is dependent only on the Bloch eigenfunctions of the system, that in turn give information on the Berry phase and the Berry curvature [70,82]. In a nutshell, the intrinsic anomalous Hall response is the result of the onset of a finite anomalous component in the electrons group velocity that is proportional to the Berry curvature of the bands, allowed to be nonzero in magnetic systems due to TR symmetry breaking. However, notice that the presence of magnetic ordering alone is not sufficient to induce a nontrivial reciprocal-space topology since it only couples with the spin degrees of freedom and not with the orbital ones. It therefore needs to be complemented with a spin-orbit interaction that, by locking the spin to the momentum, is able to effectively give rise to a nonzero Berry curvature in the Brillouin zone.

However, ferromagnetic compounds with spin-orbit interactions are not the only candidates for developing an intrinsic anomalous response. Indeed, as has been established both theoretically [82,83,119–121,138,139] and experimentally, an akin physics takes place in non-coplanar spin-structures with associated spin-chirality and real-space Berry curvature such as magnetic skyrmions, as sketched in Fig. 2.5b. In standard 2DEGs, it has been shown that the noncoplanarity of the spins entails the formation of a solid angle which can be described by a gauge field [82,83,119–121]. This gauge field, in turn, produces an emergent electromagnetic field (EEMF) that, when the spin structure is coupled with the conduction electrons, acts as an effective field allowing an anomalous kind of Hall effect to take place. In the following section we show that an analogous phenomenology, although with a number of key differences, holds for the relativistic-like carriers of graphene when the latter is coupled to a skyrmion. In spite of the unalike details, the topologically nontrivial character of the coupled 2D system-skyrmion Hamiltonian is a common feature of both Schrodinger and Dirac electrons, stemming directly from the real-space topological properties of skyrmions.

2.3 Continuum approach

In this section we describe graphene electrons interacting with a noncoplanar magnetization field $\mathbf{n}$, as given by Eq. (4.44), using a 2D Dirac Hamiltonian:

$$H = H_0 + H_{ex} = -iv_F \left(\tau \partial_x \sigma_x + \partial_y \sigma_y\right) + J\mathbf{n} \cdot \mathbf{s} \tag{2.11}$$

with $\mathbf{s} = (s_x, s_y, s_z)$ the vector of Pauli matrices acting in spin space and $\boldsymbol{\sigma} = (\sigma_x, \sigma_y, \sigma_z)$ the vector of Pauli matrices acting in pseudospin (or, equivalently, sublattice) space. Following the procedure introduced in previous works [80,83,140,141], we perform a rotation of the Hamiltonian so that in every point of space the spin quantization axis is

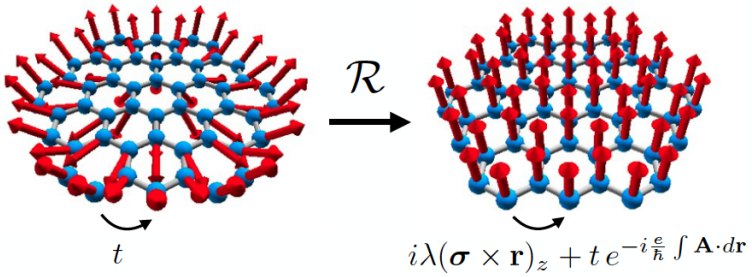

FIGURE 2.6: Mapping of a honeycomb lattice characterized by real hopping and with a double-exchange interaction with a noncoplanar magnetic texture to one with spatially uniform magnetization field and with a complex hopping function mimicking the coexistence of spin-orbit coupling with a vector gauge field.

chosen along the direction of the spin texture $\mathbf{n}$. As a result, the representation of the exchange term is diagonal in the rotated frame, but the Dirac Hamiltonian acquires new terms that encode the influence of the exchange interaction of the Dirac electrons with the noncoplanar field. This analytic model does not account for possible lattice mismatch effects between the graphene sample and the magnetic substrate, which could be responsible for valley mixing and/or coupling strenght renormalization [79]. In fact, the model is intended to qualitatively isolate the individual physical effects that sum up to give an anomalous response rather than providing an exhaustive description of the scattering problem. Microscopic effects at the lattice level will be included in the numerical tight-binding approach that is the focus of the next sections. The unitary matrix $\mathcal{R}$ that performs the above-mentioned transformation in the basis

$$\psi = (A\uparrow, B\uparrow, A\downarrow, B\downarrow)^T \tag{2.12}$$

is

$$\mathcal{R} = \begin{pmatrix} u & 0 & v & 0 \\ 0 & u & 0 & v \\ -v^* & 0 & u^* & 0 \\ 0 & -v^* & 0 & u^* \end{pmatrix} = \begin{pmatrix} u & v \\ -v^* & u^* \end{pmatrix} \sigma_0 \tag{2.13}$$

where

$$u = \cos\frac{\Theta(r)}{2} e^{i\Phi(\phi)/2} \quad \text{and} \quad v = \sin\frac{\Theta(r)}{2} e^{-i\Phi(\phi)/2} \tag{2.14}$$

The transformed Hamiltonian $H \to H' = \mathcal{R}H\mathcal{R}^{-1}$ reads

$$\begin{aligned} H' = v_F \left[\tau\sigma_x \left(p_x + \mathcal{A}_x\right) + \sigma_y \left(p_y + \mathcal{A}_y\right)\right] + \\ \frac{\hbar v_F}{2}\left[-\tau\sigma_x \left(m_y s_x + \partial_r\Theta\cos\phi s_y\right) + \sigma_y \left(m_x s_x - \partial_r\Theta\sin\phi s_y\right)\right] + Js_z \end{aligned} \tag{2.15}$$

with

$$\boldsymbol{\mathcal{A}} = \left(\mathcal{A}_x, \mathcal{A}_y\right) = \frac{\partial_\phi\Phi}{2r}\cos\Theta\left(\sin\phi, -\cos\phi\right) s_z \tag{2.16}$$

and

$$\mathbf{m} = (m_x, m_y) = \frac{\partial_\phi\Phi}{r}\sin\Theta(\cos\phi, \sin\phi) \tag{2.17}$$

In the rotated frame of reference, the exchange term is manifestly diagonal. Besides, the Hamiltonian has acquired additional kinetic terms. The $\boldsymbol{\mathcal{A}}$ field acts as a spin-dependent gauge vector potential that couples with the momenta of the Dirac electrons, whereas the

remaining two terms resemble a spin-orbit (SO) interaction of the Rashba type [6]. On the lattice, this corresponds to mapping a system characterized by a noncollinear exchange field and real hopping to a ferromagnetic system with a purely imaginary hopping mimicking the effect of SO coupling plus a complex hopping supported by a gauge field entering as a Peierls phase, as shown in Fig. 2.6. From the gauge field, one can compute the effective magnetic field acting on the system as

$$\boldsymbol{\mathcal{B}} = \nabla \times \boldsymbol{\mathcal{A}} = \frac{\partial_\phi \Phi \partial_r \Theta}{2r} \sin\Theta \, s_z \, \hat{z} \tag{2.18}$$

that, making use of the fact that $\partial_\phi \Phi = N$ and of Eq. (2.10), becomes

$$\boldsymbol{\mathcal{B}} = \begin{cases} -\frac{\pi N}{2rR} \sin\left[\pi\left(1 - \frac{r}{R}\right)\right] \, s_z \, \hat{z} & \text{for } r \leq R \\ 0 & \text{for } r > R \end{cases} \tag{2.19}$$

This transformation of the Hamiltonian allows us to interpret the topological content embedded in the skyrmion texture as a superposition of two effects: (i) the generation of an effective emergent electromagnetic field (EEMF) described by the gauge potential $\boldsymbol{\mathcal{A}}$; (ii) the coexistence of ferromagnetic exchange with a Rashba-like spin-orbit interaction, which, as discussed in subsection 2.2.2, are the fundamental ingredients allowing for the onset of an anomalous Hall phase [11,82]. Both ingredients are endowed with a topological character that the skyrmion real-space texture is able to imprint onto the Dirac electrons and are therefore responsible for generating a Hall response in the system. Expressions analogous to Eqs. (2.16), (2.18) and (2.19) have been obtained in previous works in the context of Schrodinger and band electrons [80,83,140,141], with the remarkable difference that in the strong coupling limit the spin-mixing terms vanish and the problem is exactly mapped to a spinless one-band system where the electrons' momenta are coupled to a vector potential describing an emergent magnetic field. In the case of Dirac electrons, the spin-mixing term survives at all coupling regimes and the mapping to a pure EEMF is an incomplete description of the physics taking place in the system. While this picture provides some physical insight into what happens to graphene Dirac electrons surfing a skyrmion, it does not provide a straightforward method to compute the Hall response. This will be the subject of the next sections, where we resort to a tight binding model that we address numerically, allowing us to evaluate this quantity with a transparent methodology that we introduce below.

2.4 Tight binding quantum transport approach

In this section we review the quantum transport methodology that we will employ throughout the rest of the chapter. Notice that we are implicitly assuming that the substrate material is an insulating skyrmion crystal such as Cu_2OSeO_3 [102–104] or $BaFe_{12-x-0.05}Sc_xMg_{0.05}O_{19}$, with $x = 0.16$ [105] in such a way that the current only flows through graphene. Indeed, if the system hosting the skyrmions was metallic, an anomalous current would be generated in the magnetic conductor in addition to the one produced in the graphene flake, and it would be hard if not impossible to disentangle the different contributions supplied by the two materials.

The graphene electrons are described with the standard tight-binding Hamiltonian for the honeycomb lattice with one p_z orbital per carbon atom [1], plus their exchange

interaction with the classical magnetization of the skyrmion **n**:

$$H = -t \sum_{<i,j>,\sigma} c^{\dagger}_{i\sigma} c_{j\sigma} + J \sum_{i} \mathbf{S}_i \cdot \mathbf{n}_i \tag{2.20}$$

Here $\mathbf{n}_i$ is the classical continuous magnetization texture (4.44) discretized over the graphene lattice and evaluated at site i and $\mathbf{S}_i = \sum_{\sigma\sigma'} c^{\dagger}_{i\sigma} \mathbf{s}_{\sigma\sigma'} c_{i\sigma'}$ is the spin-density operator associated with the i-th lattice site, with $\mathbf{s}$ is the vector whose components are the Pauli matrices acting in spin space. The $< i, j >$ symbol implies summation over all nearest neighboring pairs of atoms, and we are assuming that the magnitude of the magnetization J is uniform over the whole graphene lattice. This Hamiltonian has been considered before [79] for the case of 2D graphene interacting with a skyrmion lattice. In contrast, here we consider a graphene device that is coupled with an individual skyrmion. Notice that at this level we are treating the rather complex interaction of the graphene carriers with the magnetic moments of the substrate as a purely local exchange interaction, as well as neglecting the modulation of the on-site potential associated with the mismatch of the graphene lattice with that of the underlying material. While this is an approximation of the real problem, later on we will show that both assumptions are quite reliable as deviations from them do not yield considerable changes in the relevant results.

2.4.1 Landauer's formalism for transport

The mathematical framework that we use to study quantum transport is based on Landauer's formalism for conductance [88]. Given an experimental setup where a device is attached to N metallic contacts, Landauer's multi-terminal technique allows us to compute the transmission amplitude between the m-th and the n-th contact from the relation

$$T_{mn} = \mathrm{Tr}\left(G^{\dagger}_d \Gamma_n G_d \Gamma_m \right) \tag{2.21}$$

where G_d and $G^{\dagger}_d$ are respectively the retarded and advanced Green's functions of the device, that is, the Green's functions of the isolated device corrected by the self-energies Σ_m of the N leads

$$G_d(\epsilon) = \left[(\epsilon + i\delta)\, \mathbb{I} - H_d - \sum_{m=1}^{N} \Sigma_m \right]^{-1} \tag{2.22}$$

with H_d the Hamiltonian of the isolated device. The Γ_m's are antihermitian matrices associated with the leads' selfenergies as $\Gamma_m = i\left(\Sigma_m - \Sigma^{\dagger}_m\right)$. The leads' self-energies incorporate the coupling between the device and the leads as $\Sigma_m = t^{\dagger}_m g_m t_m$, with g_m the surface Green's function [142] of the m-th lead, and t_m the hopping matrix between the device and the m-th lead. From the knowledge of the transmission amplitudes, the expression for the total current flowing from the lead m follows straightforwardly:

$$I_m = \frac{e}{h} \sum_{n \neq m} \int_{-\infty}^{+\infty} d\epsilon \left[f\left(\epsilon - \mu_m\right) - f\left(\epsilon - \mu_n\right) \right] T_{mn}(\epsilon) \tag{2.23}$$

with $f(\epsilon - \mu)$ the Fermi distribution function, so that at zero temperature the previous expression reduces to

$$I_m = \frac{e}{h} \sum_{n \neq m} \int_{\mu_n}^{\mu_m} d\epsilon T_{mn}(\epsilon) \tag{2.24}$$

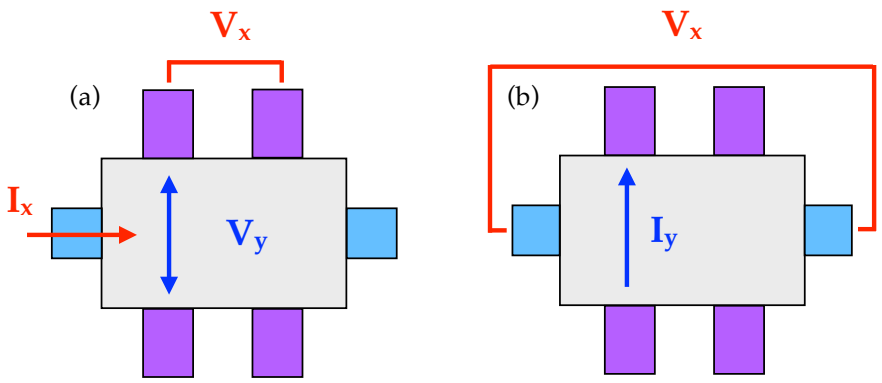

FIGURE 2.7: (a) Representative configuration for a direct Hall experiment. A voltage V_x is applied along x that generates a current I_x along the same direction. A voltage V_y is measured in the transverse direction. (b) Representative configuration for an 'inverse' Hall experiment. A voltage V_x is applied along x that generates a current I_y along the transverse direction. In both cases, the inputs have been illustrated in red and the outputs in blue.

and for a sufficiently small energy interval $\mu_m - \mu_n$ one can expand the transmission coefficient $T_{mn}(\epsilon)$ around the Fermi energy ϵ_F and stick to zeroth order. By doing so, one finally finds that the formula for the current flowing from the lead m becomes:

$$I_m = \frac{e}{h} \sum_{n \neq m} (\mu_m - \mu_n) T_{mn}(\epsilon_F) \tag{2.25}$$

This equation can be used to derive the Hall response in a given multiterminal device in two different ways, as we will see in the next subsection. In both cases, the first step of the calculation is the numerical determination of the transmission coefficients $T_{mn}(\epsilon_F)$.

2.4.2 Calculation of the Hall response in a three-terminal geometry

As mentioned, there are two alternative choices to study Hall phenomena in conductors, namely through a direct or through an inverse procedure.

The typical experimental setup for a direct Hall measurment, schematized in Fig. 2.7a is one where a voltage difference is generated across an electrical conductor, transverse to an electric current that is injected in the system. The strength of the Hall response is measured in terms of a Hall resistance, that is the coefficient relating the generated voltage with the applied current. In a two-dimensional system, the electrical resistance is a matrix $\hat{R}$, defined by the matricial relation

$$V = \hat{R} I \quad \text{or} \quad \begin{pmatrix} V_x \\ V_y \end{pmatrix} = \begin{pmatrix} R_{xx} & R_{xy} \\ R_{yx} & R_{yy} \end{pmatrix} \begin{pmatrix} I_x \\ I_y \end{pmatrix} \tag{2.26}$$

The figure of merit of such an experiment, with reference to Fig. 2.7a, is the Hall resistance $R_H = R_{yx}$ that directly links the applied current I_x to the generated voltage V_y through the relation $V_y = R_{yx} I_x$ when the current along y is zero.

Alternatively, one can go the other way around and design an inverse Hall measurement, that consists in applying a voltage to a conductor and measuring the current generated in the direction tranverse to that of the applied voltage. In this case the quantity that measures the Hall response of the system is the electrical conductance $\hat{G}$, defined as

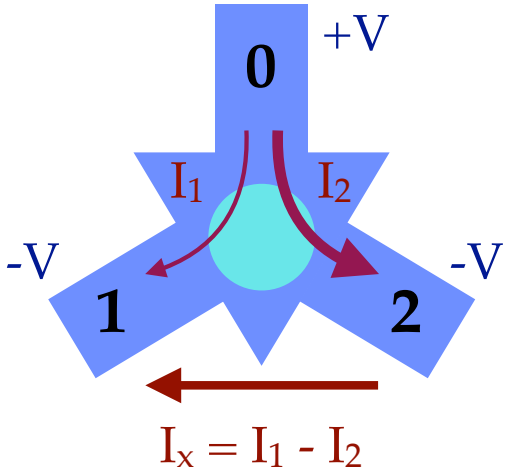

FIGURE 2.8: Schematics of the three-terminal device setup employed in our calculations for simulating an inverse Hall measurement with C_3 rotational symmetry. A voltage difference $V_y = 2V$ is applied along the y direction, and a transverse current I_x is generated along x because of the left-right asymmetry of the transmission from the lead 0 to the leads 1 and 2.

the current response of a system to an applied voltage difference,

$$I = \hat{G}V \quad \text{or} \quad \begin{pmatrix} I_x \\ I_y \end{pmatrix} = \begin{pmatrix} G_{xx} & G_{xy} \\ G_{yx} & G_{yy} \end{pmatrix} \begin{pmatrix} V_x \\ V_y \end{pmatrix} \tag{2.27}$$

It is easy to see that the two matrices are related by matrix inversion $\hat{G} = \hat{R}^{-1}$. The figure of merit of such an experiment, with reference to Fig. 2.7b, is the Hall conductance $G_{\mathrm{H}} = G_{xy}$ that directly links the applied voltage V_x to the generated current I_y through the relation $I_y = G_{yx}V_x$ when no tension along y is applied. Of course, in an isotropic medium, $R_{yx} = R_{xy}$ and $G_{yx} = G_{xy}$.

When the methods just described are implemented in an ordinary four-terminal geometry [127], the resulting relation between the Hall conductance and the transmission coefficients is far from intuitive. Here, for the sake of simplicity, we consider a three terminal device of the kind shown in Fig. 2.8. The most natural choice in such a setup is to implement an inverse Hall measurement, were we fix the chemical potentials of the three electrodes, labeled as 0, 1 and 2, and compute the resulting current. Specifically, we impose that, with reference to Fig. 2.8, $V_0 = V$ and $V_1 = V_2 = -V$. In this way, the voltage difference between leads 1 and 2 is automatically set to zero ($V_x = 0$) whereas the voltage difference between lead 0 and leads 1,2 is $V_y = V_0 - V_{1,2} = 2V$. The expression for the currents flowing from leads 1 and 2 is $I_i = 2VT_{0i}$, for $i = 1, 2$, with the transmissions T_{0i} given by Eq. (2.21). From these expressions it is straightforward to deduce the current generated along the x direction, that reflects the presence of a transverse force,

$$I_x = I_1 - I_2 = 2\frac{e^2V}{h}(T_{01} - T_{02}) \tag{2.28}$$

whence we can derive the Hall conductance in this geometry by noticing that, from Eq. (2.27),

$$I_x = G_{xx}V_x + G_{xy}V_y = G_{xy}V_y = G_{\mathrm{H}}V_y \;\Rightarrow\; G_{\mathrm{H}} = \frac{I_x}{V_y} \tag{2.29}$$

since, as noticed before, $V_x = 0$. Finally, we get the Hall conductance in this geometry

$$G_{\mathrm{H}} = \frac{I_x}{V_y} = \frac{e^2}{h}\left(T_{01} - T_{02}\right) \equiv \frac{e^2}{h}\Delta T \tag{2.30}$$

In the following we choose to present the numerical results for the normalized transmission imbalance, that is

$$T_{\mathrm{H}} = \frac{\Delta T}{T} \equiv \frac{T_{01} - T_{02}}{T_{01} + T_{02}} \tag{2.31}$$

in order to work with quantities that do not depend on the number of conduction channels in the device. This three-terminal setup simplifies considerably the analysis of the numerical results, and also matches the C_3 symmetry of the graphene lattice. However, in a real device, disorder and contact asymmetries might result in additional transmission imbalances that might obscure the detection of skyrmions. Thus, in real devices a standard four terminal geometry should be used, given that the principles and magnitude of the physical effect are expected to be the same.

2.5 Results

In this section, we present the results obtained by calculating the imbalance in the transmission coefficients T_{H} defined in Eq. (2.31) for a graphene quantum dot coupled to a skyrmion. To match the three-terminal setup proposed in the previous section, the graphene quantum dot is chosen to have the shape of an equilateral triangle with zigzag edges. For a better physical insight, we provide an estimate for the *equivalent* magnetic field B_{eq} that would give rise to a conventional Hall response of the same magnitude of that induced by the skyrmion. In order to determine this field, we have performed a calculation of the transmission imbalance T_{H} of a three-terminal triangular device where a perpendicular magnetic field $B_\perp$ is applied to the transmission region. To include such field, we retain only the hopping term of Eq. (A.1) where we perform the standard Peierls substitution $t \to t \exp\left(-i\frac{e}{\hbar}\int_{\mathbf{r}_i}^{\mathbf{r}_j}\mathbf{A}\cdot d\mathbf{r}\right)$ such that

$$H = -t\sum_{<i,j>,\sigma} c_{i\sigma}^{\dagger} c_{j\sigma} e^{-i\frac{e}{\hbar}\int_{\mathbf{r}_i}^{\mathbf{r}_j}\mathbf{A}\cdot d\mathbf{r}} \tag{2.32}$$

By calculating the transmission imbalance between left and right lead, one gets a linear relation $T_{\mathrm{H}} \approx 20\, B_\perp$ as shown in Fig. 2.9. The linear relation between $B_\perp$ and T_{H}, in the absence of a skyrmion, permits to assign an equivalent field B_{eq} to characterize the transmission imbalance calculated in the presence of a skyrmion at $B_\perp = 0$.

In the following we consider flakes with areas on the order of $\sim$ 50 nm^2, and skyrmions with radius on the order of 2-3 nm and, except when explicitly stated otherwise, winding number $N = 1$. Also, we are solely interested in realistic [143,144] weak exchange proximity effects, that do not alter the graphene spectrum substantially, so we explore coupling constants up to $J \sim 100$ meV [144–146]. DFT calculations for graphene proximitized with EuO [144], $BiFeO_3$ [145] and YIG [146] report exchange splittings on the order of 37, 70 and 50 meV, placing the range of coupling constants considered in our work fairly within the current state of the art. In order to simulate standard metallic contacts we have employed either square leads or graphene hexagonal leads with armchair edges (cfr Fig. 2.10). Results obtained with different leads geometries are consistent, and we choose to present curves associated with one or the other geometry in order to minimize effects associated with the transport properties of the leads or with resonances due to confinement inside of the central island. We note that as an anomalous current flows through the graphene dot, the magnetic skyrmion could

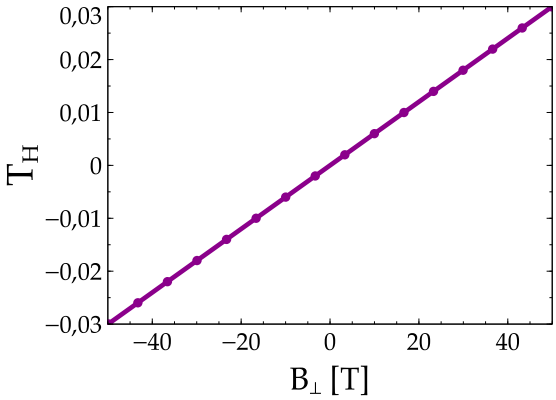

FIGURE 2.9: Normalized transmission imbalance $T_H = \delta T/T$ as a function of an applied perpendicular magnetic field $B_\perp$.

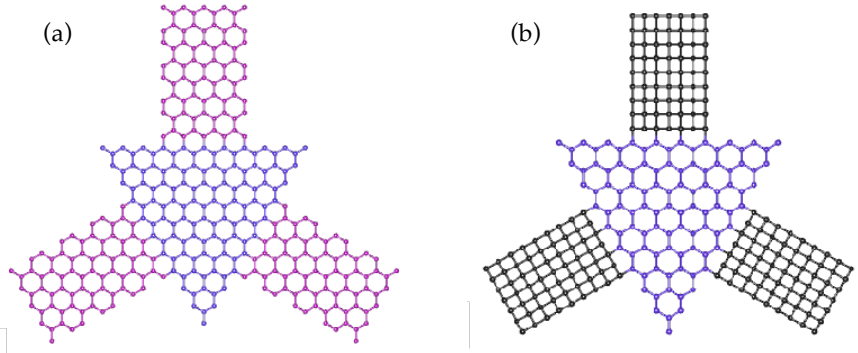

FIGURE 2.10: Comparison between two types of geometries considered. (a) Graphene triangular dot with zigzag edges coupled to hexagonal leads with armchair edges. (b) Graphene triangular dot with zigzag edges coupled to square leads with lattice parameter $a_{sq} = a/2$, with $a = 2.46$ Åthe lattice parameter of graphene.

undergo a current-driven rebound motion whose dynamics is governed by the Thiele's equation [122,125,126]. This can be avoided if the generated currents are sufficiently low, that is, below the critical depinning current needed to excite skyrmions' dynamics [114,118]. However, such a phenomenon is beyond the scope of the present work, and we refer the reader to the several theoretical and experimental works [115,125,126,147] that focus on this topic for further details.

2.5.1 Hall response in the ideal case

We start by considering the ideal case where the interaction of the graphene electrons with the magnetic moments of the substrate is treated as a purely local exchange interaction, and no account is given of the moiré potential associated with the mismatch of the graphene lattice with that of the underlying material. Computationally, this abridges to modeling the graphene dot by means of the Hamiltonian of Eq. (A.1) with no additional terms.

Dirac vs Schrodinger First of all, we investigate the magnitude and behaviour of the transmission asymmetry T_H as a function of the coupling constant J, comparing the results for Dirac electrons and Schrodinger electrons. Notice that, for semplicity and, more

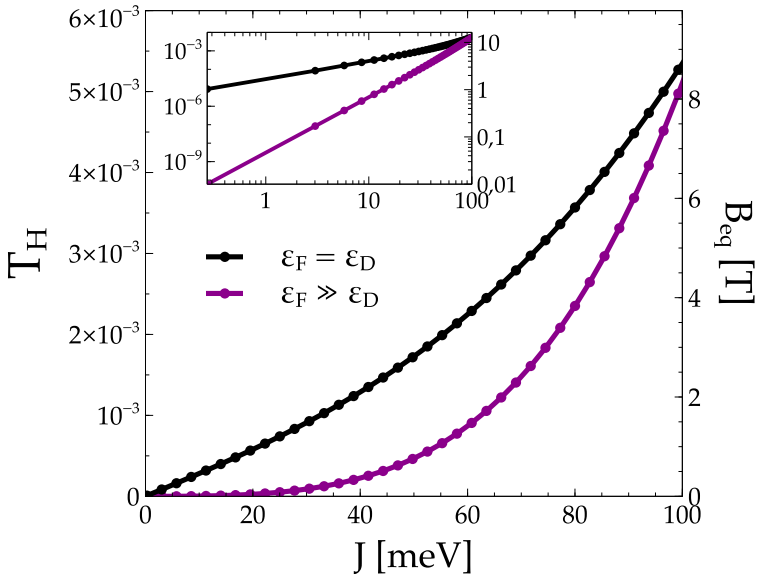

FIGURE 2.11: Normalized transmission imbalance T_H and equivalent magnetic field B_{eq} as a function of the coupling constant J; comparison of a Dirac-like (undoped graphene, with the Fermi level ε_F close to the Dirac point) and a Schrodinger-like (heavily doped graphene, with ε_F much larger than the energy of the Dirac point ε_D) material for an island with side $L = 10.6$ nm and a skyrmion radius $R = 2.3$ nm. Inset: a log-log representation of $T_H(J)$ and $B_{eq}(J)$.

importantly, to avoid introducing additional effects that could mask the difference intrinsic to the low-energy dispersions of these two classes of systems, we model Dirac electrons by means of an half filled honeycomb lattice, with the Fermi energy ε_F close to the Dirac point ($\varepsilon_F = \varepsilon_D$) and Schrodinger electrons with a heavily doped honeycomb lattice, with the Fermi energy away from the Dirac point ($\varepsilon_F \gg \varepsilon_D$). The result is shown in Fig. 2.11 in both linear and logarithmic scale, for a skyrmion with radius $R = 2.3$ nm and a device of linear dimension $L = 10.6$ nm. The first thing to notice in this plot is that in the Dirac case, even for small $J \simeq 1$ meV, the equivalent field B_{eq} is on the order of 1 Tesla, showing that the anomalous Hall effect is very large. For $J < 100$ meV the transmission imbalance T_H of Dirac electrons exhibits an approximately linear behaviour with J in contrast with the case of Schrodinger electrons for which $T_H \propto J^3$. For all the values of J, the Hall response for Dirac electrons is much larger than for Schrodinger electrons, most notably for the experimentally relevant case of small J, for which the transmission imbalance is up to 4 orders of magnitude larger. This difference is reduced and eventually canceled at higher and unrealistic couplings larger than 100 meV. This result allows us to establish with enough confidence the superiority of graphene for unveiling skyrmionic phases of matter as opposed to parabolic dispersing standard 2DEGs, likely due to the enhancement of the anomalous Hall response due to the unconventional relativistic-like properties of Dirac electrons.

Hall response as a function of the system parameters We now characterize the Hall conductance of a graphene three terminal device by investigating its dependence on the system parameters, specifically the transmission energy ε, the skyrmion size R and the linear size of the graphene island L.

The normalized transmission imbalance T_H as a function of the transmission energy is shown in Fig. 2.12b for $L = 15.5$ nm, $R = 3.4$ nm and $J = 80$ meV. This curve shows a local maximum at charge neutrality, and two other local maxima of opposite sign at symmetric electron/hole dopings, a behaviour resembling graphene coupled to a skyrmion

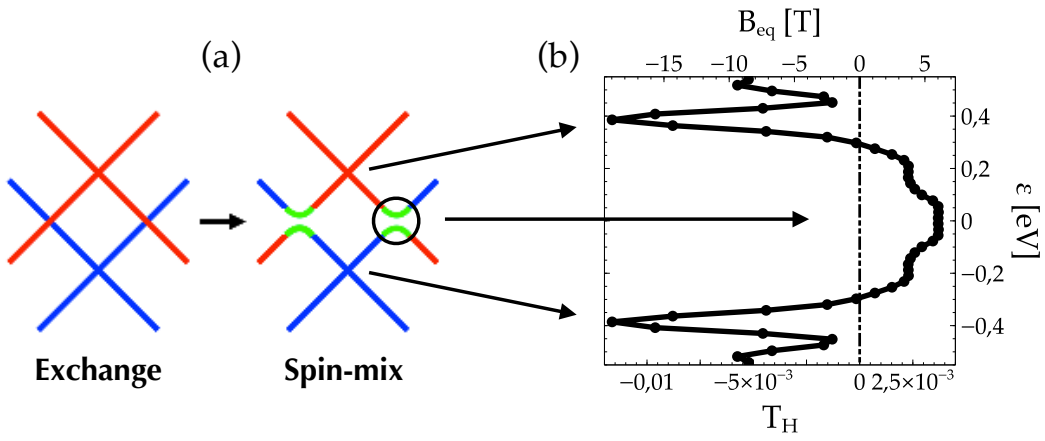

FIGURE 2.12: (a) Schematics of the effect on the electronic structure of graphene (in the thermodynamic limit) of being proximitized to a skyrmion, where the similarity with the exchange plus SOC mechanism is stressed. (b) Normalized transmission imbalance T_{H} and equivalent field B_{eq} of a graphene three terminal device as a function of the transmission energy of the leads ε for an island of side $L = 15.5$ nm, a skyrmion radius $R = 3.4$ nm and for a coupling constant $J = 80$ meV. Energies characterized by maximum absolute Berry curvature in the infinite system, corresponding to avoided crossings in the band structure, are evidenced.

crystal [79]. Such phenomenology can be understood in terms of the modification of the Dirac cone due to the noncoplanar magnetization field. As we have seen in section 2.3, the problem can be mapped to one where spatially uniform exchange field and Rashba-like spin-mixing terms coexist. The first contribution has the effect of splitting spin degeneracy, whereas the latter favors the opening of small gaps at accidental degeneracy points, corresponding to avoided band crossings both at the Fermi energy and at additional points at higher energies (in absolute value) on the order of $\pm J$. This is clearly visible in Fig. 2.12a. It is well known [82] that avoided crossings play a crucial role in quantum transport since they act as magnetic monopoles for the Berry curvature in reciprocal space, so that the latter is always strongly enhanced near these points. Remarkably, this enhancement occurs in opposite direction for the upper and lower bands involved so that when both bands are populated the effect is virtually canceled out. However, when the crossing is at the Fermi energy so that only one of the two bands is occupied, a large contribution to the Hall conductance stems from the enhanced Berry curvature. We therefore interpret the local maxima in the transmission asymmetry T_{H} of our flake as a function of the transmission energy ε as points where the absolute value of the Berry curvature is enhanced because of avoided crossings in the associated band structure. Of course, we cannot strictly speak of band structure in our problem because of the zero-dimensionality of our system. It is however natural to guess that in the limit of relatively large flakes, the energy distribution of levels in the dot will resemble more and more closely the density of the states of an infinite graphene lattice, thus inheriting its physical properties.

In Fig. 2.13a we show the behaviour of T_{H} as a function of the skyrmion radius R, keeping the dimension of the device constant and equal to $L = 10.6$ nm, and $J = 80$ meV. We consider the case of small skyrmions with nanometric radius such as those found, for instance, in systems with frustrated exchange interactions [113]. Two competing effects are at play as the radius of the skyrmion increases: on the one hand the change in magnetization as a function of the distance from the skyrmion center becomes smoother, so that the effective skew scattering is weaker, and on the other the surface where the

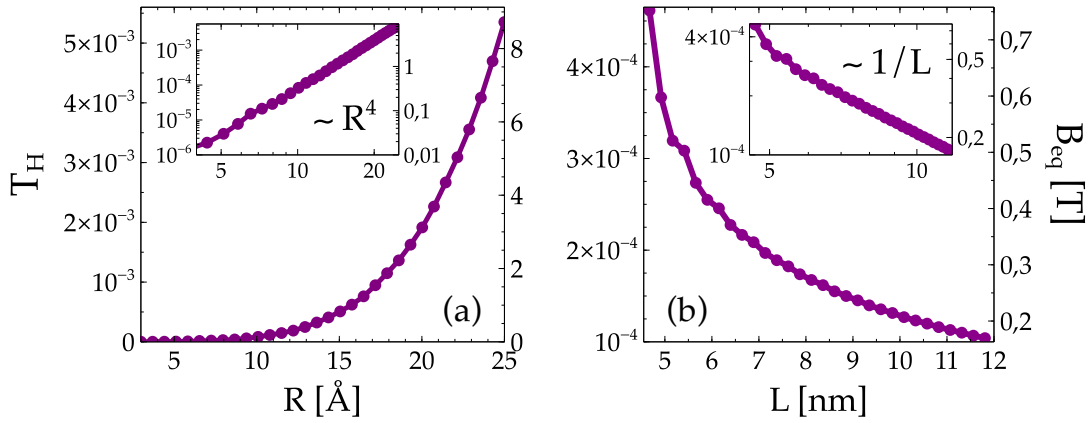

FIGURE 2.13: Transmission imbalance T_H and equivalent field B_{eq} of a graphene three terminal device as a function of (a) the skyrmion radius R, with fixed flake size of $L = 10.6$ nm, and (b) the flake size L, with fixed skyrmion radius of $R = 1.4$ nm. Both calculations have been performed for a coupling constant of 80 meV and at the Dirac energy. Insets show log-log representation of T_H and B_{eq}.

skew scattering is nonzero increases. The normalized scattering asymmetry resulting from our calculations behaves as R^4 indicating that the second mechanism is dominant, and therefore that larger skyrmions yield a stronger Hall signal. The dependence of the Hall response on the size of the graphene flake L is shown in Fig. 2.13b, for a fixed radius of $R = 1.4$ nm and an exchange of $J = 80$ meV. We see that by increasing the flake size while keeping the skyrmion radius fixed, the Hall signal decreases as L^{-1}. From these two results we infer that the Hall conductance behaves as $T_H(R, L) \sim R^4/L$ as a function of the radius and of the linear size of the central island. This scaling reflects the fact that the Hall response is proportional to the probability that the electrons surf over the skyrmion, which is manifestly an increasing function of R and a decreasing function of L. By changing both the radius and the device size by a common factor α, T_H scales as $T_H(\alpha R, \alpha L) \sim \alpha^3 T_H(R, L)$ indicating that the Hall conductance is not scale invariant under simultaneous rescaling of R and L. A general example of this nonlinear scaling trend is shown in Fig. 2.14a where a comparison of two systems with L and R scaled by a common factor is presented.

We also performed a calculation of T_H and the equivalent field B_{eq} as a function of the leads' energy for different winding numbers $N = 1, 2, 3$. We see from Fig. 2.14b that the Hall response is finite, though suppressed at the avoided crossing points as N increases. This result is interesting since it was demonstrated [79] that for an infinite monolayer of graphene coupled to a lattice of skyrmions the Chern number is $C = 2N$ for $|N| = 1$, and zero otherwise. However, given their higher energy cost, skyrmions characterized by winding numbers $|N| > 1$ are quite rare in nature since they have higher energies and are therefore generally unstable. On the other hand, switching the sign of the winding number has merely the effect of reversing the sign of the response.

We recall that most systems in the brink of hosting skyrmion lattices need a nonzero external magnetic flux to drive them into the skyrmionic phase, as they typically exhibit spiral spin phases at zero magnetic field. This implies that an additional nonzero Hall contribution is to be expected from the external field that sums up to the one driven by the skyrmion alone. An effective way to discriminate between the two effects relies on their different symmetry properties. In fact, while the skyrmionic contribution is electron-hole

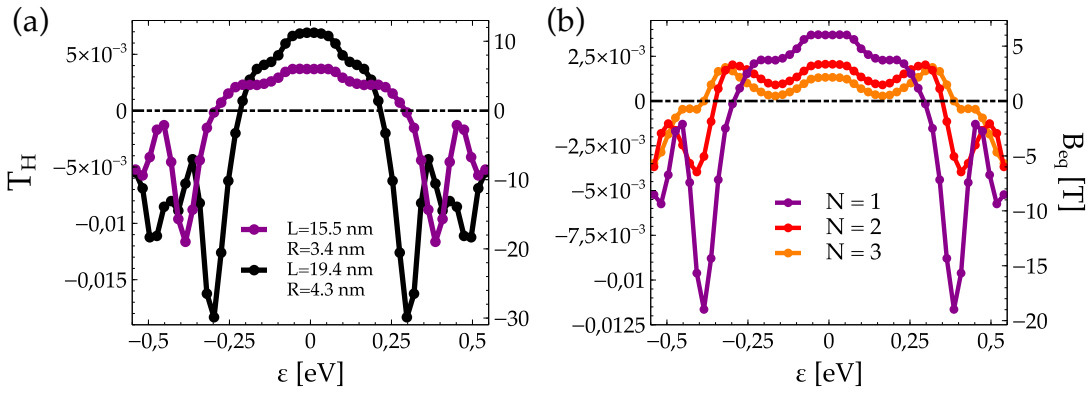

FIGURE 2.14: (a) Comparison of two calculations of T_H and B_{eq} as a function of the leads energy ε where the radius of the skyrmion and the linear size of the flake are scaled linearly by a common factor $\alpha = 1.25$, for $J = 80$ meV. The legend shows the values of L and R employed for the calculations. (b) Comparison of two calculations of T_H and B_{eq} as a function of the leads energy ε with $L = 15.5$ nm, $R = 3.4$ nm and $J = 80$ meV, for two different winding numbers, $N = 1$ (purple curve), $N = 2$ (red curve) and $N = 3$ (orange curve).

symmetric (as made clear by Fig. 2.12) and only changes sign by switching the sign of either J or N, the Hall effect induced by the magnetic field is electron-hole asymmetric as holes have opposite charge with respect to electrons and thus respond with an opposite velocity to an applied external field. It is thus the $\varepsilon \to -\varepsilon$ asymmetry of the overall scattering cross section that allows one to subtract the spurious external contribution and determine the intrinsic skyrmionic one. We also note that the anomalous Hall response will be nonzero if other noncoplanar spin textures, that are not skyrmions, are present in the background material. However, in most systems it is to be expected that the magnetic configurations that do not make it to the skyrmionic phase are structures that are coplanar but noncollinear, like spin spirals. These kinds of structures, because of coplanarity, are not able to generate an anomalous Hall signal. A very clear explanation for this feature can be found in Ref. [79].

2.5.2 Deviations from ideality

So far we have dealt with an ideal situation where the graphene flake is perfectly clean, the exchange interaction perfectly local and no account for lattice mismatch driven effects with the substrate is given. Therefore, in order to provide a more faithful description of the targeted phenomenon, in this section we explore the effects of realistic perturbations in the quantum Hall conductance. In particular, we study: (i) scalar disorder (ii) the moiré potential induced by the substrate, (iii) the renormalization effects on the exchange coupling between the graphene electrons and the substrate, associated with the mismatch between the two lattices, and (iv) the existence of a nonlocal component of the exchange interaction. As we will see, all of these results indicate that taking into account deviations from the ideal case does not affect the strength of the anomalous signal in a sizable manner, thus demonstrating the robustness of the results provided in the previous subsection.

Effects of disorder

We first analyze the Hall current degradation brought about by defects or impurities in the sample. In order to provide a more realistic estimate of the extent to which the Hall

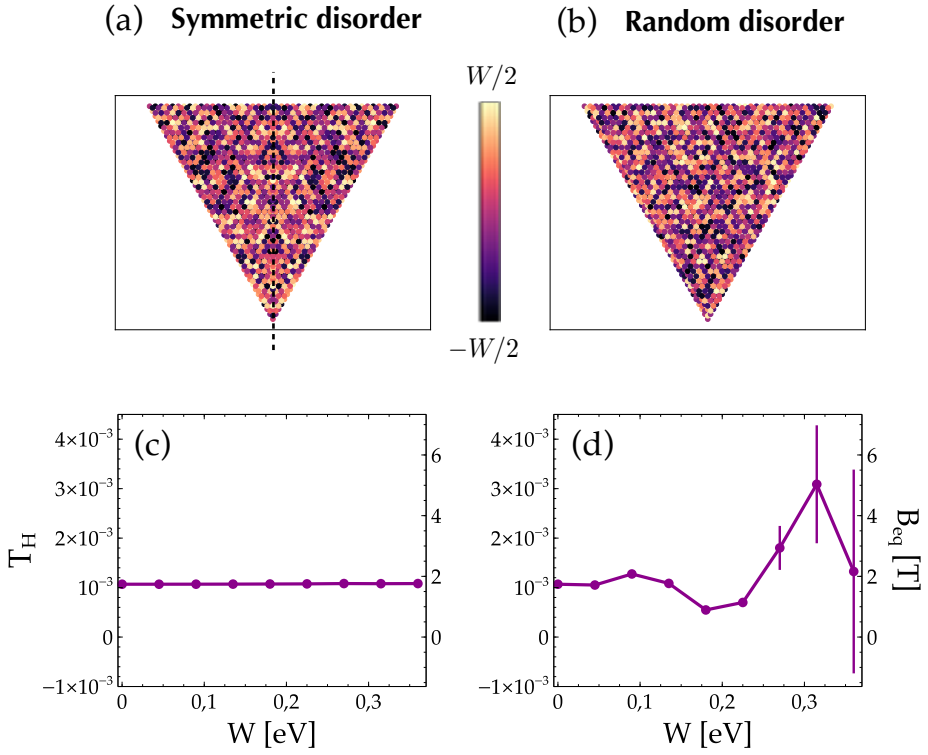

FIGURE 2.15: Panels (a) and (b) show typical realizations of disordered configurations with (a) and without (b) $y \to -y$ symmetry. In panels (c) and (d) we present the associated curves of T_{H} and B_{eq} as a function of the disorder strength W for fixed values of $J = 80$ meV, $L = 10.6$ nm and $R = 2.3$ nm. Error bars associated with the standard deviation of the data are shown.

responses that our results anticipate are robust with respect to this loss of conductance, we analyze the Hall current degradation brought about by scalar disorder, as could be ascribed to defects or impurities in the sample. We do so by averaging over $N = 50$ Anderson disorder configurations in each of which we assign a random scalar on-site potential $W_i \in [-W/2 : W/2]$ to each atom in the quantum dot and tune the parameter controlling the disorder degree W from 0 to a maximum of $\sim$ 400 meV, an upper limit for the energy scale associated with disorder that is consistent with the assumption of Coulomb long-range scattering [146,148]. The clean limit is recovered for $W = 0$.

We compare two disorder configurations with different symmetry: one where the disorder distribution preserves mirror symmetry with respect to the y axis and one where the distribution is completely random in the whole sample. A realization of each of these different disorder profiles is shown in Fig. 2.15a and b. Error bars associated with the standard deviation of the data are shown for completeness. The resulting T_{H} curves are shown in Fig. 2.15c and d, where a graphene island of side $L = 10.6$ nm, a skyrmion with radius 2.3 nm and an exchange coupling constant $J = 80$ meV have been considered. We see that symmetric disorder barely affects the Hall response of the problem, as it provokes insignificant changes in the normalized transmission imbalance. On the other hand, a randomly distributed disorder that does not respect $y \to -y$ symmetry affects the conductance more sizeably, yielding variations ΔT_{H} on the order of T_{H}. The difference is to be attributed to the fact that in the symmetric case the defects simply act as a fluctuating potential that does not contribute to the asymmetry of the scattering, whereas in the random case (that is the one natural to expect in a real sample) an additional transverse conductance driven by the disorder asymmetry rather than by the skyrmion-induced anomalous Hall effect is generated. However, significant alterations of the Hall response only take place at relatively high values of the disorder potential on the order of $\sim$ 300 meV, whereas for weaker and more reasonable disorder strengths the change in the conductance is smaller and comparable to the one obtained in the symmetric configuration. More in general, as mentioned before, this effect will be naturally wiped out in a four-terminal measurement where the geometry allows spurious contributions to the conductance to be kept out. We can therefore rely on the results obtained so far for pristine graphene, as the unavoidable presence of a low concentration of scalar defects in the actual samples is not expected to be able to turn down the figure of merit of the problem.

Effects of lattice mismatch

Here, we consider the fact that a substrate with a lattice parameter that differs from that of graphene will result in a modulation of the local potential felt by the graphene electrons on a characteristic scale that depends on the lattice parameter of the underlying material. This could have important consequences for the magnitude of the anomalous response, since the existence of a moiré pattern could fold the Brillouin zone and generate intervalley scattering. In fact, the latter has been found to be detrimental to the observation of topologically nontrivial phenomena in the case of graphene coupled to a skyrmion lattice [79]. In this situation, valley mixing has the effect of opening a trivial gap at the Fermi level with no associated finite Berry curvature. We account for the effect of the potential modulation by means of the following contribution to the graphene Hamiltonian:

$$H_m = \sum_i \mu_i c_i^\dagger c_i \quad \text{with} \quad \mu_i = \mu \left(\sum_j e^{-|\mathbf{r}_i - \mathbf{R}_j|/\Lambda} - \eta \right) \tag{2.33}$$

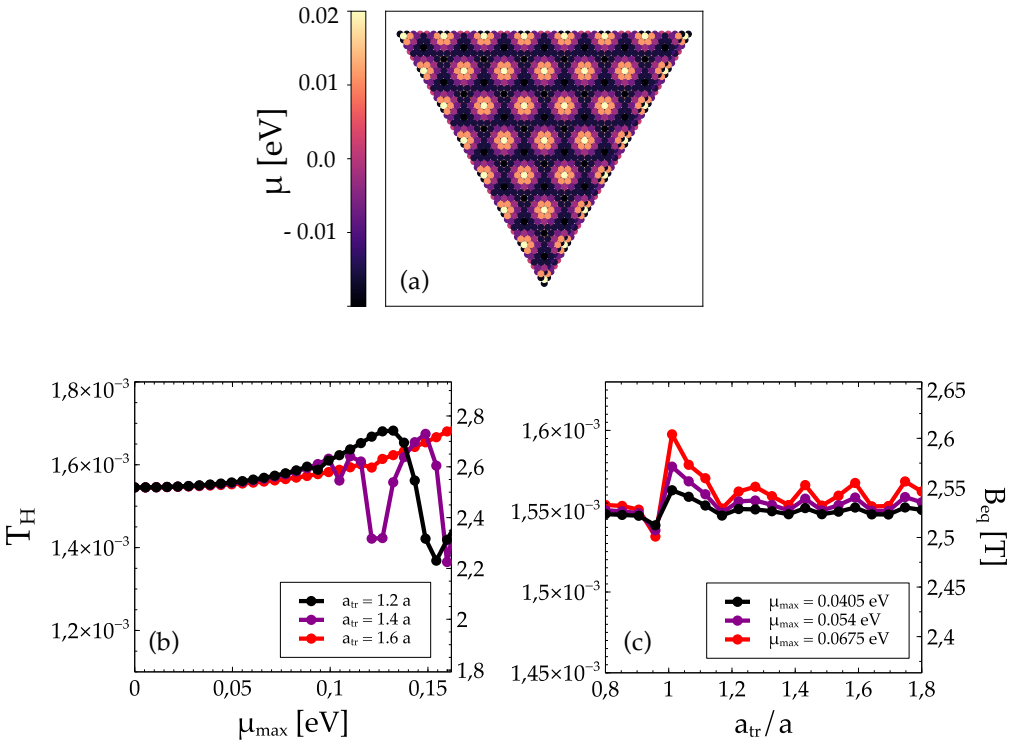

FIGURE 2.16: Panel (a) displays a specific configuration of the site-dependent potential associated with the moiré pattern for $a_{\text{tr}} = 1.4a = 3.44$, $\Lambda = 0.3a = 0.74$ nm, and $\mu_{\text{max}} = 0.04$ eV. In panels (b) and (c) we study the effect of adding the term in Eq. (2.33) to the Hamiltonian in Eq. (A.1). Specifically, panel (b) shows T_{H} and B_{eq} as functions of μ_{max} for different lattice parameters of the substrate, and panel (c) shows T_{H} and B_{eq} as functions of a_{tr} for different values of μ_{max}. Both calculations are performed for $\Lambda = 0.5a = 1.23$ Å, $L = 10.6$ nm, $R = 2.6$ nm, $J = 80$ meV and $d = 2a$.

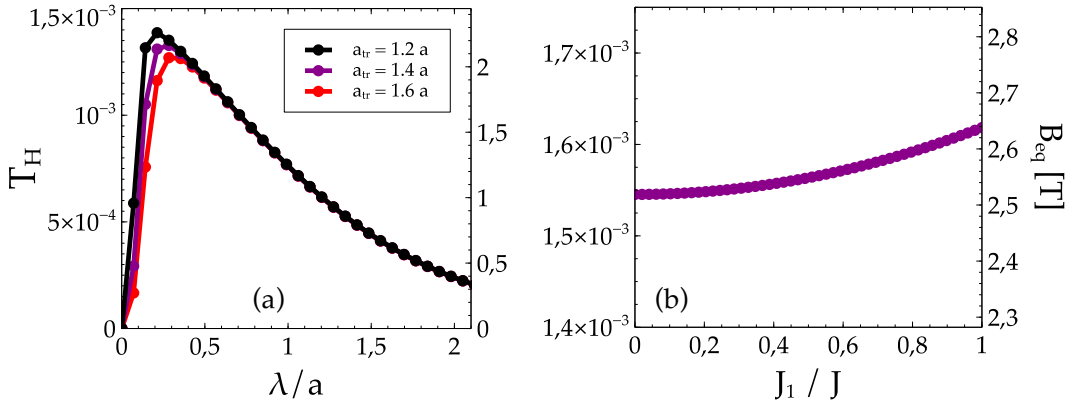

FIGURE 2.17: In panel (a) we have substituted Eq. (2.35) to the exchange Hamiltonian employed in the main text, Eq. (A.1), and calculated T_H and B_{eq} as functions of λ for three different values of a_{tr}. In (b) we show the behaviour of T_H and B_{eq} as functions of the nonlocal exchange amplitude J_1/J when the Hamiltonian term in Eq. (2.34) is added to Eq. (A.1). All calculations are performed for $L = 10.6$ nm, $R = 2.6$ nm, $J = 80$ meV, and $d = 2a$.

where we choose η such that $\langle \mu_i \rangle = 0$ which implies that the charge neutrality point is at $\varepsilon = 0$. For a fixed μ, the local potential μ_i varies within the interval $\mu_i \in [-\mu_{max}, \mu_{max}]$, depending on the value of Λ. Note that the limit $\Lambda \to \infty$ corresponds to the pristine case $\mu_i = 0$ for every site i. The vectors $\mathbf{R}_j$ indicate the positions of the atoms of the magnetic substrate, that we model as a triangular array [149] with a lattice parameter a_{tr} that is not commensurate with that of graphene, whereas the vectors $\mathbf{r}_i$ refer to the positions of the atoms in graphene. The results are shown in Fig. 3.2, where a graphene island of side $L = 10.6$ nm, a skyrmion with radius 2.6 nm, an exchange coupling constant $J = 80$ meV and a distance $d = 2a$ (with $a = 2.46$ Å the graphene lattice parameter) between the graphene plane and the substrate have been considered.

In Fig. 3.2b we plot the normalized transmission asymmetry and equivalent magnetic field as a function of $\mu_{max} = \max(\mu_i)$ for three different values of the lattice parameter of the substrate a_{tr} and for $\Lambda = 0.5a = 1.23$ Å. We observe that even in the presence of sizable on-site modulations of 0.1 eV, the anomalous Hall signal remains at a magnitude similar to that of the ideal case. Interestingly, the smaller the lattice parameter of the substrate, that is, the closer its periodicity is to that of graphene, the 'sooner' the ideal approximation breaks down, meaning that fluctuations in T_H appear at lower values of μ_{max}.

In Fig. 3.2c we report instead the normalized transmission asymmetry as a function of the lattice parameter of the substrate, for three different values of the potential modulation strength μ_{max} and for $\Lambda = 0.5a = 1.23$ Å. We see that the modifications of T_H are negligible throughout the whole range of parameters considered. Again, we see that a spike-like feature occurs in the proximity of $a_{tr} = a$.

Effects of nonlocal exchange interaction

Here we account for the fact that nonlocal exchange interactions can be present, in addition to local ones. In order to relax the assumption of purely local exchange, we introduce a term in the Hamiltonian that mimics the effect of an induced nonlocal exchange interaction. From a microscopic point of view, such term can be thought of as arising from

electrons hopping from a carbon atom to a site in the skyrmion material where the interaction with the localized magnetic moment flips their spin, and then hopping back to a different carbon atom in graphene. Such phenomena can be accounted for by a spin-dependent hopping term that we take to be the average between the induced on-site magnetization of the two sites involved. The nonlocal exchange Hamiltonian thus reads

$$H_{J_1} = \sum_{<i,j>} \mathbf{S}_{ij} \cdot \mathbf{n}_{ij} \tag{2.34}$$

where $\mathbf{S}_{ij} = \sum_{\sigma\sigma'} c^{\dagger}_{i\sigma} \mathbf{s}_{\sigma\sigma'} c_{j\sigma'}$ and $\mathbf{n}_{ij} = (\mathbf{n}_i + \mathbf{n}_j)/2$. In Fig. 2.17b we show the behaviour of the anomalous response with J_1/J for $L = 10.6$ nm, $R = 2.6$ nm and $J = 80$, whence it appears evident that the signal is left almost unchanged by values of J_1 up to J.

Effects of neighbors-averaged exchange

The last effect that we consider accounts for the renormalization of the exchange coupling constant due to the fact that the exchange exerted by each localized magnetic moment of the substrate is not contact-like but rather decays exponentially over a distance on the order of the lattice parameter. Therefore, graphene electrons feel an exchange that is given by a superposition of the slightly misaligned magnetic moments of its nearest neighboring atoms in the substrate. In order to account for such an effect, we rewrite the exchange term of the Hamiltonian as

$$H_J = J \sum_i \mathbf{S}_i \cdot \langle \mathbf{n}_i(\lambda) \rangle \tag{2.35}$$

with

$$\langle \mathbf{n}_i(\lambda) \rangle = \mathcal{C} \sum_i \mathbf{m}_j e^{-|\mathbf{r}_i - \mathbf{R}_j|/\lambda} \tag{2.36}$$

where the vectors $\mathbf{R}_j$ indicate once again the positions of the atoms of the substrate, $\mathbf{m}_j$ is a unit vector pointing in the direction of the local magnetization on the j-th site of the substrate, and $\mathcal{C}$ is a normalization constant chosen so that $\max |\langle \mathbf{n}_i \rangle| = 1$. In the limit where graphene and the substrate are commensurate (if the substrate had also a honeycomb lattice), and $\lambda \to 0$, the previous formula would yield $\langle \mathbf{n}_i \rangle = \mathbf{m}_i$ and we would recover the contact-like and commensurate limit explored in the main text. On the contrary, for noncommensurate lattices, the limit $\lambda \to 0$ would restrain the exchange only to selected atoms, so that this regime is to be considered nonphysical in the present model. In any other situation, the previous parametrization yields a local exchange in graphene that is a local average of the magnetization of the substrate, with the range of the averaging set by the length scale λ. In the limit $\lambda \to \infty$, all the sites in graphene would feel the same exchange coupling, yielding a vanishing Hall response. The result is shown in Fig. 2.17a as a function of the range of decay λ, for three different values of a_{tr} and for $L = 10.6$ nm, $R = 2.6$ nm, $J = 80$ meV and $d = 2a$. As is clear from this plot, T_{H} has a maximum on the order of the one that would be obtained for a contact-like interaction with a commensurate lattice, that is attained at a small a_{tr}-dependent value of λ, and decays smoothly as λ increases. This behaviour shows that a weighted average over the magnetic moments of the electrons' closest neighbors can moderately affect the anomalous Hall signal. This allows us to anticipate that for reasonable values of λ on the order of a the transmission asymmetry will be approximately halved with respect to the one that is expected in the (unrealistic) purely local case. However, a factor of ≈ 2, though being the most severe effect among those considered in this subsection, is not a

heavy divergence from the ideal case, so that we consider the local exchange interaction used through the main text to be a fairly acceptable approximation.

2.6 Conclusions

In this chapter we have presented numerical calculations for transport across triangular graphene quantum dots coupled to skyrmionic textures and attached to three external contacts. We have explored different exchange strengths, island sizes and skyrmion radiuses, and highlighted the different behaviour of Dirac and Schrodinger electrons. Finally, we have tested the reliability of our results by comparing the ideal Hall conductance with the one that results from taking into account several deviations from the faultless configuration of the proposed experiment.

Our results strongly indicate that graphene would be an excellent skyrmion detector at realistic exchange couplings on the order of $\sim$ 1-10 meV, exhibiting minimum Hall conductances G_{H} on the order of 10^{-5}-10^{-4} G_0 for $J \approx 1$ meV, $R \approx 2$ nm and $L \approx 10$ nm, several orders of magnitude larger than the minimum experimentally detectable conductance on the order of 10^{-10} G_0 [150,151], and corresponding to an equivalent magnetic field $B_{\mathrm{eq}} \approx 1$ T. Our results also show that Schrodinger electrons are less sensitive to the nontrivial magnetic ordering and respond with a conductance that is several orders of magnitude smaller than that displayed by Dirac electrons, especially at very weak coupling strengths, that we deem to be more realistic in actual experiments. This suggests that the underlying physical principle of our proposal, that is the anomalous Hall effect generated by the real-space topology of skyrmions, is enchanced as a consequence of the interaction between these noncoplanar spin textures and the 'unconventional' carriers of graphene.

Furthermore, we notice that in our calculations we have considered flakes of the minimum experimentally achievable dimensions proximitized with the smallest skyrmions experimentally detected so far (of the order of nanometers, whereas observation of skyrmions with radius of up to 100 nm has been reported [97,152]). It is therefore straightforward to conclude that the scaling argument provided in section 2.5, showing that the normalized transmission imbalance behaves as $T_{\mathrm{H}} \sim R^4/L$, evidences that our estimates of Hall conductances merely set a lower bound for the range of values that this parameter can assume in actual laboratory measurements where sample dimensions and skyrmion radius can be consistently larger than those considered in this work. Amongst the realistic sources of noise introduced to assess the faithfulness of our findings, the most detrimental was found to be the loss of conductance due to averaging over the misaligned magnetic moments of the electrons' closest neighbors, able to reduce the Hall response by a factor of ≈ 2. This indicates that, altogether, none of the effects taken into consideration is able to significantly turn down the figure of merit of the problem.

In conclusion, we suggest that graphene might be exploited as a preliminary tool to readout the presence of an individual skyrmion in a magnetic insulator underneath, prior to resorting to more invasive electron microscopy probes such as SP-STM [93,106,107] or TEM [97,98], thus establishing the principles of hybrid devices combining graphene Hall probes and insulating skyrmionic materials [102–104].

Chapter 3

Quantum Spin Hall Effect in Twisted Bilayer Graphene

3.1 Introduction

Topologically non-trivial phases of matter have been intensively pursued ever since the pioneering prediction that protected conducting states were to appear at the edges of HgTe/CdTe quantum wells, a material with an otherwise insulating bulk [73,153]. This remarkable feature, observed in 2007 for the first time [74] is associated to a spin-orbit coupling driven gap inversion occuring in the bulk of the system. During the following years many more materials, known as topological insulators, have been theoretically predicted and/or experimentally shown to host the same phase of matter [75–78].

Stated more rigorously, a topological insulator is a material characterized by an insulating time reversal invariant band structure where strong spin orbit interactions lead to an inversion of the band gap at an odd number of time reversed pairs of points in the Brillouin zone. This gap inversion endows the system with a nontrivial topological index associated with the emergence of conducting states that close the bulk gap at the surface similarly to a two-dimensional electron gas in the quantum Hall regime. However, whereas the latter is characterized by chiral edge modes that allow one-way transport around the sample perimeter, topological insulators host helical edge states, i. e. counterpropagating modes composed of oppositely spin polarized Kramers pairs that realize a so-called quantum spin Hall (QSH) phase [64,71], thus called because its edge states carry unidirectional spin current. Both types of edge states are protected from disorder-induced loss of conductance: the former because there are no low energy channels moving in the opposite direction available for backscattering, and the latter on account of the protection supplied by time-reversal invariance that prevents non-magnetic impurities from elastically backscattering a 'right' moving edge electron into its 'left' moving Kramers partner (and viceversa). This property underlies the outstanding hallmark of 2D topological insulators of showing a perfectly quantized conductance of $G = 2e^2/h$ in a two-terminal measurement, given that the two opposite edges behave as oppositely spin-polarized perfectly transmitting wires carrying a quantum of conductance each.

Beyond the fundamental interest intrinsic to topological phases of matter, the perfect quantization of the conductance resulting from robustness against disorder is what makes these systems attractive for many practical implementations. In addition, QSH phases proximitized with s-wave superconductors have been shown to be ideal hosts to topological superconductivity [86,154], since the time-reversal paired edge states of TIs satisfy the two basic requirements for artificially inducing p-wave superconductivity, namely a finite singlet amplitude and violation of fermion doubling (only possible at the surface by virtue of the holographic principle). This potential application fueled further both theoretical and experimental research in the field, motivated by the promise

held by Majorana anyons to revolutionize the field of quantum computation by beating decoherence at the hardware level.

Apart from the aforementioned compounds, graphene with intrinsic spin-orbit coupling has been suggested by Kane and Mele in 2005 to host a two-dimensional QSH phase.[6] This system is a time-reversal invariant realization of two identical copies of the Haldane model [81], one for each spin polarization. While the proposal of engineering a QSH phase in a versatile material as graphene is appealing, the intrinsic spin-orbit coupling of this material is too weak to yield a sizeable gap [7,155]. Ever since, alternative routes have been pursued for tailoring the properties of graphene into this special topological phase. Among them, it has been suggested that a *pseudo*-QSH phase can be realized in the QH regime by means of a combination of electron-electron interactions (triggered by strong enough magnetic fluxes) and the Zeeman field. This phase, which manifestly breaks time-reversal symmetry (hence the qualifier 'pseudo') because of the involved magnetic fields, has been demonstrated experimentally in 2014 [89]. This achievement encourages optimism towards the possibility of realizing graphene-based Majorana physics [20]. However, the strong in-plane fields required for inducing a significant Zeeman splitting of the spectrum (larger than 20 T) are hardly compatible with superconductivity, which in most systems is suppressed at much smaller magnetic fields.

This limitation calls for futher efforts to look for alternative implementations of QSH phases in graphene, that involve neither spin-orbit coupling (SOC), that is too weak to induce significant topological gaps, nor large magnetic fields, that are liable to spoil superconductivity.

In this chapter, we present an alternative implementation that meets the above criteria and is therefore highly compatible with the targeted objective of implementing topological superconductivity in a graphene-based platform. More specifically, we investigate the conditions under which twisted bilayer graphene (TwBG) in the QH regime can be driven into a *pseudo*-QSH phase prompted by the combination of an interlayer bias with electron-electron interactions. We do so motivated by an experiment performed at MIT by the group of Prof. Jarillo-Herrero that reports evidence of helical edge states in layer-biased TwBG under a perpendicular magnetic flux [91].

The reasons for choosing graphene over other candidate systems rest on its well established suitability for fabricating highly transparent junctions. More specifically, a significant degree of transparency has been demonstrated for graphene-superconductor junctions that operate in the ballistic limit [156] in the quantum Hall regime [157], enabling the use of this material as a particularly appealing platform for Majorana bound states and potentially more within reach of current lab technologies with respect to alternative and more challenging implementations involving TIs.

The chapter is organized as follows. In the second section, we review the most relevant aspects of the geometrical and electronic properties of twisted bilayer graphene. In the third section, we study the features of graphene systems in the quantum Hall regime, first focusing on the monolayer and then on the twisted bilayer. In both cases, we put an accent on the regime with interaction-induced broken symmetries and carefully study the band structure and ground-state ordering at the filling factors corresponding to broken symmetry states. In the fourth section, we consider the system at charge neutrality when an electric field that induces an interlayer bias is turned on. This regime, for a specific range of values of the bias, pushes the system into the targeted *pseudo*-QSH phase. We compare our results with those obtained experimentally in Ref. [91] and consequently adjust our interaction model to fit the measurements therein, which reveals important information about the range of interactions in the system. Finally, we discuss the order of magnitude of the QSH gap as a function of the magnetic field and of the twisting angle,

constrasting it with the competing energy scale set by the broadening of the Landau levels away from the Landau regime, in order to assess the range of parameters where we expect the examined physics to be relevant.

3.2 Twisted bilayer graphene

Bilayer graphene is a composite structure made of two graphene monolayers displaced along the z axis by a distance $d = 3.35\,\text{Å}$ and it exists in three possible stacking geometries, commonly referred to as the AA, the AB (or Bernal) and the twisted graphene bilayer [36]. The first two types are highly regular structures where the two monolayers are either perfectly superimposed on each other (AA) or displaced by the in-plane vector $\boldsymbol{\delta}$ (AB). A twisted bilayer graphene is realized instead when the two monolayers are put one on top of the other and then rotated by an angle θ around an AB stacking point.

The electronic properties of graphene bilayers are extremely sensitive to the stacking order [36]. The spectra of the two highly ordered AA and AB confugurations already exhibit dramatical differences. The AA bilayer has a spectrum that consists of two copies of the single-layer spectrum, either of which is symmetrically displaced to higher and lower energies by a energy shift proportional to the interlayer hopping. Because of this, the AA-stacked graphene bilayer is a metal at zero doping and the Fermi surface is finite. On the other hand, AB bilayer bands have parabolic dispersion near the two inequivalent valleys $\mathbf{K}$ and $\mathbf{K}'$, and they touch at the Fermi energy [33]. Therefore, the Fermi surface is pointlike and the system is a semimetal like monolayer graphene. These features are clearly visible in the spectra for these two differently stacked structures sketched in Fig. 3.1. Twisted bilayer graphene exhibits yet a different spectrum. Given that this system is the focus of the work presented in this chapter, we devote the whole next subsections to describe its geometrical and electronic structure in detail.

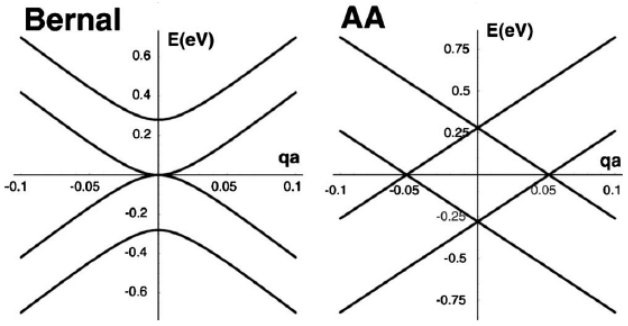

FIGURE 3.1: Low-energy band structures of pure AB (Bernal) and pure AA stacking bilayers around one valley. [Adapted with permission from Ref. [158]]

3.2.1 Geometric properties

We take the positions of the atoms of the bottom layer (that we label 'b') to be coincident with the definitions in Eqs. (1.1) and (1.4), that is $\mathbf{r}^{A_b}_{n,m} = \mathbf{r}_{n,m}$ and $\mathbf{r}^{B_b}_{n,m} = \mathbf{r}_{n,m} + \boldsymbol{\delta}$. Then, in the top layer (that we label 't') the positions are specified by $\mathbf{r}^{B_t}_{m,n} = \mathbf{r}'_{n,m} = n\mathbf{a}'_1 + m\mathbf{a}'_2$ and $\mathbf{r}^{A_t}_{m,n} = \mathbf{r}'_{n,m} - \boldsymbol{\delta}'$ where the primitive vectors in Eq. (1.2) are rotated by an angle θ as

$$\mathbf{a}'_{1,2} = \mathbf{a}_{1,2}\left(\cos\theta \pm \frac{\sin\theta}{\sqrt{3}}\right) \pm \mathbf{a}_{2,1}\frac{2\sin\theta}{\sqrt{3}} \tag{3.1}$$

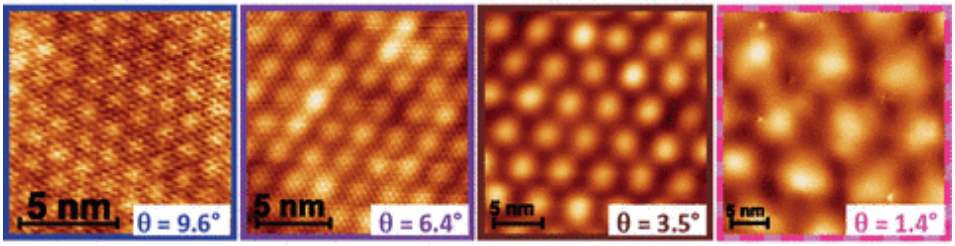

FIGURE 3.2: STM images of several moiré patterns with different twisting angles θ. The scale bar is 5 nm. [Adapted with permission from Ref. [159]]

and

$$\boldsymbol{\delta}' = a_0\,(\cos\theta, \sin\theta)\,. \tag{3.2}$$

A twisted graphene bilayer exhibits a pseudo-periodic superstructure made of alternating dark (AB-like) and light (AA-like) regions that is dubbed moiré pattern. The typical scale of these patterns is given by the moiré period

$$\ell_M = \frac{a}{2\sin(\theta/2)} = \frac{a_0\sqrt{3}}{2\sin(\theta/2)} \tag{3.3}$$

a quantity that increases continuously with decreasing angle as shown in Fig. 3.2. However, this system is not truly periodic in general and only a finite number of discrete angles yield perfectly commensurate superlattices, that is, proper structures made of supercells repeated over a definite period. In general, a supercell of a commensurate superlattice contains more a number ≥ 1 of moiré cells. The condition for a commensurate structure to occur is that given a stacking point A_bB_t placed at the origin, the exact same stacking takes place somewhere else in the structure. In other words, the positions $\mathbf{r}^{A_b}_{m,n}$ and $\mathbf{r}^{B_t}_{l,k}$ defined above need to coincide for some values of m, n and l, k different from 0. The primitive vectors of commensurate superlattices can be defined in terms of two indexes m_0 and r as

$$\mathbf{R}_1 = m_0\mathbf{a}_1 + (m_0 + r)\mathbf{a}_2 \tag{3.4}$$

$$\mathbf{R}_2 = -(m_0 + r)\mathbf{a}_1 + (2m_0 + r)\mathbf{a}_2 \tag{3.5}$$

if $r \neq 3n$, with n an integer and

$$\mathbf{R}_1 = \left(m_0 + \frac{r}{3}\right)\mathbf{a}_1 + \frac{r}{3}\mathbf{a}_2 \tag{3.6}$$

$$\mathbf{R}_2 = -\frac{r}{3}\mathbf{a}_1 + \left(m_0 + \frac{2r}{3}\right)\mathbf{a}_2 \tag{3.7}$$

if $r = 3n$. The number of sites in a supercell specified by these vectors is

$$N = \frac{4}{g}\left(3m_0^2 + 3m_0 r + r^2\right) \tag{3.8}$$

with $g = 1$ if $r \neq 3n$ and $g = 3$ if $r = 3n$. These two cases are also called odd ($r \neq 3n$) and even ($r = 3n$) according to their symmetry under sublattice exchange: superlattices with $r = 3n$ are invariant under inversion symmetry, whereas those with $r \neq 3n$ are not. In both cases, the commensurate twisting angle associated to the integers (m_0, r) is given

by

$$\cos\theta = \frac{3m_0^2 + 3m_0 r + r^2/2}{3m_0^2 + 3m_0 r + r^2} \tag{3.9}$$

For the sake of simplicity, in the rest of the chapter we choose to concentrate on the subset of commensurate structures spanned by the choice $r = 1$ and m_0 arbitrary, corresponding to a special case of the structures having odd parity symmetry and a single moiré cell per unit cell. These are so-called minimal moiré patterns. It can be shown that in the vicinity of any angle θ belonging to this subset there is an infinite set of commensurate structures with different m_0' and $r' \neq 1$. These structures have larger size supercells, but their moiré patterns are almost periodic repetitions of the structure with $(m_0, r = 1)$ [160]. As a result, the low-energy Hamiltonian for these structures can be effectively reduced to that of the structures with $r = 1$ and m_0 an arbitrary integer such that $\theta(m_0, r = 1) \approx \theta(m_0', r')$, thus allowing us to focus on the structures with $r = 1$ solely. What is peculiar about this special subset is that the moiré period coincides with the size of the superlattice unit cell $\ell_M = \ell_{SC} = |\mathbf{R}_{1,2}| = a\sqrt{N}/2$, where N is the number of sites in the elementary unit cell of the superlattice. For any other choice of $(m_0, r \neq 1)$ one has intead that $\ell_{SC} > \ell_M$, see Fig. 3.3a for comparison. For $r = 1$ a one-to-one mapping exists between the angles θ and the corresponding integers m_0, and in the following we will refer to each commensurate structure belonging to this subsect interchangeably by means of one or the other label. In table (3.1) we show how the integer m_0 links to the twisting angles θ, supercell sizes ℓ_{SC} and number of atoms in a unit cell N for $m_0 \in [1:8]$.

m_0	θ [°]	ℓ_{SC} [a_0]	N
1	21.79	4.58	28
2	13.17	7.55	76
3	9.43	10.53	148
4	7.34	13.53	244
5	6.01	16.52	364
6	5.08	19.52	508
7	4.41	22.52	676
8	3.89	25.51	868

TABLE 3.1: Table of the commensurate angles θ (in degrees), supercell sizes ℓ_{SC} (in units of the Carbon-Carbon distance a_0) and number of atoms in a unit cell N corresponding to different values of $m_0 \in [1:8]$.

The primitive vectors of the reciprocal space for the $r = 1$ case are

$$\mathbf{B}_1 = \frac{(2m_0+1)\mathbf{b}_1 + (m_0+1)\mathbf{b}_2}{3m_0^2 + 3m_0 + 1} \tag{3.10}$$

$$\mathbf{B}_2 = \frac{-(m_0+1)\mathbf{b}_1 + m_0\mathbf{b}_2}{3m_0^2 + 3m_0 + 1} \tag{3.11}$$

with

$$\mathbf{b}_1 = \frac{2\pi}{a_0}\left(\frac{1}{3}, -\frac{1}{\sqrt{3}}\right) \quad \text{and} \quad \mathbf{b}_2 = \frac{2\pi}{a_0}\left(\frac{1}{3}, \frac{1}{\sqrt{3}}\right)$$

the reciprocal lattice vectors of monolayer graphene. The Brillouin zone is an hexagon with side $Q = |\mathbf{B}_2 - \mathbf{B}_1|/3$. Given the two corners (or valleys) of the Brillouin zones of

the two separate layers

$$\mathbf{K}_b = \frac{4\pi}{3a}(0,1) = m_0\mathbf{B}_2 + \frac{1}{3}(\mathbf{B}_1 + 2\mathbf{B}_2) \tag{3.12}$$

and

$$\mathbf{K}_t = \frac{4\pi}{3a}(-\sin\theta, \cos\theta) = m_0\mathbf{B}_2 + \frac{1}{3}(\mathbf{B}_2 - \mathbf{B}_1) \tag{3.13}$$

it is easy to see that he distance between them $\Delta K = |\mathbf{K}_b - \mathbf{K}_t| = 2K\sin(\theta/2)$ (where $K = |\mathbf{K}| = 4\pi/3a$) equals the side of the Brillouin zone of the bilayer Q. Likewise, it is easy to see that the inequivalent valleys of the two layers $\mathbf{K}'_b$ and $\mathbf{K}'_t$ are equivalent respectively to $\mathbf{K}_t$ and $\mathbf{K}_b$, meaning that they are related through a reciprocal vector of the superlattice. Therefore, for any commensurate angle, there are two doubly degenerate non-equivalent Dirac points of the twisted bilayers, the two valleys

$$\mathbf{K}_1 = \frac{\mathbf{B}_1 + 2\mathbf{B}_2}{3} \quad \text{and} \quad \mathbf{K}_2 = \frac{2\mathbf{B}_1 + \mathbf{B}_2}{3} \tag{3.14}$$

coinciding respectively with the valleys $\mathbf{K}_b$ and $\mathbf{K}'_t$ and with the valleys $\mathbf{K}'_b$ and $\mathbf{K}_t$. The structure of the BZ for the superlattice corresponding to $(m_0, r) = (1,1)$ is shown explicitly in Fig. 3.3b.

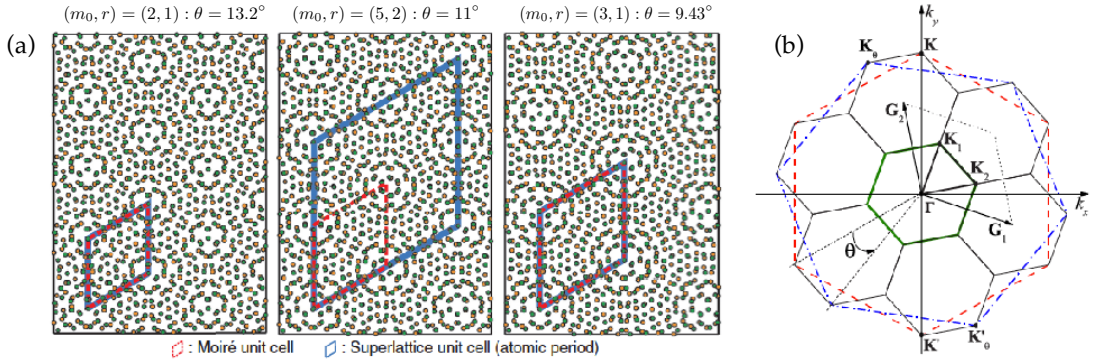

FIGURE 3.3: (a) Atomic structures of TwBGs with $\theta = 13.2°$, $\theta = 11°$ and $\theta = 9.43°$. Red and blue parallelograms correspond to the moiré unit cell and superlattice unit cell, respectively. [Adapted with permission from Ref. [161]] (b) Geometry of the reciprocal lattice for the twisted bilayer graphene. The green hexagon near the center shows the Brillouin zone of the twisted bilayer graphene corresponding to the indexes $(m_0, r) = (1,1)$. The large hexagons show the Brillouin zones of individual layers: the red dashed hexagon corresponds to the bottom layer and the blue dot-dashed hexagon to the top layer. Some of the next Brillouin zones of the TwBG are depicted by black solid hexagons. Notice that in this figure the vectors $\mathbf{G}_{1,2}$ correspond to the vectors $\mathbf{B}_{1,2}$ defined in Eqs. (3.10) and (3.11) of the main text, whereas $\mathbf{K}(\mathbf{K}')$ correspond to $\mathbf{K}_b(\mathbf{K}'_b)$ of the main text, and $\mathbf{K}_\theta(\mathbf{K}'_\theta)$ correspond to $\mathbf{K}_t(\mathbf{K}'_t)$. Notice that the vector $\Delta K = |\mathbf{K}_b - \mathbf{K}_t| = |\mathbf{K} - \mathbf{K}_\theta|$ coincides with the reciprocal vector of the superlattice. [Adapted with permission from Ref. [162]]

In general the two layers will be not only rotated one with respect to the other, but also shifted by a distance $\boldsymbol{\rho}$. In most of the literature, however, this shift is not considered. Indeed, the authors of Ref. [163] demonstrated that, by constructing an effective Hamiltonian in the continuum approximation for twisted bilayer grapehene with a non-zero shift between the layers, this Hamiltonian coincides with that for $\boldsymbol{\rho} = 0$ upon a unitary transformation, therefore the electronic spectrum is independent of the shift. This is because, in this approximation, the microscopic details of the superlattice are averaged out, and the effect of a finite $\boldsymbol{\rho}$ is reduced to shifting the whole moiré pattern in space, which

does not affect the spectrum. In the following, we will neglect this shift.

3.2.2 Band structure

Several studies employing either fully numerical calculations (often based on a combination of density functional theory with tight binding models [161,162,164–168]) or continuum low-energy approximations [29,160,163] have been performed to unveil the electronic structure of graphene bilayer systems with rotational stacking faults. Here, we choose a tight binding model for the p_z orbitals of the Carbon atoms that closely follows the one reported in Ref. [161]. Within this model, the Hamiltonian (that we take to be spinless for the moment) reads

$$H_0 = \sum_{ij} c_i^\dagger t_{ij} c_j \tag{3.15}$$

where t_{ij} is a 2×2 matrix in layer space, and the operators c_i, $c_i^\dagger$ are two-dimensional spinors acting in this space, $c_i = (c_{ib}, c_{it})^T$, where $c_{il}^\dagger$ creates an electron on the site i of layer $l = b, t$. The indexes $i, j = 1, ..., N/2$ label the in-plane two-dimensional positions $\boldsymbol{\rho}_i = (x_i, y_i)$ of the atoms within each layer. The vector indicating the position of atomic sites in three-dimensional space is $\mathbf{r}_i = (\boldsymbol{\rho}_i, z)$, where $z = d/2$ if the atom is in the top layer and $z = -d/2$ if it is in the bottom layer. The matrix t_{ij} reads

$$t_{ij} = \begin{pmatrix} t_{ij}^{bb} & t_{ij}^{bt} \\ t_{ij}^{tb} & t_{ij}^{tt} \end{pmatrix} \tag{3.16}$$

where each component $t_{ij}^{ll'} = t^{ll'}(|\boldsymbol{\rho}_i - \boldsymbol{\rho}_j|)$ indicates the distance and layer dependent hopping amplitude between site i of layer l and site j of layer l'. The hopping amplitude $t^{ll'}(\rho)$ is given by

$$\begin{cases} t^{ll'}(\rho) = -t\,(\rho/r)^2\, e^{-\beta(r-a_0)/a_0} & \text{if } r \leq R \text{ and } l = l' \\ t^{ll'}(\rho) = -t\,(\rho/r)^2\, e^{-\beta(r-a_0)/a_0} + t_1\,(d/r)^2\, e^{-\beta(r-d)/a_0} & \text{if } r \leq R \text{ and } l \neq l' \\ t^{ll'}(\rho) = 0 & \text{if } r > R \end{cases} \tag{3.17}$$

with $\rho = \sqrt{x^2 + y^2}$ the in-plane distance between two atoms, $r = \sqrt{x^2 + y^2 + z^2}$ the total distance, d the interlayer distance, β a dimensionless parameter that controls the range of the hopping function and R a threshold distance beyond which the atoms are decoupled. The parameters choice that fits best the DFT bands is $d = 2.36a_0$, $R = 4a_0$, $t_1 = -0.178t$ where we take t to be $t = -2.7\,\text{eV}$, and $\beta = 3.14$.

In Fig. 3.4 we show the band dispersion calculated with this model for an infinite lattice of twisted bilayer graphene with $r = 1$ and m_0 ranging from 1 to 6 along the $\Gamma - K_1 - M - K_2 - \Gamma$ path in the Brillouin zone of each different superlattice. Notice that particle-hole symmetry is broken in these spectra, as a result of the specific modelization employed that includes hoppings beyond nearest neighboring atoms. Specifically, the hopping between first and second nearest neighbors *within the same sublattice* is responsible for this asymmetry. whereas in Fig. 3.5 we depict the unit cells associated to m_0 ranging from 1 to 6.

As is clear from the spectra in Fig. 3.4, the low-energy spectrum for the considered angles consists of two linearly dispersing Dirac cones centered around the two inequivalent valleys K_1 and K_2, with reference to the definitions given in the previous subsection. This feature is confirmed by several theoretical studies and, more importantly, by numerous experimental studies exploiting different techniques ranging from STM [159,169,170],

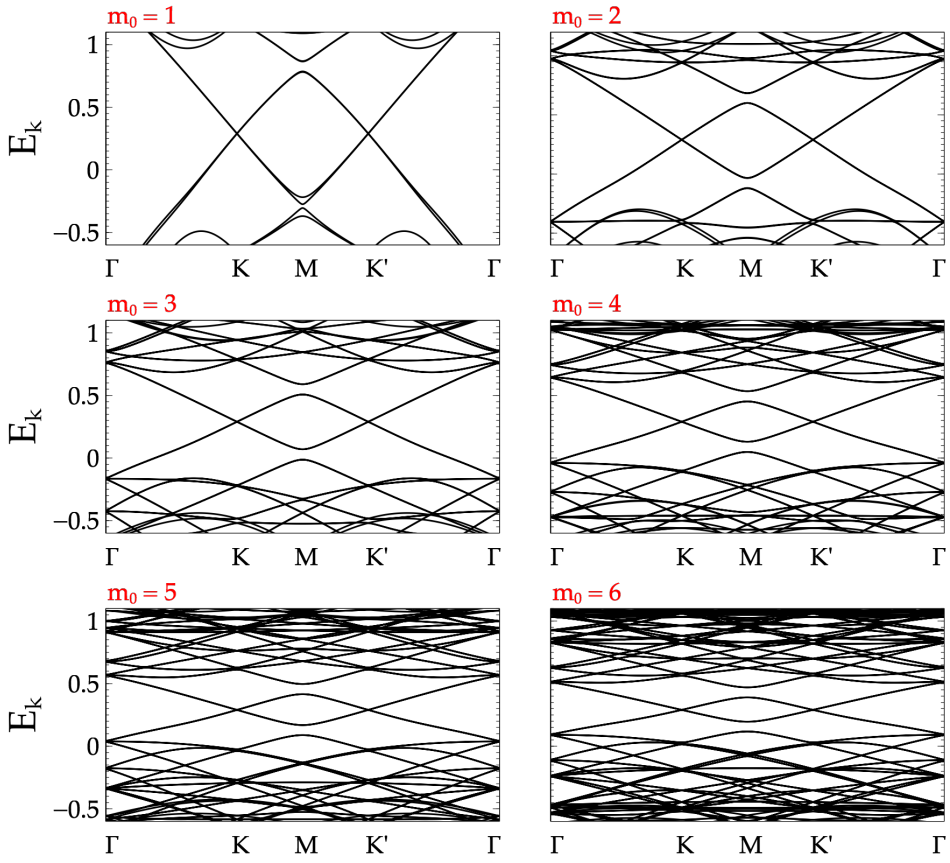

FIGURE 3.4: Spectra of infinite twisted bilayer graphene systems with $m_0 \in [1:6]$ and $r = 1$ along the high symmetry lines $\Gamma - K - M - K' - \Gamma$. Energies are in units of the hopping $t = -2.7$ eV.

ARPES [171–173], to Raman [174–177] spectroscopies. However, the Fermi velocity $\tilde{v}_F$ of the low-energy excitations in these systems appears to be strongly renormalized as a function of the twisting angle with respect to that of monolayer graphene $v_F = 3a_0 t/2$. This can be appreciated in the plots of Fig. 3.4 in the form of increasingly 'squeezed' Dirac cones with a reduced Fermi velocity $\tilde{v}_F$ as θ is reduced. The analytical and numerical dependence of the Fermi velocity on θ, $\tilde{v}_F = \tilde{v}_F(\theta)$, was addressed in several works [160,162,163]. In [29], one of the seminal paper on the topic where a continuum approach was first used, the following dependence was derived:

$$\tilde{v}_F = v_F \left[1 - \left(\frac{3\tilde{t}_\perp}{\hbar v_F \Delta K} \right)^2 \right] \tag{3.18}$$

where $\tilde{t}_\perp$ is the effective interlayer coupling of the low-energy model employed. The curve associated to this expression is presented in Fig. 3.6a, where a comparison with the one obtained numerically by exact diagonalization of the secular equation is also shown. Several approaches that followed [162,163] confirmed that for not too small angles $\theta \gtrsim 3^\circ$ the Fermi velocity is very well described by the approximate formula (3.18). However, a characteristic that was pointed out by several theoretical works [160,166,178] is that the renormalized Fermi velocity goes to zero for a set of discrete so-called *magic* angles smaller than a given critical angle θ_c, whose exact value is not derivable analytically but has been estimated to be of the order of $\theta_c \approx 1^\circ$. Specifically, Ref. [160] calculated the density of states (DOS) for different twist angles. It resulted that when $\theta > \theta_c$, the DOS is

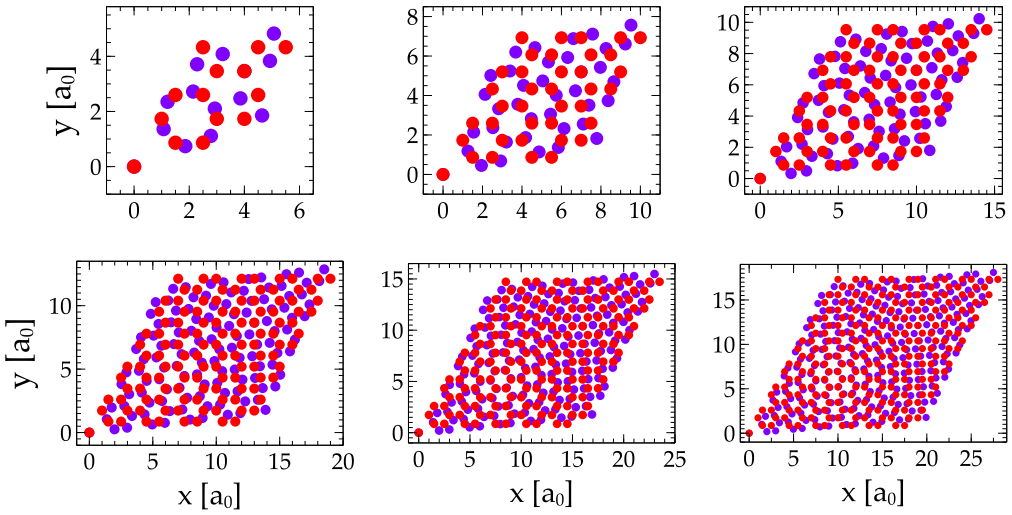

FIGURE 3.5: Sketch of the unit cells corresponding to $r = 1$ and $m_0 \in [1:6]$. Atoms from the top and bottom layers have been colored in red and purple to distinguish them. Distances are in units of the Carbon-Carbon distance a_0.

zero at the Fermi level and increases linearly at small energies, consistent with the presence of low-energy Dirac cones. For $\theta < \theta_c$, the DOS at the Fermi level is non-zero and its value oscillates as a function of the angle. These oscillations were related to a quantization condition of the electrons that for very small angles tend to be confined in the AA-like regions of moiré systems with large periods [160,178]. Such a behaviour of the density of states at small twist angles has been confirmed in STS and STM measurements by L.-J. Yin *et al.* in Ref. [179].

The strong Fermi velocity renormalization associated to this phenomenology is accompanied by the appearence of a van Hove singularity at the M high-symmetry point for notably lower energies $E_M \ll t$ than in single-layer graphene. The energy at which the saddle point makes its appearence is itself a decreasing function of the angle, as clearly visible in both the experimental local density of states curves presented in Fig. 3.6b and in the calculated spectra of Fig. 3.4. In the framework of the continuum approximation the energy of the saddle point can be estimated as [29,160,163] as

$$E_M \approx 2\hbar v_F^* K \sin(\theta/2) - 2\tilde{t}_\perp. \tag{3.19}$$

In this thesis we are interested in the effectively decoupled regime where the low-energy spectrum displays two Dirac cones that are far in energy from the saddle point, similarly to monolayer graphene. Since, as we have seen above, for very small angles ($\theta < \theta_c \approx 1°$) the validity of such a description starts to fail, in the following we stick to large twisting angles corresponding to small values of the integer $m_0 < 31$ (the integer corresponding to the first magic angle).

3.3 Theory of the quantum Hall effect in twisted bilayer graphene

We now study the electronic properties of twisted bilayer graphene in the large angle regime when an out-of-plane magnetic field is applied to the system to drive it into the

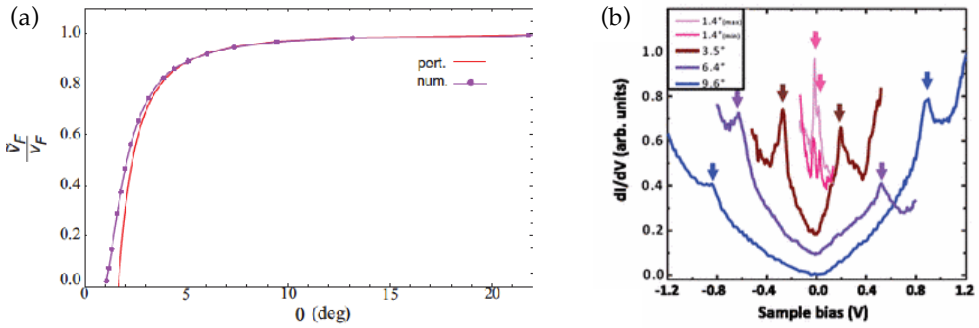

FIGURE 3.6: (a) Comparison between the velocity renormalization obtained by perturbation theory in the parameter $\tilde{t}_\perp/\hbar v_F \Delta K$ and given in Eq. (3.18) (red line), and by numerical diagonalization of the secular equation (purple line). [Adapted with permission from Ref. [160]] (b) Local density of states spectra taken on four different moiré patterns. The appearence of a van Hove singularity at ever decreasing energies with decreasing angles is evident from these plots. [Adapted with permission from Ref. [159]]

quantum Hall regime. An exhaustive account of the topological properties of two dimensional electron systems in this regime has been given in the introduction, where special emphasis has been put on the differences between this regime in standard Schroedinger-like crystals and in monolayer graphene. As for the QH effect in the latter, we have seen how its distinguishing feature, namely, the anomalous series of its conductance plauteaus, derives from the relativistic-like nature of its carriers around zero energy. However, it has also been shown that interactions play an important role in breaking the degeneracies that affect graphene Landau levels (LLs) as a result of spin and valley degeneracies. We review the role of interactions in single-layer graphene, concentrating in particular on their effect on its unique zero Landau level (ZLL). We will cover the most important theories that have been formulated in past years along with the most important experimental results, and finally back-up the discussion with numerical calculations performed within a standard tight binding description of the π orbital of carbons, with the addition of electron-electron interactions treated at the mean field level. We then proceed to tackle the more complicated issue of the properties of twisted bilayer graphene in this regime. Again, we will review the most relevant works on the topic, and present the results obtained by adding electron-electron interactions treated at the mean field level.

3.3.1 Quantum Hall effect in monolayer graphene

General theory

As already seen, both the sequence of Hall plateaus in the conductance and the degeneracy of the Landau levels are unconventional in graphene. In fact, due to its relativistic dispersion at low energies, this system exhibits a sequence of Landau levels at energies

$$E_n = \text{sign}(n)\sqrt{|n|}\hbar\omega_c = \text{sign}(n)\sqrt{2|n|\hbar v_F^2 eB} \tag{3.20}$$

where we have defined the cyclotron frequency as $\omega_c = \sqrt{2}v_F/\ell_B$, in which $\ell_B = \sqrt{\hbar/eB}$ is the magnetic length. This is to be compared with the energies of Landau levels in

standard 2DEGs:

$$E_n^{2DEG} = \hbar\omega_c \left(n + \frac{1}{2}\right) \tag{3.21}$$

with $\omega_c = eB/m$. The energies (3.20) imply the existence of a field-independent Landau level at zero energy corresponding to $n = 0$. This level, also called zero Landau level (ZLL), is responsible for altering the plateaus sequence with respect to conventional 2DEGs, where now plateaus occur at the half integer values:

$$\sigma_{xy} = \pm\frac{ge^2}{h}\left(|n| + \frac{1}{2}\right) \qquad n = 0, 1, 2, ... \tag{3.22}$$

where $g = g_s g_v = 4$ is the total degeneracy of each level, originating from the concurrence of spin and valley degeneracies ($g_s = g_v = 2$). The LLs with $n > 0$ ($n < 0$) are electron-like (hole-like) and they disperse by bending upward (downward) at the boundaries of the system. To confirm its exceptionality, the ZLL distinguishes itself from the rest of $n \neq 0$ levels in two key respects: (i) of the four levels that are degenerate in the bulk, two are electron-like and two are hole like, as corroborated by the fact that close to the edges they disperse in opposite directions; (ii) the ZLL eigenfunctions belonging to the two inequivalent valleys are localized on opposite sublattices, so that these two degrees of freedom are effectively locked and the valley degeneracy manifests as a sublattice degeneracy.

Already from the early days of graphene, however, a body of experimental works performed at relatively high magnetic fields in weakly disordered samples uncovered that the sequence of Hall plateaus is altered with respect to the one predicted theoretically (Eq. (3.22)) at the single-particle level, signaling a splitting of the multiply degenerate Landau levels [22,27,28,180–182]. This is not unexpected because the quenching of the kinetic energy induced by the strong fields renders the system susceptible to spontaneous degeneracy breaking. Pioneering experiments were only able to distinguish additional plateaus at filling factors $\nu = 0, \pm 1$ and ± 4 [22,180], triggering a huge amount of theoretical efforts aimed at explaining the full symmetry rupture at the ZLL but not at the $n \neq 0$ levels [8,10,183–188]. Successive experiments in high quality samples were able to demonstrate the appearence of all possible integer filling factors $\nu = 0, \pm 1, \pm 2, \pm 3, ...$ [28,181,182]. Several effects have been suggested to lie at the heart of this observation, ranging from lattice distortions [12,186] to the Zeeman effect [184] to interactions [8,12,183,189]. However, it is now widely accepted that the most likely responsible for inducing broken-symmetry ground states are electron-electron interactions [190]. The phenomenon of interaction-induced gaps and broken symmetries at integer filling factors in $N \geq 2$ degenerate LLs is known as quantum Hall ferromagnetism [10,182], and its concrete realization in graphene has been the focus of an impressive amount of theoretical work, based on both numerical and analytical models, aimed at determining the ground-state ordering associated to the symmetry broken states of each filling factor [12,189,191]. Below, we review some of the most relevant studies concerning the symmetry breaking effects at filling factors $\nu = 0$ and $\nu = \pm 1$.

Filling $\nu = 0$ At charge neutrality, corresponding to $\nu = 0$, it is convenient for the system to lift the SU(4) degeneracy of the ground state, while leaving a residual SU(2) degeneracy in the two splitted levels. Although long-range Coulomb interactions and Landau levels mixing have been proved able to renormalize the parameters at play [8], there is strong consensus that the many-body ground state of the system depends on the relative strength of the on-site Hubbard interaction, intersublattice repulsion and Zeeman field [12,188,189]. In the absence of in-plane components of the magnetic field,

the three ground-state candidates allowed for by the competition between these interactions are antiferromagnetic (AF), charge density wave (CDW) and ferromagnetic (FM) [12,89,189,192]. The former corresponds to a spin-density wave with both inversion symmetry and spin rotational invariance broken, with the two sublattices A and B being selectively occupied by oppositely polarized spins (see Fig. 3.7a). The charge density wave state is such that only one of the two sublattices is occupied by both spin species (see Fig. 3.7b). In this case, therefore, only inversion symmetry is broken. Finally, ferromagnetic ordering implies breaking of the spin symmetry, given that the spins of both sublattices are all aligned parallel (see Fig. 3.7c). If an in-plane magnetic field component $B_{\parallel}$ is added to the one perpendicular to the graphene sheet, the system can develop an additional ordering, namely canted antiferromagnetic (CAF) [12,89,189,192]. In this phase the orientation of the spins is tilted along the direction pointed at by the total applied magnetic field $B = \sqrt{B_{\perp}^2 + B_{\parallel}^2}$ (see Fig. 3.7d). Calculations in finite-size systems have shown

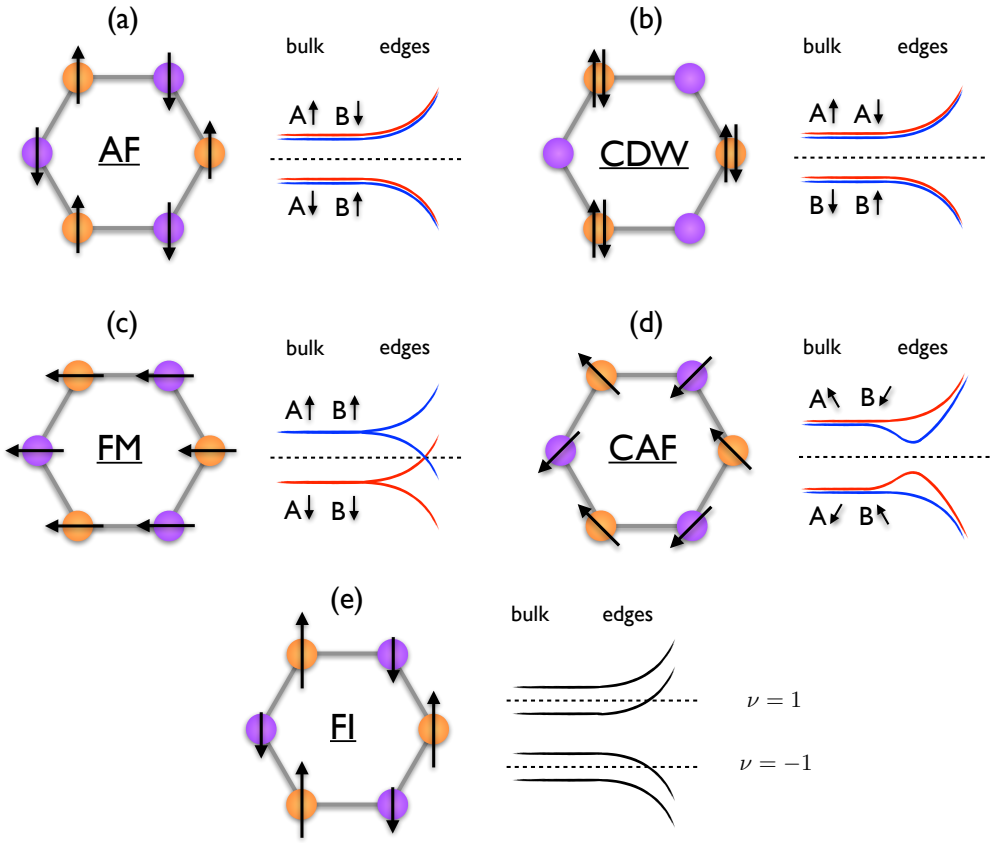

FIGURE 3.7: (a)-(d) Possible ground states at $\nu = 0$. For every ground state, the magnetic orderings and the spectra in the bulk and at the edges are shown, along with the sublattice and spin flavors of each band. (a) AF. (b) CDW. (c) FM. (d) CAF. Red and blue lines correspond to up and down spin polarizations with respect to the quantization axis. (e) Ground state at $\nu = \pm 1$. The ferrimagnetic ordering and the spectra in the bulk and at the edges are shown. Black curves indicate that the spin and sublattice polarization of each band is undetermined.

that while all these ground-states are characterized by an incompressible bulk, the AF, CDW and CAF also display gapped edges whereas the FM is gappless [189,191,192]. Remarkably, it exhibits two branches of edge states with opposite velocities for opposite spins, much like what happens in quantum spin Hall systems, the only difference being that time reversal symmetry is broken by the presence of the magnetic field. The four

competing ground states described above are sketched in Fig. 3.7a, b, c and d, where both the magnetic orderings and the schematic band dispersion in the bulk and at the edges are displayed for each.

Experiments performed at zero in-plane field invariably exhibit a high resistance at $\nu = 0$ that signals that the ground state is fully insulating, both at the edges and in the bulk [28,89,181,182]. The competition between the two configurations compatible with this observation, AF and CDW, has been shown to be sensitive to the relative strength between on-site and intersite electron-electron interactions [8,189]. For larger intra than intersite interaction the system favors AF ordering, since the large on-site repulsion results in a high energy cost for putting two electrons on the same site, so that the system prefers to accomodate one electron on each site, paying instead the energy cost of the intersite repulsion. In the opposite regime where the ratio of onsite to intersite repulsion is small, the energy cost of having one electron per site exceeds that of doubly populating each atomic site, and the system prefers to generate a CDW. It has been suggested in Ref. [189] that either ground-state might be favored or disfavored depending on the concrete experimental configuration. Specifically, the conclusion reached by the authors is that, as a result of the relatively high dielectric constant, and consequent screening effects, the former regime could be realized in graphene on SiO_2 and other typical substrates, whereas the latter could be realized in suspended graphene. To shed light on the actual ground-state of the system at half filling, a groundbreaking experiment was performed in 2014 [89] on graphene/hBN/graphite stacks in the QH regime where the in-plane component of the field was increased from zero to a maximum value of $B_{\parallel} \approx 34$ T without changing the strenght of the out-of-plane component $B_{\perp} = 1.4$ T. Two-terminal conductance measurements showed that the conductance is increased from 0 to a value close to $2G_0$, with $G_0 = e^2/h$ the conductance quantum, as $B_{\parallel}$ is ramped up, see Fig. 3.8a. These measurements are compatible with the suppression of the edge gap culminating into its full closure by means of edge states for high in-plane fields in a system with an otherwise incompressible bulk. This interpretation was confirmed by capacitance (see Fig.3.8b and c) and non-local resistance measurements. The interpretation of these measurements points to a system with an AF ordering at $B_{\parallel} = 0$ that evolves into a CAF phase for finite $B_{\parallel}$, until it reaches a FM ground state characterized by edge transport via helical states that effectively realize a time-reversal broken quantum spin Hall phase. In the simplified scenario where the ground state is determined by the competition between the scales set by the onsite and intersite interactions, this result points to the probable interpretation that the former is stronger than the latter, as expected for a dominant role of screening in the sample employed in the experiment.

Filling $\nu = \pm 1$ Determining the ground state ordering of the system at quarter filling ($\nu = -1$) and three quarter filling ($\nu = 1$) is much more straightforward than in the $\nu = 0$ case. In fact, independently of the specific mechanism at play, quantum Hall ferromagnetism requires that the spin and valley SU(4) symmetry be completely removed when the occupation of the ZLL is odd. Therefore, since each of the four singly degenerate states in which the ZLL splits is singly spin and sublattice polarized, in all possible scenarios and at both filling factors the ground-state ordering is ferrimagnetic (FI), corresponding to a spin-polarized charge density wave [8]. The associated conductance is $G = G_0$ (see Fig. 3.8a) given that the Fermi level intercepts one spin and sublattice polarized electron-like (hole-like) dispersing channel for $\nu = 1$ ($\nu = -1$). A less trivial issue is to unambiguously identify the spin and sublattice polarization of the conducting channels at these two filling factors. However, since at half filling the system is in all likelyhood in an insulating antiferromagnetic phase at zero in-plane field, it is reasonable to assume that the further lifting of the residual SU(2) degeneracy affecting the bands

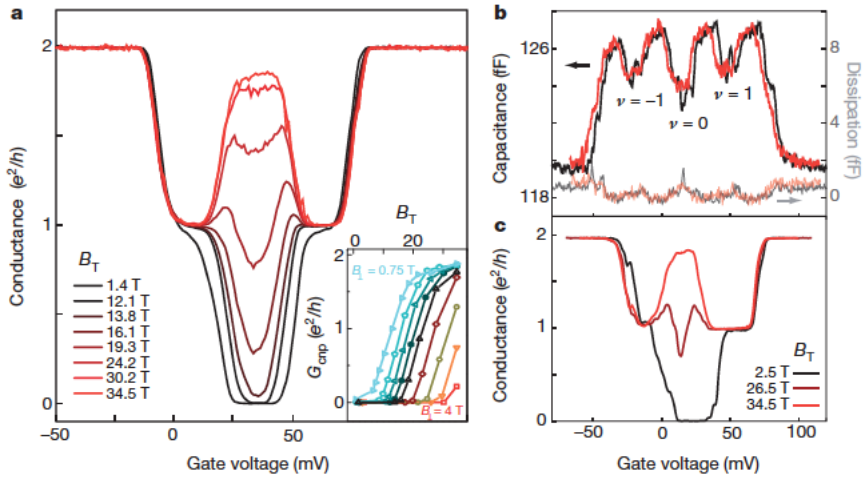

FIGURE 3.8: (a) Conductance at $B_\perp = 1.4$ T for different values of the total magnetic field B_T. As B_T increases, the insulating state at $\nu = 0$ is gradually replaced by a high conductance ($G \approx 2G_0$) state. (b) Capacitance (opaque lines) and dissipation (semi-opaque lines) at $B_\perp = 2.5$ T. The low dissipation confirms that the measurements are in the low-frequency limit, such that the dips in capacitance can be interpreted as corresponding to incompressible states. (c) Conductance under the same conditions. The absence of a detectable change in capacitance when the two-terminal conductance undergoes a transition from an insulating state to a metallic state suggests that the conductance transition is due to the emergence of gapless edge states. [Adapted with permission from Ref. [89]]

at $\nu = 0$ will take place between states with opposite spin and sublattice polarizations, cfr Fig. 3.7b. Still, it is unclear in what order. We tackle this question in what follows by selfconsistently solving a tight binding model for graphene with interactions at the mean field level. The magnetic ordering and band structure at $\nu = \pm 1$ filling have been sketched in Fig. 3.7e. We haven't colored the bands since, as we have seen, whereas determining the magnetic ordering of the ground state is straightforward, it is less clear, a priori, which spin and sublattice/valley flavour to assign to each band.

Tight binding model in the QH regime

The tight binding modelization employed for a non-interacting graphene monolayer subject to an out-of plane magnetic field B is the following:

$$H_0 = -\sum_{<ij>} t_{ij} c_i^\dagger c_j + V_Z \sum_i c_i^\dagger s_z c_i \tag{3.23}$$

Here, c_i and $c_i^\dagger$ are spinors in spin-space such that $c_i = (c_{i,\uparrow}, c_{i,\downarrow})^T$ where the operators $c_{i,\sigma}$ and $c_{i,\sigma}^\dagger$ respectively destroy and create an electron at site i and with spin $\sigma = \uparrow, \downarrow$, s_z is a Pauli matrix acting in spin space and the symbol $< ij >$ refers to restriction of summation to nearest neighboring atomic sites. The coupling of the magnetic field to the orbital degrees of freedom is included in the field-dependent hopping amplitude $t_{ij} = te^{i\phi_{ij}}$ ($t = 2.7$ eV in graphene) between the nearest neighboring sites $\mathbf{r}_i = (x_i, y_i)$ and $\mathbf{r}_j = (x_j, y_j)$, while its coupling to the spin degree of freedom is included in the Zeeman field $V_Z = g\mu_B B$. The phase ϕ_{ij} is the *Peierls* phase acquired by electrons moving in a magnetic field and it depends on the line integral of the vector potential $\mathbf{A}(\mathbf{r})$ along the

trajectory linking the two lattice sites as

$$\phi_{ij} = \int_{\mathbf{r}_i}^{\mathbf{r}_j} \mathbf{A}(\mathbf{r}) \cdot d\mathbf{r} \tag{3.24}$$

Calculations are carried out numerically by means of a Python code for graphene nanoribbons with periodic boundary conditions (PBCs) along the x direction and either zigzag or armchair terminations along the y direction. For these calculations, we choose to work within the Landau gauge, where the vector potential is chosen as $\mathbf{A}(\mathbf{r}) = B(y, 0, 0)$ to preserve translational invariance along the x direction. In this gauge, the phase ϕ_{ij} is given by $\phi_{ij} = \frac{B}{2}(x_j - x_i)(y_i + y_j)$. Calculations on ribbons with PBCs along both axes were performed as well. In this case, since the presence of a vector potential associated with the out-of-plane magnetic field breaks the translational symmetry along the y direction, we have to choose out-of-plane magnetic fluxes Φ commensurate with the lattice, or, equivalently, a system with an enlarged magnetic cell that is q times (along y) the original unit cell, such that $\Phi/\Phi_0 = 2\pi p/q$ with p and q coprime integers and $\Phi_0 = h/e$ the flux quantum. This choice allows to recover periodicity along y. In Fig. 3.9 we present the typical the band structure for $V_Z = 0$ for armchair and zigzag nanoribbons with widths $W = 30a = 8$ nm and $W = 89a_0 = 12.6$ nm respectively, and magnetic field $B = 0.05\, B_0$, where $B_0 = \hbar/ea_0^2 = 3.26\ 10^4$ T. This value of B is unphysical and much larger than the magnetic fields within the reach of typical experiments, of the order of $\approx 0 - 50$ T. Such high fields are called for due to numerical limitations. In fact, a calculation of the actual stripes, with one micron width, is beyond the reach of our computational resources, and thus we are bound to consider narrower stripes with widths W of the order of 10 nm. This forces us to consider high magnetic fields in order for the magnetic length ℓ_B, that controls interedge coupling, to be much smaller than W. In subsection 3.4.3, however, we show how a rescaling of these parameters is possible that provides for a quantitative assessment of the relevant observables, calculated at rescaled magnetic fields of the order of some Teslas and much wider nanobibbons.

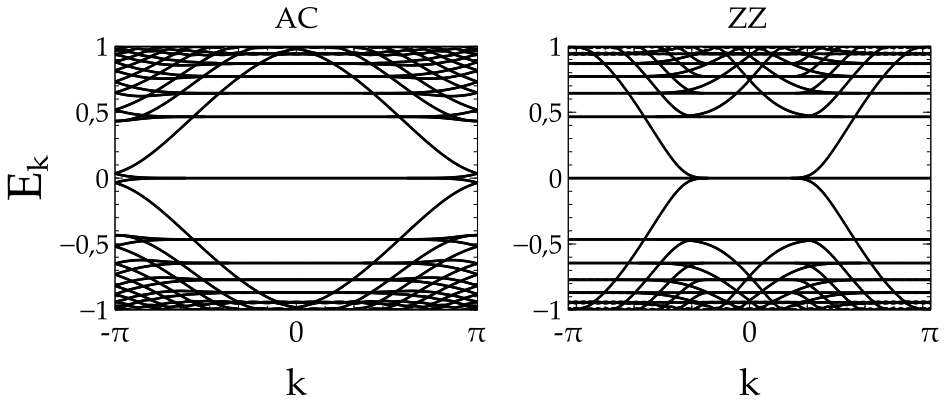

FIGURE 3.9: Noninteracting spectrum of a nanoribbon of monolayer graphene in the quantum Hall regime translationally invariant along one direction and with armchair (left) or zigzag (right) terminations along the other. The magnetic field has been chosen as $B = 0.05$ in units of B_0 and the energy is plotted in units of the hopping t.

Electron-electron interactions

As outlined above, several theoretical studies point at the conclusion that the competition between the allowed ground states is most likely settled by the relative strenght of

the on-site to intersite repulsion. This motivates us to developing an interacting model limited to short-range interactions, that is sufficient to account for the broken-symmetry ground states that the system can take on. Namely, we restrain the possible interactions to occur between electrons either on the same atomic site (parametrized by a coefficient U) or on nearest neighboring sites (parametrized by a coefficient V). We decouple these terms within a mean field approximation and solve the problem numerically with a self-consistent approach. A similar technique was employed for calculating the ground state of graphene at filling factors $\nu = 0, \pm 1$ in [192] for the case with $U \neq 0, V = 0$, that is, neglecting intersublattice interactions. As the authors show in the paper, and as we will see in the following, this model is sufficient to generate all the expected broken symmetry states of quantum ferromagnetic graphene, while not being realiable in quantitative terms when it comes to estimate the order of magnitude of the generated gaps.

We address the problem of solving the following Hamiltonian:

$$H = H_0 + H_{\text{int}} \tag{3.25}$$

where H_0 is given in Eq. (3.23), while the interaction term reads

$$H_{\text{int}} = \frac{1}{2} \sum_{ij,\sigma\sigma'} V_{ij} c^\dagger_{i,\sigma} c^\dagger_{j,\sigma'} c_{j,\sigma'} c_{i,\sigma} \tag{3.26}$$

If we limit ourselves to on-site and nearest-neighboring interactions, H_{int} becomes

$$H_{\text{int}} = \frac{U}{2} \sum_{i,\sigma} c^\dagger_{i,\sigma} c^\dagger_{i,-\sigma} c_{i,-\sigma} c_{i,\sigma} + \frac{V}{2} \sum_{<ij>,\sigma\sigma'} c^\dagger_{i,\sigma} c^\dagger_{j,\sigma'} c_{j,\sigma'} c_{i,\sigma} \tag{3.27}$$

where $U = V_{ii}$ and $V = V_{ij}$ for $|\mathbf{r}_i - \mathbf{r}_j| = a_0$. Notice that in the first (also called Hubbard) term only one of the two summations over spin indexes survives because of Pauli exclusion principle. We then operate a mean field approximation under which the many body problem turns into a single-electron problem. For a generic product of two operators A and B this approximation consists in neglecting terms which are of second order in the fluctuations of the operators with respect to their average values. To show this, we rewrite the product $\langle AB \rangle$ as

$$AB = A\langle B \rangle + \langle A \rangle B - \langle A \rangle \langle B \rangle + (A - \langle A \rangle)(B - \langle B \rangle) \tag{3.28}$$

where the last term is of second order in the fluctuations. By neglecting it, we are left with

$$AB \approx A\langle B \rangle + \langle A \rangle B - \langle A \rangle \langle B \rangle \tag{3.29}$$

which is precisely the mean field decoupling of the product AB. This is equivalent to say that the correlation function between the two operators vanishes, since from Eq. (3.29) stems that

$$\langle AB \rangle = \langle A \rangle \langle B \rangle. \tag{3.30}$$

For what concerns the interaction Hamiltonian (3.27) this approximation consists in decoupling all the physically meaningful averages of products of fermion operators. The only non-zero terms are those that act as corrections to the terms entering the non interacting Hamiltonian H_0, yielding the mean-field decoupled Hamiltonian

$$H^{\text{MF}}_{\text{int}} = U \sum_{i,\sigma} \langle c^\dagger_{i,\sigma} c_{i,\sigma} \rangle c^\dagger_{i,-\sigma} c_{i,-\sigma} + V \sum_{<ij>,\sigma\sigma'} \left(\langle c^\dagger_{i,\sigma} c_{i,\sigma} \rangle c^\dagger_{j,\sigma'} c_{j,\sigma'} - \langle c^\dagger_{i,\sigma} c_{j,\sigma'} \rangle c^\dagger_{j,\sigma'} c_{i,\sigma} \right) \tag{3.31}$$

plus an unimportant constant that has been omitted for the sake of simplicity. The original many-body Hamiltonian has been converted into a single-particle Hamiltonian bilinear in the fermionic operators such that the role of the overall electron cloud has been downgraded to that of effective fields acting on single electrons. Still, the electrons are correlated as all of these averages are computed on the ground state of the interacting Hamiltonian. The Hamiltonian, in turn, depends on these averages. A selfconsistent protocol can then be applied, where the averages in Eq. (3.31) are calculated on a trial ground-state wavefunction that is updated at each iteration until the total energies converge to six significant figures. High accuracy is required because the ground state ordering occurs primarily in the $n = 0$ Landau level, involving only a very small percentage of the electrons, so that the competing orderings are very close in energy. This accuracy proved sufficient for the algorithm to converge within a number of iterations of the order of 10^2.

At this stage, we limit ourselves to consider the case where only the Hubbard term is present ($U \neq 0, V = 0$) in combination with an arbitrarily small Zeeman field V_Z that is added to the non-interacting Hamiltonian and then subtracted from the final result. This procedure is justified in that a Zeeman field, however small, is patently present in the system owing to the applied out-of-plane field that couples to the spin degrees of freedom on top of the orbital ones. However, because of the relatively low magnetic fields needed for prompting the quantum Hall regime in graphene, the Zeeman splitting of the bands induced by such small fields is very weak and likely the smallest energy scale of the problem, so we present the final results with the V_Z contribution subtracted. This procedure is reliable since the resulting gaps that open at both $\nu = 0$ and $\nu = \pm 1$ fillings, once the Zeeman field is subtracted, are independent of V_Z. Notice also that in our study we only consider the case with no in-plane field. An in-plane component of the field, as we have seen, would have the effect of tilting the spins to give rise to a CAF phase, that is not allowed when $B_{\parallel} = 0$. The value of U is largely uncertain. It has been estimated to range approximately between 2 and 10 eV [1,189,193]. However, within the present model we are bound to explore values of the on-site interaction $U < U_c = 2.2t \approx 6$ eV, that is the value at which graphene becomes antiferromagnetic at $B = 0$ within a tight binding Hubbard interaction model solved self-consistently such as the one used here [194]. Since it is well known that no interaction-driven gaps are opened in graphene in the absence of an applied magnetic field, it is then clear that within this model we have to stick to values of U smaller than this critical threshold.

We fully characterize the system at the desired filling factor by both its band structure and its magnetic ordering. In order to define the latter, we first calculate the average spin polarization at each atomic site of the nanoribbons unit cells, defined as

$$\mathbf{m}_i = \langle \psi | \mathbf{s} | \psi \rangle \tag{3.32}$$

where the index i runs over all the lattice sites of this unit cell, and $\langle \psi | \mathbf{s} | \psi \rangle$ indicates the expectation value taken on by the vector of pauli matrices $\mathbf{s} = (s_x, s_y, s_z)$ on the ground state wavefunction $|\psi\rangle$ calculated by the iterative procedure described above. If the magnetic field is applied along the z direction as in our case, the magnetic ordering of the selfconsistent solution is completely determined by the quantity $m_i = \langle \psi | (s_z)_i | \psi \rangle$. The degree and type of magnetic ordering is then described by the following site-dependent

parameters

$$M_i = \frac{1}{2}\left| m_i + \frac{1}{\mathcal{N}} \sum_{j \in nn} m_j \right| \tag{3.33}$$

$$N_i = \frac{1}{2}\left| m_i - \frac{1}{\mathcal{N}} \sum_{j \in nn} m_j \right| \tag{3.34}$$

where $\mathcal{N}$ is the coordination number of the i-th atom, that is the number of nearest neighboring sites, and j runs over these sites. In this way, if the system is ferromagnetic, then for all sites i $N_i = 0$ whereas M_i is finite. Instead, if the order is antiferromagnetic, then adjacent A and B sites have opposite magnetizations and therefore $M_i = 0$ whereas N_i is finite. Finally, a ferrimagnetic ground state will be characterized by M_i and N_i both finite. We expect N_i and M_i to be finite and equal to the value that they would attain in a virtually infinite system only in the nanoribbon bulk whereas edge effects can substantially alter the bulk magnetic ordering, as shown in Ref. [192].

Filling $\nu = 0$ In Fig. 3.10 we present the typical band structure obtained by solving the interacting problem selfconsistently at the mean field level and at half filling for $U \neq 0, V = 0$, with the associated M_i and N_i fields as functions of the nanoribbon width W for armchair and zigzag nanoribbons (left and right panels, respectively). The magnetization in the bulk is identical for both terminations and it coincides with the value (that we indicate simply as M and N) that it would attain in an infinite graphene sheet, whereas the edges behave differently. As evident from the finite N and zero M, the magnetic ordering of the bulk fostered by on-site repulsions when no intersite repulsion is present is antiferromagnetic, characterized by an incompressible bulk and gapped edges, and the fourfold degeneracy of the ZLL of the non-interacting system is partially lifted. The analysis of the spin and sublattice polarization of these two levels (not dispalyed in the figure) shows that they have opposite spin and opposite sublattice polarizations, resulting in a state with a special spin-sublattice locked SU(2) symmetry. The bulk gap opened by the system is proportional to N as $\Delta_{AF} = UN$.

In Fig. 3.11a we present the bulk values of the AF gap Δ_{AF} as function of the applied magnetic field for different values of U, and in Fig. 3.11b as a function of U for different values of B. We see that the dependence on the field is almost linear, what confirms the experimental observations [182].

Filling $\nu = \pm 1$ In Fig. 3.12 we present the typical band structure obtained by solving the interacting problem selfconsistently at the mean field level for $U \neq 0, V = 0$ at fillings $\nu = 1$ and $\nu = -1$ (left and right panels, respectively), with the associated M_i and N_i fields as functions of the nanoribbon width W for an armchair nanoribbon. We have omitted the results for the zigzag termination since, as seen before, the magnetization in the bulk is identical for both terminations, and only the edges behave differently. Because of the finite Zeeman field present in the non-interacting Hamiltonian (and eventually subtracted, as explained above), the residual SU(2) symmetry of the ZLL observed at $\nu = 0$ is lifted, resulting in four levels separate in energy. The magnetic ordering is ferrimagnetic since both M and N are finite and the bulk gap opened by the system behaves proportionally to the difference $\chi = |M - N|$ as $\Delta_{FI} = U\chi$. The line color of the bands of the upper panel encodes the spin polarization $\langle s_z \rangle$ along the quantization axis, whereas that of the central panel expresses the sublattice polarization $\langle \sigma \rangle$ indicating whether the states live prevalently on one or the other sublattice. Interestingly, we find

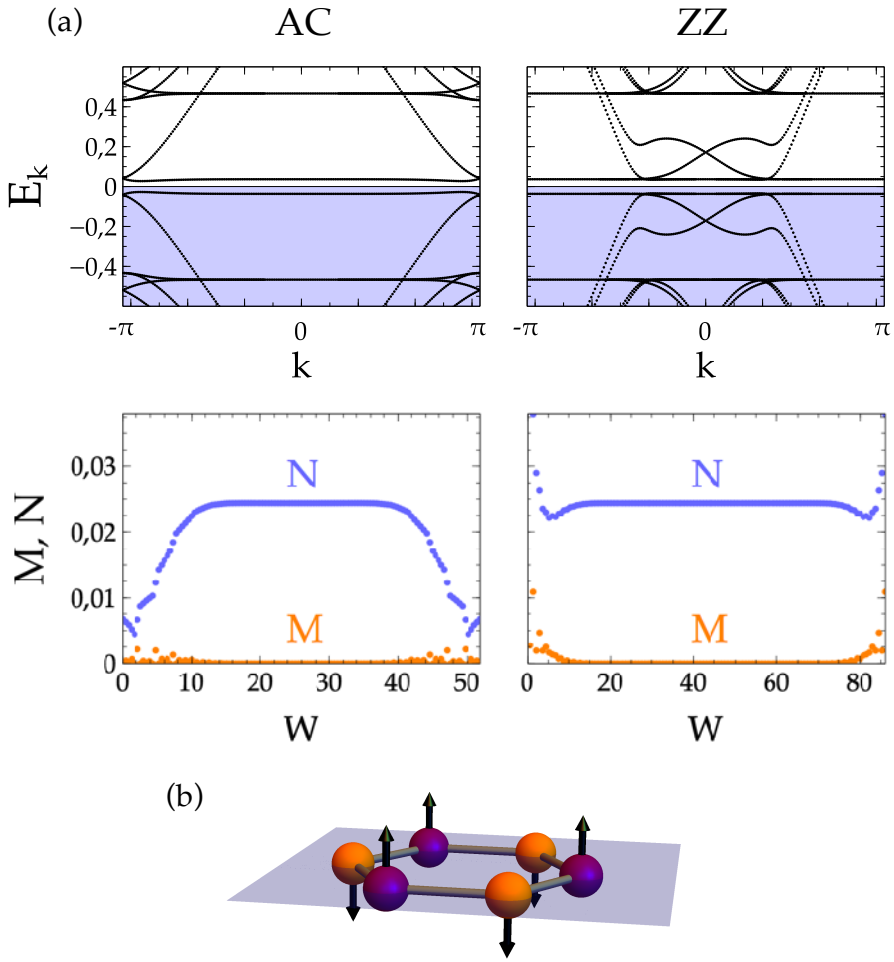

FIGURE 3.10: (a) Spectra (top panel) and magnetization parameters as defined in Eqs. (3.33) and (3.34) (bottom panels) of an interacting ($U = 1.5t, V = 0$) nanoribbon of monolayer graphene in the quantum Hall regime translationally invariant along one direction and with armchair (left) or zigzag (right) terminations along the other at $\nu = 0$. The magnetization parameters are plotted as functions of the nanoribbon width W, given in units of the Carbon-Carbon distance a_0. The shaded blue region in the top panels distinguishes the occupied from the empty levels found respectively below and above the Fermi energy. The magnetic field has been chosen as $B = 0.05$ in units of B_0 and the energies are plotted in units of the hopping t. (b) Schematic depiction of the AF ordering associated with the self-consistent solution at half filling.

that the two conducting channels for $\nu = -1$ and $\nu = 1$ have opposite spin polarizations and live on the same sublattice.

In Fig. 3.13a we present the bulk values of the AF gap Δ_{FI} as function of the applied magnetic field for different values of U, and in Fig. 3.13b as a function of U for different values of B.

3.3.2 Quantum Hall effect in twisted bilayer graphene

General theory

In this section we encompass the features of the QH phase in twisted bilayer graphene. In the absence of electron-electron interactions, this topic has been thoroughly studied in the literature [32,195–197]. It has been shown that, as is resonable to expect for what we have seen in section 3.2, the energies of the LLs and their dispersion as a function of the

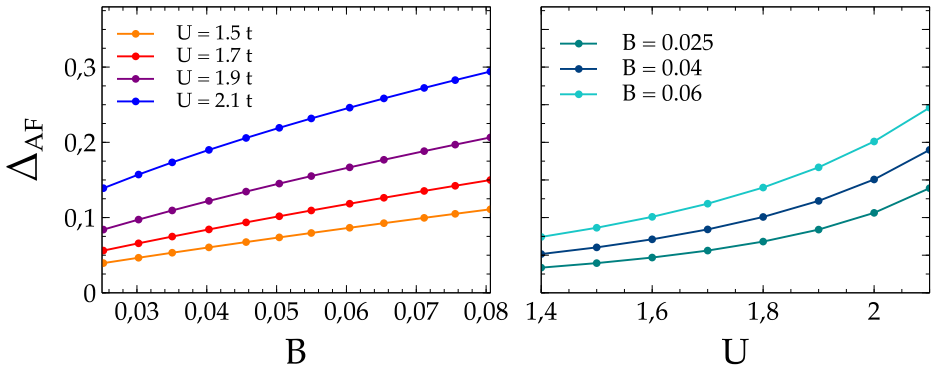

FIGURE 3.11: Behaviour of the gap Δ_{AF} opened by on-site interactions at half filling. Left panel: Δ_{AF} as a function of the magnetic field B, for different values of U. Right panel: Δ_{AF} as a function of the on-site repulsion U for different values of the applied field B. The magnetic fields are given in units of B_0 and the energies in units of t.

magnetic field strongly depend on the twisting angle, resembling that of Bernal-stacked bilayer graphene (i. e., linear in the field by virtue of the mass) at small angles while converging towards that of monolayer graphene at larger angles [195,196]. Interestingly, the situation is specular as a function of the magnetic field: for large fields the spectrum resembles that of the Bernal bilayer, whereas for small fields it behaves like of monolayer graphene [196]. In the regime of large angles or small fields, the degeneracy of each level is merely doubled because of the additional layer flavour [198]. By contrast, in the opposite regime the LLs with $n \neq 0$ undergo a splitting of the degeneracy that involves the layer degree of freedom and is likely due to a symmetry breaking induced by the interlayer coupling. On the other hand, the eightfold degenerate ZLL has been shown to be protected against this kind of splitting [195].

Another remarkable property of the QH effect in TwBG, shared by a whole class of other systems exhibiting either a moiré pattern or subject to a spatially modulated periodic potential, is that of developing a fractal support of the spectrum as a function of the field at relatively small fields [18,32,197,199]. This support is known as the Hofstadter butterfly and it characterizes periodic systems in which the magnetic flux per unit cell Φ is of the same order of magntitude or larger than the magnetic flux quantum Φ. The Hofstadter butterfly has been well known and extensively studied theoretically in both standard 2DEGs and in monolayer graphene since its first uncovering by Hofstadter in 1976 [200]. However, this effect requires fields of the order of 10^4 T, much larger that those attainable in a lab, to be visible in systems that are periodic on the Armstrong scale. Conversely, it can be observed at relatively low fields of the order of ~ 30 T, easily accessible in the lab for systems with unit cells of the order of $10 - 100$ nm, as is twisted bilayer graphene at relatively small angles (recall from 3.1, that the supercell size ℓ_{SC} is already of the order of 25 nm for a twist angle of $\approx 4^\circ$. For even smaller angles of the order of $\approx 1^\circ$, unit supercells can be as large as $\sim 10^3$ nm^2 [32]. This phenomenon has been studied in this platform theoretically [32,197], and observed experimentally [18,28,199]. As an example of the typical spectrum obtained when $\Phi/\Phi_0 \geq 1$, as compared to one observed in the opposite regime $\Phi \ll \Phi_0$, see Fig. 3.14. The top and bottom panels refer to the two rotation angles $\theta = 9.43^\circ$ and $\theta = 3.89^\circ$, respectively. Left and middle panels display the energy spectrum and the quantized Hall conductivity as functions of magnetic field, whereas the rightmost panel shows the spectrum at $B = 0$. It is easy to see that, due to the different sizes of the supercells associated to these angles ($\ell_{SC} \approx 10$ nm and $\ell_{SC} \approx 25$ nm, respectively), only the latter exhibits the Hofstadter fractal support in the range of fields

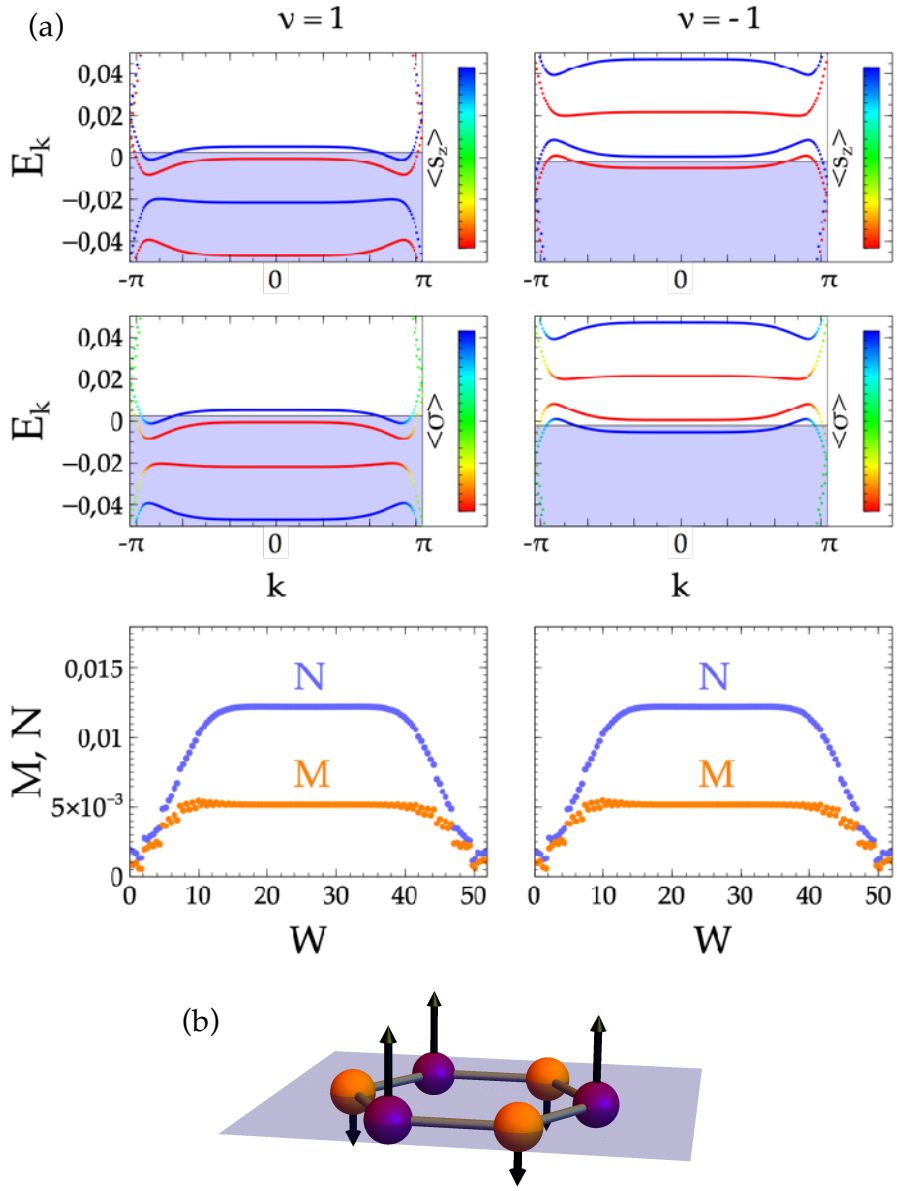

FIGURE 3.12: (a) Spectrum (top and central panels) and magnetization parameters M_i, N_i as defined in (3.33) and (3.34) (bottom panels) of an interacting ($U = 1.5t, V = 0$) nanoribbon of monolayer graphene in the quantum Hall regime translationally invariant along one direction and with armchair termination along the other at fillings $\nu = 1$ (left) and $\nu = -1$ (right). The magnetization parameters are plotted as functions of the nanoribbon width W, given in units of the Carbon-Carbon distance a_0. The shaded blue regions distinguish the occupied from the empty levels found respectively below and above the Fermi energy. The line color codes of the top and central panels encode, respectively, the spin polarization $< s_z >$ along the quantization axis and the sublattice polarization $< \sigma >$, with red and blue indicating solutions that are either oppositely spin polarized or localized on different sublattices. The magnetic field has been chosen as $B = 0.05$ in units of B_0 and the energies are plotted in units of the hopping t. (b) Schematic depiction of the FI ordering associated with the self-consistent solution at odd fillings.

considered. Another remarkable hallmark of the Hofstadter regime, visible in the middle panel of the bottom row, is that the Hall conductivity σ_{xy} is a non-monotonic function of the Fermi energy. This unconventional feature has been explained in terms of the change

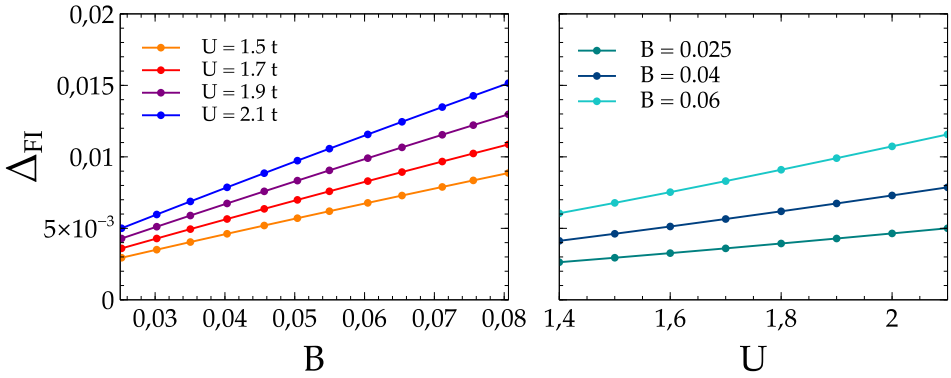

FIGURE 3.13: Behaviour of the gap Δ_{FI} opened by on-site interactions at fillings $\nu = \pm 1$. Left panel: Δ_{FI} as a function of the magnetic field B for different values of U. Right panel: Δ_{FI} as a function of the on-site repulsion U for different values of the applied field B. The magnetic fields are given in units of B_0 and the energies in units of t.

of the nature of the bands at the van Hove singularity (occuring at increasingly low energies as the twist angle is diminished, as discussed in section 3.2), that passes from being electron-like below the singularity to being hole-like above [197]. Additional changes in the convexity of the bands, resulting in a switch of electron-like to hole-like properties or viceversa, are clearly spottable at higher energies (in absolute value) as well, resulting in a further change of sign in the conductance.

In the following, we will concentrate on the large twisting angles regime, when the two graphene monolayers are virtually decoupled. In this regime, the sequence of Hall plateaus is expected to be merely doubled with respect to that of monolayer graphene, yielding, in the absence of interactions,

$$\sigma_{xy} = \pm \frac{\tilde{g} e^2}{h} \left(|n| + \frac{1}{2} \right) \qquad n = 0, 1, 2, ... \tag{3.35}$$

where $\tilde{g} = g_s g_v g_l = 8$, with $g_s = g_v = g_l = 2$ being spin, valley and layer degeneracies [198]. Here we are interested in the effect of electron-electron interactions on the ZLL, a subject that went somewhat overlooked in the past years. We recall that, as mentioned above, the ZLL is the only level that does not undergo the interlayer coupling-induced splitting of the LLs suffered by $n \neq 0$ LLs, and therefore, even in the regime very low angles and large fields, it has its layer degeneracy preserved.

Tight binding model in the QH regime

Before turning interactions on, we discuss the spectra of twisted bilayer graphene in the presence of an out-of-plane magnetic field B within our tight-binding model, see Eqs. (3.38)-(3.17). As in the case of single-layer graphene, an external magnetic field enters the tight binding Hamiltonian in Eq. (3.38) as a phase factor in the hopping amplitudes $t_{ij}^{ll'} \rightarrow t_{ij}^{ll'} e^{i\phi_{ij}}$. Notice that because the field is directed along the z direction, the z component of the trajectory linking two atoms on different layers has associated zero Peierls phase, so that the phase ϕ_{ij} only depends on the in-plane coordinates $\boldsymbol{\rho}_i$, $\boldsymbol{\rho}_j$ of the atoms and not on their layer indexes l, l'.

We construct nanoribbons that are translationally invariant along the direction fixed by the vector $\mathbf{R}_1$ given in Eq. (3.6) and terminated along the direction pointed at by $\mathbf{R}_2$ (Eq. (3.7)), with an edge that is neither zigzag nor armchair because of the θ rotation (see the unit cells of the infinite system plotted in Fig. 3.5 for comparison). For modelling the

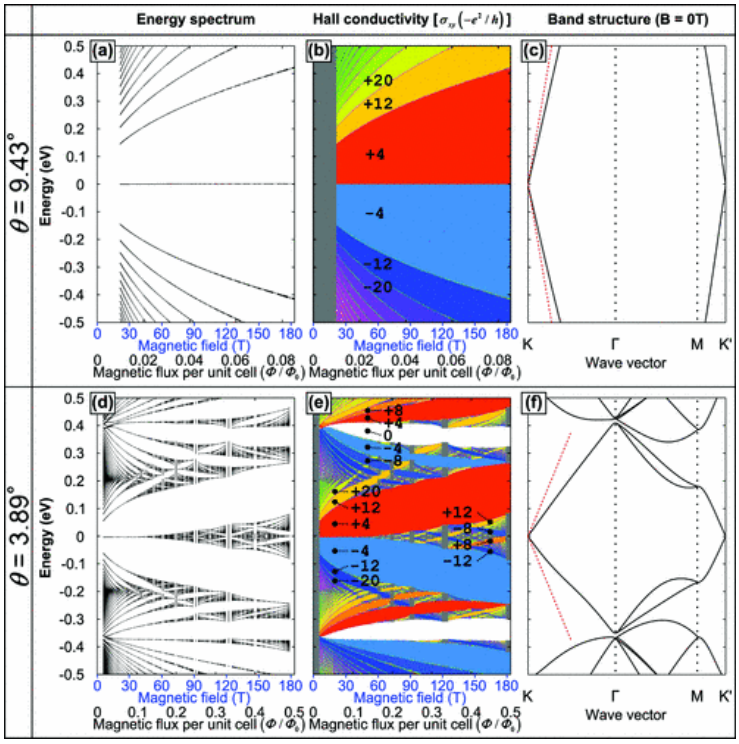

FIGURE 3.14: Energy spectrum and quantum Hall effect in TwBG with rotation angles of $\theta = 9.43°$ (top) and $\theta = 3.89°$ (bottom). In each row, the left and middle panels display the energy spectrum and the quantized Hall conductivity as functions of magnetic field strength, respectively. The rightmost panels show instead the band structure in the absence of magnetic field. Red slopes around K indicate the dispersion of monolayer graphene. In the middle panels, the quantized values of Hall conductivity inside energy gaps are indicated by numbers as well as colors filling the gaps. [Adapted with permission from Ref. [197]]

effect of an out-of-plane magnetic field that doesn't break translational invariance in such a nanoribbon, we choose a gauge such that the directional derivative of the vector potential $\mathbf{A}$ is zero along the $\mathbf{R}_1$ direction, that is we set $\nabla_{\mathbf{R}_1} A_x = \nabla_{\mathbf{R}_1} A_y = 0$ or, equivalently $\mathbf{R}_1 \cdot \nabla A_x = \mathbf{R}_1 \cdot \nabla A_y = 0$. The easiest, though non-symmetric choice, is that of setting one component to zero, e.g. $A_y = 0$ and impose that $\mathbf{R}_1 \cdot \nabla A_x = 0$ holds for the other. This results, for $r = 1$ and a generic m_0, in

$$A_x = -x + \frac{\sqrt{3}}{2}(2m_0 + 1)\, y \tag{3.36}$$

affecting the hopping amplitude with the Peierls phase

$$\phi_{ij} = \int_{\boldsymbol{\rho}_i}^{\boldsymbol{\rho}_j} \mathbf{A} \cdot d\boldsymbol{\rho} \tag{3.37}$$

The non-interacting Hamiltonian thus reads

$$H = \sum_{ij} c_i^+ t_{ij} e^{i\phi_{ij}} c_j + V_Z \sum_{ij,ll'} c_i^\dagger s_z c_i \tag{3.38}$$

Where, as in Eq. (3.23) we consider a Zeeman field besides the kinetic term. Notice that by t_{ij} we indicate the a 4×4 matrix $t_{ij} s_0$ diagonal in spin space and with a structure in

layer space given by Eq. (3.16). Analogously, with s_z we indicate the four-dimensional matrix $s_z\tau_0$ where τ_0 indicates the identity matrix in layer space. The operators c_i, $c_i^\dagger$ are now four-dimensional spinorial operators such that $c_i = (c_{ib\uparrow}, c_{ib\downarrow}, c_{it\uparrow}, c_{it\downarrow})^T$ where $c_{il\sigma}^\dagger$ creates an electron on the site i of layer $l = b, t$, with spin polarization $\sigma = \uparrow, \downarrow$. In Fig.

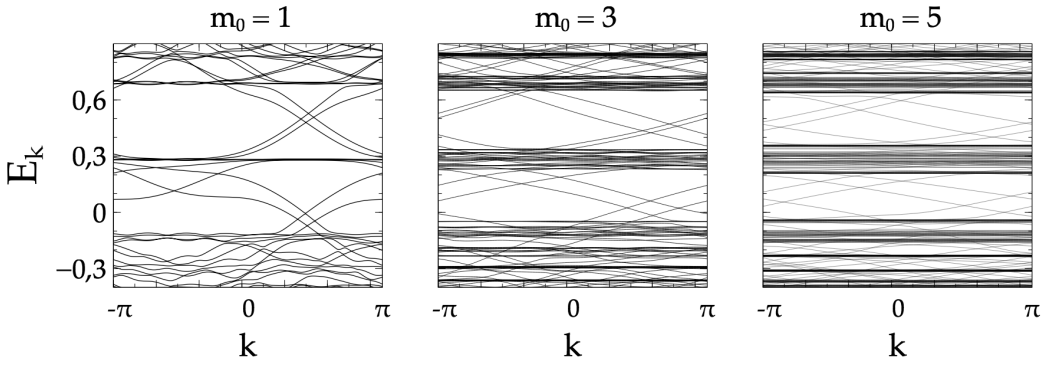

FIGURE 3.15: Bands in the QH regime for $r = 1$, $m_0 = 1, 3, 5$ and an applied magnetic field of $B = 0.05\, B_0$ for TwBG nanoribbons with a unit cell made of 10 superlattice unit cells of the infinite 2D system stacked along $\mathbf{R}_2$.

3.15 we present the spectrum of TwBG nanoribbons translationally invariant along $\mathbf{R}_1$ and with a unit cell along the $\mathbf{R}_2$ direction made of 10 repeated superlattice unit cells such as those depicted in Fig. 3.5, for $r = 1$ and $m_0 = 1, 3$ and 5 under the application of a perpendicular magnetic field $B = 0.05\, B_0$. We see that the Landau level structure arising in monolayer graphene ribbons is preserved, but with a qualitative difference residing in the broadening undergone by these levels to a finite width with spaghetti-like shape, at odds with the monolayer graphene case where they are perfectly flat (cfr Fig. 3.9), for an equivalent value of B. A second difference is that the number of edge states within each gap between two adjacent LLs is doubled with respect to the monolayer case, as expected from the doubling of the levels degeneracy due to the layer degree of freedom. Each level is therefore, in the absence of interactions, SU(8)-symmetric because of the simultaneous spin, valley and layer degeneracy. The broadening is consistent with the manifestation of the Hofstader butterfly support of the spectrum that is expected for large enough magnetic fluxes as discussed above and shown in Fig. 3.14. To get a better insight onto this feature, in the top row of figure (3.16) we show how the lowest LLs behave at $k = 0$ as a function of the magnetic field for $m_0 = 1, 3$ and 5. In the bottom row, we zoom the spectra around zero energy to focus on the broadening of the ZLL, δ_{ZLL}. A very interesting feature that can be seen from these spectra is that because of their fractal nature, they appear to be repetitions of each other for given combinations of the magnetic field B and twist angle θ. In fact, each spectrum exibiths the replication of the same pattern at a given scale that is set by the ratio between these two quantities, that can be expressed in terms of the dimensionless parameter ℓ_B/ℓ_{SC}. To prove this self-similarity, we have plotted the ZLL broadening δ_{ZLL} as a function of $B \in [0 : 0.1]\, B_0$ for four different angles in Fig. 3.17a associated to $m_0 \in [3 : 6]$ (in the inset, corresponding to the grey shaded area of the main figure, we show the behaviour at smaller fields $B \in [0 : 0.01]\, B_0$). We then show that such a behaviour scales identically if renormalized with respect to the magnetic flux over a unit cell area, that is we replot δ_{ZLL} as a function of $\Phi_0/\Phi \propto (\ell_B/\ell_{SC})^2$ in Fig. 3.17b. This plot shows that the curves do all collapse on a single curve, thus exhibiting a universal behaviour as a function of the ratio Φ_0/Φ in the inspected regime of angles and fields (it has been noticed elsewhere [197] that for angles smaller than the critical angle θ_c this behaviour changes qualitatively as the system

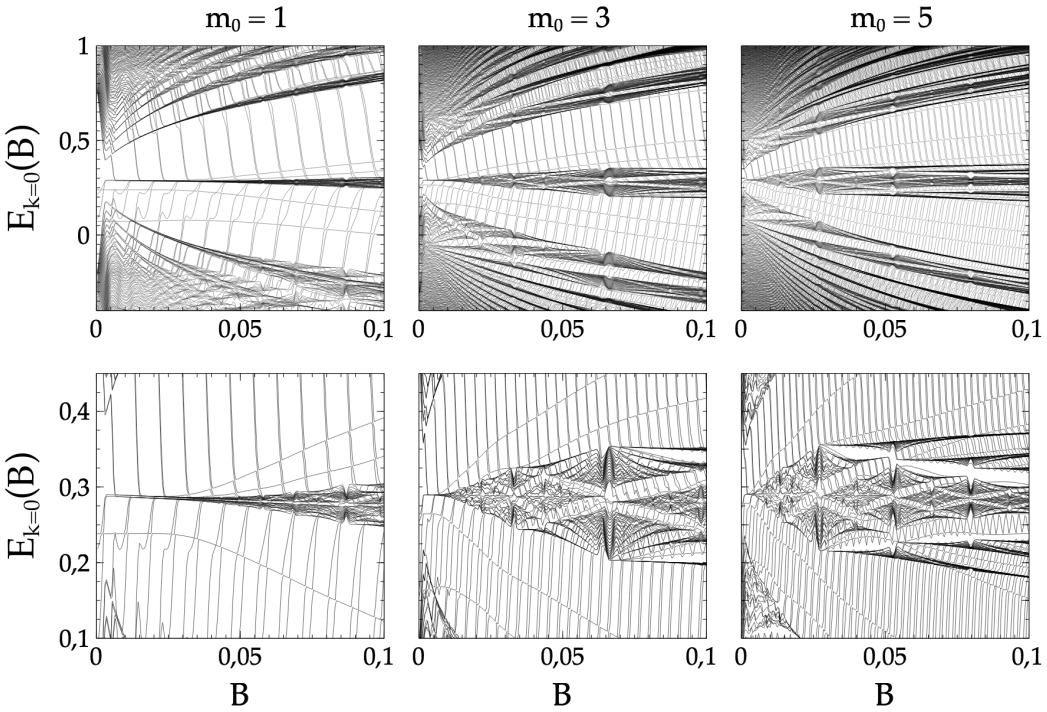

FIGURE 3.16: Top row: spectra of TwBG nanoribbons at $k = 0$ as a function of the magnetic field B expressed in units of B_0. Each panel corresponds to a different value of $m_0 = 1, 3, 5$. Bottom row: zoom of the spectra of the top row around the ZLL.

increasingly converges to Bernal-stacked bilayer graphene limit) Finally, in Fig. 3.17c we plot the behaviour of the ZLL for $m_0 = 6$ as a function of the dimensionless parameter Φ/Φ_0, that, as we have commented above, discriminates between the flat Landau regime and the dispersing Hofstadter regime, and goes as inverse of the squared magnetic field. We compare this behaviour of the spectrum around zero energy, obtained with our tight-binding simulations for an angle $\theta \approx 5^\circ$, with that derived within the continuum limit in [32] for a twisting angle of $\theta = 2^\circ$, plotted in Fig. 3.17d as a function of $\alpha = \Phi/\Phi_0$. The two spectra are in a very nice agreement, in spite of the different models employed. There are some differences between the two pictures: (i) our system is 1D at odds with the infinite 2D system considered in [**MacDonald**]: due to the finiteness of the ribbon along one direction, edge states appear within the gaps between different LLs and, even more remarkably, in those gaps arising within each individual level as the magnetic flux is ramped up (their number is associated to the conductance calculated in [] and shown in Fig. 3.14e); (ii) our modelization doesn't have electron-hole symmetry due to hoppings between atoms farther away than nearest neighors; (iii) the unit cell area associated to the angle that we consider is significantly smaller than the one associated to the angle considered in [**MacDonald**] and we consider a limited range of magnetic fields $B \in [0 : 0.1]\, B_0$, therefore we are able to discern only a portion of the whole butterfly support.

Electron-electron interactions

To study interactions, we add a term such as the one first introduced in Eq. (3.27), and decoupled as in Eq. (3.31), to the non-interacting Hamiltonian for TwBG in a magnetic field, Eq. (3.38). Again, by doing this we limit ourselves to the case where only on-site

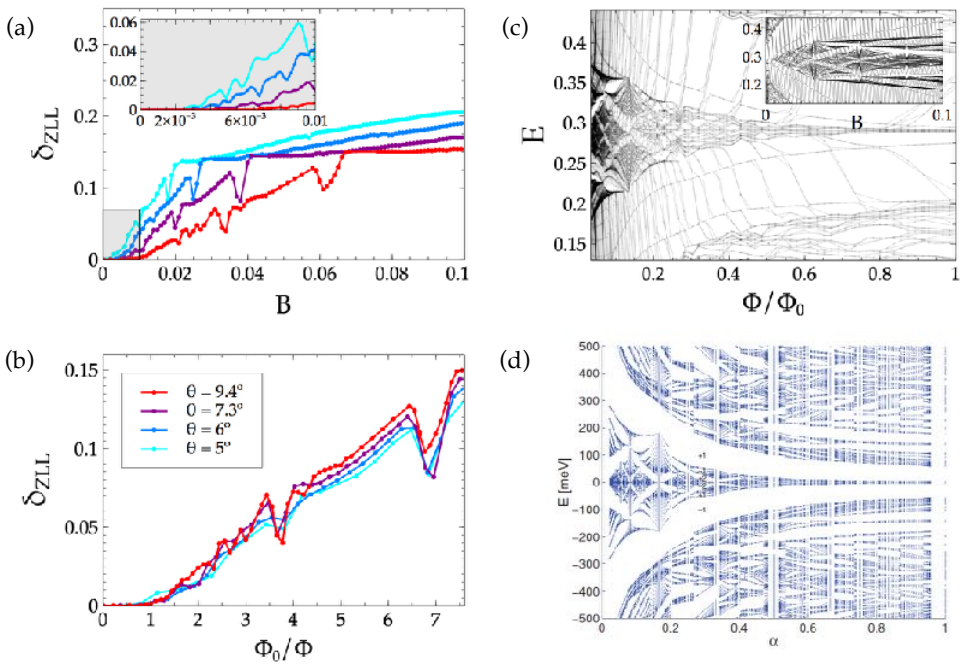

FIGURE 3.17: Study of the spectrum support as a function of the magnetic field and twisting angle. (a) and (b) Behaviour of the ZLL width δ_{ZLL} as a function of the magnetic field B in units of B_0 and of the parameter Φ_0/Φ for four different twist angles corresponding to $m_0 \in [3:6]$. When plotted against Φ_0/Φ, all curves collapse on one another, thus following a universal dispersion as a function of this parameter. (c) Spectrum at $k = 0$ as a function of Φ/Φ_0 in the regime where $\Phi \leq \Phi_0$ (Hofstadter regime) for $m_0 = 6$. The fractal figure that emerges is known as the Hofstadter butterfly. Inset: Same spectrum as a function of B. (d) The Hofstadter butterfly calculated by Bistritzer and McDonald in [32] within the continuum low-energy model for a twist angle $\theta = 2°$. Here $\alpha = \Phi/\Phi_0$.

and nearest neighbors repulsions are considerable. The mean-field decoupled interaction Hamiltonian for TwBG therefore reads

$$H_{\text{int}}^{\text{MF}} = U \sum_{i,l,\sigma} \langle c_{i,l,\sigma}^{\dagger} c_{i,l,\sigma} \rangle c_{i,l,-\sigma}^{\dagger} c_{i,l,-\sigma} + V \sum_{<ij>,l,\sigma\sigma'} \left(\langle c_{i,l,\sigma}^{\dagger} c_{i,l,\sigma} \rangle c_{j,l,\sigma'}^{\dagger} c_{j,l,\sigma'} - \langle c_{i,l,\sigma}^{\dagger} c_{j,l,\sigma'} \rangle c_{j,l,\sigma'}^{\dagger} c_{i,l,\sigma} \right) \tag{3.39}$$

where, with respect to the monolayer case treated previously, we have added the layer index to the creation and annihilation operators. Notice that no interlayer repulsions are taken into consideration and that, as before, we have omitted an unimportant constant.

Employing the same definitions used before for the parameters M_i and N_i (cfr Eqs. (3.33) and (3.34)), we can evaluate the magnetization as a function of the nanoribbon width W, along with computing the band structure at different filling factors. We characterize the filling of the bilayer system with the tuple (ν_b, ν_t), where ν_b and ν_t are the filling factors of the bottom and top layers, respectively. In this section we will focus on phases where the fillings of the two layers are the same, and therefore the state of the system can be fully characterized by defining the total filling factor $\nu_{\text{tot}} = \nu_b + \nu_t$. In the next section, in turn, we will explore the regime in which they are different, giving a special emphasis to the case in which they are opposite. Independent filling of the two layers can be achieved by applying an electric field to the bilayer system by means of top and bottom gates. When these gatings are equal, no electric field is present and the $\nu_b = \nu_t$ regime is achieved. When they are different, a finite electric field is generated across the

bilayer that allows looking into the richer scenario where $\nu_b \neq \nu_t$. We will provide a more quantitative description of this physics in the next section.

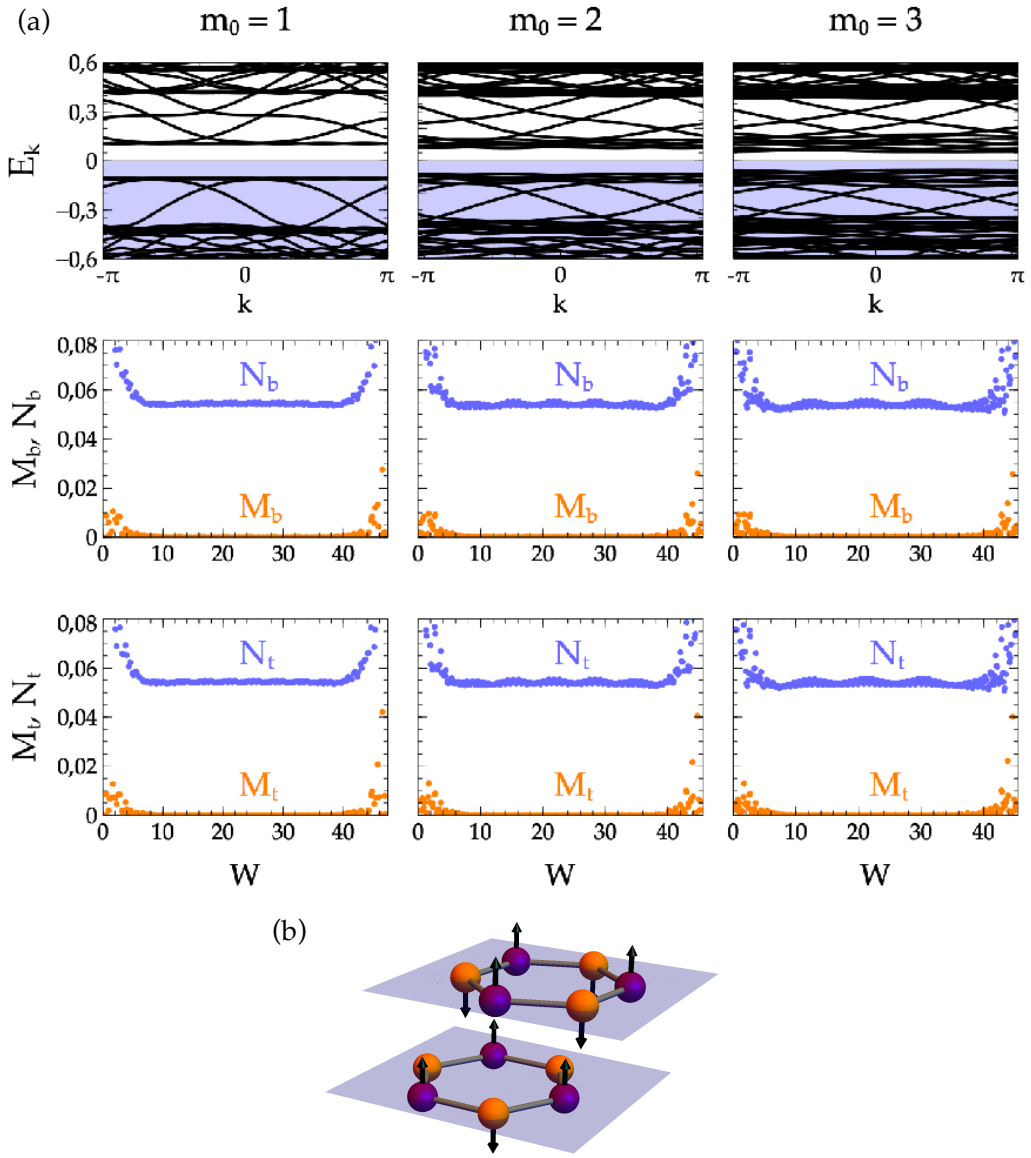

FIGURE 3.18: (a) Spectrum (top panels) and magnetization parameters of the bottom and top layers as defined in Eqs. (3.33) and (3.34) (central and bottom panels, respectively) of an interacting ($U = 2t, V = 0$) nanoribbon of twisted bilayer graphene in the quantum Hall regime at $\nu_{\text{tot}} = 0$. The magnetization parameters are plotted as functions of the nanoribbon width W, given in units of the Carbon-Carbon distance a_0. The shaded blue region in the top panels distinguishes the occupied from the empty levels found respectively below and above the Fermi energy. The magnetic field has been chosen as $B = 0.05$ in units of B_0 and the energies are plotted in units of the hopping t. (b) Schematic depiction of the AF ordering associated with the self-consistent solution at half filling.

Filling $\nu_{\text{tot}} = 0$ In Fig. 3.18 we present the typical band structures for $U \neq 0, V = 0$ at half filling with the associated M_i and N_i fields for the three twisting angles associated to $m_0 = 1, 2$ and 3. The applied magnetic field is $B = 0.05\, B_0$ and the on-site interaction

strength is $U = 2t$. Again, the magnetic ordering of the bulk favored by on-site repulsion alone is antiferromagnetic as illustrated by the bulk parameters M and N, and the originally eightfold degenerate ZLL splits into two spin-sublattice-layer locked fourfold degenerate bands such that intial fourfold degeneracy of the ZLL of the non-interacting system is only partially lifted. The system, as expected, is gapped both in the bulk and at the edges. We notice that, while the spin and sublattice (or valley) characters are perfectly defined, the layer index is not, since a non-zero tunneling amplitude exists between the two layers. Nonetheless, as we will show later on in greater detail, the degree of layer polarization is quite high for the regime of large twisting angles considered here.

Interestingly, several features stand out with respect to the monolayer case: (i) the bulk parameters M and N do not depend on the angle; (i) the parameter N exhibits oscillations over a scale given by the superlattice period ℓ_{SC}; (ii) the magnetic ordering is equal in the two layers (as shown in the cartoon of Fig. 3.18b); (iii) the interaction-driven antiferromagnetic gap Δ_{AF} is reduced with decreasing angle as a consequence of the increasing broadening of the levels; (iv) the value of N differs from that of monolayer graphene (compare UN to the magnitude of the gap Δ_{AF} for the same value of $U = 2t$ shown in Fig. 3.11), being comparatively larger. This last feature is due to the fact that the system tendency to develop interaction-induced broken symmetry states depends on the ratio between the on-site repulsion U and the Fermi velocity, with the latter (as seen in section 3.2) being reduced in TwBG as a decreasing function of the angle, with respect of that of the monolayer.

Filling $\nu_{\mathbf{tot}} = \pm 2$ In Fig. 3.19 we present the typical band structure obtained by solving the interacting problem selfconsistently at the mean field level for $U \neq 0, V = 0$ at fillings $\nu_{\text{tot}} = 2$ and $\nu_{\text{tot}} = -2$ (left and right panels, respectively), with the associated M_i and N_i fields as functions of the nanoribbon width for a TwBG with $m_0 = 1$. Similarly to before, the residual SU(4) symmetry of the splitted ZLL is lifted, resulting in four levels separate in energy where a SU(2) layer symmetry is still present. The magnetic ordering is ferrimagnetic and the bulk gap opened by the system behaves proportionally to the difference $\chi = |M - N|$ as $\Delta_{FI} = U\chi$. Notice that, because of the parameters chosen, the FI gap Δ_{FI} is smaller than the ZLL broadening. This has the effect of concealing this gap, in such a way that it is not possible to discern the edge states therein. It is reasonable to assume that the bulk gap is closed at the edges by two states equally spin-polarized and prevalently localized on one layer or the other. Different values of the parameters, however, would lead to a finite gap, at least for a given set of fields and angles. A quantitative analysis of the minimum ratio ℓ_B/ℓ_{SC} needed in order for this kind of gap to be visible will be performed in subsection 3.4.5.

3.4 Quantum spin Hall effect in Twisted bilayer graphene

3.4.1 Twisted bilayer graphene in an electric field

As anticipated, in this section we explore more exotic combinations of filling factors of the two layers, away from the case $\nu_t = \nu_b$ considered above. This can be achieved by applying an electric field to the bilayer system by means of uneven gating potentials applied to the top and bottom layers. In this subsection we explore, specifically, the regime relevant to the QSH phase, that is the one where $(\nu_b, \nu_t) = (\pm 1, \mp 1)$. To do so, we begin by introducing the onsite potentials applied to the bottom and top layers respectively, $\mathcal{V}_b$ and $\mathcal{V}_t$, and combining them into the two parameters

$$\mathcal{V}_g = (\mathcal{V}_b + \mathcal{V}_t)/2 \qquad \mathcal{V}_{\text{bias}} = \mathcal{V}_b - \mathcal{V}_t \tag{3.40}$$

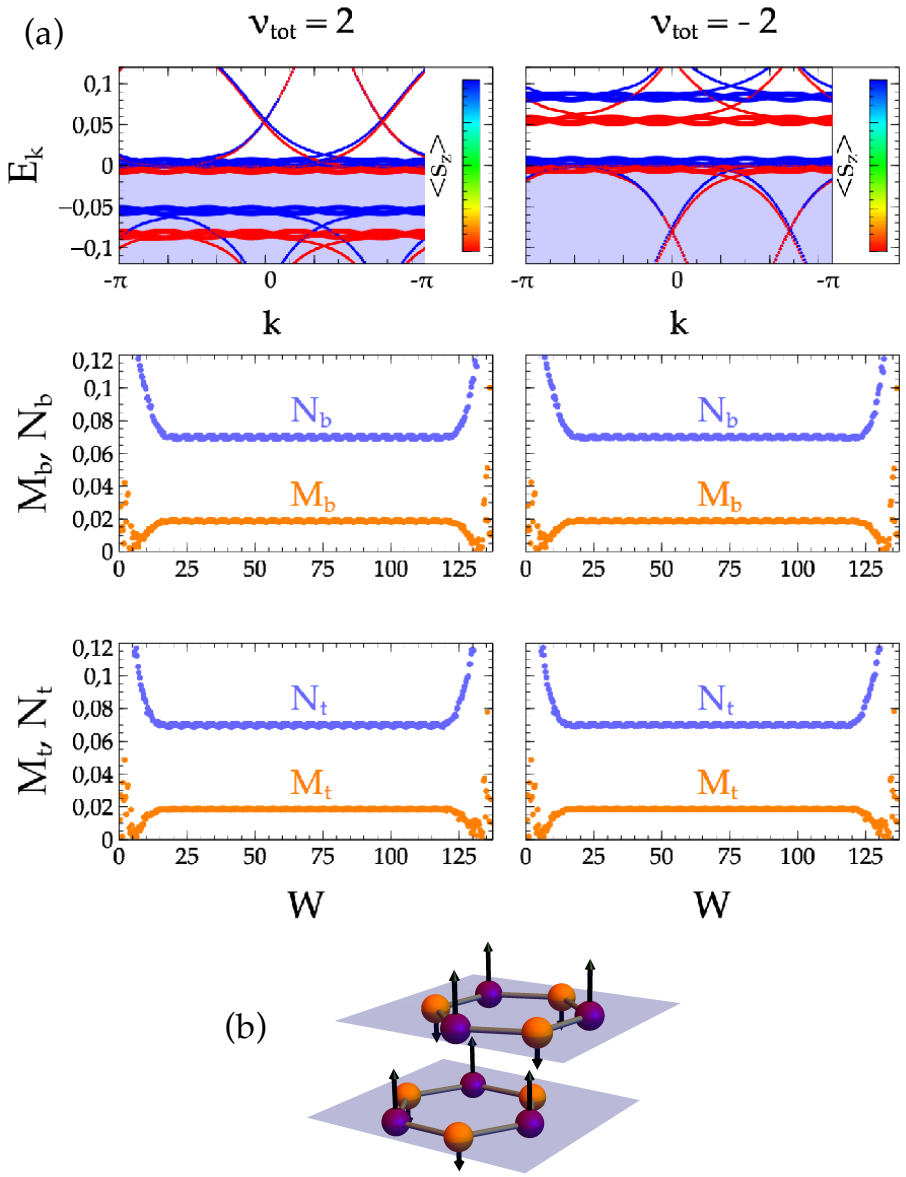

FIGURE 3.19: (a) Spectrum (top panel) and magnetization parameters of the bottom and top layers as defined in (3.33) and (3.34) (central and bottom panels, respectively) of an interacting ($U = 1.5t, V = 0$) nanoribbon of twisted bilayer graphene in the quantum Hall regime at $\nu_{tot} = 2$ (left) and $\nu_{tot} = -2$ (right). The magnetization parameters are plotted as functions of the nanoribbon width W, given in units of the Carbon-Carbon distance a_0. The shaded blue region in the top panels distinguishes the occupied from the empty levels found respectively below and above the Fermi energy. The magnetic field has been chosen as $B = 0.05$ in units of B_0 and the energies are plotted in units of the hopping t. (b) Schematic depiction of the FI ordering associated with the self-consistent solution at filling factors $\nu_{tot} = \pm 2$.

where the former indicates the total gating of the two layers, and the latter the bias induced between them by means of the applied field. In this language, the regime explored before is the one where $\mathcal{V}_g \neq 0$, $\mathcal{V}_{\text{bias}} = 0$ whereas now we consider the case $\mathcal{V}_g = 0$, $\mathcal{V}_{\text{bias}} \neq 0$. To explore this physics, we add the following term to the Hamiltonian

$$H_{EF} = \sum_{i,\sigma} c^{\dagger}_{i\sigma} \left[\mathcal{V}_{\text{bias}} \tau_z + \mathcal{V}_g \tau_0 \right] c_{i\sigma} \tag{3.41}$$

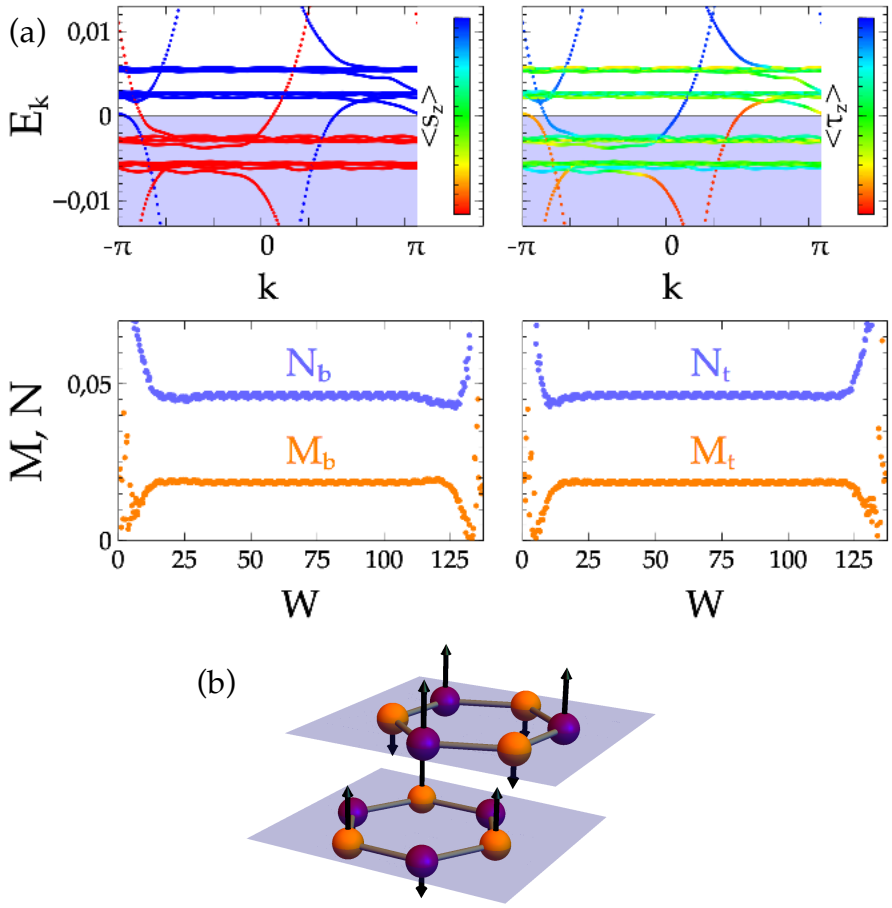

FIGURE 3.20: (a) Spectrum (top panel) and magnetization parameters of the bottom and top layers as defined in (3.33) and (3.34) (left and right panels of the bottom row, respectively) of an interacting ($U = 1.5t, V = 0$) nanoribbon of twisted bilayer graphene in the quantum Hall regime at $(\nu_b, \nu_t) = (1, -1)$. The line color of the top left and right panels encode spin and layer polarization, indicated as $< s_z >$ and $< \tau_z >$. The magnetization parameters are plotted as functions of the nanoribbon width W, given in units of the Carbon-Carbon distance a_0. The left and right central panels display the magnetization of the bottom and top layers respectively. The shaded blue region in the top panels distinguishes the occupied from the empty levels found respectively below and above the Fermi energy. The magnetic field has been chosen as $B = 0.06$ in units of B_0 and the energies are plotted in units of the hopping t. (b) Schematic depiction of the FI ordering associated with the self-consistent solution at filling factors $(\nu_b, \nu_t) = (1, -1)$.

to the Hamiltonian $H = H_0 + H^{\text{int}}_{\text{MF}}$, where H_0 is given in Eq. (3.38) and $H^{\text{int}}_{\text{MF}}$ is given in Eq. (3.39), with $V = 0$. We recall that the operators $c_{i\sigma}, c^\dagger_{i\sigma}$ in Eq. (3.41), are four-dimensional spinors in spin and layer space. The matrices τ_z and τ_0 act in layer space. Their spin structure is implied since they both behave like the identity in this space. According to what we observed in monolayer graphene, we expect that by superimposing the spectra of two graphene monolayers at filling factors $\nu = 1$ and $\nu = -1$ respectively, the gap will be closed at the edges by a pair of helical states, each of which is perfectly spin and layer polarized. This situation corresponds to the ideal case of a TwBG with uncoupled individual layers. We now study how this picture is changed when dealing with a true bilayer where interlayer tunneling is allowed. To so so, we consider a TwBG nanoribbon with $m_0 = 1$ to which we apply a nonzero electric field such that $\mathcal{V}_b = -\mathcal{V}_t = \mathcal{V}$. At odds with what we did in the previous section, no total gating $\mathcal{V}_g$ is applied in this case

so that the overall system is at charge neutrality, even though each individual layer is not. For an opportunely chosen value of $\mathcal{V}$, the spin-sublattice locked degeneracy of each layer is simultaneously broken, and a FI gap opens, as shown in Fig. 3.20. As expected, four edge states populate the gap (two for each edge) that are perfectly spin polarized (left panel of Fig. 3.20), what prevents them to backscatter into one another. The layer localization of the bands is shown in the right panel Fig. 3.20, where we see that though not perfectly, oppositely spin-polarized edge states are strongly confined on different layers. The system in this phase thus effectively realizes a quantum spin Hall insulator, where helical edge states that are protected from non magnetic disorder-induced backscattering close the gap at the edges of the system. We recall, however, that our system lacks time-reversal invariance, what places it in the unitary symmetry class A, like the QH phase, characterized by a $\mathbb{Z}$ invariant in 2D, instead of the symplectic class AII of the conventional QSH phase, characterized by a $\mathbb{Z}_2$ invariant [66].

3.4.2 Experimental evidence

We compare our results with a closely related experimental effort that has been performed concomitantly with our theoretical investigation by the MIT group of Prof. Jarillo-Herrero in Boston [91]. In their work, Prof. Jarillo-Herrero and coworkers, carry out two-probe conductance and non-local resistance measurements in a graphene bilayer encapsulated in hexagonal boron nitride (hBN) and dual-gated with a top and bottom gate electrodes (see Fig. 3.21b). The two graphene monolayers have a relatively large twist misalignment (see Fig. 3.21a) causing them to be virtually decoupled, and they are contacted with graphite leads. Because graphite has a work function similar to that of graphene, the graphite-graphene contact interface presents no local doping, thus preserving the electron/hole/neutral character of the graphene sample. The QH regime of this system is explored for a range of external magnetic fields B applied perpendicular to the graphene plane between 0 and 8 T. The double-gating allows to separately control the filling factors of the two monolayers upon independently varying the top and bottom electrostatic potentials $\mathcal{V}_t$ and $\mathcal{V}_b$ (notice that in this subsection we partly adapt the notation used in the paper to the one introduced above). Appying equal top and bottom gatings $\mathcal{V}_b = \mathcal{V}_t$ changes the filling factor of the two layers in the same fashion, thus charging them evenl. In turn, applying uneven gatings $\mathcal{V}_t \neq \mathcal{V}_b$ generates an interlayer bias that causes the two layers to have different filling factors. Changes in these two parameters have been absorbed into two parameters, the total filling factor $\nu_{\text{tot}} = hn_{\text{tot}}/eB$, where $n_{\text{tot}} = (C_t\mathcal{V}_t + C_b\mathcal{V}_b)/e$ is the total induced density, and the displacement field $D = (C_t\mathcal{V}_t - C_b\mathcal{V}_b)/2$, that measures the charge imbalance between the two layers. C_t and C_b are the capacitances per unit area of the top and bottom layers respectively. Notice that $\nu_{\text{tot}}$is the analogue of our total gating $\mathcal{V}_g$, whereas the displacement field D is proportional to our interlayer bias $\mathcal{V}_{\text{bias}}$.

The sequence of two-probe conductance plateaus that results from equally gating the two layers ($D = 0$) at the relatively small field $B = 1$ T is twice that of monolayer graphene, namely $G/G_0 = 4, 12, 20, ...$ ($G_0 = e^2/h$), where the additional factor 2 represents the layer degeneracy (see Fig. 3.21d). This sequence is a confirmation of the large twist misalignment, i. e. that the layers are sufficiently rotated one with respect to the other so to be weakly coupled and far away from the Bernal-stacked bilayer limit, where the electronic properties of the QH regime change dramatically. When the magnetic field is increased further to $B = 4$ T and a small non-zero displacement field D is imposed, interactions are able to break all degeneracies, thus yielding a sequence of QH plateaus in the conductance at every integer multiple of G_0, see Fig. 3.21e. Additional two-probes conductance measurements were performed by exploring the region of the phase space

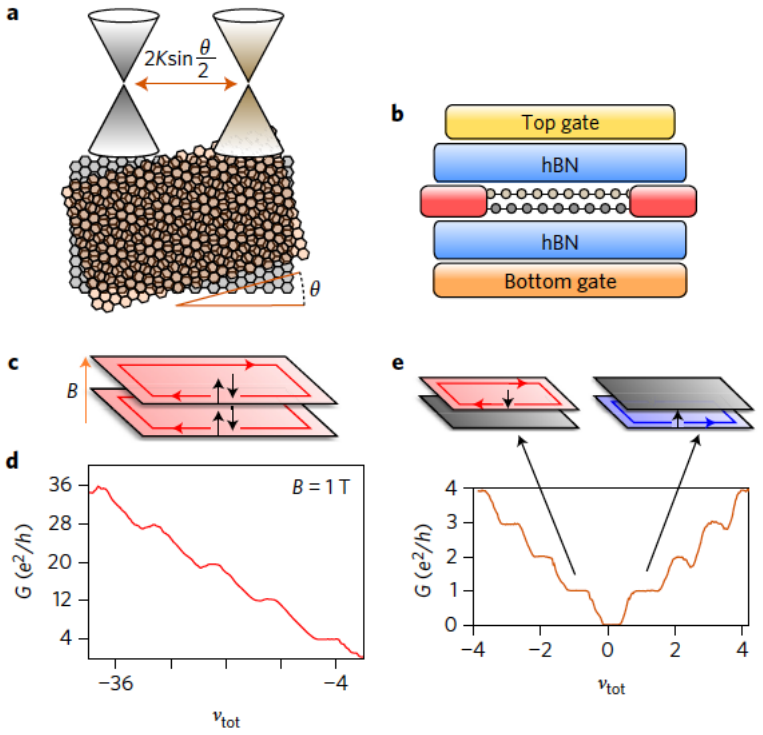

FIGURE 3.21: (a) Sketch of a twisted bilayer graphene system, with the angle-dependent low-energy Dirac spectrum explicitly shown. (b) Device schematic of twisted bilayer graphene encapsulated in hBN with dual gates and contacted with metallic leads at the extremities. (c) Cartoon of twisted bilayer QH edge states when both layers are at filling factor $\nu_{\text{tot}} = -2$. (d) Two-probe conductance at $B = 1$ T as a function of the total filling factor ν_{tot}. The sequence doubles exactly that of monolayer graphene. (e) Two-probe conductance of the same device at $B = 4$ T showing broken-symmetry states. These data have been taken with a small interlayer displacement field $D \neq 0$ in order to observe all integer steps. Cartoons depict the edge states configurations in the $(0,1)$ and $(1,0)$ states. [Adapted with permission from Ref. [91]]

where the total filling is zero, while D is varied. Remarkably, it was found that by incrementing the displacement field D to negative and positive values upon oppositely doping the two layers with $\mathcal{V}_t = -\mathcal{V}_b \neq 0$, the conductance jumps from its zero value at $D = 0$ (indicating that both layers are fully insulating at half filling) to a non-zero value at $|D| \neq 0$. This value varies from 0.8 to 1.5 in units of G_0 for samples with different edge lengths ranging from 0.2 to 16 μm. By increasing $|D|$ further, the conductance drops again to zero. This behaviour of the conductance at $\nu_{\text{tot}} = 0$ is compatible with the transition from the state $(0,0)$ to the states $(1,-1)$ and $(-1,1)$ (for negative and positive values of D, respectively), associated to conductance values oscillating around G_0, and successively to the states $(2,-2)$ and $(-2,2)$, associated to zero values of the conductance. The explanation for the latter feature is that at filling factors $\nu_t = -\nu_b = \pm 2$, no symmetry protects the edge states agains backscattering because of fermion doubling. In fact, channels with the same spin polarization that are predominantly localized on different layers can backscatter owing to the allowed interlayer tunneling. (see bottom panel of Fig. 3.22a). If the $(\pm 1, \mp 1)$ states were associated to equally spin polarized states, similar interlayer backscattering processes would be allowed resulting in a cancellation of the conductance that would yield a zero value in this regime as well. The fact that the conductance is finite suggests a different scenario where some source of protection against backscattering

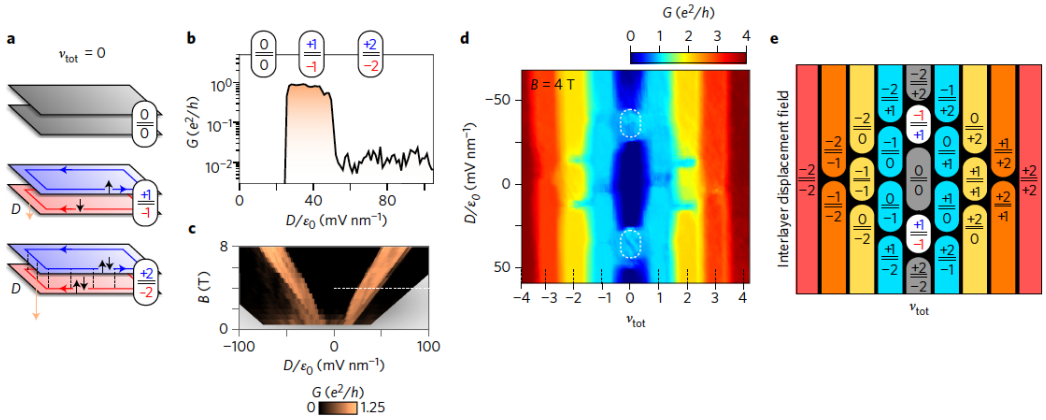

FIGURE 3.22: (a) Cartoons depicting edge state configurations with $\nu_t = -\nu_b$. (b) Two-probe conductance for $\nu_{\text{tot}} = 0$ as a function of displacement field D at $B = 4$ T. The $(-1, 1)$ state is conductive while the $(-2, 2)$ state is insulating. (c) Magnetic field dependence of the $\nu_{\text{tot}} = 0$ line (white dashed line shows the location of the line trace in (b). (d) Two-probe conductance map as function of ν_{tot} and D. (e) Schematic map of all possible filling factor combinations. [Adapted with permission from Ref. [91]]

must be present, likely connected with the opposite spin polarization of the two counterpropagating channels. However, the expected conductance in such a regime would be ideally $2G_0$. The discrepancy of the experimental data with respect to this prediction led to further investigation into the nature of these states, to rule out other possible explanations such as conductance through bulk states or through chiral in spite of helical edge carriers. This was done by means of non-local resistance measurements. In these measurements, a non-local voltage was measured at $B = 4$ T away from the source and drain electrodes. This resistance was found to be from 10 to 1000 times larger than that of any other conductive state, signaling that: (i) the conductance of the order of G_0 cannot be attributed to a single chiral edge state carrying a quantum of conductance because in that case the non-local voltage drop would be zero; (ii) the measured signal cannot be ascribed to bulk states since in a diffusive bulk conductor the voltage drop away from the drain and source electrodes is suppressed. This leaves one with the only possibility that conduction occurs through counterpropagating edge modes that have a suppressed backscattering probability likely connected with their opposite spin polarization. A more thorough investigation of the whole pahse space as a function of the total filling factor ν_{tot} and D was performed, yielding the two-probe conductance map shown in Fig. 3.22d. A systematic assignment of the different conductance states to different (ν_b, ν_t) was carried out and is presented in Fig. 3.22e. The measured conductances of nearly all the filling factor configurations are given by $G/G_0 = \nu_{\text{tot}}$, with only the $(\pm 1, \mp 1)$ states departing from this pattern.

To sum up, these results are highly compatible with the observation of a time-reversal broken quantum spin Hall regime characterized by helical edge states when the magnetic field is such as to prompt quantum Hall ferromagnetism in the system, and by opportunely doping individual graphene layers. The observed conductance of $\approx G_0$ is reduced by a factor 2 with respect to the expected conductance of $G = 2G_0$, likely due to the presence of some source of spin-active backscattering. The data are nonetheless encouraging since four-probe measurements suggest that the backscattering leading to the loss of conductance in the $(\pm 1, \mp 1)$ states decreases to zero with increasing magnetic field.

3.4.3 Rescaling of the parameters

In this subsection, we present a scaling (coarse graining) approach for monolayer graphene that allows us to accurately obtain the low-energy electronic properties of the model with numerical efficiency. Up to here, we have worked with observables expressed as functions of the parameters t, a_0 and B_0. As previously noticed, by using the actual values of these parameters in physical units, that is $t = 2.7$ eV, $a_0 = 1.42$ Å and $B_0 = 3.26\ 10^4$ T, the fields that we are able to explore due to the contraints imposed by the relatively narrow ribbons that we can address numerically ($W \approx 10$ nm) are of the order of 10^4 T. These fields are indeed unphysical, so we resort to a rescaling procedure that allows us to work with more down-to-earth magnetic fields, of the order of $1 - 10$ T. To do so, we rescale the Carbon-Carbon distance a_0 by a factor λ, $\tilde{a}_0 = \lambda a_0$. If this parameter is changed, then the hopping between nearest neighboring atoms needs to be rescaled as well $t \to \tilde{t}$ in such a way that the Fermi velocity stays fixed, $v_F = 3ta_0^2/2 = 3\tilde{t}\tilde{a}_0^2/2$, whence $\tilde{t} = t/\lambda$. The parameter B_0 is consequently rescaled as $\tilde{B_0} = \hbar/e\tilde{a}_0^2 = \hbar/e\lambda^2 a_0^2 = 3.26/\lambda^2\ 10^4$. We make the choice that the fields employed in the simulations, $B = \eta\ 10^{-2}\ \tilde{B}_0$, be equal to η T in physical units. From this choice, it follows that $\lambda^2 = 3.26\ 10^2$, that is, $\lambda \approx 18$. In order to obtain the value of any other observable in physical units, we have to use the rescaled parameters in spite of the original ones. This reduces to the very simple rule that the adimensional energies of the rescaled system must be multiplied by a factor $t/\lambda = 0.15$ eV, and the lengths by a factor $a_0\lambda = 2.56$ nm.

A similar rescaling procedure is possible in twisted bilayer graphene (see e. g. the protocol followed in [201]), but it yields reliable results only for $\lambda < 4$. We cannot, therefore, perform an analogue rescaling of the parameters to supply us with physically meaningful observables in the regime of magnetic fields that is relevant for the experimens. As a consequence, all the quantitative results of this work, except those regarding estimates of δ_{ZLL} (provided in subsection 3.4.5), are the outcome of calculations performed on single-layer graphene. This is justified by the previously shown validity of the uncoupled layers approximation in the regime where the angles are sufficiently large. The rigurous assessment of the range of validity of this assumption will be the focus of subsection 3.4.5.

3.4.4 Effects of intersite repulsion

In order to make our comparison with the experimental results more quantitative, we reproduce the phase diagram shown in Fig. 3.22c, where a map of the two-terminal conductance as a function of the displacement field and of the magnetic field is show. We do so by employing two decoupled monolayers of graphene instead of a twisted bilayer having shown in the previous section that for relatively large angles the interlayer coupling plays virtually no role in the QSH phase that we are interested in. We evaluate the phase diagram in terms of the FI gap that is opened at odd filling factors (see Fig. 3.13), where, in spite of the displacement field, we use as a control parameter the interlayer bias $\mathcal{V}_{\text{bias}}$ defined in Eq. (3.40). In this section, we present the results in physical units, where the rescaling procedure presented in subsection 3.4.3 has been applied, so to obtain quantitative predictions that can be juxtaposed with the experimental data. We obtain the map shown in Fig. 3.23. By comparing this phase diagram with that in Fig. 3.22c, it appears evident that while the relative sizes of the the FI gaps and of the AF gaps are comparable in the experimental results, our theoretical calculations hinging on purely on-site interactions yield FI gaps of about an order of magnitude smaller than the AF gaps (see as well Figs. 3.11 and 3.13). We therefore conjecture that the computation of the phase diagram in Fig. 3.22c, with $\Delta_{AF}/\Delta_{FI} \approx 1$, that is, a ratio that closely matches the experiment, requires the inclusion of the so-far neglected nearest-neighbour interactions $V \neq 0$. We

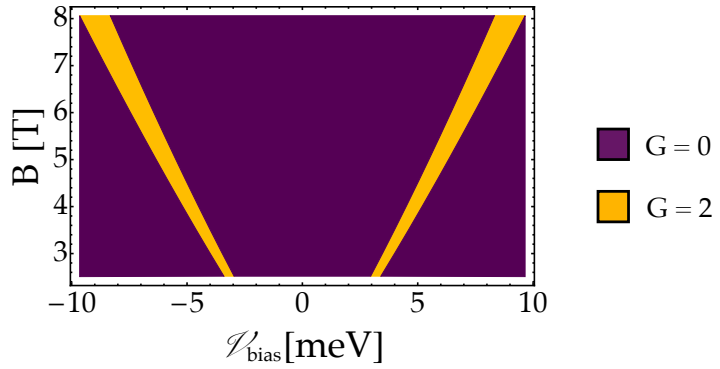

FIGURE 3.23: Map of the two terminal conductance G (in units of G_0), calculated theoretically as the number of edge states propagating in a given direction for $U = 1.5t$ and $V = 0$, in the $(\mathcal{V}_{\text{bias}}, B)$ space.

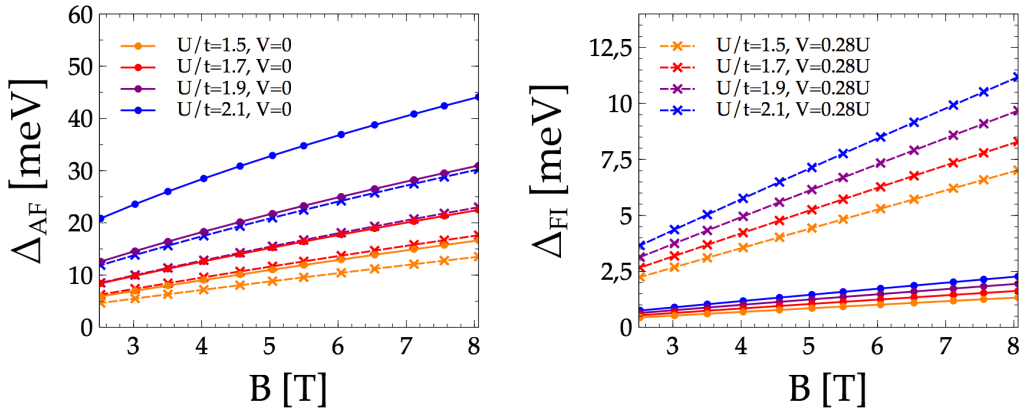

FIGURE 3.24: Comparison of the size of the AF gap opened at $\nu = 0$ (left panel) and of the FI gap opened at odd fillings (right panel) in monolayer graphene as functions of the magnetic field, for the two cases where the intersublattice repulsion is either $V = 0$ and $V = 0.28U$, with varying values of U. The legends refer to both panels.

therefore turn on the intersite repulsion $V \neq 0$, and calculate the change in the resulting gaps for different values of V. A value that yields a nice agreement between theory and results is found to be $V \approx 0.28U$. In Fig. 3.24a we show how both the Δ_{AF} and the Δ_{FI} gaps are renormalized by this value of V. We see that switching on the repulsion between nearest neighbors has the effect of slightly reducing the magnitude of the AF gap while at the same time strongly enchancing the FI gap. This is reasonable in that this kind of interaction favors a charge density wave ground state, that on the one hand competes with the AF order at half filling, thus reducing the gap induced by the latter, while at the same time favoring the spin-polarized charge density wave ordering that occurs at odd fillings. Indeed, since this kind of ordering naturally breaks inversion symmetry, we are now allowed to get rid altogether of the Zeeman field that we employed at $V = 0$ to break spin invariance (we recall that the two twofold degenerate level in which the ZLL splits at half filling have a locked spin-sublattice SU(2), that can be lifted by breaking either inversion or spin symmetry).

In Fig. 3.25a we plot the renormalized phase diagram of the conductance in the $(\mathcal{V}_{\text{bias}}, B)$ space at $U = 1.5t, V = 0.28U$ (compare with Fig. 3.23 where the $U = 1.5t, V = 0$

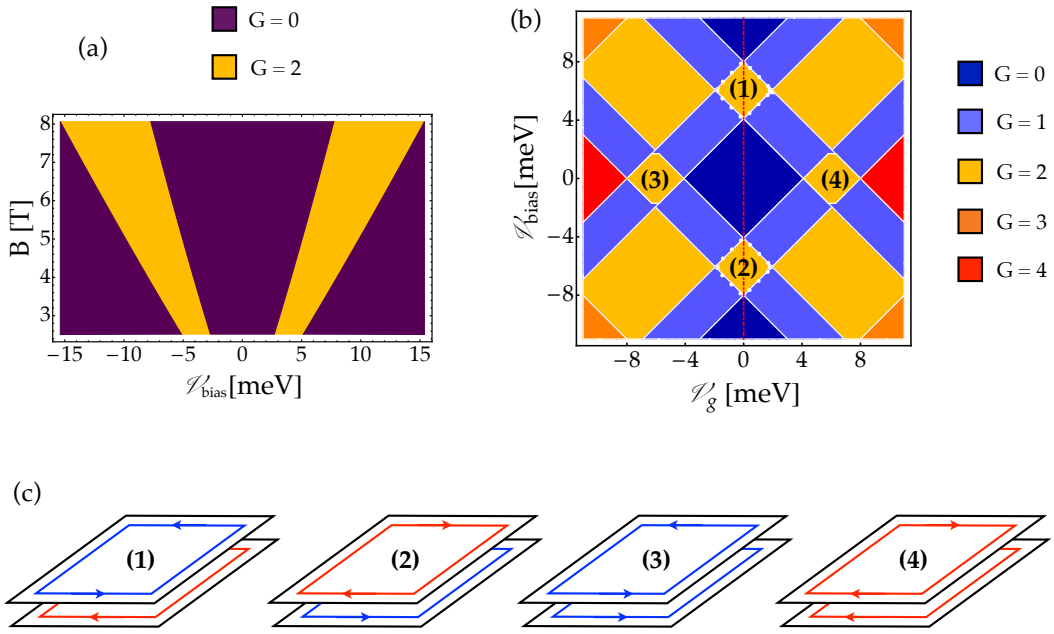

FIGURE 3.25: (a, b) Map of the two terminal conductance G (in units of G_0), calculated theoretically as the number of edge states propagating in a given direction for $U = 1.5t$ and $V = 0.28U$ (a) in the $(\mathcal{V}_{\rm bias}, B)$ space, (b) in the $(\mathcal{V}_g, \mathcal{V}_{\rm bias})$ space. (c) Sketch of the edge state spin-polarization (indicated by red and blue for opposite polarizations), direction of propagation and layer localization in the four regions indicated with numbers in panel (b). The regions labeled by (1) and (2), encircled with a white dotted line, correspond to the two possible realizations of the QSH phase, and are associated respectively with the states $(-1, 1)$ and $(1, -1)$. The regions labeled by (3) and (4) correspond instead to two-fold degenerate QH phases associated to the states $(1, 1)$ and $(-1, -1)$, where each layer supplies the total conductance $G = 2G_0$ with an equally spin polarized quantum of conductance.

case is shown, and with Fig. 3.22). It is obvious that this calculation matches the experimental data very closely.

In Fig. 3.25b we calculate the phase diagram of the conductance of the system with $U = 1.5t, V = 0.28U$ in the $(\mathcal{V}_{\rm bias}, \mathcal{V}_g)$ space, to compare it with the experimental one (Fig. 3.22d). Deviations between the two phase diagrams occur mostly in the shape of each region. This is expected, as the control parameters in the experiment are not the actual potentials $\mathcal{V}_{\rm bias}$ and $\mathcal{V}_g$ on the two layers, but rather the applied potentials before interlayer screening. Notice that, of the regions colored in yellow that are characterized by an ideal conductance $G = 2G_0$, only those labeled by numbers represent broken-symmetry states of the bilayer system, whereas the remnant areas represent the four non-interacting states $(0, \pm 2)$ and $(\pm 2, 0)$, characterized by a layer that is at charge neutrality and the other with two oppositely spin-polarized edge states that propagate with the same chirality. On the other hand, the possible broken symmetry states with total conductance $G = 2G_0$, labeled by numbers, are $(1, 1)$, $(-1, -1)$, corresponding to the states with zero interlayer bias and nonzero total gating (numbers 3 and 4), and the states $(-1, 1)$, $(1, -1)$, corresponding to the QSH states with finite interlayer bias and zero total gating (numbers 1 and 2). In Fig. 3.25c we present a skecth of the edge states for these four states,

Finally, we present the conductance phase diagram in the $(\mathcal{V}_{\rm bias}, U)$ space at fixed $B = 5$ T, by comparing the two cases where $V = 0$ and $V = 0.28U$.

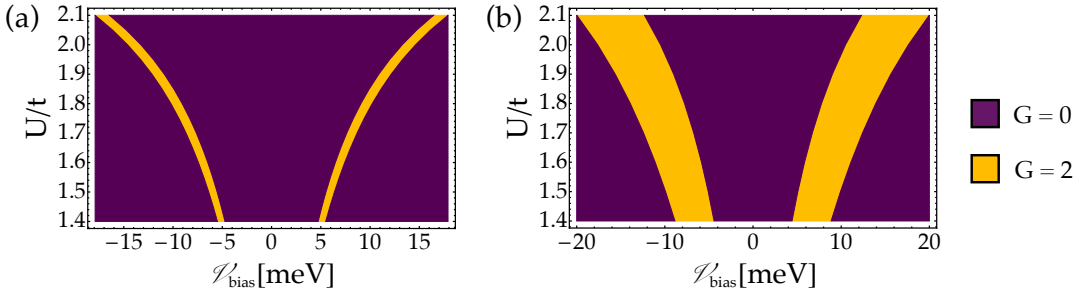

FIGURE 3.26: Map of the two terminal conductance G (in units of G_0), calculated theoretically as the number of edge states propagating in a given direction, for $B = 5$ T and (a) $V = 0$, (b) $V = 0.28U$, in the $(\mathcal{V}_{\text{bias}}, U)$ space.

3.4.5 Discussion

In this subsection, we present analytical expressions for the curves previously derived and establish the quantitative bounds required for the onset of a robust pseudo-QSH regime in twisted bilayers, an important issue in view of future implementations of this regime within quantum technological applications, such as the generation of Majorana bound states in twisted graphene bilayers without spin-orbit or Zeeman couplings. In standard QSH insulators, the essential condition that must be satisfied for the QSH phase to be robust is that the associated gap be larger than thermal excitations and bulk disorder amplitude. However, in the system under examination, the scale set by the QSH gap competes with an additional scale, that is the broadening of the ZLL due to the potential modulation introduced by the moiré pattern that could, in a given regime of parameters, be able to wipe out the former completely. For the gap to be appreciable, it is therefore crucial that the ZLL broadening does not exceed the FI gap, $\delta_{ZLL} \ll \Delta_{FI}$. From the simulations of Fig. 3.17, we obtain a phenomenological equation for δ_{ZLL} that reads

$$\delta_{ZLL} = \begin{cases} 0 \quad \text{for} \quad (\ell_{SC}/\ell_B)^2 \leq x_c \\ \alpha \left[(\ell_{SC}/\ell_B)^2 - x_c \right] \quad \text{for} \quad (\ell_{SC}/\ell_B)^2 > x_c \end{cases} \tag{3.42}$$

with $\alpha \approx 57$ meV and $x_c \approx 0.9$. Such a fit is valid for every twisting angle $\theta > 0.64^\circ$ for fields up to 10 T, that is, angles well within the range for which the decoupled layer approximation considered in the paper holds. On the other hand Δ_{FI} (Fig. 3.24) can be accurately fitted to

$$\Delta_{FI} = \begin{cases} \beta(U - \delta U)B \quad \text{for} \quad U > \delta U \\ 0 \quad \text{for} \quad U \leq \delta U \end{cases} \tag{3.43}$$

where the parameters β and δU depend on the choice of V. For $V = 0$, we have $\beta = 7.2\ 10^{-5}$ T^{-1} and $\delta U = 1.73$ eV, while for the value adjusted to the experiment $V = 0.28U$, we have $\beta = 3.2\ 10^{-4}$ T^{-1} and $\delta U = 1$ eV.

We recall that the relevant value of U is unknown. Here we choose a reasonable value of $U = 1.8t \approx 5$ eV, roughly consistent with calculations [1,193,194] and with the experimentally observed ZLL splitting [22,28,91,180,182]. Then, at a field B of 1 Tesla ($\ell_B = 25.66$ nm), we have an FI gap $\Delta_{FI} \approx 1.2$ meV (14 K) whereas at a field of 10 Tesla ($\ell_B = 8.1$ nm), the gap is $\Delta_{FI} \approx 12$ meV (140 K). This scale sets the maximum temperature at which QSH phenomena could in principle be visible in this system, and, importantly, comes out much larger than in any other QSH platform based on spin-orbit

coupling. The condition $\delta_{ZLL} < \Delta_{FI}$ at a given field B then becomes a constraint on the twist angle $\theta > \theta_c$ for the pseudo-QSH phase, since θ enters Eq. (3.42) through ℓ_{SC}. The Landau regime $\delta_{ZLL} \approx 0$ of virtually decoupled layers is reached for $(\ell_{SC}/\ell_B)^2 \leq x_c$, which corresponds to $\theta_c = 1.83^\circ$ at 10 T and $\theta_c = 0.58^\circ$ at 1 T. This implies that for the range of fields $B < 10$ T most relevant to realistic experiments, an angle $\theta \gtrsim 2^\circ$ is already guaranteed to satisfy the condition $\delta_{ZLL} < \Delta_{FI}$. Note that this also corresponds to the high-angle regime with weakly renormalized Fermi energy in twisted graphene bilayers [29].

3.5 Conclusions

To summarize, we have characterized theoretically the electronic structure of twisted bilayers in the quantum Hall regime, including interactions and interlayer bias. We have found that, in agreement with previous results for monolayers [8,12,189,192], the SU(4)-symmetric zero Landau level on each layer experiences spontaneous symmetry breaking associated to interaction-induced quantum Hall ferromagnetism, with either an antiferromagnetic or ferrimagnetic ground state depending on the filling. We demonstrated that at realistic magnetic fields and for large enough angles ($\theta \gtrsim 2^\circ$), the interlayer coupling does not qualitatively modify this picture. The ferrimagnetic phase, in combination with an interlayer bias that leaves the overall system at charge neutrality, allows for the implementation of a pseudo-QSH phase with helical edge states for conveniently tuned top and bottom gatings of the two layers that drive the system in the desired $(\nu_b, \nu_t) = (\pm 1, \mp 1)$ filling factor phase. This implementation of a QSH phase is unique, in that neither spin-orbit nor Zeeman couplings are involved, unlike in all previous approaches [6,182]. Despite the broken time-reversal symmetry, the pseudo-QSH edge states remain gapless in this system for arbitrary spin-independent disorder, like in a conventional QSH insulator. The spin-polarization of the carriers is a consequence of interactions alone, which control the scale of the associated QSH gap. Our theoretical description matches the measurements performed in this system [91], which allow us to constrain the relevant set of microscopic parameters, such as the interaction model and the interlayer rotation angle. In particular, we find that non-local interactions beyond the Hubbard model are required to explain the experimental results. In fact, while purely local interactions in graphene account for the type of symmetry breaking of the QH regime observed experimentally, a quantitative agreement requires sizeable interactions at least between nearest neighbouring atoms. This observation matches ab initio calculations that predict non-negligible interactions beyond the local Hubbard U model [193]. This is a natural conjecture, given the poor screening of interactions expected in twisted bilayer graphene around neutrality, where the density of states vanishes as in the monolayer. We note that the problem with fully unscreened non-local interactions is considerably more subtle, and has been predicted to give ferromagnetic ground states in graphene monolayers at charge neutrality, with Luttinger liquid-like helical edge states [183]. Such a pseudo-QSH phase is different from the one discussed here, and has not yet been demonstrated experimentally.

Given the fundamental importance of QSH phases in the emergent field of topological quantum computation [86], along with the substantial advantages and potential of the graphene-based implementation discussed here, twisted graphene bilayers in the quantum Hall regime under the special conditions assessed in this chapter and contacted with an s-wave superconductor promise to realize a valuable platform for implementing topological superconductivity, that in turn supports Majorana modes and can therefore be exploited to design protected Majorana qubits. As already stressed, the presented phenomenology depends on interactions rather than on spin-orbit coupling or Zeeman

fields. This entails a great advantage for the purpose of engineering topological superconductivity in that, on the one hand, the gaps will be significantly larger than those provided by spin-orbit related mechanisms (which leads to strongly confined Majorana zero energy modes), and, on the other, in that no large Zeeman fields that could spoil the proximity-induced superconductivity are needed.

Chapter 4

Topological π-junctions from crossed Andreev reflection in the quantum Hall regime

4.1 Introduction

The pursuit of Majorana zero modes (MZMs) in condensed matter has witnessed a huge boost in the past decade, both theoretically and experimentally [51,52,86,202–211]. The pivotal motivation fueling this quest is the aspiration to design a Majorana-based scheme for implementing fault-tolerant topological quantum computation [212]. While an unambiguous experimental signature of these quasiparticle has remained elusive for a long time, with experimental efforts providing nonconclusive evidence of their detection [202,204,206], a number of recent breakthroughs are finally providing convincing proof of their observation in a variety of different platforms and by means of several independent detection protocols [51,210,211].

On the theoretical side, many proposals have been cast so far for both Majorana modes generation [86,154,213,214] and implementation of quantum gates to manipulate them [215–217]. However, an important obstacle remains that hampers the way towards the achievement of universal Majorana-based quantum computation, that is the inadequacy of the operations implemented by braiding for realizing a universal set of quantum gates [86,212]. In fact, the remarkable non-Abelian statistics obeyed by these anyons only allows for a restricted set of single-qubit quantum gates [86,215,218]. Nonetheless, optimism is sanctioned since progress have been made with theoretical proposals that rely on mechanisms alternative to braiding for quantum gates implementation [92,216,217,219–224]. In addition, extending the range of allowed operations upon adding unprotected gates has been predicted to exhibit remarkably high error thresholds that make topological qubits less prone to decoherence with respect to conventional quantum computing platforms [92,212,225–233].

In this chapter we put forward a scheme for Majoranas generation and manipulation that combine simple ingredients within reach of the current experimental state of the art, namely the integer quantum Hall effect and *s*-wave superconductivity. This scheme allows to overcome some of the issues obstructing the way towards the realization of a universal set of single-qubit gates.

The proposed device, sketched in Fig. 4.1, involves a two-dimensional electron gas (2DEG) subject to an out-of-plane magnetic field to drive it into a quantum Hall (QH) phase with well-developed edge modes. Since the fields needed to induce a robust QH regime in a 2DEG are relatively weak, we expect only orbital effects from this field to be sizeable and disregard its coupling with the spin degree of freedom. The 2DEG is contacted with a narrow stripe of a superconductor (SC) able to induce, by proximity, s-wave

superconductivity in the region below the strip. Such an effect is well demonstrated experimentally [49,51,234,235] and it has been shown that remarkably hard gaps can be induced in this way in the limit of sufficiently transparent contacts [49,50,52,53]. We thus consider the proximitized portion of the 2DEG as a superconducting region that inherits all the properties of the parent superconductor. Finally, by applying a large enough magnetic field directed along the strip that couples with the spin degree of freedom, a Zeeman interaction can be generated that lifts spin degeneracy. This allows to selectively populate the Landau levels with the desired integer filling factor by tuning the chemical potential of the 2DEG. In the following, we will concentrate on the $\nu = 1$ regime where only the lowest Landau level is occupied. We notice that for superconductivity to survive the application of an external magnetic field, the latter has to be smaller than the characteristic critical field of the superconductor H_{c2} [236]. Indeed, for fields $H < H_{c2}$ the superconductor expels the field by generating superficial persistent currents that induce an opposite field able to cancel the total magnetic field within the bulk. This phenomenon is known as the Meissner effect [237]. However, when the field is too large, this effect breaks down and the field penetrates the superconductor, thus destroying superconductivity. In our calculations, we employ out-of-plane magnetic fields of the order of less than half a Tesla, already sufficient to generate a robust QH phase. On the other hand, the in-plane magnetic fields needed to open a sizeable Zeeman gap of the order of the meV are larger and critically depend on the g-factor of the 2DEG. For g-factors of the order of unity, magnetic fields of the order of ≈ 10 T are needed, whereas for higher g-factors of the order of 10, magnetic fields of ≈ 1 T are already sufficient. It is therefore crucial to make use of superconductors with a critical magnetic field H_{c2} larger than these fields. Superconductors that meet the above requirement are typically type-II superconductors among which, remarkably, Niobium-based alloys such as NbTi ($H_{c2} = 15$ T), Nb_3Sn ($H_{c2} = 30$ T) and Nb_3Ge ($H_{c2} = 37$ T), are appealing candidates for implementing the proposed device, by virtue of their especially high crticial fields of the order of dozens of Teslas. An alternative possibility consists in employing more conventional superconductors that exhibit an anisotropic out-of-plane to in-plane critical field, because of the significantly higher in-plane fields required by our set-up. Along this line, it was recently shown [51] that by growing thin epitaxial layers of Al on top of shallow InAs quantum wells, the hybrid structure develops a hard superconducting gap, ballistic tunneling contact, and in-plane critical fields up to 3 T, significantly enhanced with respect to the critical out-of-plane field, of the order of ~ 10 mT. We then show that if some source of spin-orbit coupling (SOC) is present either in the 2DEG or in the superconductor, edge states from opposite sides of the superconducting region of the system can pair to open a topological gap. The mechanism underlying this phenomenon is the so-called crossed Andreev reflection [236,238,239]. Loosely speaking, Andreev reflection is a process whereby an electron impinging on a superconductor from a normal lead is reflected as a hole. If this phenomenon occurs locally at a single normal-superconductor (NS) interface so that the hole is retroreflected, we speak of local Andreev reflection (LAR). If it occurs at a normal-supeconductor-normal (NSN) junction instead, and the hole is reflected to the normal lead opposite to that of the incoming electron, then crossed Andreev reflection (CAR) is at play. This effect aquires an additional twist when the normal leads are in the QH phase due to the chirality of the carriers [234,240–242].

The idea of inducing superconducting correlations in the edge states of quantum Hall systems to engineer non-Abelian phases of matter is not new. It traces back to a number of pioneering works [241,243–246] where it was put forward that a device assembled by contacting two 2DEGs in the QH regime at fractional filling factors (especially, focus has been devoted to the $\nu = 1/m$ and $\nu = 2/3$ regimes) with a superconductor supports parafermionic zero modes, that is, a generalization of Majoranas involving a

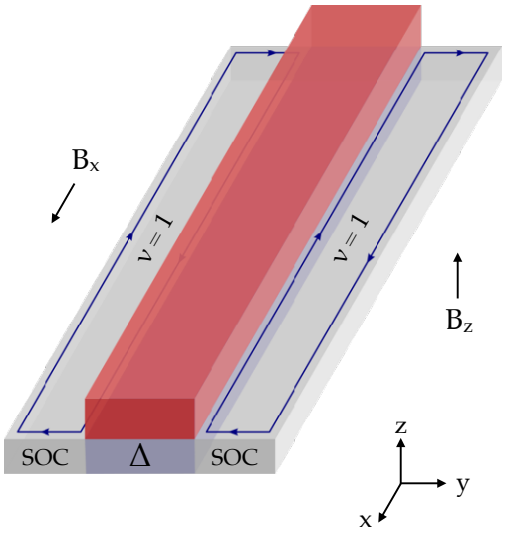

FIGURE 4.1: Schematic depiction of the geometry considered.

further fractionalization of the degrees of freedom. These anyons have been pointed out to be specially appealing as they underpin a richer non-Abelian statistics than Majoranas allowing for a wider set of quantum logical operations under spatial braiding [241,243]. As a pathological case of this phenomenon, it appears natural to postulate that the $\nu = 1$ filling factor with a finite spin-singlet amplitude should support Majorana modes in spite of parafermions as end modes excitations.

Despite the potential of the above proposals, experimental signatures of superconductivity in the QH regime have remained scarce and elusive for a long time. Fundamental steps forward in this direction were taken in recent years [157,247], reporting the observation of a supercurrent in graphene in the QH regime, thus setting an important precedent in the quest for exotic topological excitations such as Majorana modes and parafermions in hybrid QH-SC systems. Short afterwards, an outstanding experiment lead by the MIT group of Prof. Kim in Boston was able to demonstrate the occurrence of CAR processes in a graphene sample in the quantum Hall regime contacted with a narrow superconducting finger at integer filling factors [234]. Kim and coworkers performed non-local resistance measurements in a multi-terminal hBN-encapsulated graphene device with a superconducting drain electrode as shown in Fig. 4.2a. NbN was chosen for the latter, since its high upper critical field ($H_{c2} \approx 25$ T) and high critical temperature ($T_c = 12$ K) enable to experimentally access a wide range of magnetic fields where superconductivity and the QH effect in graphene coexist. The non-local measurements were performed by monitoring the voltage drop V_D between the electrodes e and c shown in Fig. 4.2a, when a current I flows between the electrodes a and d. The resistance associated to this voltage drop, $R_D = V_D/I$, is shown in Fig. 4.2b as a function of the filling factor ν of graphene that is controlled by the back-gate voltage V_{bg}, at $B = 14$ T and for different temperatures. The measurement of a negative resistance at very low temperatures $T \ll T_c$ and for given integer filling factors (namely, $\nu = 1, 2, 6$) signals the presence of a downstream flow of crossed Andreev converted holes, thus proving the occurrence of CAR processes enabled by the superconducting electrode. As expected, when the filling is away from the bulk-gapped regime so that the current flows through the bulk part of the graphene, the resistance R_D recovers its positive value. Remarkably, the observation of a negative resistance at $\nu = 1$ suggests that a non-zero spin singlet amplitude, allowing for pairing and likely resulting from the large SOC inherited from NbN, has been induced into the edge

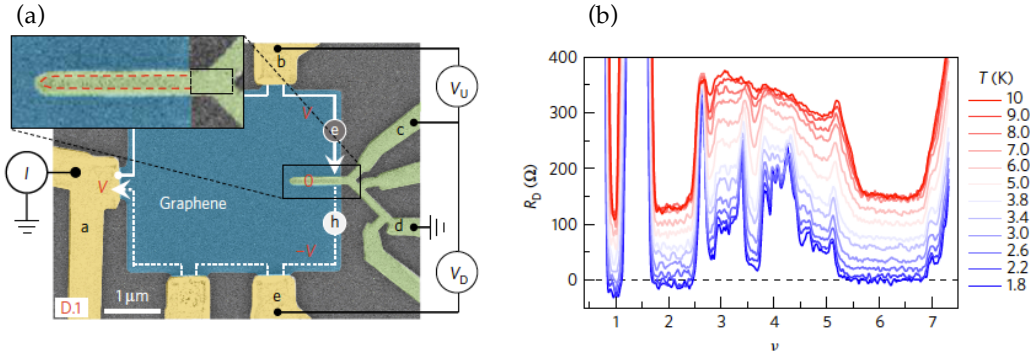

FIGURE 4.2: (a) False-colour scanning electron microscopy image of one of the devices used in the experiment with a skecth of the measurement configuration. Ti/Au normal electrodes (yellow) and a NbN superconducting electrode (green) contact the graphene Hall bar (blue). In the inset, the narrow NbN contact is highlighted with a dashed red line. The distance between two graphene/NbN contacts is estimated to be 50 nm. V_U and V_D are the upstream and downstream chemical potentials, respectively, and I is the current. (b) Filling factor dependence of the downstream resistance R_D at different temperatures, for $B = 14$ T. [Adapted with permission from Ref. [234]]

states. The system at this special filling factor is indicated by the authors as a promising candidate for hosting topological superconductivity and, accordingly, Majorana zero modes at its edges.

In this work we show that this is indeed the case in a generic 2DEG at $\nu = 1$. Moreover, we demonstrate that the sign of the CAR-induced topological gap depends periodically on the Fermi wavelength and superconducting region width and can be externally tuned. As we will see, this allows one to engineer an unconventional kind of topological π-junction, that is found to be more robust against fluctuations in the system parameters than externally tuned π-junctions. We propose to exploit this phenomenon to implement tunnel-braid operations [92] on systems of Majoranas coupled to quantum dots.

The chapter is organized as follows. In the second section, we introduce Majorana bound states contextualizing them in the field of consensed matter. After a brief account of the most important concepts underlying quantum computation, we show how the non-Abelian statistics of Majoranas renders them promising candidates for implementing topologically protected qubits. Finally, we review the pivotal theoretical proposals that have been put forward for Majoranas generation. We then present, in the third section, the mechanism that is at the basis of our proposal: the crossed Andreev reflection in QH systems. We proceed to calculate the CAR-induced gap, first analytically (third section) and then numerically (fourth section). We exploit the numerical tool to fully characterize finite-size systems, thus unveiling the generation of MZMs. Remarkably, we will show that by tuning the system parameters, a domain wall hosting a topological π junction with two localized Majoranas can be created. Finally, in the fifth section we review the proposal originally cast by Flensberg [92] of performing non-Abelian operations on sets of Majoranas coupled to a quantum dot and study how, by applying this protocol to our CAR-induced π junction, most of the issues presented by the original implementation can be elegantly overcome.

4.2 Majorana zero modes

It has been long known that in three dimensions quantum mechanics restrains the possible statistics obeyed by elementary excitations to be either the Fermi-Dirac or the Bose-Einstein, implying respectively that the wavefunction either stays invariant or changes sign upon exchanging particles [212]. In essence, this is due to the fact that a *double* exchange of two particles that restore their initial positions is equivalent to a process where one particle is adiabatically taken around the other. In turn, this is equivalent to a process where none of the particles moves at all, and therefore the final wavefunction must be identical to the initial one. This restricts the wavefunction transformations under a single exchange to the two cases listed above. In two dimensions, however, the exchange statistics can be richer. In fact, due to the dimensional confinement, the trajectory of a particle that encircles another one cannot be continuously deformed to a point without intercepting the other. Consequently, the double interchange of two particles involves a nontrivial winding of the wavefunction, that needs now not be the same as the initial one. The particles that obey these more exotic statistics are called anyons. Anyons can be divided into two subclasses depending on whether the order in which successive exchanges are performed matters or not. In the latter case one talks about Abelian anyons, whose wavefunction simply acquires a phase $e^{i\phi}$ under interchange of particles. In this sense, bosons and fermions can be thought of as particular cases of Abelian anyons whose wavefunction acquires a phase that is repsectively zero and π under exchange. On the other hand, non-Abelian anyons are characterized by a ground state degeneracy that allows the initial state to be rotated in the ground state manifold in a non-trivial fashion under particle exchange, so that the end state of the operation can be a completely different state from the inital one. This rotation in the degenerate subspace is implemented by a unitary tranformation whose matrix representation is non-commutative, hence the non-Abelianity of this kind of statistics. MZMs probably constitute the best known and most studied class of non-Abelian anyons, with a statistics that is determined by the braid group. We will go through this topic in detail in the next subsection. Here we briefly mention that even more exotic classes of non-Abelian anyons have been theoretically put forward, such as the parafermions arising in some fractional quantum Hall phases [241,243,246] or the Fibonacci anyons [212,248] that obey non-Abelian statistics different from the one followed by Majoranas.

Majorana anyons were first introduced by the italian physicist Ettore Majorana in the context of high-energy physics as a special class of particles that have the remarkable property of being their own self-adjoint [249,250]. The wavefunctions of these particles obey an alternative representation of the Dirac equation, namely

$$(i\tilde{\gamma}^{\mu}\partial_{\mu} - mc)\tilde{\psi} = 0 \tag{4.1}$$

where the matrices $\tilde{\gamma}^{\mu}$ satisfy the Clifford algebra $\{\tilde{\gamma}^{\mu}, \tilde{\gamma}^{\nu}\} = 2\eta^{\mu\nu}$ with $\eta^{\mu\nu} = \text{diag}(-1, 1, 1, 1)$ the Minkowski metric like in Dirac's equation, but are imaginary and specifically given by

$$\begin{aligned} \tilde{\gamma}^0 &= \sigma_y \otimes \sigma_x \\ \tilde{\gamma}^x &= i\sigma_x \otimes \sigma_0 \\ \tilde{\gamma}^y &= i\sigma_z \otimes \sigma_0 \\ \tilde{\gamma}^z &= i\sigma_y \otimes \sigma_y \end{aligned} \tag{4.2}$$

where with σ_x, σ_y and σ_z represent Pauli matrices, σ_0 is the identity and the structure of a tensor product of the kind $\sigma_y \otimes \sigma_x$ is

$$\sigma_y \otimes \sigma_x = \begin{pmatrix} 0 & \sigma_y \\ \sigma_y & 0 \end{pmatrix}$$

Since the matrices $i\tilde{\gamma}^\mu$ are purely real, the corresponding field $\tilde{\psi}$ is also real, which leads to the so-called *reality condition* that $\tilde{\psi} = \tilde{\psi}^\dagger$. This property implies that creating a Majorana is the same physical process as annihilating it.

While in the particle physics community the debate on whether neutrinos could be Majorana excitations (following Majorana's initial suggestion) is still open, in the condensed matter world it is natural to look at superconductors as potential hosts for these exotic particles. Loosely speaking, the reason can be sought in the fact that the Bogoliubov-de Gennes (BdG) quasiparticles are complex fermions given by a superpositions of electrons an holes, with the latter being the antiparticles of the former. A simplicistic expression for operators that create and annihilate the excitations in a superconducting condensate is

$$\gamma = uc_\uparrow^\dagger + vc_\downarrow \qquad \gamma^\dagger = v^* c_\downarrow^\dagger + u^* c_\uparrow$$

It is clear from these expressions that γ and $\gamma^\dagger$ are physically distinct operators so that generic BdG quasiparticles are not Majorana anyons. However, the distinction can be removed by imposing that $u = v^*$ and, more importantly, by getting rid of the spin degree of freedom. In this situation, the creation and annihilation operators for Bogoliubov quasiparticles are the same, so that $\gamma = \gamma^\dagger$, that is, they obey the reality condition encountered above. Furthermore, it can be shown that BdG quasiparticles at zero energy are MZMs. This derives from the redundancy of the Bogloliubov Hamiltonian, resulting in the particle-hole symmetry that Bogoliubov quasiparticles satify, that is, for any solution with positive energy E there must be a solution with energy $-E$, and that these two solutions are related by

$$\gamma(E) = \gamma^\dagger(-E)$$

This implies, in turn, that excitations at zero energy in a superconductor obey the Majorana condition that $\gamma = \gamma^\dagger$. Also, it implies that Majoranas always come in pairs.

4.2.1 Elements of quantum computation

Quantum computing is a form of computation based on qubits, that is two-states (that we label $|0\rangle$ and $|1\rangle$ for convenience) quantum-mechanical systems that differ from classical bits in that they exist in a coherent superposition of the two basis states $|0\rangle$ and $|1\rangle$. By extension, the quantum state of an n-qubit system (or n-size quantum register) is a superposition of 2^n states, and it is represented by a 2^n-dimensional complex vector, where each entry represents the probability amplitude of each of the possible 2^n basis states of the system. Therefore, while an n-size classical register is able to store a single value of the 2^n possibilities spanned by n classical bits, a quantum register is able to store all 2^n possibilities spanned by quantum pure qubits at the same time.

An algorithm performed by a quantum computer usually begins with an inizialization of the qubits, similarly to a classic computer. Then a set of quantum gates performs the logic operations, and the calculation ends with a measurement. The fundamental difference with respect to classical computation is that whereas the initialization and measurement of a qubit has the same possible realizations as a bit (namely, $|0\rangle$ or $|1\rangle$), a huge amount of additional information is stored in the quantum correlations between all the

qubits in an ensemble while the logic operations are performed. The basis vectors that span the space of all possible quantum states of the system are therefore the possible outcomes of a measurement, and a quantum state is a linear combination of these outcomes.

A quantum logic gate is a *basic* quantum circuit operating on a small number of qubits. Complex quantum circuits can be built by composing several gates. Quantum gates acting on n qubits are represented by $2^n \times 2^n$ unitary matrices and the quantum states of an n-qubit register are the variables that the gates act upon. The most common quantum gates operate on spaces of one or two qubits. A single qubit can be represented as

$$|\psi\rangle = \alpha|0\rangle + \beta|1\rangle \tag{4.3}$$

where α and β are probability amplitudes and are in general complex numbers. When we measure this qubit in the standard basis, the probability of outcome of $|0\rangle$ is $|\alpha|^2$ and the probability of outcome of $|1\rangle$ is $|\beta|^2$, and these two probabilities must sum to unity, $|\alpha|^2 + |\beta|^2 = 1$. There are therefore only three degrees of freedom left, which can be treated as the equation for a 3-sphere embedded in 4-dimensional space with a radius of 1 (unit sphere). This means, with a suitable change of coordinates, that one can eliminate one of the degrees of freedom. By choosing *Hopf coordinates*, for instance, one can express

$$\begin{aligned} \alpha &= e^{i\psi}\cos(\theta/2) \\ \beta &= e^{i(\psi+\phi)}\sin(\theta/2) \end{aligned} \tag{4.4}$$

and since the overall phase $e^{i\psi}$ has no observable physical consequences, we can choose α to be real such that two degrees of freedom remain and the possible states for a single qubit can be visualised using a Bloch sphere, where the states $|0\rangle$ and $|1\rangle$ identify the north and south pole, respectively (see Fig. 4.3). A set of universal quantum gates is any

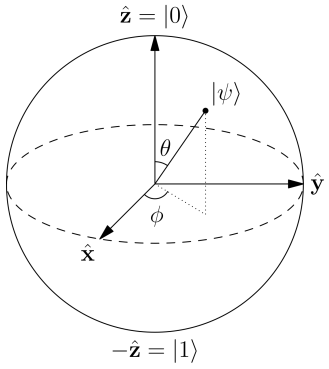

FIGURE 4.3: Sketch of the Bloch sphere that identifies the possible quantum states of a qubit.

set of gates to which any operation possible on a quantum computer can be reduced, that is, any other unitary operation can be expressed as a finite sequence of gates from the set.

The *DiVincenzo Criteria* [251] that a quantum computer implementation must satisfy are:

1. A scalable physical system with well-characterized qubits
2. The ability to initialize the state of the qubits to arbitrary states
3. A universal set of quantum gates
4. Decoherence times much longer than gate-operation times
5. Capability of reading out the qubits

The harshest challenge for meeting the DiVincenzo criteria rests on the need for long coherence times. In fact, interaction with the environment causes the system to decohere in most implementations relying on standard qubits (for instance, the polarization of photons or the spin polarization of spin-1/2 electrons) [252]. As a result, time consuming tasks may render some quantum algorithms inoperable, as maintaining the state of qubits for a long enough duration may corrupt the quantum superposition during the execution of the logic operation, thus spoiling the whole quantum computation. It is because of this complication that the idea of a topological quantum computation resting on Majorana-based qubits has taken root. As we will see, on account of the high non-locality of the ground state wavefunction, the quantum states generated by these anyons are insensitive to local perturbations. This topological protection is inherited by the quantum computation protocols that employ Majorana states as building blocks for qubits, provided the logic operations are performed adiabatically such that the ground state manifold remains decoupled from external degrees of freedom.

4.2.2 Non-Abelian statistics and braiding

By virtue of the 'spinlessness' of the superconductors supporting Majoranas, these anyons have half the degrees of a freedom of a regular fermion. Two Majoranas can be therefore combined to give rise to a fermion characterized by creation and annihilation operators expressed as function of the two Majorana operators γ_1 and γ_2 as

$$d = \frac{1}{2}\left(\gamma_1 + i\gamma_2\right) \qquad d^\dagger = \frac{1}{2}\left(\gamma_1 - i\gamma_2\right) \tag{4.5}$$

so that, in turn,

$$\gamma_1 = d + d^\dagger \qquad \gamma_2 = -i(d - d^\dagger) \tag{4.6}$$

These relations allow to derive the anticommutation relations obeyed by the Majoranas from those of regular fermions, yielding

$$\left\{\gamma_i, \gamma_j\right\} = 2\delta_{ij} \tag{4.7}$$

whence $\gamma^2 = (\gamma^\dagger) = 1$. If the Majoranas are sufficiently far apart so that their wavefunctions do not overlap, they are true zero energy solutions of the system. Since the wavefunction of an excitation in a superconducting condensate lives on a scale given by the coherence length $\xi = \hbar v_F / \pi\Delta$, the Majoranas will not overlap as long as they are located at a distance $L \gg \xi$. If they are brought closer together, they will split by an energy that scales exponentially with the distance as $e^{-L/\xi}$. At this point it is crucial to note that the composite fermions into which Majoranas can be combined are regular fermions in that they obey standard Fermi-Dirac statistic, still they have a peculiar feature that distinguish them from normal fermions. In the regime where $L \gg \xi$, the composite fermion is higly delocalized on the scale set by L and, more importantly, it will be a zero-energy solution of the problem, meaning that one can empty or fill the non-local state described by d with no energy cost, which results in a degeneracy of the ground state. Namely, the two states $|0\rangle$ and $|1\rangle = d^\dagger|0\rangle$ are degenerate in energy. This fermionic state is topologically protected by virtue of its high non-locality, since no local perturbation (that is, no environmental degrees of freedom that couple locally to fermionic field operators) can measure its quantum state. It is on account of this protection that a qubit defined by these two states is envisioned as the ideal basis for implementing quantum computational logic operations able to beat decoherence. In the opposite regime where $L < \xi$ the degeneracy of the ground state is lifted and it costs a finite energy to excite the composite fermion

described by d. In this regime, no topological protection holds and the fermion is in most respects a standard one.

In order to understand how the the ground state degeneracy (and consequent non-Abelian statistics) arises, one can consider a system of $2N$ Majoranas $\gamma_1, \gamma_2, ..., \gamma_{2N}$. Similarly as argued above, these $2N$ Majoranas can be arbitrarily combined to generate N complex fermions defined by operators $d_j = (\gamma_{2j-1} + i\gamma_{2j})/2$ and $d_j^\dagger = (\gamma_{2j-1} - i\gamma_{2j})/2$, with $j = 1, ..., N$. If the Majoranas are sufficiently far apart from each other such that they all have energies pinned to zero, the N fermions they combine into are zero-energy states, and do not change the ground state energy by being filled or empty. As a consequence, $2N$ MZMs give rise to a 2^N degenerate ground state of zero-energy states, that can be labeled by specifying the occupation numbers (that can be either 0 or 1) of the N composite fermions d_j, $n_j = d_j^\dagger d_j$:

$$|\psi_{\text{gs}}\rangle = |n_1, n_2, ..., n_N\rangle \tag{4.8}$$

Therefore in principle, given an initial state, swapping the positions of two Majoranas can have the effect of unitarily rotating the wavefunction in the ground state manifold in a non-commutative fashion, with the system ending up in a final state given by an arbitrary superposition of states of the kind of Eq. (4.8) characterized by different strings of occupation numbers. This possibility is demonstrated in the following.

In order to provide a simple and intuitive account of how the non-Abelian statistics of the Majorana emerges from their exchange, we follow the treatment first given by Ivanov [215]. The model system is that of a p-wave superconductor either spinless and allowing for single-quantum vortices or spinful and allowing for half-quantum vortices as low-lying subgap excitations, but applies equally well to all the platforms for Majorana anyons engineering that have been put forward in the last decade (see next subsection). The non-Abelian statistics of half-quantum vortices in spinful p-wave superconductors was first derived by Moore and Read [253] for the Pfaffian state, corresponding to fractional quantum Hall states with even denominators. The excitations of the Pfaffian state are vortices and their statistics has been obtained in the context of quantum field theory. Ivanov proposes a much more intuitive treatment relying on the transformation properties of MZMs under U(1) gauge transformations. The phase of the superconducting order parameter changes by 2π at a vortex. If the superconducting gap is changed by ϕ as $\Delta = \langle dd \rangle \to e^{i\phi}$, the fermionic operators change as $d \to de^{i\phi/2}$, and $d^\dagger \to d^\dagger e^{-i\phi/2}$. Therefore, Majorana operators defined as functions of the fermionic operators as $\gamma = d + d^\dagger$, change as $\gamma \to \psi e^{i\phi/2} + \psi^\dagger e^{-i\phi/2}$. Under a change of phase of $\phi = 2\pi$ of the order parameter, therefore, the Majorana operator γ goes to $de^{i\pi} + d^\dagger e^{-i\pi} = -(d + d^\dagger) = -\gamma$, indicating that the Majoranas carry odd charge with respect to the vortex gauge field. Since MZMs are trapped by vortices in topological superconductors, one can describe this phenomenology by introducing a branch cut emanating from each vortex such that the phase of the order parameter is single-valued away from the branch cut and jumps by 2π when the branch cut is crossed. As a consequence, during the clockwise exchange of two Majoranas γ_1 and γ_2 that are nearest neighbors, that is, that have no other Majoranas between them such as the one shown in Fig. 4.4, one of them necessarily has to cross a branch cut and consequently change sign, whereas the other stays invariant, resulting in the transformation rule:

$$T : \begin{cases} \gamma_1 \to \gamma_2 \\ \gamma_2 \to -\gamma_1 \end{cases} \tag{4.9}$$

where T is the generator of the elementary interchanges between γ_1 and γ_2 for the braid group B_2. For $2N$ Majorana modes, the braid group B_{2N} comprises all the interchanges between Majoranas that return the particles to their initial positions but in a different

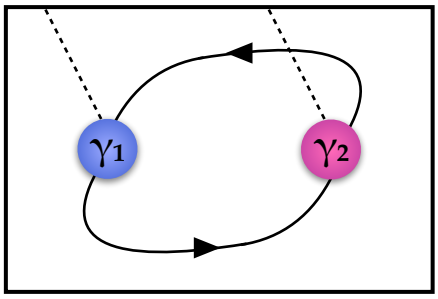

FIGURE 4.4: Clockwise braid of γ_1 and γ_2. While moving, γ_1 crosses a branch cut (dashed lines), thus acquiring a minus sign, whereas γ_2 remains unchanged. This sign change of only one of the two Majoranas leads to non-Abelian statistics.

order. The generators of B_{2N} are the operators T_i, with $i = 1, 2, ..., 2N-1$, that satisfy the relations

$$\begin{aligned} T_i T_j &= T_j T_i \qquad |i-j| > 1 \\ T_i T_j T_i &= T_j T_i T_j \quad |i-j| = 1 \end{aligned} \tag{4.10}$$

and result in the general transformation rule for Majorana operators

$$T_i : \begin{cases} \gamma_i \to \gamma_{i+1} \\ \gamma_{i+1} \to -\gamma_i \\ \gamma_j \to \gamma_j \quad \text{for } j \neq i, i+1 \end{cases} \tag{4.11}$$

The statistics of the braid group is defined by the unitary operators that act on the 2^N degenerate ground state manifold to represent the elements of the group, whose expressions can be given in terms of Majorana operators. These operators, that we call $\tau(T_i)$ must be such that

$$\tau(T_i)\gamma_j \left[\tau(T_i)\right]^{-1} = T_i(\gamma_j) \tag{4.12}$$

with $T_i(\gamma_j)$ given by Eq. (4.11). The expression for $\tau(T_i)$ that satisfies 4.12 is

$$\tau(T_i) = e^{\pi \gamma_{i+1}\gamma_i/4} = \frac{1 + \gamma_{i+1}\gamma_i}{\sqrt{2}} \tag{4.13}$$

In the case of two Majoranas γ_1 and γ_2 there is only one generator of the group, and it obeys Eq. (4.9). The unitary operator that represents this braid group element can be expressed as

$$\tau(T) = e^{\pi \gamma_2 \gamma_1/4} = e^{i\pi(2di^\dagger d - 1)/4} = e^{-i\pi\sigma_z/4} \tag{4.14}$$

where σ_z is the Pauli matrix acting in the space spanned by the states $|0\rangle$ and $|1\rangle = d^\dagger|0\rangle$. In this space the operator $\tau(T)$ performs a rotation of the wavefunction by an angle $\pi/2$ around the z axis, and as a consequence the wavefunction only acquires a phase. Therefore, at this level, no change of state from the inital to a fundamentally different one is observed. This is due to the fact that the braiding operation leaves the parity of the Majorana system unchanged (mathematically, this is reflected by the fact that the $\tau(T_i)$ operators are even in Majorana operators), so that it is not possible for the system to go from $|0\rangle$ to $|1\rangle$ or viceversa, because this would violate parity conservation. To observe the non-commutative statistics of Majoranas, one has to consider a system with a higher number of MZMs. The smallest of such systems involves four Majoranas

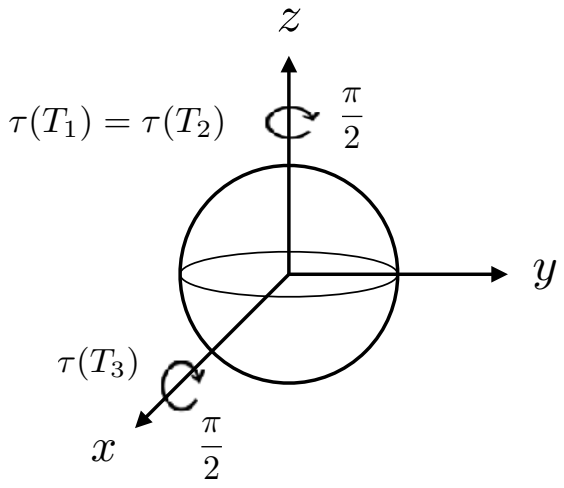

FIGURE 4.5: Illustrative sketch of the operations implemented on the Bloch sphere by the operators $\tau(T_i)$ representing the Braid group B_4 elements T_i with $i = 1, 2, 3$ defined in Eq. (4.15).

γ_1, γ_2, γ_3 and γ_4. One can form two composite fermions described by $d_1 = (\gamma_1 + i\gamma_2)/2$ and $d_2 = (\gamma_3 + i\gamma_4)/2$ that act in the space generated by the tensor product of the basis states of the two fermions: $\{|00\rangle, |01\rangle, |10\rangle, |11\rangle\}$ and because parity is conserved the even and odd parity blocks (respectively, $\{|00\rangle, |11\rangle\}$ and $\{|01\rangle, |10\rangle\}$) are decoupled. It is easy to see that the three operators representing the generators T_1, T_2, T_3 of the braid group B_4 in the even parity subsector (or, equivalently, in the odd parity one) read

$$\begin{aligned} \tau(T_1) &= e^{\pi\gamma_2\gamma_1/4} = e^{-i\pi\sigma_z/4} \\ \tau(T_2) &= e^{\pi\gamma_4\gamma_3/4} = e^{-i\pi\sigma_z/4} \\ \tau(T_3) &= e^{\pi\gamma_3\gamma_2/4} = e^{-i\pi\sigma_x/4} \end{aligned} \tag{4.15}$$

From these expression, it is evident that braiding Majoranas that belong to the same fermion has the trivial effect of multiplying the wavefunction by a phase (the same effect that it had for a system of only two Majoranas), whereas exchanging two nearest neighboring Majoranas that belong to two different fermions results in a non-trivial rotation of the wavefunction within the even-parity subspace of the ground-state manifold.

It is now clearer why it is customary to refer to the exchange of two non-Abelian anyons with the term braiding: because of the presence of branch cuts emanating from MZMs-trapping vortices, when interchanging the positions of the anyons it is fundamental to keep track of their history in order to know whether branch cuts are being crossed during the exchange. In other words, the *world lines* of Majorana anyons need to be known at all times, the world line being the $2+1$-dimensional (two spatial and one temporal dimensions) trajectory of the particle consisting of the sequence of spacetime events in the history of its motion in the two-dimensional space in which it is embedded. Whenever a trajectory crosses a brach cut, the sign of the involved Majorana changes. The visual effect of the drawn world lines of multiple Majoranas interchanging positions has the appearence of a braid, as schetched in Fig. 4.6. The braiding operation corresponds, as we have seen, to a rotation of a single qubit by $\pi/2$. Because of the topological protection supplied by the spatial delocalization of Majoranas, this operation serves as a protected single-qubit quantum gate for performing topolgical quantum computational tasks. However, this braiding-based single-qubit operation does not exhaust single-qubit operations since not all the Hilbert space can be explored by means of rotations by $\pi/2$.

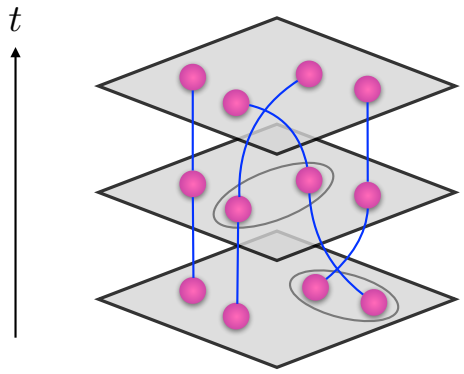

FIGURE 4.6: Sketch of the world lines of four Majorana anyons interchanging positions. The vertical axis indicates the time evolution of the system.

One needs to be able to perform rotations by arbitrary angles, in addition to two-qubits operations.

Summarizing, the previous discussion shows how Majoranas provide, through real-space exchange or braiding, a topologically stable realization of unitary operators for quantum computing. However, in order to obtain a universal gate set, one needs to supplement braiding with two-qubit measurements plus a single-qubit $\phi = \pi/8$ phase gate [212], implemented by the operator

$$R_\phi = \begin{pmatrix} 1 & 0 \\ 0 & e^{i\phi} \end{pmatrix} \tag{4.16}$$

that has the effect of leaving the basis state $|0\rangle$ unchanged and maps $|1\rangle$ to $e^{i\phi}|1\rangle$. The probability of measuring a $|0\rangle$ or $|1\rangle$ is unchanged, however it modifies the phase of the quantum state. It is equivalent to tracing a horizontal circle on the Bloch sphere of ϕ, and thus allows to extend the range of rotations on the Bloch sphere allowed by braiding (restricted to $\pi/2$ angles) to rotations by arbitrary angles.

4.2.3 Platforms that support Majoranas

The first among the countless amount of proposed platforms for Majorana anyons generation can be thought to be the Pfaffian state introduced by Moore and Read in a seminal paper [253]. Subsequent works were able to prove that a possible realization of this state is the $\nu = 5/2$ filling factor of the fractional quantum Hall state [212,254–256]. Later on, it was recognized by Read and Green that topological spinless two-dimensional $p + ip$ superconductors share the same non-Abelian statistics as the Pfaffian state [257]. The quantum vortices present in this system host Majorana anyons, and in addition chiral Majoranas circulate at the boundaries [64,258]. Ivanov further showed that a spinless p-wave superconductor with single quantum vortices is equivalent to a spinful p-wave superconductor with half-quantum vortices [215].

Besides these 'intrinsically' topological states, a significant body of work has been devoted to looking for engineered topological phases in hybrid platforms. These phases result from combining different physical systems and interactions in a clever way so as to cause non-trivial Majorana physics to emerge. Remarkably, most of the proposals include all ingredients that are well within the reach of current laboratory technologies and easy

to find in nature, such as *s*-wave superconductivity, semiconductors with strong spin-orbit interaction and magnetic fields. These hybrid structures are highly needed since intrinsic *p*-wave superconductivity is extremely rare in nature.

As we will see later in more detail, there are three ingredients that allow for Majorana bound states generation, namely:

1. Proximity effect, consisting in the tunneling of Cooper pairs from a superconductor to a normal conductor when they are placed close to each other.

2. Time reversal symmetry breaking (usually induced by means of magnetic fields).

3. Spin orbit coupling (SOC).

The first ingredient allows to induce superconductivity (of the *s*-wave standard kind) into the desired platforms. The two last ingredients, combined, allow to overcome the fermion doubling problem and to effectively get rid of one of the two spin degrees of freedom, at the same time as ingeniously endowing counterproagating carriers with oppositely spin-canted polarizations so that they are able to form the spin singlet needed for superconducting pairing. The candidate systems exploiting this wise combination of ingredients can be collected into two classes depending on whether the platform is one-dimensional or two-dimensional.

The groundbreaking proposal for 1D quantum wires to support bound Majorana zero modes at their ends was cast simultaneously in the two seminal papers by Lutchyn et al [213] and Oreg et al [214] in what is generally called the Oreg-Lutchyn model. The host system is a semiconducting wire with Rashba SOC made of e.g. InAs or InSb in the limit where only the lowest transverse subband is populated. Upon proximitising the wire with an *s*-wave superconductor, and appliying a magnetic field B_x along the direction of the wire (chosen as the x direction, see Fig. 4.7a), the system is described by a Hamiltonian

$$H = H_{1\mathrm{D}} + H_{\Delta} \tag{4.17}$$

where

$$H_{1\mathrm{D}} = \int dx \psi^{\dagger}(x) \left(-\frac{\partial_x^2}{2m} - \mu - i\alpha\sigma_y\partial_x + V_Z\sigma_x \right) \psi(x) \tag{4.18}$$

and

$$H_{\Delta} = \int dx \left(\Delta\psi_{\uparrow}(x)\psi_{\downarrow}(x) + \mathrm{H.\,c.} \right) \tag{4.19}$$

In the expressions above, V_Z is the strength of the Zeeman splitting induced by the applied magnetic field B_x, α is the magnitude of Rashba SOC, μ is the chemical potential in the wire and Δ is the pairing potential induced by proximity to the *s*-wave superconductor. The system described by $H_{1\mathrm{D}}$ is spinless for values of the chemical potential $|\mu| < V_Z$ (see right panel of Fig. 4.7b) and it is easy to show that the system described by the full Hamiltonian H can be driven into a topologically non trivial phase for values of the Zeeman energy such that $V_Z > \sqrt{\Delta^2 + \mu^2}$ (see Fig. 4.7c and d). It is interesting to notice that the Hamiltonian in Eq. (4.17) is mappable to the Kitaev toy model Hamiltonian [259], describing spinless fermions hopping on a 1D chain with *p*-wave superconductivity

$$H_K = -\mu \sum_n c_n^{\dagger} c_n - \frac{t}{2} \sum_n \left(c_n^{\dagger} c_{n+1} + \mathrm{H.\,c.} \right) - \frac{\Delta}{2} \sum_n \left(e^{i\phi} c_n c_{n+1} + \mathrm{H.\,c.} \right) \tag{4.20}$$

The formal proof is given explicitly in [260].

On the other hand, we have the 2D platforms. Pioneering in this sense was the proposal for using 2D topological insulators proximitized with *s*-wave superconductors first

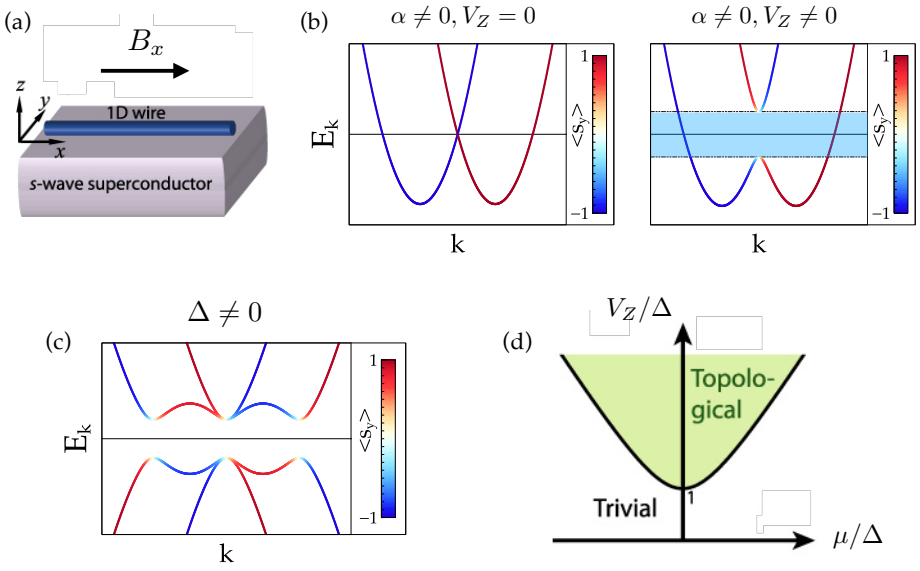

FIGURE 4.7: (a) Illustrative representation of a 1D Rashba quantum wire proximitised with an s-wave superconductor and with a magnetic field B_x applied along the wire direction. (b) Evolution of the single-particle spectrum of a 1D quantum wire (with a parabolic band dispersion in the absence of interactions) as SOC (left panel) and a Zeeman field (right panel) are progressively added to the system. The blue shaded region indicates the effectively spinless energy window, where topological superconductivity can arise via proximity-induced pairing. (c) Bogoliubov spectrum of the 1D wire with an induced pairing Δ when the Fermi level is in the spinless energy window. The line color of these spectra represents the spin polarization along the direction of the spin-orbit field. (d) Phase diagram of the system in the $(V_Z/\Delta, \mu/\Delta)$ plane. [Adapted with permission from Ref. [86]]

cast by Fu and Kane [154]. A 2D topological insulators is characterized by an insulating bulk with conducting gapless helical edge states, that is, oppositely spin-polarized counterpropagating states connected by time-reversal symmetry (see Fig. 4.8a and b). Provided this symmetry is preserved, backscattering between the two spin-filtered edge states is prohibited. This property provides the system with one crucial ingredient, that is the fermion doubling removal, since when the Fermi level is tuned within the bulk gap there is only a pair of Fermi points. These states can be gapped out by proximitization with a standard superconductor, and the pairing gap arising is topological because of the 'spinless' feature exemplified above. The Hamiltonian describing such a system is

$$H = H_{\text{2DTI}} + H_{\Delta} \tag{4.21}$$

with

$$H_{\text{2DTI}} = \int dx \psi^{\dagger}(x) \left(-\mu - iv\sigma_z \partial_x\right) \psi(x) \tag{4.22}$$

and

$$H_{\Delta} = \int dx \left(\Delta \psi_{\uparrow}(x) \psi_{\downarrow}(x) + \text{H. c.}\right) \tag{4.23}$$

Again, the phase of matter described by this Hamiltonian is mappable to the Kitaev model (Eq. (4.20)) if a Zeeman field that breaks time-reversal symmetry perpendicular to the spin-orbit coupling field (chosen along z) is applied (see Fig. 4.8b):

$$H \to H' = H_{\text{2DTI}} + H_{\Delta} + H_Z \tag{4.24}$$

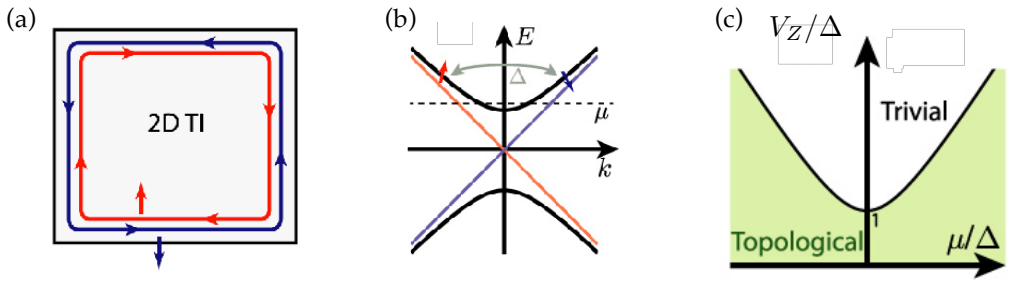

FIGURE 4.8: (a) Illustrative representation of the helical edge states of a 2D topological insulator. (b) Spectrum of a 2D topological insulator with and without magnetic field (gapless colored and gapped black spectra, respectively). (c) Phase diagram of the system in the $(V_Z/\Delta, \mu/\Delta)$ plane. [Adapted with permission from Ref. [86]]

with

$$H_Z = -V_Z \int dx \psi^\dagger(x) \sigma_x \psi \tag{4.25}$$

It can be shown that the system described by H' can be driven in a topologically non trivial phase for values of the Zeeman energy such that $V_Z < \sqrt{\Delta^2 + \mu^2}$ (see Fig. 4.8).

Another class of 2D platforms that has become increasingly attractive is that of SNS junctions with strong Rashba SOC in the normal part. It has been recently shown [261,262] that by inducing a phase difference of π between the two superconducting leads (see Fig. 4.9a), the magnetic field applied along the direction of the quasi-1D region occupied by the 2DEG needed to originate topological superconductivity in the system is sensibly reduced (see Fig. 4.9b). Even more remarkably, in a setup where the phase is not controlled externally, the system is found to undergo a first-order topological phase transition when the Zeeman field is varied. At the transition, the phase difference between the superconducting leads changes abruptly from a value close to zero, for which the system is trivial, to a value close to π, for which the system is topological (see Fig. 4.9c).

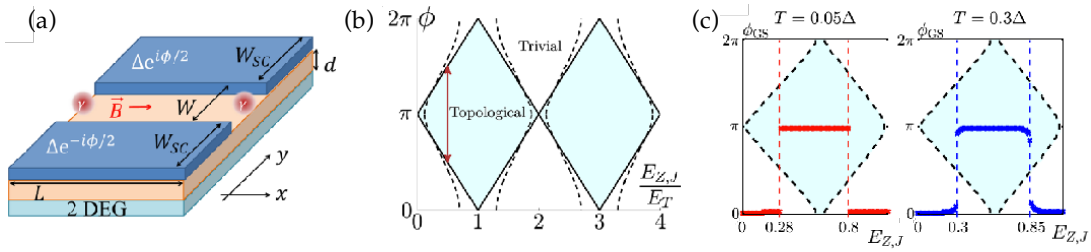

FIGURE 4.9: (a) Sketch of the SNS planar junction considered in [261]. (b) Phase diagram of the system as a function of the phase difference ϕ between the two superconducting leads and of the in-plane Zeeman field $E_{Z,J}$. The shaded region indicates the superconducting topological phase. (c) The phase difference ϕ_{GS} that minimizes the ground state energy calculated for two different temperatures as a function of the applied Zeeman field obtained numerically from a tight binding model of the junction. [Adapted with permission from Ref. [261]]

We conclude this section by mentioning that another interesting class of platforms for Majorana engineering is that of time-reversal invariant systems. In these systems Kramers doublets of protected Majoranas that do not split despite their spatial proximity

(as long as time reversal symmetry is preserved) appear at the borders of conveniently prepared systems [263–267].

4.3 The Crossed Andreev reflection (CAR) mechanism in quantum Hall systems

In this section we discuss Andreev reflection processes in several types of junctions and with different kinds of physical ingredients.

4.3.1 Andreev reflection processes in normal platforms

The term local Andreev reflection (LAR) refers to the remarkable property of normal-superconducting (NS) junctions of retroreflecting a hole when an electron with an energy smaller than the superconducting gap tunnels into the superconductor from the normal lead [238,239,268]. During this process, a Cooper pair forms in the superconductor (see Fig. 4.10a). This hallmark of NS junctions reflects the capability of superconductors to accept electrons only in pairs, such that a single electron cannot penetrate a superconductor if another electron is not available to form a pair. As a consequence, when an electron tunnels, another has to tunnel at the same time. The Andreev reflected hole is nothing but the empty state left behind by the electron that is captured with the incident one to form a Cooper pair. Phase-coherence is mantained between the incoming electron and outgoing hole during this reflection process.

Since Cooper pairs are composed by states related by time reversal, that is electrons with opposite momenta and spins, the reflected hole will have opposite spin and velocity, but equal momentum, with respect to the incoming electron. As an important consequence, if the system is spin-polarized and only one spin is occupied by the conduction electrons, Andreev reflection is impossible because there are no available states in the normal conductor to form a Cooper pair, or, alternatively, there is no channel for retroreflected holes with opposite spin.

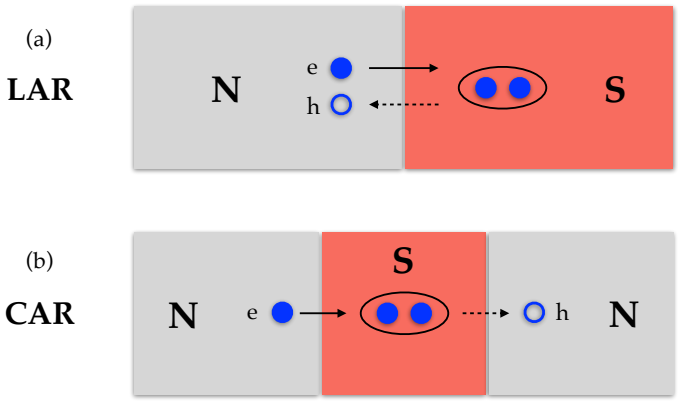

FIGURE 4.10: (a) Schematic illustration of a local Andreev reflection (LAR) at a NS junction. (b) Schematic illustration of a crossed Andreev reflection (CAR) at a NSN junction.

When multiple interfaces are present, exotic physics can take place. In SNS junctions, for instance, bound states of co-existing electrons and holes with energies below the superconducting gap can be formed, called Andreev bound states [238].

A process similar to LAR, termed crossed Andreev reflection (CAR), is instead peculiar to NSN junctions and occurs when an electron is injected from one of the normal terminals to the superconductor, and a hole is reflected out at the other normal terminal. In this process a Cooper pair forms in the superconductor as was the case with LAR, with the difference that the 'matching' electron that forms a pair with the incoming electron comes from the opposite lead [269–272]. This process takes place on a characteristic length given by the coherence length of the superconductor $\xi = v_F/\hbar\Delta$, and as a consequence CAR can only occur if the width of the superconducting region is smaller than this length. For larger widths, this process is exponentially suppressed. In a generic SNS junction the CAR process competes with the LAR one, with the latter occurring independently at each of the two individual NS junctions. Which of the two dominates critically depends on the specific system taken into account and on the width of the superconducting region, that controls the strength of CAR while leaving the LAR unaltered. Notice that if the LAR can be suppressed and the width of the central region is shorter than the coherence lenght, the CAR dominates the transport features of the junction. This is the central aspect of our proposal.

The inverse process of Andreev reflection is the Cooper-pair splitting, consisting in a process where a Cooper pair tunnels in a normal conductor proximitised with a superconductor. Again, this process can be either local (at a single NS interface) or crossed (if there are two successive NS interfaces with a narrow superconductor in between). This splitted pair of electrons is phase-coherent and, therefore, entangled. It is interesting to note that there is an intimate connection between the process of Cooper pair splitting and the proximity effect, since the latter is nothing but the leakage of Cooper pairs from a superconductor to a normal metal.

4.3.2 Andreev reflection processes in quantum Hall systems

This picture qualitatively changes when a strong magnetic field perpendicular to the NS interface is applied. In this situation time-reversal symmetry is broken and a special kind of Andreev bound state, that was first introduced in [240], can originate. Provided that the magnetic flux is strong enough to prompt quantum Hall physics in the normal lead and can nevertheless be expelled by the superconductor, the bound state that forms is a coherent superposition of an electron and a hole that propagates in the same direction along the interface.

In a classical description of the dynamics of an electron moving in two dimensions in an external magnetic field, the LAR processes that occur at the NS interface can be thought of as an alternating path of skipping orbits of electrons and holes, as shown in Fig. 4.11a. Quantum-mechanically, the more appropriate model for describing this mechanism is in term of quantum Hall edge states characterized by mixed electron and hole currents that flow parallel to the interface and in the same direction, as shown in Fig. 4.11b and c. The fact that electrons and holes propagate in the same direction stems from the intrinsic chirality of the carriers associated to the breaking of time reversal symmetry of the QH phase. This has the remarkable consequence that, at odds with what happens at standard NS junctions, the Andreev bound state characterized by chiral copropagating electron-like and hole-like edge states arising at NS interfaces in the QH regime is a gapless edge mode. In fact, having the same velocity, the electrons and holes forming this LAR-induced bound state cannot couple to develop a gap.

If we now introduce a second NS interface so as to generate an NSN junction as in Fig. 4.12, it is easy to see that, because of chirality, the two interfaces host oppositely propagating edge states [234,241,242,273]. Because of this, in the limit where the superconducting region is narrower than the coherence length, an electron-like state with momentum at

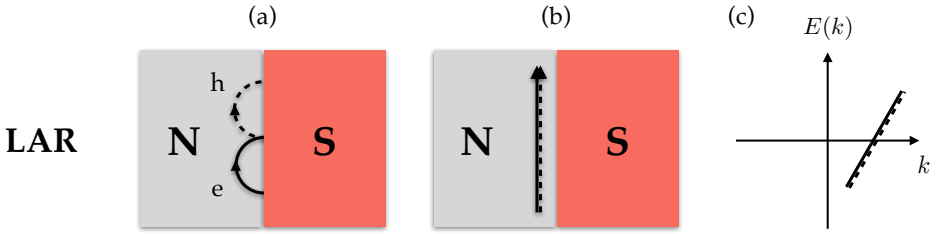

FIGURE 4.11: (a) Classical picture of electrons and holes in alternating skipping orbits at the boundary bewteen a QH system and a superconductor. (b) Quantum-mechanical picture of the Andreev bound state generated at the boundary bewteen a QH system and a superconductor via LAR processes. (c) Qualitative picture of the LAR-induced Andreev bound state dispersion.

the first interface can be reflected as a hole-like state at the opposite interface with the same momentum and opposite velocity. Analogously, an electron-like state at the second interface (that has opposite velocity and momentum with respect to electron-like states at the first interface) can be scattered across the superconducting region and reflected as a hole at the first interface, with the hole having the same momentum as the incoming electron and opposite velocity because of chirality (see panel a of Fig. 4.12a for the classical picture, and panel b for the quantum-mechanical one). Now, since electron and hole states at opposite interfaces have equal momenta and opposite velocities, unlike LAR-induced electron-hole pairs, they can combine to open a gap (see Fig. 4.12c). Note how-

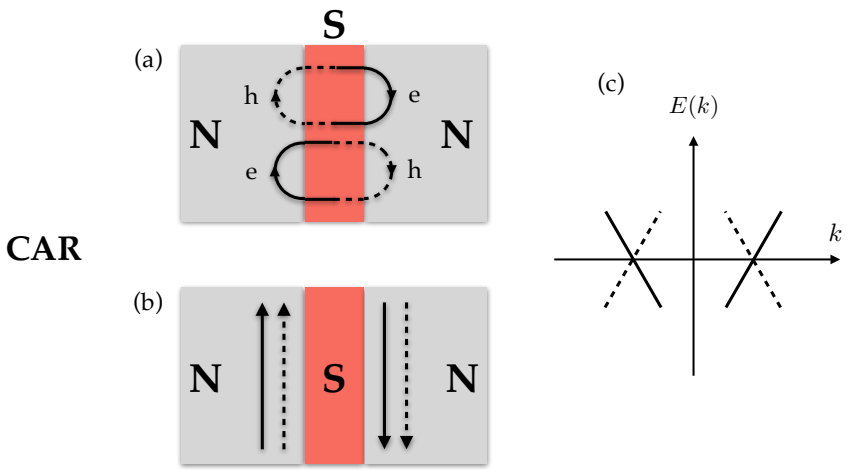

FIGURE 4.12: (a) Classical picture of CAR processes at a NSN junction when the normal leads are in the QH regime. (b) Quantum-mechanical picture of CAR-induced electron and hole states at a NSN junction when the normal leads are in the QH regime. (c) Qualitative picture of the CAR-induced electron and hole edge states dispersion.

ever that the pairing induced by the CAR mechanism does not guarantee the opening of a topological superconducting gap. In fact, a gap is allowed only if a non-zero singlet amplitude is present, that is, a channel for reflected holes with a spin component opposite to that of the incoming electron. Moreover, this gap may be topologically nontrivial, but only if the system is effectively 'spinless'.

4.3.3 Induced pairing

We now wish to develop a more rigorous understanding of the kind of gap that can arise as a result of crossed Andreev reflection. In this first subsection, we compute the pairing $\tilde{\Delta}$ induced in the 2DEG by a superconducting strip that is translationally invariant along the x axis and confined between $y = 0$ and $y = W_S$ along the y axis.

The effect of this strip on the surrounding 2DEG (that we take to be infinite in the xy plane) can be taken into account upon integrating out its degrees of freedom. This induces a self-energy $\Sigma(\omega)$ in the 2DEG, whose off-diagonal Nambu components, in the limit of zero frequency, are proportional to the induced pairing $\tilde{\Delta}$. If we neglect spin-orbit and Zeeman interaction effects in the strip, the induced pairing is formally given by

$$\tilde{\Delta} = \frac{1}{2}\mathrm{Tr}\left[\tau_x \Sigma(\omega = 0)\right] \tag{4.26}$$

with τ_x acting in the particle-hole space spanned by the two-component Nambu spinor $\Psi = (\psi_\uparrow, \psi_\downarrow^\dagger)^T$. Neglecting SOC in the strip is justified because its role is merely that of canting the spin polarizations of the edge states along a direction perpendicular to that of the Zeeman field. We take into consideration the dependence of the induced gap on this canting in the next subsection, by inserting a SOC term in the effective Hamiltonian for the edge states of the 2DEG in the QH phase. The same holds for the Zeeman field, even though a more profound reason for neglecting this interaction in the superconducting strip is rooted in the screening of the field associated to Meissner effect, a phenomenon 'inherited' by the proximitised region from the parent superconductor. On the other hand, taking the zero frequency limit is justified in the physically relevant situation where $\tilde{\Delta} \ll \Delta$, with Δ the parent gap. In this regime, the frequency dependence of the parent Green's function becomes negligible.

The self energy $\Sigma(\omega)$ induced between the two NS boundaries by the strip, in turn, is related to the tight binding Green's function of the isolated system $G_{\mathrm{tb}}^{(0)}(\omega; y, y')$, evaluated at the edges, by the relation

$$\Sigma(\omega) = t'^* G_{\mathrm{tb}}^{(0)}(\omega; y, y') t' \Big|_{y=0, y'=W_S} \tag{4.27}$$

with t' the coupling amplitude between the superconducting strip and the 2DEG. When $t' = 0$, the superconductor cannot pair the chiral states from opposite edges, and consequently the system is gapless with counterpropagating states at both side of the strip. It is only fot $t' \neq 0$ that the superconductor becomes able to pair the edge states, thus opening a SOC and Zeeman dependent gap.

The tight-binding Green's function $G_{\mathrm{tb}}^{(0)}(\omega; y, y')$ is related to that of the continuous limit as

$$G^{(0)}(\omega; y, y') = \lim_{a \to 0} \frac{G_{\mathrm{tb}}^{(0)}(\omega; y, y')}{a}$$

with a the lattice parameter of the system. However, we cannot simply make use of this equality in computing the self-energy in Eq. (4.27), since the former has to be calculated at the boundaries ($y = 0, y' = W_S$), where the continuum Green's function vanishes by definition. As was shown in [274], the tight binding Green's function at the outermost sites of an isolated system can be directly related to the double derivative with respect to y and y' of the continuous Green's function as

$$G_{\mathrm{tb}}^{(0)}(\omega; y, y') = -a^3 \partial_y \partial_{y'} G^{(0)}(\omega; y, y') \tag{4.28}$$

in the limit where $a \to 0$. Therefore one has that, by making successive use of equations (4.26)-(4.28) backwards, the following expression for $\tilde{\Delta}$ as a function of the continuum Green's function $G^{(0)}(\omega; y, y')$ is found

$$\tilde{\Delta} = -\frac{a^3|t'|^2}{2}\partial_y\partial_{y'}\left(\mathrm{Tr}\left[\tau_x G^{(0)}(\omega = 0; y, y')\right]\right)_{y=0,y'=W_S} \tag{4.29}$$

We are now left with the task of computing the continuum Green's function $G^{(0)}(\omega; y, y')$. To this end, we consider an isolated superconducting strip described by the Hamiltonian

$$H_S = \left(-\frac{\partial_x^2}{2m} - \frac{\partial_y^2}{2m} - \mu\right)\tau_z + \Delta\tau_x \tag{4.30}$$

where m is the effective mass, μ is the chemical potential and Δ the pairing potential induced in the strip by the parent superconductor. The τ's are Pauli matrices acting in the Nambu space, spanned by the previously introduced two-dimensional spinor $\Psi = (\psi_\uparrow, \psi_\downarrow^\dagger)^T$. When solving the eigenvalue problem associated with this system, translational invariance in the x direction allows us to write the wavefunction as

$$\Psi(x, y) = e^{ik_x x}\varphi(y)$$

with $\varphi = (\varphi_\uparrow, \varphi_\downarrow^\dagger)^T$ a two-component spinor in Nambu space. The eigenvalue equation for $\varphi(y)$ becomes therefore

$$\left[\left(-\frac{\partial_y^2}{2m} - \tilde{\mu}\right)\tau_z + \Delta\tau_x\right]\varphi(y) = \epsilon\varphi(y)$$

Where we have defined

$$\tilde{\mu} = \mu - \frac{k_x^2}{2m} \tag{4.31}$$

If we further assume that

$$\varphi(y) = \begin{pmatrix} u \\ v \end{pmatrix} e^{ik_y y}$$

The eigenvalue problem becomes

$$\left[\left(\frac{k_y^2}{2m} - \tilde{\mu}\right)\tau_z + \Delta\tau_x - \epsilon\right]\varphi(y) = 0$$

That yields the solutions

$$\epsilon_\eta = \eta\sqrt{\left(\frac{k_y^2}{2m} - \tilde{\mu}\right)^2 + \Delta^2} = \eta\sqrt{\xi^2 + \Delta^2} \qquad \eta = \pm 1$$

where we have defined

$$\xi = \frac{k_y^2}{2m} - \tilde{\mu}$$

and the associated normalized spinor is given by

$$\varphi_\eta = \begin{pmatrix} u_\eta \\ v_\eta \end{pmatrix}$$

where

$$u_\eta = \eta\sqrt{\frac{\epsilon_\eta + \xi}{2\epsilon_\eta}} \qquad v_\eta = \sqrt{\frac{\epsilon_\eta - \xi}{2\epsilon_\eta}}$$

For a given eigenvalue of the problem, the most general solution is given by

$$\varphi_\eta(y) = \begin{pmatrix} u_\eta \\ v_\eta \end{pmatrix} \left[A_\eta e^{ik_y y} + B_\eta e^{-ik_y y}\right] \tag{4.32}$$

The coefficients A_η and B_η are found by imposing the boundary conditions that the wavefunction of the isolated strip needs to vanish at the boundaries:

$$\varphi_\eta(y=0) = \varphi_\eta(y=W_S) = 0$$

that yields $A_\eta = -B_\eta$ and the quantization of the wavevector along the y direction

$$k_y^n = n\pi/W_S \tag{4.33}$$

The energy, dependent on k_y, is quantized as well

$$\epsilon_\eta^n = \eta\sqrt{\left(\frac{(k_y^n)^2}{2m} - \tilde{\mu}\right)^2 + \Delta^2} = \eta\sqrt{\left(\frac{n^2\pi^2}{2mW_S^2} - \tilde{\mu}\right)^2 + \Delta^2} = \eta\tilde{\mu}\sqrt{\left(\frac{n^2\tilde{\lambda}_F^2}{4W_S^2} - 1\right)^2 + \left(\frac{\Delta}{\tilde{\mu}}\right)^2} \tag{4.34}$$

where we have introduced the Fermi wavelength

$$\tilde{\lambda}_F = \frac{2\pi}{\sqrt{2m\tilde{\mu}}} \tag{4.35}$$

The spinors become n-dependent as well

$$\varphi_\eta^n(y) = \frac{i}{\sqrt{2\epsilon_\eta^n}} \begin{pmatrix} u_\eta^n \\ v_\eta^n \end{pmatrix} \sin(k_y^n y)$$

where u_η^n and v_η^n depend on n through k_y^n (Eq. (4.33)) and ϵ_η^n (Eq. (4.34)). We are now able to compute the Green's function of the system

$$G^{(0)}(\omega; y, y') = \sum_{n=0}^{\infty} G_n^{(0)}(\omega; y, y') = \sum_{n=0}^{\infty} \sum_{\eta=\pm1} \frac{\varphi_\eta^n(y) \otimes [\varphi_\eta^n(y')]^\dagger}{\omega - \epsilon_\eta^n} \tag{4.36}$$

where

$$G_n^{(0)}(\omega; y, y') = \sum_{\eta=\pm1} \frac{\varphi_\eta^n(y) \otimes [\varphi_\eta^n(y')]^\dagger}{\omega - \epsilon_\eta^n}$$

At zero frequency:

$$G_n^{(0)}(y, y') = G_n^{(0)}(\omega = 0; y, y') = \sum_{\eta=\pm1} \frac{\varphi_\eta^n(y) \otimes [\varphi_\eta^n(y')]^\dagger}{\epsilon_{-\eta}^n}$$

Calculation of the off-diagonal or anomalous component of $G_n^{(0)}(y,y')$ yields

$$\frac{1}{2}\mathrm{Tr}\left[\tau_x G_n^{(0)}(y,y')\right] = \frac{2\sin(k_y^n y)\sin(k_y^n y')}{W_S}\sum_{\eta=\pm1}\frac{\sqrt{(\epsilon_\eta^n)^2-\xi_n^2}}{2(\epsilon_\eta^n)^2} \tag{4.37}$$

In order to obtain the induced gap, we have to take the double derivative, sum over n and evaluate the result at the boundaries as explained in eqs. (4.28)-(4.29) and Eq. (4.36). We perform the derivatives and evaluate the result at $y=0, y'=W_S$ first:

$$\partial_y\partial_{y'}\left(\frac{1}{2}\mathrm{Tr}\left[\tau_x G_n(y,y')\right]\right)_{y=0,y'=W_S} = \frac{1}{W_S^3\Delta}\frac{(n\pi)^2\cos(n\pi)}{1+(\tilde{\mu}/\Delta)^2\left[1-(n\tilde{\lambda}_F/2W_S)^2\right]^2}$$

Finally, upon performing the sum over n one gets:

$$\tilde{\Delta} = -a^3|t'|^2\sum_{n=0}^{\infty}\partial_y\partial_{y'}\left(\frac{1}{2}\mathrm{Tr}\left[\tau_x G_n(y,y')\right]\right)_{y=0,y'=W_S} = a^3|t'|^2\frac{4\pi^2}{\tilde{\mu}W_S\tilde{\lambda}_F^2}\mathrm{Im}(z\csc z) \tag{4.38}$$

where

$$z = \frac{2\pi W_S\sqrt{1+i\Delta/\tilde{\mu}}}{\tilde{\lambda}_F} \tag{4.39}$$

We recall that both $\tilde{\mu}$ and $\tilde{\lambda}_F$ depend on the wavevector k_x along the translationally invariant direction. One can rearrange the expression for $\tilde{\Delta}$ in order to facilitate its understanding. We rewrite

$$z = \alpha\sqrt{1+i\beta}$$

where $\alpha = 2\pi W_S/\tilde{\lambda}_F$ and $\beta = \Delta/\tilde{\mu}$. To find the real and imaginary parts of z, we write $\sqrt{1+i\beta} = \rho e^{i\phi}$, such that $1+i\beta = \rho^2 e^{i2\phi}$. From this equality, one sees that $\rho = [1+\beta^2]^{1/4}$ and $\phi = \arctan(\beta)/2$. Therefore

$$z = \alpha[1+\beta^2]^{1/4}e^{i\frac{\arctan(\beta)}{2}} = x+iy \tag{4.40}$$

where

$$\begin{aligned} x &= \alpha[1+\beta^2]^{1/4}\cos\left(\tfrac{\arctan(\beta)}{2}\right) \\ y &= \alpha[1+\beta^2]^{1/4}\sin\left(\tfrac{\arctan(\beta)}{2}\right) \end{aligned} \tag{4.41}$$

Through some simple algebra, $\tilde{\Delta}$ can be rewritten as a function of x and y as

$$\mathrm{Im}(z\csc z) = \frac{x\cos x\sinh y + y\sin x\cosh y}{(\cos x\sinh y)^2+(\sin x\cosh y)^2} \tag{4.42}$$

From this expression, combined with eqs. (4.38) and (4.41) one already can see that $\tilde{\Delta}$ is an oscillatory function of the ratio $\alpha = 2\pi W_S/\tilde{\lambda}_F$. We can relate this behaviour of $\tilde{\Delta}$ with the number of transverse modes in the superconducting region. This number is as a function of the strip width and of the chemical potential of the proximitized region. In fact, the chemical potential of a quasi-1D system translationally invariant along the x direction and confined along the y direction with n transverse modes pupulated, is given by

$$\mu = \frac{k_x^2}{2m}+\frac{(k_y^n)^2}{2m} \tag{4.43}$$

with $k_y^n = \pi n / W_S$ as noted above. Eq. (4.43) can be therefore rewritten as

$$\tilde{\mu} = \frac{(\pi n)^2}{2mW_S^2}$$

(remebering Eq. (4.31)) whence the number of modes

$$n = \left\lfloor W_S \frac{\sqrt{2m\tilde{\mu}}}{\pi} \right\rfloor = \left\lfloor \frac{2W_S}{\tilde{\lambda}_F} \right\rfloor \tag{4.44}$$

Now that we have identified the number of transverse modes entering the superconducting strip with $\lfloor 2W_S/\tilde{\lambda}_F \rfloor$, it is easy to see that the sign of the induced gap changes with the number of modes hosted by the superconductor (see Fig. 4.14). We will give a more quantitative description of this sign change in the next section.

4.3.4 Induced gap

We now have to calculate the effective gap Δ^* opened by the chiral edge states of the 2DEG in the presence of a Zeeman field and a Rashba spin-orbit interaction.

To this aim, we employ a simple model to describe the transport properties of the 2DEG at the boundaries with the superconducting strip. When the chemical potential is within the bulk gap, one is entitled to focus only on the chiral edge states of the $\nu = 1$ filling factor, that intersect the Fermi level at the two wavevectors $\pm k_F$. At the boundaries, they move along the x direction so they can be effectively considered one-dimensional. At $t' = 0$, that is, when the 2DEG is uncoupled to the superconducting strip, and upon including both Zeeman and SO interactions, the edge states can be modeled by the continuum Hamiltonian

$$H_{1D} = -\frac{\partial_x^2}{2m} - \mu_N + V_Z\sigma_x - i\alpha\partial_x\sigma_y \tag{4.45}$$

where the σ's are Pauli matrices acting in spin space. Coupling to a narrow superconducting strip ($t' \neq 0$) induces an effective pairing $\tilde{\Delta}$ in the counterpropagating and oppositely spin polarized chiral states, that we have calculated in the previous subsection as the off-diagonal component of the zero-frequency self-energy of the isolated strip. In the 4-dimensional spinorial basis $\Psi = (\psi_\uparrow, \psi_\downarrow, \psi_\uparrow^\dagger, \psi_\downarrow^\dagger)^T$ we can write the Hamiltonian of the edge modes coupled to the superconductor as

$$H_{1D} + H_{\tilde{\Delta}} = \left(-\frac{\partial_x^2}{2m} - \mu_N + V_Z\sigma_x - i\alpha\partial_x\sigma_y \right) \tau_z - \tilde{\Delta}\tau_y\sigma_y \tag{4.46}$$

where μ_N is the chemical potential in the unproximitised region, τ acts in particle hole space and σ in spin space. When acting on plane waves dispersing along the x direction, Eq. (4.46) becomes

$$H_{1D} + H_{\tilde{\Delta}} = \left(\frac{k_x^2}{2m} - \mu_N + V_Z\sigma_x + \alpha k_x\sigma_y \right) \tau_z - \tilde{\Delta}\tau_y\sigma_y \tag{4.47}$$

In this expression, remember that $\tilde{\Delta}$ is itself a function of the wavevector k_x at which the edge states intersect the Fermi level. This Hamiltonian is equivalent to the of the Oreg-Lutchyn Hamiltonian [213,214] presented in the introduction (cfr. Eq. (4.17)), although expressed in a different basis. The gap opened at $\mu_N = 0$ by the system described by Eq.

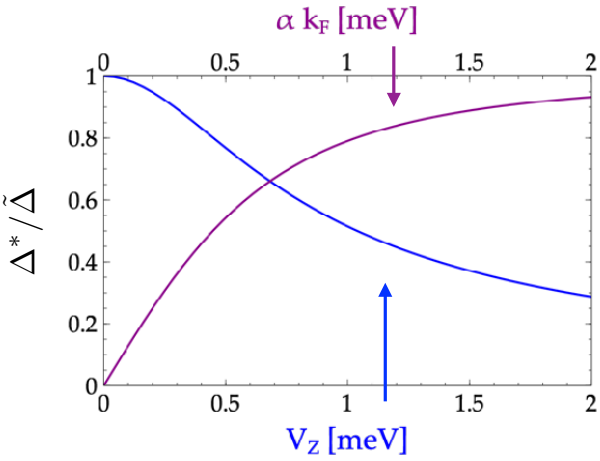

FIGURE 4.13: Plot of the ratio $\Delta^*/\tilde{\Delta}$ between the induced gap and the induced pairing as a function of the spin-orbit energy αk_F when the Zeeman energy is fixed at $V_Z = 0.6meV$ (purple line) and of the Zeeman energy V_Z when the spin-orbit energy is fixed at $\alpha k_F = 0.6meV$ (blue line).

(4.47) is given by

$$\Delta^*(k_x) = \frac{1}{m}\sqrt{k_x^2 + 4m^2(\gamma - \Gamma/m)} \tag{4.48}$$

where

$$\gamma = V_Z^2 + (\alpha k_x)^2 + \tilde{\Delta}^2 \quad \text{and} \quad \Gamma = \sqrt{(\alpha k_x^3)^2 + (V_Z k_x^2)^2 + (2mV_Z\tilde{\Delta})^2}$$

In the approximation where $\tilde{\Delta}$ is the smallest scale of the problem, the wavevector at which the gap opens can be approximated by the Fermi wavevector of the unproximitised 2DEG k_F (corresponding to the $t' = 0$ limit, described by Eq. (4.45) with $\mu_N = 0$), given by

$$k_x \approx k_F = \sqrt{2m^2\alpha^2 + m\sqrt{V_Z^2 + m^2\alpha^4}} \tag{4.49}$$

By inserting the expression for k_F in Eq. (4.48) one obtains

$$\Delta^* \approx \Delta^*(k_F) = 2\sqrt{\beta\left[1 + \frac{\tilde{\Delta}^2}{\beta} - \sqrt{1 + \left(\frac{2V_Z\tilde{\Delta}}{\beta}\right)^2}\right]} \tag{4.50}$$

where

$$\beta = 2(V_Z^2 + \alpha^2 k_F^2) \tag{4.51}$$

One can now expand Δ^* in series as a function of $\tilde{\Delta}$ to obtain, to first order,

$$\Delta^* \approx \sqrt{1 - \frac{2V_Z^2}{\beta}}\tilde{\Delta} = \frac{\tilde{\Delta}}{\sqrt{(V_Z/\alpha k_F)^2 + 1}} \tag{4.52}$$

By defying

$$\theta = \arcsin\left(\frac{1}{\sqrt{(V_Z/\alpha k_F)^2 + 1}}\right) \tag{4.53}$$

we can write

$$\Delta^* = \sin\theta\tilde{\Delta} \tag{4.54}$$

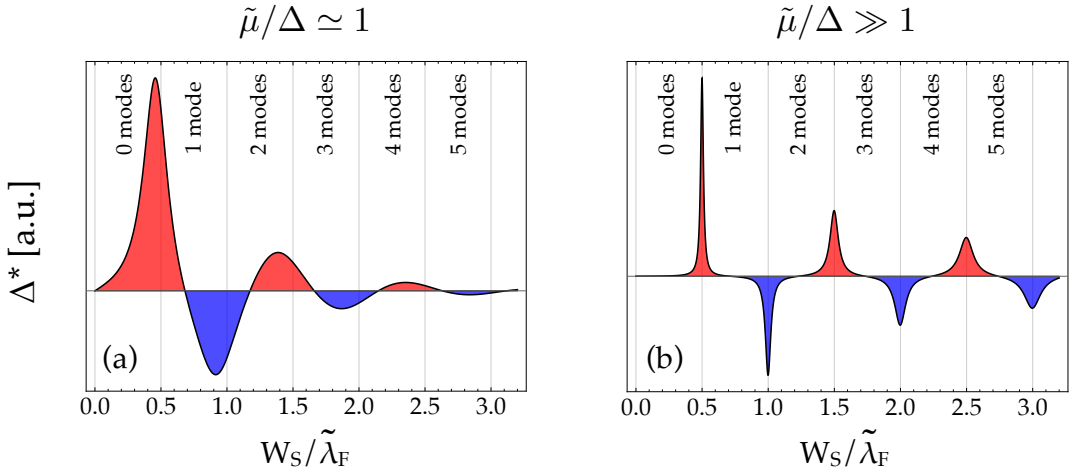

FIGURE 4.14: Behaviour of the gap Δ^* obtained analytically as a function of $W_S/\tilde{\lambda}_F$. Vertical lines indicate the number of normal modes $n = \lfloor W_S/\tilde{\lambda}_F \rfloor$ in the strip. Panel (a) refers to a ratio $\tilde{\mu}/\Delta = 1.95$, whereas (b) refers to a ratio $\tilde{\mu}/\Delta = 20$, one order of magnitude larger.

where θ is an angle measuring the spin-orbit-induced deviation of the edge states spin polarization away from the direction of the Zeeman field. In Fig. 4.13 we show the behaviour of Δ^* as a function of V_Z for a finite value of α (blue curve) and as a function of αk_F for a finite value of V_Z (purple curve). From these behaviours, we see that when only the Rashba interaction is present ($\alpha \neq 0, V_Z = 0$) a finite gap is opened. However, even if spin degeneracy is lifted, at any energy there are four Fermi points. Thefeore, the gap that opens is not topological. If, on the other hand, only the Zeeman field is present ($\alpha = 0, V_Z \neq 0$), the spin degeneracy is lifted but no spin singlet can be formed since the spins are parallel. In this case, no gap (either trivial or non-trivial) can open. Finally, when both interactions are turned off ($\alpha = 0, V_Z = 0$) and the filling factor is adjusted to $\nu = 2$ a gap opens, but it is topologically trivial because of spin degeneracy.

In Fig. 4.14 we present two plots of Δ^* as a function of the ratio $W_S/\tilde{\lambda}_F$ for two different values of the ratio $\tilde{\mu}/\Delta$, with $\tilde{\mu}$ the chemical potential of the proximitized region normalized with respect to the wavevector along the translationally invariant direction and Δ the gap induced into the 2DEG by the parent superconductor. We recall from Eq. (4.44) that the quantity $W_S/\tilde{\lambda}_F$ corresponds to half the number of transverse modes in the central strip. From the behaviour of Δ^*, it is clear that the induced gap changes sign with the parity of the number of modes. This feature is more evident in the regime where $\Delta \ll \tilde{\mu}$. It is also interesting to note that the induced gap rapidly decays to zero as W_S increases, a clear indication that the CAR processes on which the pairing mechanism is rooted are being exponentially suppressed as the width of the superconducting strip exceeds the superconducting coherence length ξ. Notice that, in line with this argument, the induced gap of panel (b) outlives that of panel (a) because the parent gap Δ is one order of magnitude smaller, which in turn yields a larger coherence length that ensures a non-zero CAR amplitude for a wider range of strip widths.

4.4 Numerical calculations

In this section, we confirm the previous analysis with full numerical calculations based on a tight binding approximation for square lattice ribbons supplied with all the ingredients described in section 4.1. We calculate the spectra of systems with both periodic

boundary conditions (PBC) and open boundary conditions (OBC), that is finite-size systems that allow us to investigate the end modes that develop at the boundaries of our platform. We will consider two configurations. In the first the Rashba SOC is intrinsic to the 2DEG and thus present in the whole system (case I). In the second, the 2DEG has no SO interaction of its own, and this interaction is present only in the superconductor. This may happen if the superconducting compound is made of heavy elements, and in this case the SO interaction is inherited only from the region of the 2DEG that is contacted with the superconducting strip[1] (case II). Interestingly, the physics does not change qualitatively, and the reason is that the SO interaction is merely needed for canting the spins of the edge states in opposite directions at opposite boundaries.

4.4.1 Tight binding model

We consider a two-dimensional square lattice that extends from $-L/2$ to $L/2$ along the x axis, and from $-W/2$ to $W/2$ along the y axis. The central superconducting strip, oriented along the x axis, occupies the area that goes from $y = -W_S/2$ to $y = W_S/2$ (see for reference Figs. 4.21-4.23). The tight binding Hamiltonian that we use for all the calculations is given by

$$H = H_0 + H_Z + H_S + H_{SOC} \tag{4.55}$$

where

$$H_0 = -\sum_{mn} \mu_n c^\dagger_{mn} c_{mn} - t \sum_{\langle mn,m'n'\rangle} c^\dagger_{mn} c_{m'n'} e^{-i\phi_{mn,m'n'}} \tag{4.56}$$

$$H_Z = \sum_{mn} V^Z_n c^\dagger_{mn} \sigma_x c_{mn} \tag{4.57}$$

$$H_S = \sum_{mn} \Delta_n \left[c_{mn,\downarrow} c_{mn,\uparrow} + c^\dagger_{mn,\uparrow} c^\dagger_{mn,\downarrow} \right] \tag{4.58}$$

$$H_{SOC} = i \sum_{\langle mn,m'n'\rangle} \left(\alpha_n / a^2\right) c^\dagger_{mn} \left(\boldsymbol{\sigma} \times \mathbf{r}_{mn}\right)_z c_{m'n'} \tag{4.59}$$

Where

- $\mathbf{r}_{mn} = (ma, na)$, with a the lattice parameter of the square lattice.
- $\langle mn, m'n'\rangle$ indicates restriction to nearest neighboring sites.
- $\mu_n = \mu_N$ for $n \in [-W/2, -W_S/2]$ and $n \in [W_S/2, W/2]$, and $\mu_n = \mu \neq \mu_N$ for $n \in [-W_S/2, W_S/2]$.
- $\phi_{mn,m'n'}$ is the Peierls phase acquired by the electrons under an external magnetic field, defined as $\phi_{mn,m'n'} = \int_{\mathbf{r}_{m'n'}}^{\mathbf{r}_{mn}} \mathbf{A} \cdot d\mathbf{r}$ if $n \in [-W/2, -W_S/2]$ and $n \in [W_S/2, W/2]$ and that is 0 if $n \in [-W_S/2, W_S/2]$ due to the Meissner effect. Under the choice of the gauge $\mathbf{A} = (A_x(n), 0, 0)$, with

$$A_x(n) = \begin{cases} B(na + W_S/2) & \text{for } n \in [-W/2, -W_S/2] \\ 0 & \text{for } n \in [-W_S/2, W_S/2] \\ B(na - W_S/2) & \text{for } n \in [W_S/2, W/2] \end{cases} \tag{4.60}$$

[1] Notice that this possibility has been demonstrated in [234], where a CAR-mediated electron-to-hole conversion has been experimentally detected in the $\nu = 1$ filling factor of quantum Hall ferromagnetic graphene, a circumstance that is made possible only by the presence of SOC. In turn, such an interaction cannot be ascribed to graphene since this interaction is negligibly small in this compound [6,7,90,275], so that one has to conclude that the NbN superconducting electrode was able to imprint a SO interaction in the graphene portion underneath it.

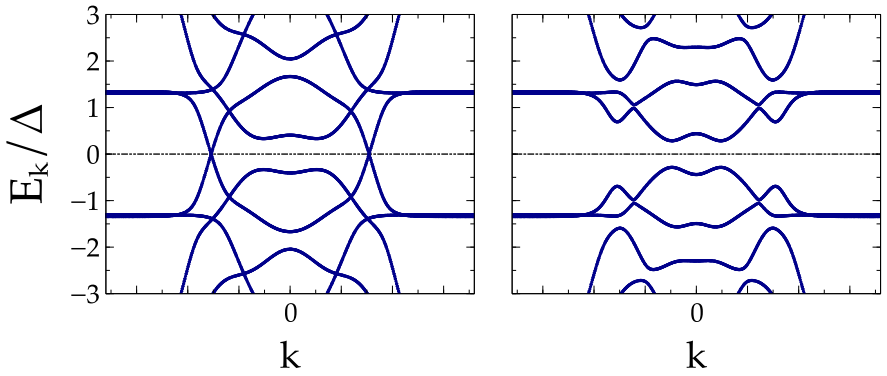

FIGURE 4.15: Spectra of a NSN junction with PBC along both x and y for $\alpha, V_Z = 0$ at $\nu = 2$. (a) Spectrum of the system with pairing $\Delta = 0$. (b) Spectrum of the system with pairing $\Delta \neq 0$. The energies are plotted in units of the superconducting gap $\Delta = 0.95$ meV.

and performing the integral, $\phi_{mn,m'n'}$ becomes

$$\phi_{mn,m'n'} = \begin{cases} Ba(m-m')\,[a(n+n')/2 + W_S/2] & \text{for } n \in [-W/2, -W_S/2] \\ 0 & \text{for } n \in [-W_S/2, W_S/2] \\ Ba(m-m')\,[a(n+n')/2 - W_S/2] & \text{for } n \in [W_S/2, W/2] \end{cases} \tag{4.61}$$

- $V_n^Z = V_Z \neq 0$ for $n \in [-W/2, -W_S/2]$ and $n \in [W_S/2, W/2]$ and $V_n^Z = 0$ for $n \in [-W_S/2, W_S/2]$.
- $\Delta_n = 0$ for $n \in [-W/2, -W_S/2]$ and $n \in [W_S/2, W/2]$ and $\Delta_n = \Delta \neq 0$ for $n \in [-W_S/2, W_S/2]$.
- $\alpha_n = \alpha \neq 0$ for $n \in [-W/2, W/2]$ (case I); $\alpha_n = \alpha \neq 0$ for $n \in [-W_S/2, W_S/2]$ (case II).
- The creation and annihilation operators are two-component vectors in spin space

$$c_{mn}^\dagger = \left(c_{mn,\uparrow}^\dagger, c_{mn,\downarrow}^\dagger\right)$$

4.4.2 Spectra of systems with PBC

Here we calculate the band structure of ribbons with periodic boundary conditions along both the x and the y directions, for which the discussion presented in subsection 3.3.1 of previous chapter holds. We consider a system with $W_S = 100$ nm, $W = 700$ nm, $B = 0.34$ T, $\Delta = 0.95$ meV, $\mu = 4.4$ meV and: (i) $\alpha = 0$, $V_Z = 0$; (ii) $\alpha = 0$, $V_Z = 0.5$ meV; (iii) $\alpha = 1.3\ 10^{-13}$ eV m, $V_Z = 0.5$ meV. We calculate the band structures for these three to see how the low-energy sector evolves upon adding these interactions.

(i) $\alpha = 0, V_Z = 0$ We consider the situation where both interactions are absent and the Fermi level is tuned in such a way that only the lowest Landau level ($\nu = 2$, taking into account spin degeneracy) is occupied. Because both spin polarizations are poulated, CAR processes will pair spin up (down) electronic states from an interface with spin down (up) holes from the other interface, thus opening a gap. This is clear from Fig. 4.15, where the Bogoliubov spectrum of an NSN junction at $\nu = 2$ with and without pairing (panels (a) and (b) respectively) is shown. This gap, associated to the pairing induced in the edge modes from opposite interfaces by the superconducting region, is not topological.

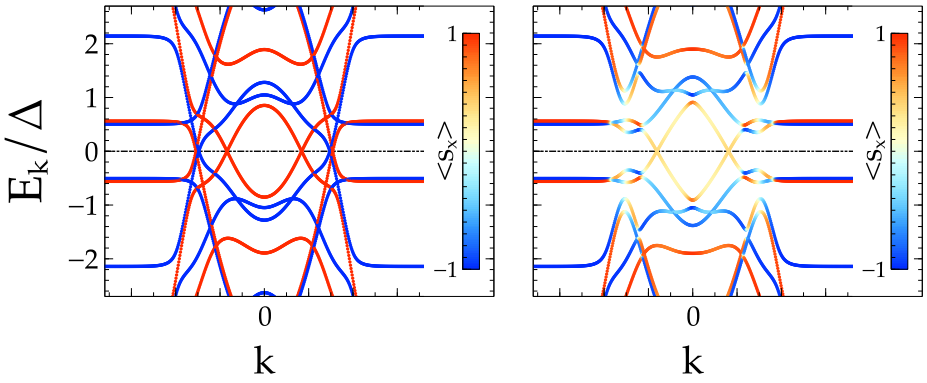

FIGURE 4.16: Spectra of a NSN junction with PBC along both x and y for $\alpha = 0, V_Z \neq 0$ at $\nu = 1$. (a) Spectrum of the system with pairing $\Delta = 0$. (b) Spectrum of the system with pairing $\Delta \neq 0$. The line color encodes the spin polarization along the direction of the applied magnetic field. The energies are plotted in units of the superconducting gap $\Delta = 0.95$ meV.

In fact, in order to engineer p-wave like superconductivity, it is fundamental to freeze out the spin degree of freedom. In a finite system this can be interpreted in terms of two MZMs appearing at each termination, each arising from one of the two gaps that open (spin-up electrons paired with spin-down holes, and spin-down electrons paired with spin-up holes), or, equivalently, from the double degenereracy of the Hamiltonian eigenstates. These Majoranas are spatially close and not protected by any symmetry, so they are allowed to couple to form a standard fermion with non-zero energy. Notice that a similar scenario occurs for every even filling factor, even in the presence of Rashba and Zeeman interactions.

(ii) $\alpha = 0, V_Z \neq 0$ A different scenario can arise by getting rid of one of the two spin flavours, what can be realized by applying a magnetic field along the x direction that couples with the electronic spin degree of freedom to produce a Zeeman field. This has the effect of spin splitting the bands. Now, if the Fermi level is tuned in such a way that only one spin species conducts (say, spin up) corresponding to filling factor $\nu = 1$, CAR processes are suppressed since there is no available state with spin down for reflected holes to occupy. This is reflected in Fig. 4.16, where the Bogoliubov spectrum of an NSN junction at $\nu = 1$ with and without pairing is shown. When the pairing is turned on (panel (b)), no gap opens.

(iii) $\alpha \neq 0, V_Z \neq 0$ If a degree of spin mixing is introduced in the $\nu = 1$ filling factor as a result of SOC (that in this case we choose to be present only in the superconducting region, case II), the spins of the edge states acquire a component that is orthogonal to their velocity. Since carriers at opposite NS interfaces propagate with opposite velocities, their spins will cant in opposite fashion along the direction perpendicular to their motion, the y axis. As a consequence, CAR processed are allowed since a reflected hole due to the injection of an electron at one interface, with a given canting of the spin polarization, has an available channel to occupy with opposite canting of the spin a the other interface and they can pair to open a gap, as shown in Fig. 4.17. This gap is topological since the system is effectively spinless, and it supports individual Majorana zero modes at its ends, as we will see in the next subsection. Notice furthermore that any other odd filling factor phase endowed with a finite singlet amplitude will always generate one protected pair of spatially separated Majorana zero modes.

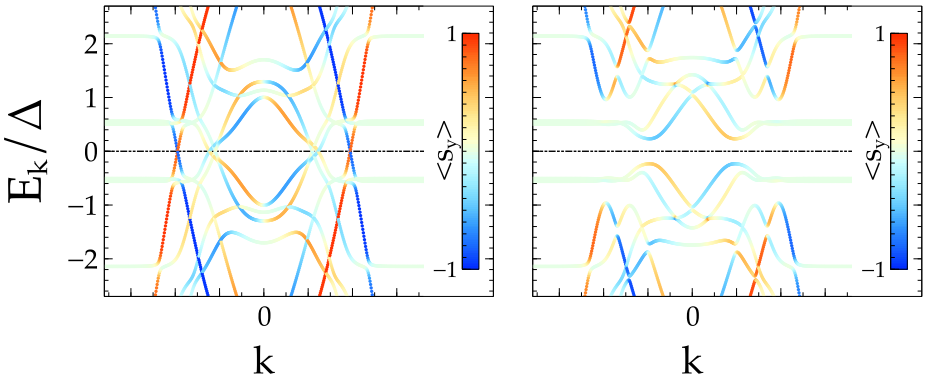

FIGURE 4.17: Spectra of a NSN junction with PBC along both x and y for $\alpha, V_Z \neq 0$ at $\nu = 1$ with Rashba SOC only in the superconducting strip (case II). (a) Spectrum of the system with pairing $\Delta = 0$. (b) Spectrum of the system with pairing $\Delta \neq 0$. The line color encodes the spin polarization along the direction of the spin-orbit field. The energies are plotted in units of the superconducting gap $\Delta = 0.95$ meV.

In Fig. 4.18 we present examples of bands structures (with both $\alpha \neq 0, V_Z \neq 0$) in two different regimes, namely $W_S \ll \xi$ (panels (a) and (c)) and $W_S \gg \xi$ (panels (b) and (d)), where panels (a) and (b) have been calculated for case I (SOC everywhere) whereas panels (c) and (d) for case II (SOC only in the proximitised region). The parameters used for these calculations are: $B = 0.87$ T, $\Delta = 0.95$ meV, $\alpha = 3\ 10^{-13}$ eV m, $V_Z = 0.8$ meV, $\mu = 10$ meV, and $W_S = 190$ nm, $W = 380$ nm (panels (a) and (c)) or $W_S = 1.3$ μm, $W = 1.45$ μm (panels (b) and (d)). As expected, in both cases I and II, the spectrum is gapped in the former regime and gapless in the latter. The only qualitative difference between the two cases is the dispersion of the edge states at the edges of the Brillouin zone.

In Fig. 4.19a we present the induced gap calculated numerically for case I and for $W - W_S = 800$ nm, $B = 0.52$ T, $\Delta = 0.05$ meV, $V_Z = 0.76$ meV, $\mu = 1.9$ meV and $W_S \in [0 : 600]$ nm. Notice that we have used the same ratio $\mu/\Delta \approx 1.95$ as in the analytical result of Fig. 4.14a, replotted in Fig. 4.19b to make the comparison clearer. From these curves, one sees clearly that the analytical and numerical results are in very nice agreement. Notice however that the parameter used in the numerical calculation is μ as opposed to $\tilde{\mu} = \mu - k_x^2/2m$, and consequently also λ_F differs from the $\tilde{\lambda}_F$ employed in the analytical calculation. This explains why the nodes and the maxima of Δ^* are slightly displaced in the numerical results with respect to the analytically predicted curve. In Fig. 4.20 we compare the induced gaps obtained for the same set of parameters in cases I and II. We see that the two curves, as expected, are highly consistent.

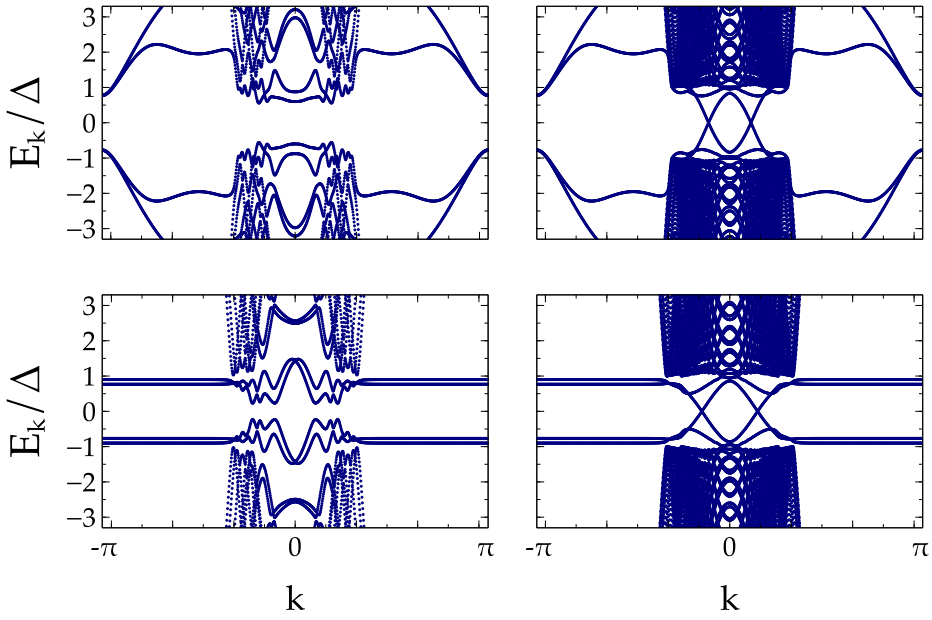

FIGURE 4.18: Spectra of a NSN junction with PBC along both x and y for $\alpha, V_Z \neq 0$ at $\nu = 1$. (a) Regime $W_S \ll \xi$, case I. (b) Regime $W_S \gg \xi$, case I. (c) Regime $W_S \ll \xi$, case II. (d) Regime $W_S \gg \xi$, case II. The energies are plotted in units of the superconducting gap $\Delta = 0.95$ meV.

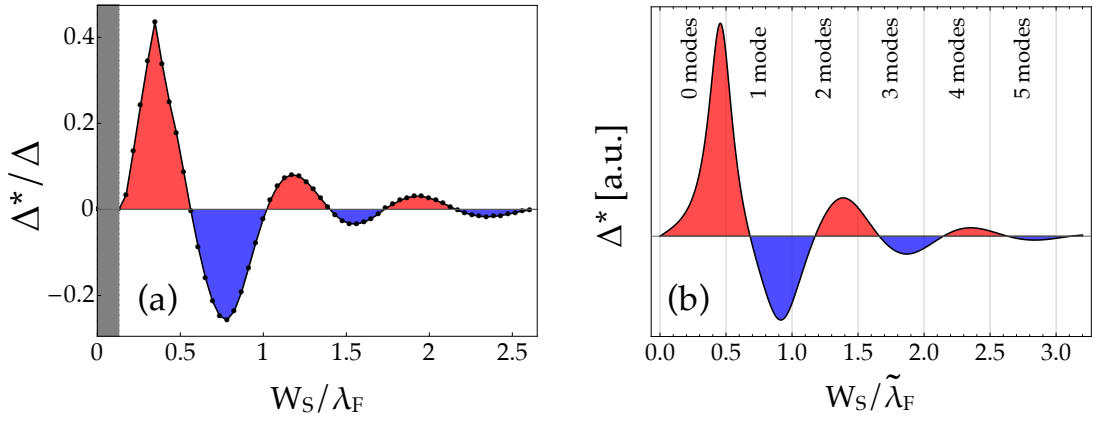

FIGURE 4.19: (a) Induced gap Δ^* in units of the parent gap Δ as a function of W_S/λ_F obtained from tight binding calculations on the lattice. The grey region corresponds to the trivial gap that is connected adiabatically with the nonzero bulk gap of the QH regime opened at $W_S = 0$. (b) Induced gap Δ^* (arbitrary units) as a function of $W_S/\tilde{\lambda}_F$ obtained analytically in section 4.3.

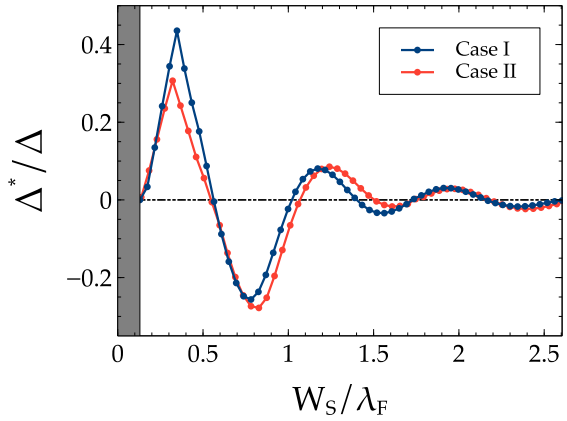

FIGURE 4.20: Comparison of Δ^*/Δ as a function of W_S/λ_F obtained from tight binding calculations on the lattice in case I (blue curve) and case II (red curve). The grey region corresponds to the trivial gap that is connected adiabatically with the nonzero bulk gap of the QH regime opened at $W_S = 0$.

4.4.3 Spectra of finite-size systems

We now proceed to calculate the spectra of finite size systems (with either the whole ribbon being finite or just the superconducting region) in order to confirm that the gaps induced by CAR across the superconducting strip are indeed topological and to explore their end excitations. In particular, we expect that Majorana anyons will appear as zero-energy modes at the terminations of the proximitized region with a topological gap. Notice that all the calculations of this subsection and in the next section are performed for the configuration where the SOC is only inherited by the superconducting region (case II). We will therefore omit this information in what follows. The parameters used in figs. 4.21 and 4.22 are $W_S = 98$ nm, $W = 587$ nm, $B = 0.52$ T, $\Delta = 0.95$, $\alpha = 2.3\ 10^{-13}$ eV m, $V_Z = 0.76$ meV and $\mu = 7.6$ meV. In Fig. 4.21 we consider a ribbon with PBC along both the x and the y directions but such that the proximitised region occupies only half the length of the whole ribbon. It thus has two ends embedded inside the bulk of the 2DEG, where the system is gapped because it is in the QH regime. As a consequence, by calculating the spectrum of the system one finds two zero-energy eigenmodes within the topological gap (panel (a) of Fig. 4.21). Notice that we employ PBC in order to get rid of the external edge states of the 2DEG in the QH regime and obtain a fully gapped spectrum. We calculate the local density of the states (LDOS) at zero energy as

$$N(\mathbf{r}, \epsilon = 0) = \sum_{\psi_\epsilon : \epsilon = 0} |\langle \mathbf{r} | \psi_\epsilon \rangle|^2 \tag{4.62}$$

where ψ_ϵ is the eigenfunction associated to the eigenvalue ϵ. The LDOS at zero energy of a strip with both ends inside the 2DEG is shown in panel b of Fig. 4.21. As expected, two zero energy Majorana modes have localized at the ends of the strip.

In Fig. 4.22 we consider a ribbon with OBC along both the x and the y directions. Again, the proximitized region occupies only half the length of the whole ribbon but it is such that the strip has one end inside de 2DEG (as before), whereas the other end lies close to its boundary Two Majorana modes pinned at zero energy appear at the two ends (see inset of Fig. 4.22a). However, since the 2DEG is now finite, it has chiral edge states propagating at its boundaries. This is clearly discernable in the spectrum of Fig. 4.22a where the topological gap, apart from the two Majoranas localized at zero energy, is now occupied by a continuum of states that cross zero-energy, associated to the dispersing

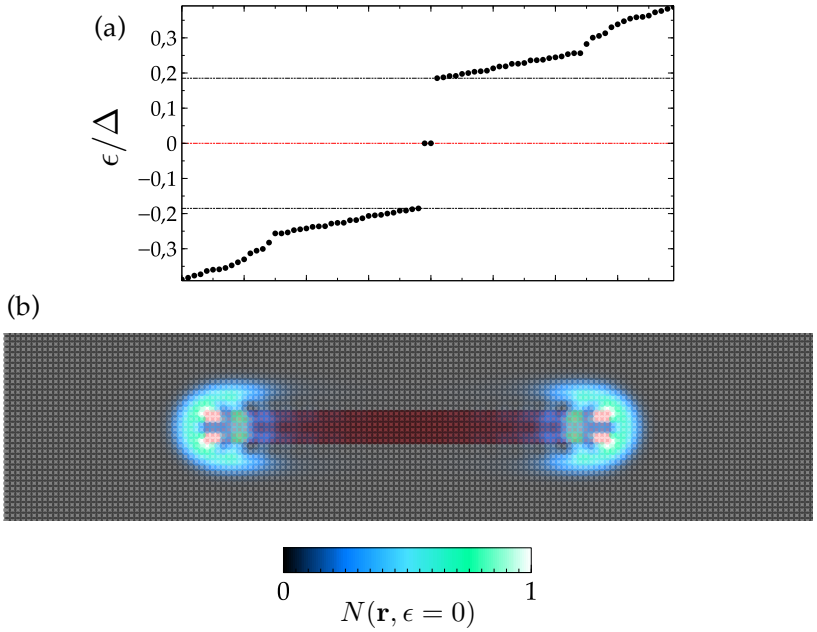

FIGURE 4.21: Ribbon with PBC along both x and y and with a strip that occupies half of the ribbon along the x direction. (a) Eigenvalues (in units of the parent gap Δ) in the low-energy sector of the spectrum. (b) LDOS at zero energy $N(\mathbf{r}, \epsilon = 0)$.

edge states of the QH regime. As a consequence, the Majorana end mode that appears close to the system boundary delocalizes into the continuum away from the end of the strip. The LDOS at zero energy of a system in this configuration is shown in Fig. 4.22b, where it appears clearly that while one Majorana is perfectly localized at one end as before, the other has now delocalized into the continuum.

4.4.4 Topological π junctions

The most strinking feature of the behaviour of the induced gap Δ^*, first derived analitically in subsection 4.3.4 and then calculated numerically with tight binding simulations on a square lattice, is its periodic sign change as a function of the number of transverse modes that enter the strip. As shown above, the number of transverse modes can be controlled either through the chemical potential of the contacted region or through the width W_S of the superconducting strip. Modulating the chemical potential of hybrid semiconductor-superconductor structures has been shown to be feasible in several recent experiments [51,235]. Moreover, apart from litographically, the effective width of the strip can also be tuned electrostatically, since a strong and positive gate potential, even if largely screened by the superconductor, would deplete the electrons at either side of the strip, thus reducing the effective value of W_S.

The possibility of controlling the sign of the gap by tuning these external parameters opens an interesting scenario. Indeed, being able to abruptly change either of them across the strip, one can effectively generate a domain wall where the sign of the induced gap at the two interfacing halves is opposite. This kind of set-up is a realization of an unconventional topological π junction. We recall that Josephson junctions, either topological or not, are usually engineered by threading a superconducting ring with a magnetic flux Φ [276]. By separating two sides of the ring by a thin insulating barrier, the superconducting order parameter at the two opposing edges of the junction develops a phase

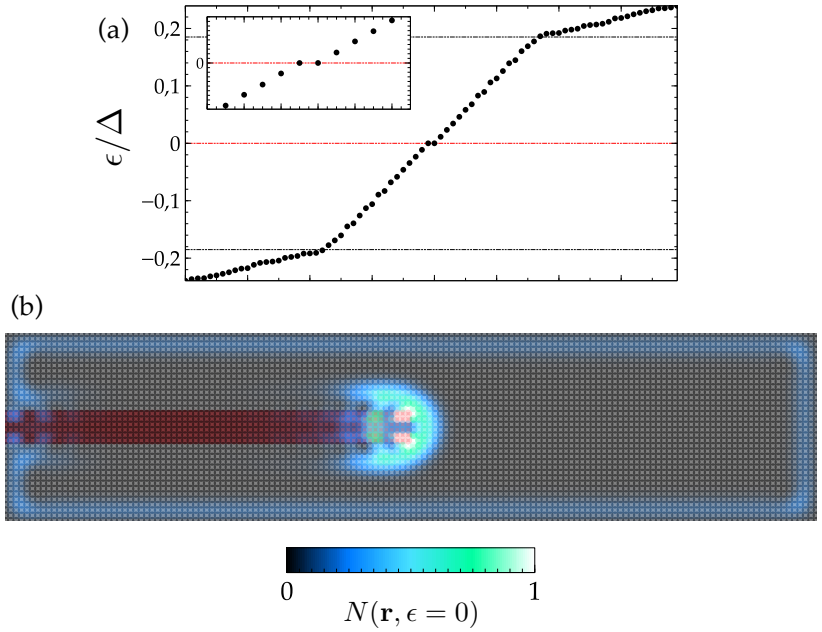

FIGURE 4.22: Ribbon with OBC along both x and y and with a strip that occupies half of the ribbon along the x direction. (a) Eigenvalues (in units of the parent gap Δ) in the low-energy sector of the spectrum. In the inset we zoom on the eigenvalues closer to zero energy. (b) LDOS at zero energy $N(\mathbf{r}, \epsilon = 0)$.

difference of $\phi = \Phi/\Phi_0$, with $\Phi_0 = h/2e$ being the superconducting flux quantum. If the applied magnetic field is then tuned to a value such that $\Phi = \pi\Phi_0/2$, a so-called π junction is generated where if the pairing is equal to Δ at one side of the junction, at the other it is given by $\Delta e^{i\pi} = -\Delta$. However, to generate this kind of junction following the conventional approach, the magnetic flux through the ring needs to be finely tuned. Any deviation from this finely tuned value would result in a complex phase of the pairing gap at either side of the strip that cannot be gauged away. A π junction is especially interesting if the gap Δ is topological, since in this case two Majorana zero modes that do not split despite their spatial overlap localize at the junction [213,214]. To confirm that this is indeed the case in the unconventional kind of π junction propsed here, in Fig. 4.23 we consider a ribbon with PBC along both the x and y directions, with a superconducting strip that covers the overall length of the ribbon along the x direction, and has PBC as well. The parameters employed are: $W_S = 163$ nm, $W = 652$ nm, $B = 0.52$ T, $\Delta = 0.95$ meV, $\alpha = 2.3\ 10^{-13}$ eV m and $V_Z = 0.76$ meV. We then consider two cases: one in which the chemical potential (and therefore the ratio W_S/λ_F, our control parameter) is uniform throughout the whole strip ($\mu = 17$ meV), and another where it varies discontinuously across the strip ($\mu_1 = 17$ meV and $\mu_2 = 12$ meV). In the former case the induced gap has uniform sign, whereas in the latter the control parameter W_S/λ_F of half of the strip is such that the induced gap Δ_1^* if finite and positive whereas in the other it is such that the induced gap Δ_2^* is finite and negative. Notice that because of PBC, two separate topological π junctions are generated in this configuration. In Fig. 4.23a we compare the spectra of these two systems, where we see that in the former case the system is fully gapped because of the PBC applied along the x direction (even though the gap is topological, no zero modes arise since the ribbon has no edges), whereas in the latter four Majorana zero modes appear at zero energy, two at each junction. We then show the LDOS at zero energy for this case in Fig. 4.23b, where it is easy two see that these zero modes are localized

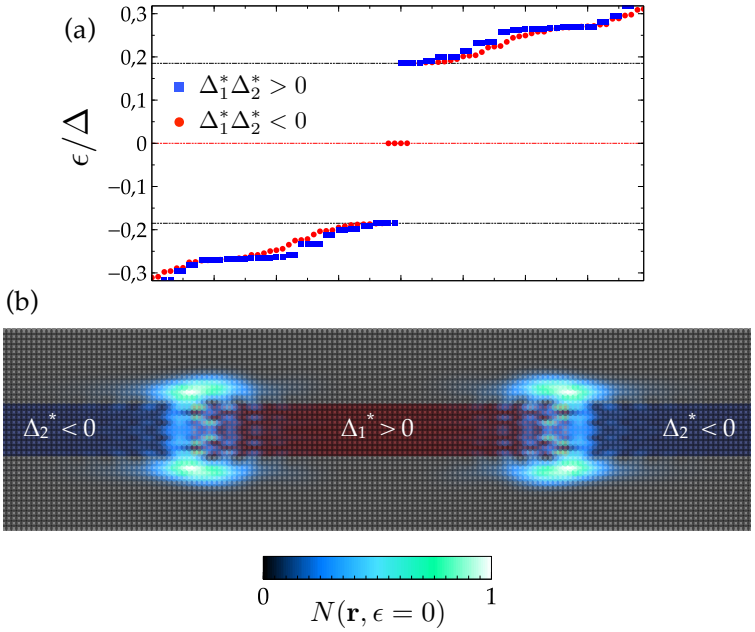

FIGURE 4.23: Ribbon with PBC along both x and y and with the strip occupying the whole ribbon length along x. The strip is divided in two halves whose induced gaps Δ_1^* and Δ_2^* can be tuned independently. (a) Comparison of the eigenvalues (in units of the parent gap Δ) in the low-energy sector of the spectrum for the two cases $\Delta_1^*\Delta_2^* > 0$ (blue squares) and $\Delta_1^*\Delta_2^* < 0$ (red circles). (b) LDOS at zero energy $N(\mathbf{r}, \epsilon = 0)$ for the case $\Delta_1^*\Delta_2^* < 0$.

at the two domain walls between induced gaps with opposite signs.

4.4.5 Stability of CAR-induced topological π junctions

Now that the possibility of enigineering a topological π junction through CAR-induced pairing is established, it seems reasonable to ask oneself whether this configuration is a stable solution for the system. To do so, we allow for variations in the phase difference ϕ of the parent superconducting gap at the junction and check that the Josephson free energy as a function of phase difference ϕ has indeed a stable minimum at $\phi = \pi$. Bardeen et al. [277] and Beenakker and van Houten [278] demonstrated, using complementary approaches, that the free energy of a generic Josephson junction may be written, at fnite temperature T and up to a phase-independent constant, as

$$E_J(\phi) = -k_B T \sum_{\epsilon<0} \ln\left(2\cosh\frac{\epsilon(\phi)}{2k_B T}\right) \tag{4.63}$$

Notice that the sum is performed over both spin flavours and over both particle- and hole-like levels. In the low temperature limit $E_J(\phi)$ reduces to

$$\lim_{T\to 0} E_J(\phi) = -\frac{1}{2}\sum_{\epsilon<0}\epsilon(\phi) \tag{4.64}$$

We employ the same configuration as the one considered in the previous subsection, where the system has PBC along both directions and the proximitised region is split in two halves with independently controllable W_S/λ_F ratios such that two different gaps Δ_1^* and Δ_2^* are induced in the two portions. We define $\phi^* = \phi - \mathrm{Arg}(\Delta_1^*/\Delta_2^*)$ as the total

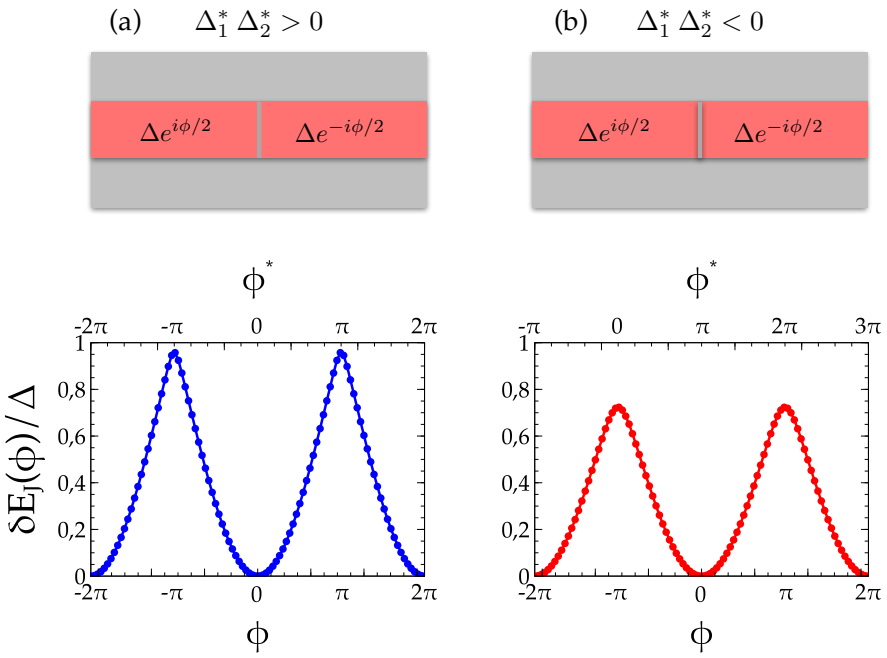

FIGURE 4.24: Study of the stability of two different Josephson junctions, one where the two facing superconducting strips have induced gaps of the same sign ($\Delta_1^*\Delta_2^* > 0$, panel (a)) and one where they have induced gaps of opposite signs ($\Delta_1^*\Delta_2^* < 0$, panel (b)). The bottom row of both panels show the Josephson free energy $\delta E_J(\phi)/\Delta$ as a function of the phase difference ϕ in the parent superconductor and of the overall phase difference calculated as $\phi^* = \phi - \mathrm{Arg}(\Delta_1^*/\Delta_2^*)$ in the two configurations described above. The minimum of the free energy shows that the junctions are thermodynamically stable at $\phi^* = 0$ and $\phi^* = \pi$ respectively.

phase difference at each junction (we recall that there are two junctions because of PBC) that takes into account both the phase difference developed as a consequence of CAR processes ($\mathrm{Arg}(\Delta_1^*/\Delta_2^*)$) and the one deriving from changes in the phase of the parent gap (ϕ). We consider the two different scenarios already studied before, namely $\Delta_1^*\Delta_2^* > 0$ and $\Delta_1^*\Delta_2^* < 0$, and calculate the variation in Josephson free energy $\delta E_J(\phi) = E_J(\phi) - E_J(0)$ in units of Δ as a function of both ϕ and ϕ^*.

The result of this calculation is plotted in Fig. 4.24 where the panel a represents the former case and the panel b the latter. Remarkably, in both cases the minimum of the Josephson free energy is found at $\phi = 0$, corresponding to an overall phase $\phi^* = 0$ and $\phi^* = \pi$ respectively. It is interesting to notice that the range of variation of $\delta E_J(\phi)/\Delta$ is of unity in the former case, indicating that the phase rigidity of the junction is entirely controlled by the order parameter of the parent superconductor, whereas in the latter it is smaller, indicating that there is a competition between the phase rigidities of the parent gap and of the CAR-induced gap. The fact that the minimum of the energy is found in $\phi = 0$ in this case is a strong indication that the phase rigidity of the parent gap is larger with respect to that of the induced gap, and as a consequence fluctuations in the former do not affect the stability of the latter. Rephrasing it, for the system it is energetically more convenient to support a phase difference of π in the induced gap than to generate an equal phase in the parent gap that compensates the former to induce a zero overall phase difference at the junction. We deduce that, in the case where $\Delta_1^*\Delta_2^* < 0$, the $\phi^* = \mathrm{Arg}(\Delta_1^*/\Delta_2^*) = \pi$ configuration is thermodynamically stable.

4.5 Tunnel-Braid operations

As we have seen in section 4.2, the great limitation of braiding in two dimensions is its inability to exhaust the universal set of operations needed for quantum computation. A number of methods have been proposed to bypass this problem, but they mostly rest on supplementing the protected gates supplied by braiding with non-protected operations that involve merging Majoranas [226] or combining topological and conventional qubits [229,231,232]. While these operations exhibit extraordinary high error thresholds, it would nonethless be ideal to generate all the quantum gate operations needed for universal computation in a protected fashion. Another route that is being actively pursued is that of topological quantum error-correcting codes [279].

In a letter from 2011 [92], Flensberg proposed an alternative route to achieve effective rotations of the Majorana wavefunction in the ground state manifold with no need for real space exchange of the anyons. These so-called *tunnel-braid* operations are based on the exchange of electrons between a quantum dot and a set of MZMs. There are, however, a number of drawbacks that make them sensitive to small fluctuations in some of the system parameters.

In this section, we review the idea of tunnel-braid operations as originally presented by Flensberg. We will then put forward an alternative implementation of the tunnel-braiding scheme performed on a platform based on CAR-induced unconventional topological π junctions, where we show that the most severe limitation of the original set-up can be overcome.

4.5.1 Conventional topological π junctions

In essence, the idea of tunnel-braid operations is based on the adiabatical exchange of electrons between a quantum dot and a set of Majorana zero modes. When the dot is in the Coulomb blockade regime, the electrons create strong repulsions preventing other electrons to flow, such that only a single, spin-polarized quantum state is available and the number of electrons is bound to fluctuate between N and $N+1$. If n MZMs are coupled to the dot, the dot-Majoranas Hamiltonian can be written as

$$H = H_D + H_t \tag{4.65}$$

where

$$H_D = \varepsilon c^\dagger c \tag{4.66}$$

is the isolated dot Hamiltonian, and

$$H_t = \sum_i^n \left(v_i c \gamma_i + \text{H. c.}\right) = \sum_i^n \left(v_i c \gamma_i + v_i^* \gamma_i c^\dagger\right) = \sum_i^n \left(v_i c - v_i^* c^\dagger\right) \gamma_i \tag{4.67}$$

In the previous expressions, $c^\dagger$ and c are the dot creation and annihilation operators, v_i is the tunneling amplitude from the dot to the i-th MZM and viceversa, γ_i is the Majorana operator such that $\gamma_i = \gamma_i^\dagger$ and $\gamma_i^2 = 1$ and ϵ is the dot energy measured relative to the chemical potential in the superconductor.

Coupling to a single Majorana When the dot is coupled to a single Majorana, that we label γ_1, the total Hamiltonian of the system is simply

$$H = \varepsilon c^\dagger c + \left(v_1 c - v_1^* c^\dagger\right) \gamma_1 \tag{4.68}$$

However, since Majoranas always come in pairs, a second Majorana γ_2 exists (see Fig. 4.25a) that, together with γ_1, defines a fermionic operator

$$d = \frac{1}{2}(\gamma_1 + i\gamma_2) \qquad d^\dagger = \frac{1}{2}(\gamma_1 - i\gamma_2) \tag{4.69}$$

such that $\gamma_1 = d + d^\dagger$ and $\gamma_2 = -i(d - d^\dagger)$. Therefore, we can rewrite

$$H = \varepsilon c^\dagger c + \left(v_1 c - v_1^* c^\dagger\right)\left(d + d^\dagger\right) \tag{4.70}$$

The Hilbert space of the dot-Majoranas system is given by the tensor product of the quantum states of the dot (D) and the d fermion: $|\psi\rangle = |i\rangle_D \otimes |j\rangle_d$, and the basis of such space is

$$\{|0\rangle_D \otimes |0\rangle_d, |0\rangle_D \otimes |1\rangle_d, |1\rangle_D \otimes |0\rangle_d, |1\rangle_D \otimes |1\rangle_d\} \tag{4.71}$$

where the 0 or 1 denotes respectively an empty or full fermionic state. The states $|0\rangle_D \otimes |0\rangle_d$ and $|1\rangle_D \otimes |1\rangle_d$ have even fermion parity, whereas the states $|0\rangle_D \otimes |1\rangle_d$ and $|1\rangle_D \otimes |0\rangle_d$ have odd fermion parity. Since parity is conserved by H, the Hamiltonian is block-diagonal in the basis of even and odd parity states, with the even and odd blocks H_e and H_o having the same form

$$H_e = H_o = \begin{pmatrix} 0 & v_1 \\ v_1^* & \varepsilon \end{pmatrix} \tag{4.72}$$

We now introduce an operation P that evolves ϵ/t from $-\infty$ to $+\infty$ adiabatically (the charging energy is assumed even larger than this range, so that double dot occupancy is never reached) . We assume that the dot is initially full, that is, in the state $|1\rangle_D$, and that the system of the two Majoranas is the state $|i\rangle_d = \alpha|0\rangle_d + \beta|1\rangle_d$. While the operation P_1 is performed, the dot state passes from full to empty, and its evolution with ϵ/t can be expressed as

$$|\psi\rangle(\varepsilon) = a(\varepsilon)|1\rangle_D \otimes (\alpha|0\rangle_d + \beta|1\rangle_d) + b(\varepsilon)|0\rangle_D \otimes (\alpha|1\rangle_d + \beta|0\rangle_d)$$

where the evolution is such that $a(\varepsilon) = 1, b(\varepsilon) = 0$ for $\varepsilon/t \to -\infty$ and $a(\varepsilon) = 0, b(\varepsilon) = 1$ for $\varepsilon/v_1 \to +\infty$. Except for these two limiting states, the system is entangled during the whole operation, and its overall energy is

$$E = \frac{\varepsilon}{2} - \sqrt{\frac{\varepsilon}{2} + |v_1|^2} \tag{4.73}$$

This operation has the effect of adding the electron to the Majorana system, thus changing its parity (such that the component that was in the state $|0\rangle_d$ with probability amplitude α evolves to the state of opposite parity $|1\rangle_d$ with the same probability amplitude, and the same happens for $|1\rangle_d$ that transforms to $|0\rangle_d$ with probability amplitude β), see Fig. 4.25a. This inversion of occupation of the Majorana system is described by the operator γ_1, in fact

$$\gamma_1(\alpha|0\rangle_d + \beta|1\rangle_d) = (d + d^\dagger)(\alpha|0\rangle_d + \beta|1\rangle_d) = \alpha d^\dagger|0\rangle_d + \beta d|1\rangle_d = \alpha|1\rangle_d + \beta|0\rangle_d \tag{4.74}$$

that is, formally:

$$P_1 : |i\rangle_d \to \gamma_1|i\rangle_d \tag{4.75}$$

If the dot is connected to a number of Majorana modes $\{\gamma_1, \gamma_2, ..., \gamma_m\}$, upon performing consequent operations $P_1, P_2, ..., P_m$, the Majorana state $|i\rangle$ is acted upon by the sequence

of operators $\gamma_1\gamma_2...\gamma_m$:

$$P_1P_2...P_m : |i\rangle_d \rightarrow \gamma_1\gamma_2...\gamma_m|i\rangle_d \tag{4.76}$$

implying that the repeated application of tunnel operations that empty or fill by one electron the dot rotates the wavefunction in the degeneracy manifold of the ground states. However, owing to the anticommutation relation $\{\gamma_i, \gamma_j\} = 2\delta_{ij}$ satisfied by the Majorana operators, the set of possible operations that can be performed this way is limited.

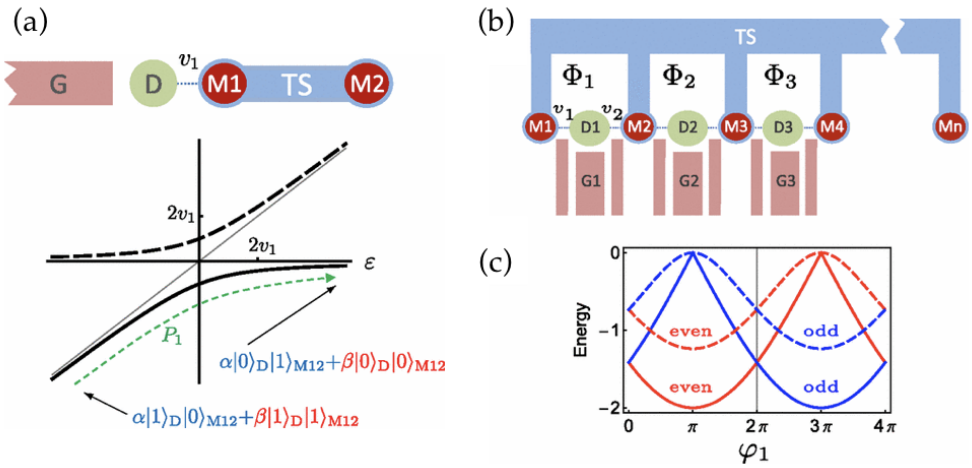

FIGURE 4.25: (a) Top: scheme of a single Majorana (M1) coupled to a quantum dot (D). Bottom: evolution of the energy spectrum of the system as the parameter ε/v_1 is varied adiabatically from $-\infty$ to $+\infty$, corresponding to the operation P_1 defined in the main text. This operation empties the dot while inverting the parity of the Majorana system so that the total parity of the system remains unchanged. The subscript M12 is the equivalent of the subscript d employed in the main text. (b) Top: scheme of multiple MZMs coupled to a number of quantum dots. Bottom: Total energy of even and odd parity sectors of a quantum dot coupled to two Majoranas as the phase between the two is swept from 0 to 4π. [Adapted with permission from Ref. [92]]

Coupling to two Majoranas A different scenario arises when the dot is coupled simultaneously to two Majoranas γ_1 and γ_2 (see Fig. 4.25b) that form a fermion such that $\gamma_1 = d + d^\dagger$ and $\gamma_2 = -i(d - d^\dagger)$. The total Hamiltonian of the system in this case is

$$H = \varepsilon c^\dagger c + \left(v_1 c - v_1^* c^\dagger\right)\gamma_1 + \left(v_2 c - v_2^* c^\dagger\right)\gamma_2 =$$

$$\varepsilon c^\dagger c + (v_1 - iv_2)cd - (v_1^* - iv_2^*)c^\dagger d + (v_1 + iv_2)cd^\dagger - (v_1^* + iv_2^*)c^\dagger d^\dagger$$

that, by defining $v_e = v_1 - iv_2$ and $v_o = v_1 + iv_2$, can be rewritten as

$$H = \varepsilon c^\dagger c + v_e cd - v_o^* c^\dagger d + v_o cd^\dagger - v_e^* c^\dagger d^\dagger \tag{4.77}$$

The operators cd and $c^\dagger d^\dagger$ act on the even parity sector (hence the subscript e) and the operators $c^\dagger d$ and $cd^\dagger$ act on the odd parity sector (hence the subscript o), so that the total Hamiltonian has again a block form but now the even and odd parity sectors differ in the tunneling amplitudes:

$$H_{e/o} = \begin{pmatrix} 0 & v_{e/o} \\ v_{e/o}^* & \varepsilon \end{pmatrix} \tag{4.78}$$

The energies associated to the even and odd parity sectors of the system are now different:

$$E_{e/o} = \frac{\varepsilon}{2} - \sqrt{\frac{\varepsilon}{2} + |v_{e/o}|^2} = \frac{\varepsilon}{2} - \sqrt{\frac{\varepsilon}{2} + |v_1|^2 + |v_2|^2 \mp 2|v_1||v_2|\sin(\varphi_1/2)} \tag{4.79}$$

where $\varphi_1 = 2(\phi_1 - \phi_2)$ and $v_1 = |v_1|e^{i\phi_1}$, $v_2 = |v_2|e^{i\phi_2}$. It is straightforward to see that these two energies are different unless $\varphi_1 = 2n\pi$ as also shown in Fig. 4.25c, that is, for fine-tuned values of the phase difference between the tunneling amplitudes. These may be adjusted by means of a magnetic flux Φ that threads the superconducting loop at whose ends the Majoranas γ_1 and γ_2 reside, such that $\Phi_1/\Phi_0 = \varphi_1$ (see Fig. 4.25b). This energy difference for generic values of the phase difference between the Majoranas implies that the minimal duration of the adiabatic process that removes (or add) an electron from (to) the dot is limited by the inverse of the energy difference between the even and odd sectors. Only at the degeneracy points $\varphi_1 = 2n\pi$ this operation is topologically protected, but this protection is weak since the magnetic flux needs to be finely tuned. At $\varphi_1 = 2n\pi$, $\sin(\varphi_1/2) = 0$, and therefore

$$E_e = E_o = \frac{\varepsilon}{2} - \sqrt{\frac{\varepsilon}{2} + |v_1|^2 + |v_2|^2} = \frac{\varepsilon}{2} - \sqrt{\frac{\varepsilon}{2} + |v|^2} \tag{4.80}$$

with $|v|^2 = |v_1|^2 + |v_2|^2$ and the Hamiltonian can be rewritten as

$$H = \varepsilon c^\dagger c + \left(v_1 c - v_1^* c^\dagger\right)\gamma_1 + \left(v_2 c - v_2^* c^\dagger\right)\gamma_2 = \varepsilon c^\dagger c + \left(vc - v^* c^\dagger\right)\frac{|v_1|\gamma_1 + |v_2|\gamma_2}{|v|}$$

where $v = |v|e^{i\phi_1}$. Therefore, the case of a dot connected to two MZMs simultaneously at the degeneracy point is described by an Hamiltonian that has the same structure of the case of a dot connected to a single MZM. By analogy, application of an adiabatic operation P_{12} that empties the dot by one electron, has the effect of applying the operator

$$\gamma_{12} = \frac{|v_1|\gamma_1 + |v_2|\gamma_2}{|v|} = u_1\gamma_1 + u_2\gamma_2$$

with $u_1 = |v_1|/|v|$ $u_2 = |v_2|/|v|$, to the initial state $|i\rangle$ of the Majorana system:

$$P_{12}|i\rangle : |i\rangle \rightarrow \gamma_{12}|i\rangle \tag{4.81}$$

As before, we ask ourselves which rotations are realized by one or more successive applications of the P_{12} operation in the Bloch sphere where the possible quantum states of the topological qubit realized by the Majoranas live. We define a set of Pauli matrices acting on the two levels space spanned by the two Majoranas γ_1 and γ_2: $\sigma_x = \gamma_1$, that realizes a rotation of π about the x axis, $\sigma_y = \gamma_2$, that realizes a rotation of π about the y axis, and $\sigma_z = -i\gamma_1\gamma_2$ that realizes a rotation of π about the z axis. With this choice, the operation P_{12} realizes a rotation by π around the axis $u_1\hat{x} + u_2\hat{y}$ in the xy plane (see Fig. 4.26a). As a consequence, upon varying the ratio u_1/u_2 it is possible to tune the axis around which the rotation occurs. Upon applying the operator P_{12} twice, i. e. first emptying the dot ($N+1 \rightarrow N$ operation) and then refilling it ($N \rightarrow N+1$ operation), and varying the coupling strengths between the two operations, one gets

$$P'_{12}P_{12} = (u'_1\gamma_1 + u'_2\gamma_2)(u_1\gamma_1 + u_2\gamma_2) = u'_1u_1 + u'_2u_2 + i(u'_1u_2 - u_1u'_2)\sigma_z$$

thus obtaining a rotation about the z axis by an arbitrary angle determined by the tunneling amplitudes employed (see Fig. 4.26a). In contrast, we recall that the standard braiding that is performed in real space by physically moving two Majoranas only rotates the ground state around the z axis by a fixed angle of $\pi/2$ (see Fig. 4.5 for comparison).

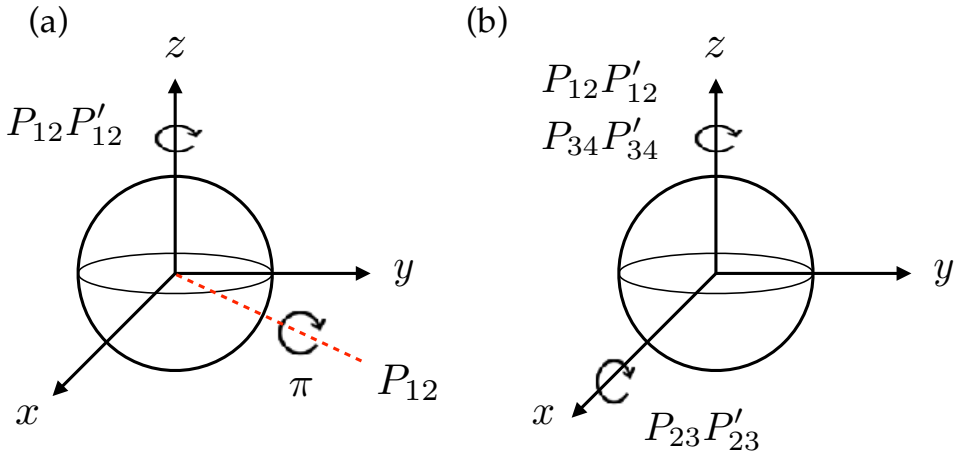

FIGURE 4.26: Illustrative sketch of the operations implemented on the Bloch sphere by applying the operations P and PP' between a quantum dot in the Coulomb blockade regime and a system of (a) two MZMs, (b) four MZMs.

Coupling to four Majoranas Even more strikingly, it is possible to generate a universal set of single-qubit operations by connecting the dot to four Majorana states $\gamma_1, \gamma_2, \gamma_3$ and γ_4 that combine to generate two standard fermions $d_1 = (\gamma_1 + i\gamma_2)/2$ and $d_2 = (\gamma_3 + i\gamma_4)/2$, and stick to the even parity sector spanned by $|0\rangle_{12} \otimes |0\rangle_{34}$ and $|1\rangle_{12} \otimes |1\rangle_{34}$. This space defines a qubit, and pairs of successive P operations such as those defined in Eq. (4.81) can be shown to allow universal single-qubit operations. In fact, while the operators $P'_{12}P_{12}$ and $P'_{34}P_{34}$ (acting on Majorana pairs that belong to the same composite fermion) perform a rotation about z by an arbitrary angle as in the two Majoranas case, the operator $P'_{23}P_{23}$ that act on Majoranas belonging to two different composite fermions performs a rotation by an arbitrary angle about the x axis (see Fig. 4.26b). Again, a comparison with braiding of four MZMs reveals that tunnel-braid operations extend the range accessed by the former, that only allows for rotations by $\pi/2$ (see Fig. 4.5 for comparison).

While this result is quite nice and extends the range of possible operations performed by braiding sets of Majorana zero modes, it is in order to notice that the tunnel-braid operations are sensitive to electrical noise on the tunneling amplitudes and, most importantly, that they are strictly protected only for a fine-tuned phase difference between the involved Majoranas. The first complication renders quite challenging the possibility of designing with precision the wavefunction rotations that one wants to perform, because small errors may make the system end up in a different state with respect to the targeted one. The second one is even more insidious as any small deviation from the finely tuned values of $\varphi = 2\pi n$ hinders the completion of time-independent protected operations as would be desirable.

4.5.2 CAR-induced topological π junctions

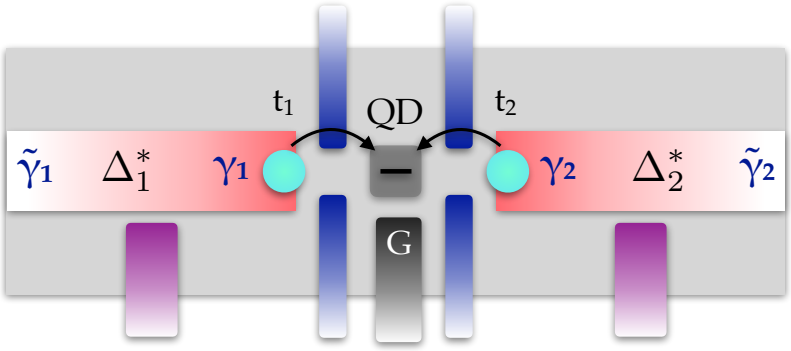

FIGURE 4.27: Sketch of a tunnel-braiding operation performed in our set-up, with the two inner MZMs γ_1 and γ_2 from strips 1 and 2 coupled to a dot (QD) in the Coulomb blockade regime through tunnel barriers. The dot occupancy is controlled by a gate (G), which shifts the dot level ε_D.

We now demonstrate the improved stability of the tunnel-braid operations that can be performed in a platform that involves CAR-induced Majorana zero modes. We employ a set-up like the one shown in Fig. 4.27, where a 2DEG is contacted with two separate superconducting strips (red regions in the figure) whose ratios W_S/λ_F can be independently controlled by means of two independent gates (purple regions in the figure). Specifically, in this subsection we will employ the Fermi energy of the superconducting regions as the control parameter. This gives rise, in turn, to two independent topological gaps Δ_1^* and Δ_2^* with tunable magnitudes and signs. One end of each strip terminates inside the 2DEG, so that the corresponding MZMs γ_1 and γ_2 lie within a finite distance from each other, and both coupled to a common quantum dot. The MZMs $\tilde{\gamma}_1$ and $\tilde{\gamma}_2$ generated at the other two ends of the strips are assumed sufficiently far from the junction so as to become decoupled from γ_1 and γ_2. We will thus disregard them in the following as they do not play any role. If the two strips are completely decoupled by a very high barrier, then the two 'inner' Majorana modes γ_1 and γ_2 do not overlap. However, they can be coupled through the quantum dot upon independently tuning the energy barriers that separate them (dark blue regions in the figure). Now, as exemplified in the previous subsection, if the dot is in the Coulomb blockade regime, one can adiabatically sweep its energy through a gate (in dark grey in the figure) ε_D from $-\infty$ to $+\infty$ in order to change its occupation by one electron (P operation). If the available dot level is initially full, this operation has the effect of transferring the electron to the Majoarana system of γ_1 and γ_2, thus changing its parity. We perform this operation in two configurations, namely one where $\Delta_1^*\Delta_2^* > 0$ and one where $\Delta_1^*\Delta_2^* < 0$. The parameters used for this calculation are: $W_S = 115$ nm, $W = 575$ nm, $B = 0.4$ T, $\Delta = 0.95$ meV, $\alpha = 1.25\ 10^{-13}$ eV m, $V_Z = 0.95$ meV and $\mu_1 = 9$ meV, $\mu_2 = 4.2$ meV. The resulting Bogoliubov spectrum of the coupled dot-Majoranas system is shown in Fig. 4.28a where we indicate the Majorana-like energy levels with solid lines and the dot-like levels with dashed lines. We see that in the case where the gaps have the same sign (blue curves), the energies of the two Majoranas split when they become resonant with the dot. This has the consequence of rendering the P operation time-dependent, as explained in the previous subsection. By contrast, when they have opposite signs (red curves), their energies stay pinned in zero throughout the whole operation. The operation of emptying the dot is then independent of timing and insensitive to noise in the dot energy ε_D. If we now fix the dot energy to be $\varepsilon_D = 0$ (that is,

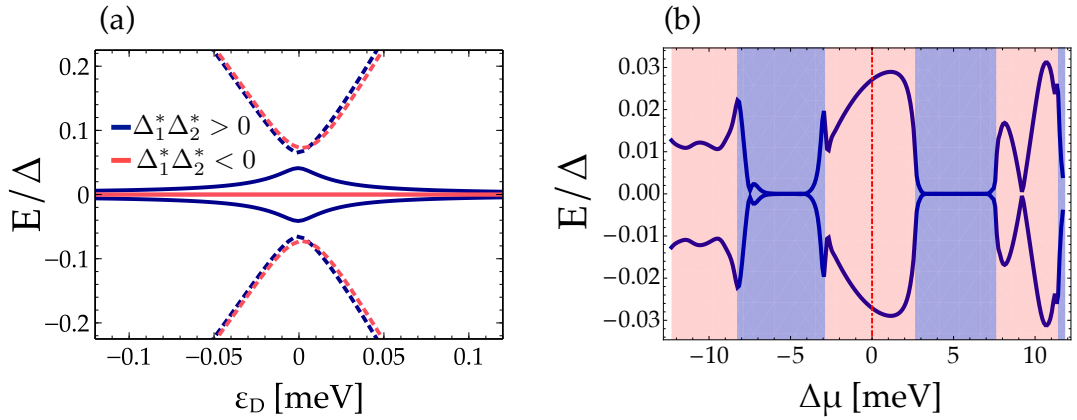

FIGURE 4.28: (a) Comparison of the low energy spectra of the composite system for gaps $\Delta_{1,2}^*$ in the two strips of equal (blue) and opposite (red) sign. The dotted and solid lines correspond predominantly to dot and Majorana states, respectively. (b) Energy of the MZMs as they hybridize through the dot as a function of the changing chemical potential between the left and right strips $\Delta\mu = \mu_1 - \mu_2$, for $\mu_2 = 4.2$ meV and $\varepsilon_D = 0$ fixed. The blue regions indicate phases where $\Delta_{1,2}^*$ have opposite sign, and $\gamma_{1,2}$ do not hybridise through the dot.

the energy at which the composite dot-Majoranas system is resonant) and the Fermi level of one of the two proximitized regions while continuously varying the Fermi level of the other, we obtain the spectrum of Fig. 4.28b. This spectrum represent the energies of the two Majoranas as the chemical potential is varied through gating while that of the other stay fixed. The control parameter is thus the chemical potential difference $\Delta\mu = \mu_1 - \mu_2$ between the two. While the gate voltage is swept, the induced gap of the associated strip oscillates periodically between positive and negative values, while closing in between. This is reflected in the alternation of the red and blue shaded regions in Fig. 4.28b, corresponding respectively to regions where $\Delta_1^*\Delta_2^* > 0$ and $\Delta_1^*\Delta_2^* < 0$. At the boundaries between these regions, the curves exhibit a cusp because of the gap closures. This curve is reminescent of the one plotted in Fig. 4.25b where the control parameter was the phase difference φ between the tunneling couplings t_1 and t_2 between the Majoranas and the dot. As is clear from comparing these curves, the regions where the Majoranas have energies pinned to zero are finite in the control parameter $\Delta\mu$ in the present case, whereas in Flensberg's set-up they are degenerate only for finely tuned values of the control parameter satisfying $\varphi = 2\pi n$.

Finally, we put forward a protocol for performing a universal set of single qubit operations, relying on the coupling of the dot with four Majorana zero modes $\gamma_1, \gamma_2, \gamma_3$ and γ_4 generated at the edges of four superconducting strips. These Majoranas combine to give rise to two conventional fermions d_1 and d_2. The strips parameters are adjusted in such a way that two of them have a positive CAR-induced gap (Δ_2^* and Δ_4^*, depicted as red strips in Fig. 4.29) and the remaining two have negative induced gaps (Δ_1^* and Δ_3^*, depicted as blue strips in Fig. 4.29). In this way, by transferring an electron from the dot to two Majoranas belonging to the same fermion ($\gamma_{1,2}$, corresponding to $t_{3,4} = 0$ and $\gamma_{3,4}$, corresponding to $t_{1,2} = 0$) and viceversa (which amounts to performing two successive P operations) a rotation by an arbitrary angle controlled by either $t_{1,2}$ or $t_{3,4}$ about the z axis is performed, much alike the case of having a dot coupled to only two Majoranas. However, if one couples Majoranas from two different fermions ($\gamma_{2,3}$, corresponding to $t_{1,4} = 0$ and $\gamma_{1,4}$, corresponding to $t_{2,3} = 0$) and viceversa, a rotation by an arbitrary angle about the x axis is achieved. Both these operations (between Majoranas from the same

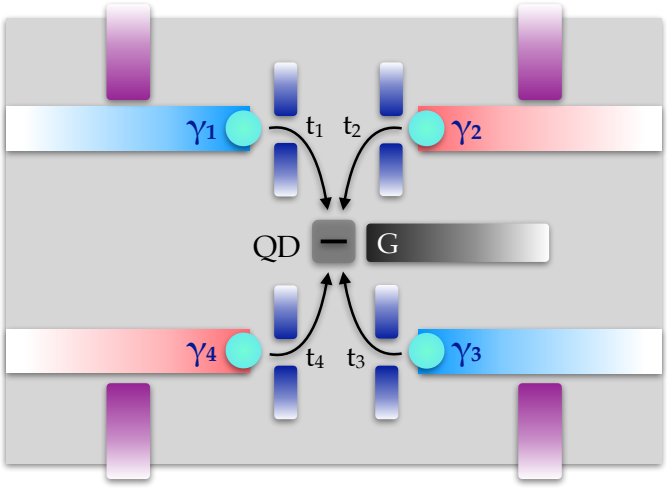

FIGURE 4.29: Sketch of the set-up ideal for performing tunnel-braid operations between four Majorana modes and one quantum dot. Transferring an electron from the dot to two Majoranas and viceversa allows to explore the whole Hilbert space of states defined on the Bloch sphere.

fermion or from different fermions) are topologically protected since they always involve zero modes hosted by strips with opposite CAR-induced gaps. Therefore, by combining this kind of operations with variable tunneling amplitudes one is allowed to explore the whole Hilbert space, thus obtaining a universal set of protected and time-independent single-qubit operations.

4.6 Conclusions

Wrapping up, we have presented a scheme towards one-dimensional topological superconductivity that extends previous approaches based on the proximity effect of spinless helical electronic phases coupled to superconductors [154,213,214]. While such approaches produce a topological order parameter, its phase is fixed by that of the parent superconductor. By contrast, schemes that rest on crossed Andreev reflection processes, relevant in geometries as those discussed here, produce a topological order parameter with a sign that may be either the same as or opposite to that of the parent one, depending on the CAR amplitude itself. We note that a closely related class of systems where a similar phenomenology occurs is that of double nanowires contacted with a superconductor [264,280,281]. However, at odds with our platform where chirality forbids local Andreev pairing of the carriers, these systems allow for both LAR and CAR processes. A theoretical work by Reeg et al. [280] investigates the interplay between these two processes in a noninteracting double-nanowire system as a function of the interwire separation. They find out that the two pairing types always interfere destructively, leading to up to an order of magnitude reduction in the size of the excitation gap of the system. Interestingly, they also find out that, similarly to our case, the excitation gap of the system varies periodically on the scale of the Fermi wavelength. However, no sign change of the gap is observable due to the competition of the two processes. Going in this direction, a very recent experiment lead by Prof. Tarucha [282] reported the observation of Cooper-pair splitting (a phenomenon that is complementary to the CAR mechanism) in a related platform, namely an InAs double nanowire device coupled to a superconducting electrode, demonstrating an interwire interaction, paving the way for the realization of a physics closely related to the one discussed in [280].

The control of the sign of the topological gap, unique to our platform, has many ramifications. Here, we have concentrated on how it may be exploited to produce topological π junctions that are robust against fluctuations in the system parameters. These junctions are interesting because they host pairs of Majorana zero modes that do not split in energy despite their spatial overlap. Importantly, we have demonstrated that these junctions are energetically stable with respect to fluctuations in the phase of the parent superconductor, and therefore that, under the appropriate combination of the involved parameters, the CAR-induced topological π-junction is a true ground state of the system. We have proposed to employ these unconventional junctions to perform parametric non-Abelian operations on Majoranas that do not involve their spatial exchange. Specifically, we have concentrated on how to implement tunnel-braiding schemes in platforms based on CAR-induced topological superconductivity, what allows the original proposal by Flensberg to become significantly more realistic. It is also interesting to note that the specific implementation of the CAR-induced topological gap described here, based on QH phases enriched with Zeeman and Rashba interactions at odd filling factors, is just one conceptually simple possibility, but it is not unique. Other phases, such as the quantum anomalous Hall states exhibited by topological insulators with magnetic dopants, could also support the requisite $\nu = 1$ spin-singlet states. CAR-induced topological superconductivity is thus proposed as a promising road forward towards the next landmark in the field, the realization of protected non-Abelian operations in the lab.

Chapter 5

Disorder in Transition Metal Dichalcogenides

5.1 Introduction

Two-dimensional monolayers of seminconducting transition metal dichalcogenides (TMDCs), with general formula MX_2, where M=Mo, W and X=S, Se, have been attracting a lot of attention in recent years for being promising candidates for applications in electronics [283–287], optoelectronics [288–291], spintronics [292] and valleytronics [293–296]. Their hallmarks include an appealing multivalley structure and a strong spin-orbit coupling that, together with the lack of inversion symmetry, is able to spin-split the bands substantially [43,46,58]. Also, the time reversal symmetry connecting the two valleys results in a singular spin-valley coupling that has been proposed to be exploited in several different configurations [58,297,298]. Interestingly, this spin-orbit-induced spin-valley coupling protects the valley degree of freedom against nonmagnetic defects in lightly hole doped samples (that is, the regime of motion where the Fermi energy resides in between the two spin-splitted valence bands) [58]. In fact, due to their different orbital composition [43,46,292,299], the conduction and valence bands are unevenly affected by SOC, in such a way that the fomer remains virtually degenerate at the K, K' points whereas the latter splits by a consistent amount (ranging from $\lambda \approx 148$ meV in MoS_2 to $\lambda \approx 460$ meV in WSe_2 [300], see Tab. 5.1). As a consequence, flipping of either index cannot happen without the simultaneous flipping of the other, so that a special protection of the quantum state of the carriers can be achieved. In a recent work [301], it has been shown that, besides the spin-valley coupling, the symmetry and position of atomic defects give rise to unconventional selection rules for intervalley scattering in 2D TMDCs. Specifically, the authors find that for defects with threefold rotational symmetry C_3, intervalley scattering in the conduction band is forbidden for defects centered on the X site while being allowed for M centered defects. In the valence band, intervalley scattering is forbidden in both cases.

Because of all of the above reasons, studying disorder in these systems is crucial in order to assess the conditions under which one can obtain sufficiently long valley and spin lifetimes, that are important prerequisites for the implementation of valleytronics and spintronics applications. The way that external perturbations couple to the low-energy degrees of freedom around a high-symmetry point of the Brillouin zone is derivable by symmetry arguments. The power of the resulting analysis is that one can then classify the type of perturbation corresponding to each term, and study disorder-dependent phenomena accordingly. Nice examples of the usefulness of classifying disorder according to symmetry in TMDCs can be found in Refs. [56,298,300,302], whereas similar analyses have been performed in graphene [303–307]. Here, we develop a low energy model for time-reversal invariant disorder in TMDCs based on group theoretical arguments, thus

	λ_c [meV]	λ_v [meV]
MoS_2	3	148
$MoSe_2$	22	186
WS_2	-32	430
WSe_2	-37	460

TABLE 5.1: Spin-orbit splittings $\lambda_{c/v}$ of the conduction and valence bands of the four compounds of the family of monolayer semiconducting TMCDs.

spawning a readily accessible inventory of the disorder potential terms allowed by symmetry in different cases of interest, what can be employed in a number of different applications, among which, remarkably, assessment of spin and valley relaxation mechanisms [300,302], study of quantum transport effects [56,304], study of coherent spin transport and related phenomena (spin Hall effect, spin to charge conversion..) [308–310], study of adatom/vacancy-induced resonances [311], computation of cross-sections for scattering off different kind of defects and in different regimes of motion [308].

The chapter is organized as follows. We first of all perform, in the second section, a symmetry analysis of the compounds of interest, by using a peculiar approach where the unit cell is tripled with respect to the original one (what enables to treat the two inequivalent valleys on the same grounds) and determine the character table of the corresponding point group at the high symmetry points $\mathbf{K}_\pm$. In the third section, we classify the Bloch functions of the orbitals that dominate the conduction and valence bands at $\mathbf{K}_\pm$ according to the irreducible representations of the point group, and in the fourth section we do the same but for the electronic operators acting on the space spanned by the valence and conduction band states around the two valleys. This allows determining the most general form of the low-energy Hamiltonian in the fifth section, by requiring that it trasnforms as a scalar under the symmetry group of the system. Finally, in the sixth section, we build the most general form of a disorder Hamiltonian that breaks all symmetries but time reversal, and discuss its microscopic origin.

5.2 Symmetry analysis

Transition metal dichalcogenides are Van der Waals layered materials with general formula MX_2. Bulk MX_2 crystals show different polytypes which vary in stacking and atom coordination [312,313]. Their electronic properties range from metallic to semiconducting, depending, overall, on the transition metal. In this chapter we focus on semiconducting monolayers [57] such as molybdenum disulfide (MoS2), tungsten disulfide (WS2), molybdenum diselenide (MoSe2), and tungsten diselenide (WSe2). The main difference between the bulk and monolayer materials is that the bulk structure is centrosymmetric, whereas the monolayer is not. As seen in the introductory chapter, two-dimensional unit cells of semiconducting TMDCs consist of a X-M-X sequence of atomic planes, with each plane being arranged in a triangular array with lattice parameter $a = 3.16$ Å. The chalcogen layers are perfectly stacked one on top of the other, sandwiching in the middle a transition-metal layer that is rotated in such a way that the overall structure realizes a honeycomb lattice. This lattice is generated by the two primitive vectors

$$\mathbf{a}_{1,2} = \frac{a}{2}\left(\pm 1, \sqrt{3}\right), \tag{5.1}$$

see Fig. 5.1a for reference. The point group of this family of compounds is D_{3h}. This group can be obtained as the direct product of either D_3 or C_{3v} with C_{1h}, where both D_3

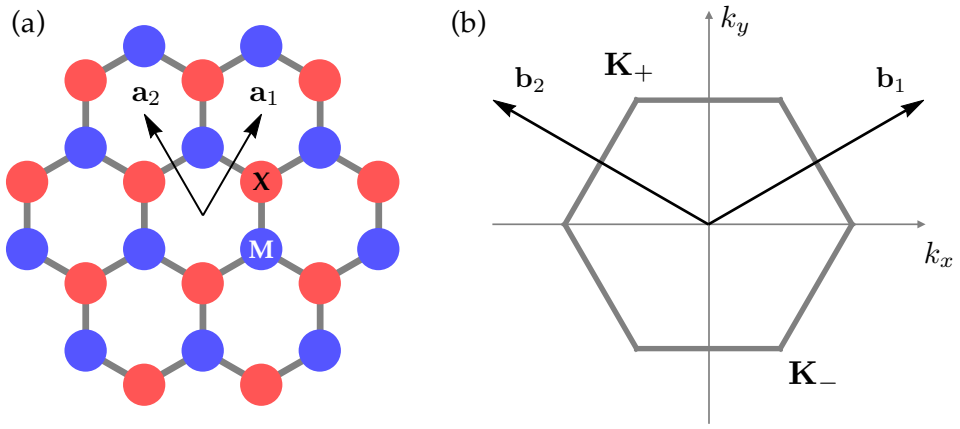

FIGURE 5.1: (a) Lattice of MX_2 compounds with the basis vectors of the lattice $\mathbf{a}_{1,2}$ explicitly shown. (b) Hexagonal Brillouin zone with the reciprocal lattice vectors $\mathbf{b}_{1,2}$ and the inequivalent valleys $\mathbf{K}_\pm$ explicitly shown.

and C_{3v} comprise the identity E, a three-fold rotational axis perpendicular to the crystal plane C_3 and, respectively, three two-fold in-plane axes $C_2'^i$ with $i = 1, 2, 3$ or three vertical mirror planes that pass for the three-fold rotational axis σ_{vi}, with $i = 1, 2, 3$, so that

$$C_{3v} = \{E, C_3, C_3^2, \sigma_{v1}, \sigma_{v2}, \sigma_{v3}\}$$

and

$$D_3 = \{E, C_3, C_3^2, C_2'^1, C_2'^2, C_2'^3\}$$

and $C_{1h} = \{E, \sigma_h\}$ contains the identity and inversion with respect to a horizontal mirror σ_h. The direct product group $D_{3h} = D_3 \times C_{1h} = C_{3v} \times C_{1h}$ includes all the possible composite operations (twelve) formed by pairing members of these groups. These elements are divided into six conjugacy classes, what yields six irreducible representations.

The Brillouin zone of monolayer semiconducting TMDCs is an hexagon with corners

$$\mathbf{K}_+ = \frac{2\pi}{3a}(-1, \sqrt{3}) = \mathbf{K} \qquad \mathbf{K}_- = -\mathbf{K}_+ = -\mathbf{K}, \tag{5.2}$$

see Fig. 5.1b for reference. Notice that they are the same as those defined in Eq. (5.2) modulo a reciprocal lattice vector, even though we have slightly changed the notation for reasons that will become clearer later on. The group of the wavevector at the $\mathbf{\Gamma}$ point has the full symmetry of the point group, whereas the symmetry at the two inequivalent $\mathbf{K}_+$ and $\mathbf{K}_-$ valleys is lowered to that of the group $C_{3h} = \{E, C_3, C_3^2\} \times C_{1h}$ on account of the fact that a reflection about one of the verical planes σ_{vi}, with $i = 1, 2, 3$ interchanges $\mathbf{K}_+$ with $\mathbf{K}_-$. However, for our purpose of classifying time-reversal invariant disorder we are interested to treat the two valleys on equal grounds so that our description will naturally account for the presence of scattering centers able to generate intervalley scattering. A rather compact way to do this is to consider the new point group $D_{3h}'' = D_{3h} + D_{3h} \times t_{\mathbf{a}_1} + D_{3h} \times t_{\mathbf{a}_2}$, where $t_{\mathbf{a}_{1,2}}$ are the operations generating the two elementary translations $\mathbf{a}_{1,2}$ defined in Eq. (5.1) that generate the lattice. This group is obtained by tripling the area of the unit cell such that it contains nine inequivalent sites in spite of three, see Fig. 5.2 (remember that the number of chalcogen atoms is to be doubled). This is equivalent to factorizing the two elementary vectors $\mathbf{a}_{1,2}$ of the translation group and adding them

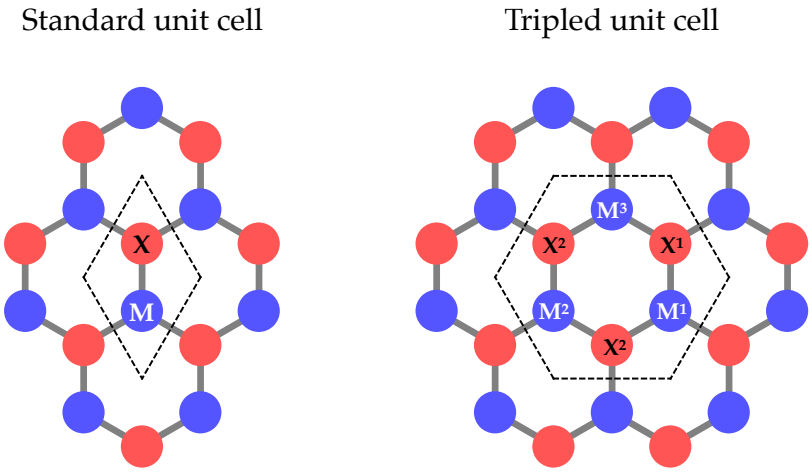

FIGURE 5.2: Comparison between standard (left) and tripled (right) unit cells.

to the D_{3h} point group. The unit vectors of the lattice with enlarged unit cell are

$$\mathbf{a}'_{1,2} = \frac{a}{2}(\pm 3, \sqrt{3}) \tag{5.3}$$

The new reciprocal lattice vectors are

$$\mathbf{b}'_{1,2} = \frac{2\pi}{3a}(\pm 1, \sqrt{3}) \tag{5.4}$$

and the inequivalent valleys of the new Brillouin zone are

$$\mathbf{K}'_{\pm} = \frac{4\pi}{3\sqrt{3}a} 4\pi(0, \pm 1) \tag{5.5}$$

The new Brillouin zone is folded in such a way that the old $\mathbf{\Gamma}$ point and the old $\mathbf{K}_{\pm}$ points are mapped onto the new $\mathbf{\Gamma}'$ point (see Fig. 5.3), thus allowing us to treat them on equal grounds. This, in turn, implies that the point group at the $\mathbf{K}_{\pm}$ points is the full D''_{3h} group.

The most convenient way for determining the character table of this group is to first consider the groups $C''_{3v} = C_{3v} + C_{3v} \times t_{\mathbf{a}_1} + C_{3v} \times t_{\mathbf{a}_2}$ and $C_{1h} = \{E, \sigma_h\}$ separately, and successively obtaining the character table of the product group $D''_{3h} = C''_{3v} \times C_{1h}$ as the direct product of their characters table. This is possible on account of the fact that all elements in C''_{3v} commute with all the elements in C_{1h}. To derive the character table of C''_{3v}, one needs to first compute the multiplication table of the group, that is composed of eighteen elements:

$$C''_{3v} = \{E, t_{\mathbf{a}_1}, t_{\mathbf{a}_2}, C_3, C_3^2, t_{\mathbf{a}_1}C_3, t_{\mathbf{a}_2}C_3, t_{\mathbf{a}_1}C_3^2, t_{\mathbf{a}_2}C_3^2,$$

$$\sigma_{v1}, \sigma_{v2}, \sigma_{v3}, t_{\mathbf{a}_1}\sigma_{v1}, t_{\mathbf{a}_2}\sigma_{v1}, t_{\mathbf{a}_1}\sigma_{v2}, t_{\mathbf{a}_2}\sigma_{v2}, t_{\mathbf{a}_1}\sigma_{v3}, t_{\mathbf{a}_2}\sigma_{v3}\}$$

The multiplication table of the group is useful in that it allows to group the elements in conjugacy classes, that is sets of elements $A_1, ..., A_n$ related by a similarity transformation $A_i = XA_jX^{-1}$ where X is an element of the group. We will not go through the full derivation of the multiplication table and the conjugacy classes because it is lenghty and quite standard, and will just claim that the elements of C''_{3v} are divided into 6 conjugacy

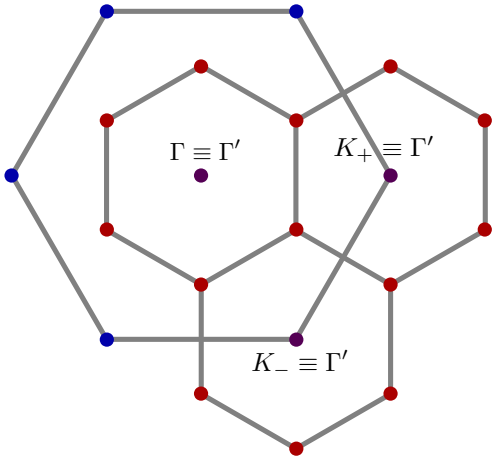

FIGURE 5.3: Folded and unfolded Brillouin zone.

C''_{3v}	$\mathcal{C}_1$	$\mathcal{C}_2$	$\mathcal{C}_3$	$\mathcal{C}_4$	$\mathcal{C}_5$	$\mathcal{C}_6$
$\Gamma^{(1)} \equiv A_1$	1	1	1	1	1	1
$\Gamma^{(2)} \equiv A_2$	1	1	1	1	1	-1
$\Gamma^{(3)} \equiv E$	2	2	-1	-1	-1	0
$\Gamma^{(4)} \equiv E_1$	2	-1	2	-1	-1	0
$\Gamma^{(5)} \equiv E_2$	2	-1	-1	2	-1	0
$\Gamma^{(6)} \equiv E_3$	2	-1	-1	-1	2	0

TABLE 5.2: Character table of the group C''_{3v}.

classes:

$$\mathcal{C}_1 = E,\ \mathcal{C}_2 = \{t_{\mathbf{a}_1}, t_{\mathbf{a}_2}\},\ \mathcal{C}_3 = \{C_3, C_3^2\},$$
$$\mathcal{C}_4 = \{t_{\mathbf{a}_1}C_3, t_{\mathbf{a}_2}C_3^2\},\ \mathcal{C}_5 = \{t_{\mathbf{a}_2}C_3, t_{\mathbf{a}_1}C_3^2\},$$
$$\mathcal{C}_6 = \{\sigma_{v1}, \sigma_{v2}, \sigma_{v3}, t_{\mathbf{a}_1}\sigma_{v1}, t_{\mathbf{a}_2}\sigma_{v1}, t_{\mathbf{a}_1}\sigma_{v2}, t_{\mathbf{a}_2}\sigma_{v2}, t_{\mathbf{a}_1}\sigma_{v3}, t_{\mathbf{a}_2}\sigma_{v3}\}$$

The number of irreducible representations for the group is the same as the number of classes, and the following rule for determining their dimensionalities hold:

$$\sum_{i=1}^{6} \ell_i^2 = 18 \tag{5.6}$$

The only possible combination of positive values for $\{\ell_i\}$, with $i = 1, ...6$ that satisfy Eq. (5.6) is the following:

$$\ell_1 = \ell_2 = 1,\ \ell_3 = \ell_4 = \ell_5 = \ell_6 = 2$$

that is, there are two one-dimensional representations (one of them being the identical representation) and four two-dimensional representations. The character table of this group is easy to determine, yielding the result tabulated in Tab. 5.2. The character table of D''_{3h} is obtained by taking the direct product of this table with that of the group C_{1h}, shown in Tab. 5.3 (notice that is it an abelian group where each class contains only an element). The character table of D''_{3h} is obtained straightforwardly, and it is shown in Tab. 5.4. where both the number of classes and of irreducible representations has doubled, and the latter have been classified according to their symmetry properties with respect to the $z \to -z$

C_{1h}	E	σ_h
$\Gamma^{(1)} \equiv A'$	1	1
$\Gamma^{(2)} \equiv A''$	1	-1

TABLE 5.3: Character table of the group C_{1h}.

D''_{3h}	$\mathcal{C}_1$	$\mathcal{C}_2$	$\mathcal{C}_3$	$\mathcal{C}_4$	$\mathcal{C}_5$	$\mathcal{C}_6$	$\sigma_h\mathcal{C}_1$	$\sigma_h\mathcal{C}_2$	$\sigma_h\mathcal{C}_3$	$\sigma_h\mathcal{C}_4$	$\sigma_h\mathcal{C}_5$	$\sigma_h\mathcal{C}_6$
$\Gamma^{(1)} \equiv A'_1$	1	1	1	1	1	1	1	1	1	1	1	1
$\Gamma^{(2)} \equiv A'_2$	1	1	1	1	1	-1	1	1	1	1	1	-1
$\Gamma^{(3)} \equiv E'$	2	2	-1	-1	v	0	2	2	-1	-1	-1	0
$\Gamma^{(4)} \equiv E'_1$	2	-1	2	-1	-1	0	2	-1	2	-1	-1	0
$\Gamma^{(5)} \equiv E'_2$	2	-1	-1	2	-1	0	2	-1	-1	2	-1	0
$\Gamma^{(6)} \equiv E'_3$	2	-1	-1	-1	2	0	2	-1	-1	-1	2	0
$\Gamma^{(7)} \equiv A''_1$	1	1	1	1	1	1	-1	-1	-1	-1	-1	-1
$\Gamma^{(8)} \equiv A''_2$	1	1	1	1	1	-1	-1	-1	-1	-1	-1	1
$\Gamma^{(9)} \equiv E''$	2	2	-1	-1	-1	0	-2	-2	1	1	1	0
$\Gamma^{(10)} \equiv E''_1$	2	-1	2	-1	-1	0	-2	1	-2	1	1	0
$\Gamma^{(11)} \equiv E''_2$	2	-1	-1	2	-1	0	-2	1	1	-2	1	0
$\Gamma^{(12)} \equiv E''_3$	2	-1	-1	-1	2	0	-2	1	1	1	-2	0

TABLE 5.4: Character table of the group D_{3h}.

reflection: even (representations that have a *prime* symbol) and odd (representations that have a *double prime* symbol). The classes $\sigma_h\mathcal{C}_i$, with $i = 1, ..., 6$ contain new symmetry elements for the system, namely the operations of C''_{3v} followed by the σ_h operation:

$$\sigma_h\mathcal{C}_1 = \sigma_h,\ \sigma_h\mathcal{C}_2 = \{\sigma_h t_{\mathbf{a}_1}, \sigma_h t_{\mathbf{a}_2}\},\ \sigma_h\mathcal{C}_3 = \{\sigma_h C_3 = S_3, \sigma_h C_3^2 = S_3^2\},$$

$$\sigma_h\mathcal{C}_4 = \{\sigma_h t_{\mathbf{a}_1} C_3 = t_{\mathbf{a}_1} S_3, \sigma_h t_{\mathbf{a}_2} C_3^2 = t_{\mathbf{a}_2} S_3^2\},\ \sigma_h\mathcal{C}_5 = \{\sigma_h t_{\mathbf{a}_2} C_3 = t_{\mathbf{a}_2} S_3, \sigma_h t_{\mathbf{a}_1} C_3^2 = t_{\mathbf{a}_1} S_3^2\},$$

$$\sigma_h\mathcal{C}_6 = \{\sigma_h\sigma_{v1} = C_2'^1, \sigma_h\sigma_{v2} = C_2'^2, \sigma_h\sigma_{v3} = C_2'^3,$$

$$\sigma_h t_{\mathbf{a}_1}\sigma_{v1} = t_{\mathbf{a}_1} C_2'^1, \sigma_h t_{\mathbf{a}_2}\sigma_{v1} = t_{\mathbf{a}_2} C_2'^1,$$

$$\sigma_h t_{\mathbf{a}_1}\sigma_{v2} = t_{\mathbf{a}_1} C_2'^2, \sigma_h t_{\mathbf{a}_2}\sigma_{v2} = t_{\mathbf{a}_2} C_2'^2,$$

$$\sigma_h t_{\mathbf{a}_1}\sigma_{v3} = t_{\mathbf{a}_1} C_2'^3, \sigma_h t_{\mathbf{a}_2}\sigma_{v3} = t_{\mathbf{a}_2} C_2'^3\}$$

5.3 Classification of the Bands at $\mathbf{K}_\pm$

In this section, we develop a theory for classifying the bands around the $\mathbf{K}_\pm$ points according to the irreducible representations of the point group D''_{3h}. Notice that, because $\mathbf{K}_+$ and $\mathbf{K}_-$ are related by time reversal, in order to classify the Bloch wavefunctions at $\mathbf{K}_-$ it is sufficient to classify the functions at $\mathbf{K}_+ = \mathbf{K}$ and then obtain those for $\mathbf{K}_- = -\mathbf{K}$ by complex conjugation. To do so, we first remind that the Bloch wavefunction associated to the wavevector $\mathbf{k}$ in a crystal with a basis of N_b atoms with positions $\{\mathbf{R}_i + \mathbf{t}_\eta\}_{\eta=1}^{N_b}$ within the i-th unit cell is a N_b-dimensional vector whose entries represent the amplitude of the relevant atomic orbitals at the N_b different atoms of the unit cell:

$$\phi_{\mathbf{k}}(\mathbf{r}) = \sum_i \begin{pmatrix} e^{i\mathbf{k}\cdot(\mathbf{R}_i+\mathbf{t}_1)}\varphi(\mathbf{r}-\mathbf{R}_i-\mathbf{t}_1) \\ \cdots \\ e^{i\mathbf{k}\cdot(\mathbf{R}_i+\mathbf{t}_{N_b})}\varphi(\mathbf{r}-\mathbf{R}_i-\mathbf{t}_{N_b}) \end{pmatrix} \tag{5.7}$$

Here, i sums over the lattice sites and $\varphi(\mathbf{r}-\mathbf{R}_i-\mathbf{t}_\eta)$ is a vector whose components are the relevant atomic orbitals for the atom centered around position $\mathbf{t}_\eta$ within the i-th unit cell. In our problem, we can consider the M and X atoms as decoupled as they are not mixed by any of the operations of the group. We therefore consider functions of the kind:

$$\phi^{\mathrm{M}}_{\mathbf{K}}(\mathbf{r}) = \sum_i \begin{pmatrix} e^{i\mathbf{K}\cdot(\mathbf{R}_i+\mathbf{t}^1_{\mathrm{M}})}\varphi^{\mathrm{M}}(\mathbf{r}-\mathbf{R}_i-\mathbf{t}^1_{\mathrm{M}}) \\ e^{i\mathbf{K}\cdot(\mathbf{R}_i+\mathbf{t}^2_{\mathrm{M}})}\varphi^{\mathrm{M}}(\mathbf{r}-\mathbf{R}_i-\mathbf{t}^2_{\mathrm{M}}) \\ e^{i\mathbf{K}\cdot(\mathbf{R}_i+\mathbf{t}^3_{\mathrm{M}})}\varphi^{\mathrm{M}}(\mathbf{r}-\mathbf{R}_i-\mathbf{t}^3_{\mathrm{M}}) \end{pmatrix} \tag{5.8}$$

$$\phi^{\mathrm{X(b/ab)}}_{\mathbf{K}}(\mathbf{r}) = \sum_i \begin{pmatrix} e^{i\mathbf{K}\cdot(\mathbf{R}_i+\mathbf{t}^1_{\mathrm{X}})}\varphi^{\mathrm{X(b/ab)}}(\mathbf{r}-\mathbf{R}_i-\mathbf{t}^1_{\mathrm{X}}) \\ e^{i\mathbf{K}\cdot(\mathbf{R}_i+\mathbf{t}^2_{\mathrm{X}})}\varphi^{\mathrm{X(b/ab)}}(\mathbf{r}-\mathbf{R}_i-\mathbf{t}^2_{\mathrm{X}}) \\ e^{i\mathbf{K}\cdot(\mathbf{R}_i+\mathbf{t}^3_{\mathrm{X}})}\varphi^{\mathrm{X(b/ab)}}(\mathbf{r}-\mathbf{R}_i-\mathbf{t}^3_{\mathrm{X}}) \end{pmatrix} \tag{5.9}$$

where

$$\mathbf{t}^1_{\mathrm{M}} = a_0\left(\sqrt{3},-1\right)/2, \quad \mathbf{t}^2_{\mathrm{M}} = a_0\left(-\sqrt{3},-1\right)/2, \quad \mathbf{t}^3_{\mathrm{M}} = a_0\,(0,1) \tag{5.10}$$

and

$$\mathbf{t}^1_{\mathrm{X}} = a_0\left(\sqrt{3},1\right)/2, \quad \mathbf{t}^2_{\mathrm{X}} = a_0\,(0,-1), \quad \mathbf{t}^3_{\mathrm{X}} = a_0\left(-\sqrt{3},1\right)/2 \tag{5.11}$$

with reference to the labels assigned in Fig. 5.2, and with $a_0 = a/\sqrt{3}$. Notice that, in the case of the X atoms, in spite of considering a 6-dimensional vector comprising three orbitals from the top X atoms and three orbitals from the bottom X atoms, we have built either bonding (b) or antibonding (ab) combinations of top (T) and bottom (B) orbitals from these atoms, as

$$\varphi^{(\mathrm{b/ab})}(\mathbf{r}) = \frac{1}{2}\left[\varphi^{(\mathrm{T})}(\mathbf{r}) \pm \varphi^{(\mathrm{B})}(\mathbf{r})\right] \tag{5.12}$$

This is quite convenient since these combinations of orbitals have defined symmetry properties with respect to the mirror reflection about the xy plane, σ_h.

The way to proceed in order to classify the bands at the $\mathbf{K}_\pm$ points according to the irreducible representations of the group of the crystal is the following. We first of all consider the orbital character of the conduction and valence bands at the high symmetry points of interest. DFT calculations [43,46] show that at $\mathbf{K}_+$ and $\mathbf{K}_-$ the valence band is predominantly composed of the $d_{x^2-y^2}$ and d_{xy} atomic orbitals of the M atoms, whereas the conduction band is mainly composed of the d_{z^2} atomic orbital of the M atoms. Both have also a smaller component from the p_x and p_y atomic orbitals of the S atoms. Starting with these atomic orbitals, one has to build Bloch functions with defined symmetry properties under the elements of the group, that is, functions that are eigenfunctions of the symmetry operators of the group. As we have seen, the symmetry group of MX_2 at both the $\mathbf{\Gamma}$ and the $\mathbf{K}_\pm$ point is $D''_{3h} = C''_{3v} \times C_{1h}$, but we can stick with C''_{3v} and successively classisfy the functions as even or odd with respect to σ_h. The relevant operations of this group are the rotations C_3 and C_3^2 around the z axis, the translations $t_{\mathbf{a}_1}$, $t_{\mathbf{a}_2}$, the reflections $\sigma_{v1}, \sigma_{v2}, \sigma_{v3}$ and all the composite operations that can be built from these. For starters, functions that are eigenstates of C_3 and C_3^2 are the spherical armonics Y_l^m, such that $C_n Y_l^m = e^{2\pi i/n} Y_l^m$. Specifically, one has that

$$C_3 Y_l^m = e^{2\pi i/3} Y_l^m = w_3 Y_l^m \tag{5.13}$$

and

$$C_3^2 Y_l^m = e^{-2\pi i/3} Y_l^m = w_3^* Y_l^m \tag{5.14}$$

where $w_3 = e^{2\pi i/3}$. We therefore build the symmetry-adapted basis functions

$$\varphi_{d_{z^2}} \sim Y_2^0 \quad \varphi_{d_{xz}\pm id_{yz}} \sim Y_2^{\pm 1} \quad \varphi_{d_{x^2-y^2}\pm id_{xy}} \sim Y_2^{\pm 2}$$

and

$$\varphi_{p_z} \sim Y_1^0 \quad \varphi_{p_x \pm ip_y} \sim Y_1^{\pm 1}$$

These symmetrized atomic orbitals are relevant for the M atoms and X atoms respectively. However, these functions are not eigenstates of the reflections σ_{vi}, $i = 1,2,3$ as these operations have the effect of mixing opposite projections of the angular momenta along z. Specifically, if we take σ_{v1} to be the reflection about the y axis, one has that

$$\sigma_{v1} \begin{cases} Y^0_{0,1,2} = Y^0_{0,1,2} \\ Y^{\pm 1}_{1,2} = -Y^{\mp 1}_{1,2} \\ Y^{\pm 2}_2 = Y^{\mp 2}_2 \end{cases} \tag{5.15}$$

And, from the multiplication table, it is easy to see to derive the effect of the other two reflections, given that $\sigma_{v2} = C_3^2 \sigma_{v1}$ and $\sigma_{v3} = C_3 \sigma_{v1}$. Finally, the effect of the elementary translations $t_{\mathbf{a}_{1,2}}$ is that of shifting rigidly the atoms. All these operations have also the property of interchanging the (inequivalent by contruction) atoms within the unit cell, since, as seen in Eqs. (5.8) and (5.9) our Bloch functions are three-dimensional vectors.

An element C of the group that does not involve a translation is represented by a matrix that, for an atom in position t_η^α, operates on the $(\mathbf{K}, lm)$ component of the Bloch function as

$$C\phi^{\eta,\alpha}_{\mathbf{K},lm}(\mathbf{r}) = e^{i\mathbf{K}\cdot(\mathbf{t}^\alpha_\eta - \mathbf{t}^\beta_\eta)} \omega_{mm'}(C) \phi^{\eta,\beta}_{\mathbf{K},lm'}(\mathbf{r}) \tag{5.16}$$

where $\omega_{mm'}(C)$ is a phase factor that depends on the m and m' indexes and on the symmetry operation C. For pure rotations, $m' = m$, whereas for reflections, if $m \neq 0$, then $m' \neq m$. Similarly, a translation $t_{\mathbf{a}_i}$ of the group is represented by a matrix that, for an atom in position t^α_η, operates on the $(\mathbf{K}, lm)$ component of the Bloch function as

$$\mathbf{t}_{\mathbf{a}_i} \phi^{\eta,\alpha}_{\mathbf{K},lm}(\mathbf{r}) = e^{-i\mathbf{K}\cdot\mathbf{a}_i} \phi^{\eta,\beta}_{\mathbf{K},lm}(\mathbf{r}) \tag{5.17}$$

where $\mathbf{t}^\beta_\eta = \mathbf{t}^\alpha_\eta + \mathbf{a}_i$. From the last equality it is clear that (as expected) the translations, as well as the pure rotations, do not mix different projections of the angular momentum along the out of plane direction, and the wavefunction merely acquires a phase under their effect. On the other hand, as made explicit by Eq. (5.15), the operations invoving a mirror reflection σ_{vi}, with $i = 1,2,3$, change m to $-m$. However, we can notice the following. Because of our choice of treating the two inqeuivalent valleys (degenerate in energy) on equal grounds, we have by default a double degeneracy calling for two-dimensional representations alone to classify the low-energy spectrum around the $\mathbf{K}_\pm$ points. The two dimensional representations of C''_{3v} are E, E_1, E_2 and E_3. Remarkably, all these two-dimensional irreps have characters equal to zero for the reflection operations σ_{vi} and $t_{\mathbf{a}_j}\sigma_{vi}$ with $i = 1,2,3$ and $j = 1,2$, that flip the sign of the m index when $m \neq 0$. Therefore, these operations will have virtually no role in our classifications at $\mathbf{K}_\pm$, so that we can make use of a three-dimensional basis with fixed m:

$$\phi^{\mathrm{M}}_{\mathbf{K},lm}(\mathbf{r}) = \sum_i \begin{pmatrix} e^{i\mathbf{K}\cdot(\mathbf{R}_i + \mathbf{t}^1_{\mathrm{M}})} \varphi^{\mathrm{M}}_{lm}(\mathbf{r} - \mathbf{R}_i - \mathbf{t}^1_{\mathrm{M}}) \\ e^{i\mathbf{K}\cdot(\mathbf{R}_i + \mathbf{t}^2_{\mathrm{M}})} \varphi^{\mathrm{M}}_{lm}(\mathbf{r} - \mathbf{R}_i - \mathbf{t}^2_{\mathrm{M}}) \\ e^{i\mathbf{K}\cdot(\mathbf{R}_i + \mathbf{t}^3_{\mathrm{M}})} \varphi^{\mathrm{M}}_{lm}(\mathbf{r} - \mathbf{R}_i - \mathbf{t}^3_{\mathrm{M}}) \end{pmatrix} = \begin{pmatrix} \phi^{\mathrm{M},1}_{\mathbf{K},lm}(\mathbf{r}) \\ \phi^{\mathrm{M},2}_{\mathbf{K},lm}(\mathbf{r}) \\ \phi^{\mathrm{M},3}_{\mathbf{K},lm}(\mathbf{r}) \end{pmatrix} \tag{5.18}$$

and

$$\phi^{\mathrm{X(b/ab)}}_{\mathbf{K},lm}(\mathbf{r}) = \sum_i \begin{pmatrix} e^{i\mathbf{K}\cdot(\mathbf{R}_i+\mathbf{t}^1_{\mathrm{X}})}\varphi^{\mathrm{X(b/ab)}}_{lm}(\mathbf{r}-\mathbf{R}_i-\mathbf{t}^1_{\mathrm{X}}) \\ e^{i\mathbf{K}\cdot(\mathbf{R}_i+\mathbf{t}^2_{\mathrm{X}})}\varphi^{\mathrm{X(b/ab)}}_{lm}(\mathbf{r}-\mathbf{R}_i-\mathbf{t}^2_{\mathrm{X}}) \\ e^{i\mathbf{K}\cdot(\mathbf{R}_i+\mathbf{t}^3_{\mathrm{X}})}\varphi^{\mathrm{X(b/ab)}}_{lm}(\mathbf{r}-\mathbf{R}_i-\mathbf{t}^3_{\mathrm{X}}) \end{pmatrix} = \begin{pmatrix} \phi^{\mathrm{X(b/ab)},1}_{\mathbf{K},lm}(\mathbf{r}) \\ \phi^{\mathrm{X(b/ab)},2}_{\mathbf{K},lm}(\mathbf{r}) \\ \phi^{\mathrm{X(b/ab)},3}_{\mathbf{K},lm}(\mathbf{r}) \end{pmatrix} \tag{5.19}$$

From Eq. (5.2) and Eqs. (5.10)-(5.11) we have:

$$e^{i\mathbf{K}\cdot(\mathbf{t}^1_{\mathrm{M}}-\mathbf{t}^2_{\mathrm{M}})} = e^{i\mathbf{K}\cdot(\mathbf{t}^2_{\mathrm{M}}-\mathbf{t}^3_{\mathrm{M}})} = e^{i\mathbf{K}\cdot(\mathbf{t}^3_{\mathrm{M}}-\mathbf{t}^1_{\mathrm{M}})} = w_3^*$$

$$e^{i\mathbf{K}\cdot(\mathbf{t}^1_{\mathrm{X}}-\mathbf{t}^2_{\mathrm{X}})} = e^{i\mathbf{K}\cdot(\mathbf{t}^2_{\mathrm{X}}-\mathbf{t}^3_{\mathrm{X}})} = e^{i\mathbf{K}\cdot(\mathbf{t}^3_{\mathrm{X}}-\mathbf{t}^1_{\mathrm{X}})} = w_3$$

$$e^{i\mathbf{K}\cdot\mathbf{a}_1} = w_3 \qquad e^{i\mathbf{K}\cdot\mathbf{a}_2} = w_3^*$$

In order to see to which irreps a given function $\phi^{\eta}_{\mathbf{K},lm}(\mathbf{r})$ belongs, we calculate the coefficients

$$a_i = \frac{1}{g}\sum_R \chi(R)\chi^{(i)}(R)^* \tag{5.20}$$

where g is the number of elements of the group. Also, we do not consider the reflections σ_{vi} with $i = 1, 2, 3$ as they play no practical role by virtue of having zero associated character for the irreps relevant for the low-energy description around the valleys. If, for a given function $\phi^{\eta}_{\mathbf{K},lm}(\mathbf{r})$, $a_i = 0$, it means that the function has no components transforming like the i-th irrep. In turn, if $a_i \neq 0$, then the function has a component transforming like the i-th irrep. Once the factors a_i are calculated, in order to see which combination of the $\phi^{\eta}_{\mathbf{K},lm}(\mathbf{r})$ Bloch function transforms according to each representation to which it belongs, we make use of the projection operator, defined as

$$P^{(i)} = \sum_R \chi^{(i)}(R)^* P_R \tag{5.21}$$

where P_R is the matricial representation of the symmetry operation R on the basis functions. To give a concrete example of how this protocol for the classification works, we consider for instance the Bloch function $\phi_{\mathbf{K},22}$, relevant for M atoms at the valence band:

$$\phi^{\mathrm{M}}_{\mathbf{K},22}(\mathbf{r}) = \begin{pmatrix} \phi^{\mathrm{M},1}_{\mathbf{K},22}(\mathbf{r}) \\ \phi^{\mathrm{M},2}_{\mathbf{K},22}(\mathbf{r}) \\ \phi^{\mathrm{M},3}_{\mathbf{K},22}(\mathbf{r}) \end{pmatrix} \tag{5.22}$$

We operate on this function with the relevant elements of the group C''_{3v}:

$$t_{\mathbf{a}_1}\phi^{\mathrm{M}}_{\mathbf{K},22}(\mathbf{r}) = w_3^* \begin{pmatrix} \phi^{\mathrm{M},2}_{\mathbf{K},22}(\mathbf{r}) \\ \phi^{\mathrm{M},3}_{\mathbf{K},22}(\mathbf{r}) \\ \phi^{\mathrm{M},1}_{\mathbf{K},22}(\mathbf{r}) \end{pmatrix} = \begin{pmatrix} 0 & w_3^* & 0 \\ 0 & 0 & w_3^* \\ w_3^* & 0 & 0 \end{pmatrix} \phi^{\mathrm{M}}_{\mathbf{K},22}(\mathbf{r}) \tag{5.23}$$

$$t_{\mathbf{a}_2}\phi^{\mathrm{M}}_{\mathbf{K},22}(\mathbf{r}) = w_3 \begin{pmatrix} \phi^{\mathrm{M},3}_{\mathbf{K},22}(\mathbf{r}) \\ \phi^{\mathrm{M},1}_{\mathbf{K},22}(\mathbf{r}) \\ \phi^{\mathrm{M},2}_{\mathbf{K},22}(\mathbf{r}) \end{pmatrix} = \begin{pmatrix} 0 & 0 & w_3 \\ w_3 & 0 & 0 \\ 0 & w_3 & 0 \end{pmatrix} \phi^{\mathrm{M}}_{\mathbf{K},22}(\mathbf{r}) \tag{5.24}$$

$$C_3\phi^{\mathrm{M}}_{\mathbf{K},22}(\mathbf{r}) = w_3^* \begin{pmatrix} w_3\phi^{\mathrm{M},3}_{\mathbf{K},22}(\mathbf{r}) \\ w_3\phi^{\mathrm{M},1}_{\mathbf{K},22}(\mathbf{r}) \\ w_3\phi^{\mathrm{M},2}_{\mathbf{K},22}(\mathbf{r}) \end{pmatrix} = \begin{pmatrix} 0 & 0 & 1 \\ 1 & 0 & 0 \\ 0 & 1 & 0 \end{pmatrix} \phi^{\mathrm{M}}_{\mathbf{K},22}(\mathbf{r}) \tag{5.25}$$

$$C_3^2\phi^{\mathrm{M}}_{\mathbf{K},22}(\mathbf{r}) = w_3 \begin{pmatrix} w_3^*\phi^{\mathrm{M},2}_{\mathbf{K},22}(\mathbf{r}) \\ w_3^*\phi^{\mathrm{M},3}_{\mathbf{K},22}(\mathbf{r}) \\ w_3^*\phi^{\mathrm{M},1}_{\mathbf{K},22}(\mathbf{r}) \end{pmatrix} = \begin{pmatrix} 0 & 1 & 0 \\ 0 & 0 & 1 \\ 1 & 0 & 0 \end{pmatrix} \phi^{\mathrm{M}}_{\mathbf{K},22}(\mathbf{r}) \tag{5.26}$$

$$t_{\mathbf{a}_1}C_3\phi^{\mathrm{M}}_{\mathbf{K},22}(\mathbf{r}) = w_3 \begin{pmatrix} w_3\phi^{\mathrm{M},1}_{\mathbf{K},22}(\mathbf{r}) \\ w_3\phi^{\mathrm{M},2}_{\mathbf{K},22}(\mathbf{r}) \\ w_3\phi^{\mathrm{M},3}_{\mathbf{K},22}(\mathbf{r}) \end{pmatrix} = \begin{pmatrix} w_3^* & 0 & 0 \\ 0 & w_3^* & 0 \\ 0 & 0 & w_3^* \end{pmatrix} \phi^{\mathrm{M}}_{\mathbf{K},22}(\mathbf{r}) \tag{5.27}$$

$$t_{\mathbf{a}_2}C_3\phi^{\mathrm{M}}_{\mathbf{K},22}(\mathbf{r}) = \begin{pmatrix} w_3\phi^{\mathrm{M},2}_{\mathbf{K},22}(\mathbf{r}) \\ w_3\phi^{\mathrm{M},3}_{\mathbf{K},22}(\mathbf{r}) \\ w_3\phi^{\mathrm{M},1}_{\mathbf{K},22}(\mathbf{r}) \end{pmatrix} = \begin{pmatrix} 0 & w_3 & 0 \\ 0 & 0 & w_3 \\ w_3 & 0 & 0 \end{pmatrix} \phi^{\mathrm{M}}_{\mathbf{K},22}(\mathbf{r}) \tag{5.28}$$

$$t_{\mathbf{a}_1}C_3^2\phi^{\mathrm{M}}_{\mathbf{K},22}(\mathbf{r}) = \begin{pmatrix} w_3^*\phi^{\mathrm{M},3}_{\mathbf{K},22}(\mathbf{r}) \\ w_3^*\phi^{\mathrm{M},1}_{\mathbf{K},22}(\mathbf{r}) \\ w_3^*\phi^{\mathrm{M},2}_{\mathbf{K},22}(\mathbf{r}) \end{pmatrix} = \begin{pmatrix} 0 & 0 & w_3^* \\ w_3^* & 0 & 0 \\ 0 & w_3^* & 0 \end{pmatrix} \phi^{\mathrm{M}}_{\mathbf{K},22}(\mathbf{r}) \tag{5.29}$$

$$t_{\mathbf{a}_2}C_3^2\phi^{\mathrm{M}}_{\mathbf{K},22}(\mathbf{r}) = w_3^* \begin{pmatrix} w_3^*\phi^{\mathrm{M},1}_{\mathbf{K},22}(\mathbf{r}) \\ w_3^*\phi^{\mathrm{M},2}_{\mathbf{K},22}(\mathbf{r}) \\ w_3^*\phi^{\mathrm{M},3}_{\mathbf{K},22}(\mathbf{r}) \end{pmatrix} = \begin{pmatrix} w_3 & 0 & 0 \\ 0 & w_3 & 0 \\ 0 & 0 & w_3 \end{pmatrix} \phi^{\mathrm{M}}_{\mathbf{K},22}(\mathbf{r}) \tag{5.30}$$

We now calculate the characters of the above matrices in order to determine to which irreps of the group C''_{3v} the Bloch function $\phi^{\mathrm{M}}_{\mathbf{K},22}(\mathbf{r})$ belongs:

$$\chi(t_{\mathbf{a}_1}) = \chi(t_{\mathbf{a}_2}) = \chi(C_3) = \chi(C_3^2) = \chi(t_{\mathbf{a}_2}C_3) = \chi(t_{\mathbf{a}_1}C_3^2) = 0$$

$$\chi(E) = 3 \qquad \chi(t_{\mathbf{a}_1}C_3) = 3w_3^* \qquad \chi(t_{\mathbf{a}_2}C_3^2) = 3w_3$$

whence:

$$a_E = a_{E_1} = a_{E_3} = 1 \qquad a_{E_2} = 0$$

implying that it belongs to the irreps E, E_1 and E_3. To find out which combination of the functions $\phi^{\mathrm{M},\alpha}_{\mathbf{K},22}(\mathbf{r})$ belongs to E, we employ the projection operator defined in Eq. (5.21) to $\phi^{\mathrm{M}}_{\mathbf{K},22}(\mathbf{r})$:

$$P^{(E)}\phi^{\mathrm{M}}_{\mathbf{K},22}(\mathbf{r}) = \left[2E + 2t_{\mathbf{a}_1} + 2t_{\mathbf{a}_1} - C_3 - C_3^2 - t_{\mathbf{a}_1}C_3 - t_{\mathbf{a}_2}C_3^2 - t_{\mathbf{a}_2}C_3 - t_{\mathbf{a}_1}C_3^2\right]\phi^{\mathrm{M}}_{\mathbf{K},22}(\mathbf{r}) =$$

$$3 \begin{pmatrix} 1 & w_3^* & w_3 \\ w_3 & 1 & w_3^* \\ w_3^* & w_3 & 1 \end{pmatrix} \phi^{\mathrm{M}}_{\mathbf{K},22}(\mathbf{r}) = \begin{pmatrix} \varphi \\ w_3\varphi \\ w_3^*\varphi \end{pmatrix}$$

where we have defined

$$\varphi = 3\left[\phi^{\mathrm{M},1}_{\mathbf{K},22}(\mathbf{r}) + w_3^*\phi^{\mathrm{M},2}_{\mathbf{K},22}(\mathbf{r}) + w_3\phi^{\mathrm{M},3}_{\mathbf{K},22}(\mathbf{r})\right]$$

By applying the operator C_3 to this function, one gets

$$C_3\varphi = 3\left[\phi^{\mathrm{M},3}_{\mathbf{K},22}(\mathbf{r}) + w_3^*\phi^{\mathrm{M},1}_{\mathbf{K},22}(\mathbf{r}) + w_3\phi^{\mathrm{M},2}_{\mathbf{K},22}(\mathbf{r})\right] = w_3^*\varphi$$

implying that $\phi^{\mathrm{M}}_{\mathbf{K},22}(\mathbf{r})$ acquires a phase w_3^* under C_3 when transforming according to the irrep E. To find out which combination of the functions $\phi^{\mathrm{M},\alpha}_{\mathbf{K},22}(\mathbf{r})$ belongs to E_1, we employ the projection operator defined in Eq. (5.21) to $\phi^{\mathrm{M}}_{\mathbf{K},22}(\mathbf{r})$:

$$P^{(E_1)}\phi^{\mathrm{M}}_{\mathbf{K},22}(\mathbf{r}) = \left[2E - t_{\mathbf{a}_1} - t_{\mathbf{a}_1} + 2C_3 + 2C_3^2 - t_{\mathbf{a}_1}C_3 - t_{\mathbf{a}_2}C_3^2 - t_{\mathbf{a}_2}C_3 - t_{\mathbf{a}_1}C_3^2\right]\phi^{\mathrm{M}}_{\mathbf{K},22}(\mathbf{r}) =$$

$$3\begin{pmatrix} 1 & 1 & 1 \\ 1 & 1 & 1 \\ 1 & 1 & 1 \end{pmatrix}\phi^{\mathrm{M}}_{\mathbf{K},22}(\mathbf{r}) = \begin{pmatrix} \varphi \\ \varphi \\ \varphi \end{pmatrix}$$

where we have defined

$$\varphi = 3\left[\phi^{\mathrm{M},1}_{\mathbf{K},22}(\mathbf{r}) + \phi^{\mathrm{M},2}_{\mathbf{K},22}(\mathbf{r}) + \phi^{\mathrm{M},3}_{\mathbf{K},22}(\mathbf{r})\right]$$

By applying the operator C_3 to this function, one gets

$$C_3\varphi = 3\left[\phi^{\mathrm{M},3}_{\mathbf{K},22}(\mathbf{r}) + \phi^{\mathrm{M},1}_{\mathbf{K},22}(\mathbf{r}) + \phi^{\mathrm{M},2}_{\mathbf{K},22}(\mathbf{r})\right] = \varphi$$

meaning that $\phi^{\mathrm{M}}_{\mathbf{K},22}(\mathbf{r})$ acquires a phase 1 under C_3 when transforming according to the irrep E_1. Finally, to find out which combination of the functions $\phi^{\mathrm{M},\alpha}_{\mathbf{K},22}(\mathbf{r})$ belongs to E_3, we employ the projection operator defined in Eq. (5.21) to $\phi^{\mathrm{M}}_{\mathbf{K},22}(\mathbf{r})$:

$$P^{(E_3)}\phi^{\mathrm{M}}_{\mathbf{K},22}(\mathbf{r}) = \left[2E - t_{\mathbf{a}_1} - t_{\mathbf{a}_1} - C_3 - C_3^2 - t_{\mathbf{a}_1}C_3 - t_{\mathbf{a}_2}C_3^2 + 2t_{\mathbf{a}_2}C_3 + 2t_{\mathbf{a}_1}C_3^2\right]\phi^{\mathrm{M}}_{\mathbf{K},22}(\mathbf{r}) =$$

$$3\begin{pmatrix} 1 & w_3 & w_3^* \\ w_3^* & 1 & w_3 \\ w_3 & w_3^* & 1 \end{pmatrix}\phi^{\mathrm{M}}_{\mathbf{K},22}(\mathbf{r}) = \begin{pmatrix} \varphi \\ w_3^*\varphi \\ w_3\varphi \end{pmatrix}$$

where we have defined

$$\varphi = 3\left[\phi^{\mathrm{M},1}_{\mathbf{K},22}(\mathbf{r}) + w_3\phi^{\mathrm{M},2}_{\mathbf{K},22}(\mathbf{r}) + w_3^*\phi^{\mathrm{M},3}_{\mathbf{K},22}(\mathbf{r})\right]$$

By applying the operator C_3 to this function, one gets

$$C_3\varphi = 3\left[\phi^{\mathrm{M},3}_{\mathbf{K},22}(\mathbf{r}) + w_3\phi^{\mathrm{M},1}_{\mathbf{K},22}(\mathbf{r}) + w_3^*\phi^{\mathrm{M},2}_{\mathbf{K},22}(\mathbf{r})\right] = w_3\varphi$$

meaning that $\phi^{\mathrm{M}}_{\mathbf{K},22}(\mathbf{r})$ acquires a phase w_3 under C_3 when transforming according to the irrep E_3. Since this function is symmetric under σ_h, one has that

$$\phi^{\mathrm{M}}_{\mathbf{K},22}(\mathbf{r}) \sim E' + E_1' + E_3'$$

Performing an analogous analysis for the rest of all the orbitals relevant for the M and for the X atoms, one can build Tabs. (5.5) and (5.6) respectively.

D''_{3h}	σ_h	C_3 (**K**)	Wavefunctions (**K**)	C_3 ($-$**K**)	Wavefunctions ($-$**K**)
E'	1	$w_3^{\mp 1}$	$\phi^{\mathrm{M}}_{\mathbf{K},2\pm 2}(\mathbf{r})$	$w_3^{\mp 1}$	$\phi^{\mathrm{M}}_{-\mathbf{K},2\mp 2}(\mathbf{r})$
E''	-1	$w_3^{\pm 1}$	$\phi^{\mathrm{M}}_{\mathbf{K},2\pm 1}(\mathbf{r})$	$w_3^{\pm 1}$	$\phi^{\mathrm{M}}_{-\mathbf{K},2\mp 1}(\mathbf{r})$
E'_1	1	1	$\phi^{\mathrm{M}}_{\mathbf{K},2\pm 2}(\mathbf{r})$	1	$\phi^{\mathrm{M}}_{-\mathbf{K},2\mp 2}(\mathbf{r})$
E''_1	-1	1	$\phi^{\mathrm{M}}_{\mathbf{K},2\pm 1}(\mathbf{r})$	1	$\phi^{\mathrm{M}}_{-\mathbf{K},2\mp 1}(\mathbf{r})$
E'_2	1	w_3	$\phi^{\mathrm{M}}_{\mathbf{K},20}(\mathbf{r})$	w_3^{-1}	$\phi^{\mathrm{M}}_{-\mathbf{K},20}(\mathbf{r})$
E''_2	-1	$-$	$-$	$-$	$-$
E'_3	1	$w_3^{\pm 1}$	$\phi^{\mathrm{M}}_{\mathbf{K},2\pm 2}(\mathbf{r})$	$w_3^{\pm 1}$	$\phi^{\mathrm{M}}_{-\mathbf{K},2\mp 2}(\mathbf{r})$
E''_3	-1	$w_3^{\mp 1}$	$\phi^{\mathrm{M}}_{\mathbf{K},2\pm 1}(\mathbf{r})$	$w_3^{\mp 1}$	$\phi^{\mathrm{M}}_{-\mathbf{K},2\mp 1}(\mathbf{r})$

TABLE 5.5: Classification of the Bloch functions built from the atomic orbitals of the M atoms. The phases acquired under the operations C_3 and σ_h are shown.

D''_{3h}	σ_h	C_3 (**K**)	Wavefunctions (**K**)	C_3 ($-$**K**)	Wavefunctions ($-$**K**)
E'	1	w_3^{-1}	$\phi^{\mathrm{X(b)}}_{\mathbf{K},1\pm 1}(\mathbf{r})$	w_3	$\phi^{\mathrm{X(b)}}_{-\mathbf{K},1\pm 1}(\mathbf{r})$
E''	-1	w_3^{-1}	$\phi^{\mathrm{X(ab)}}_{\mathbf{K},1\pm 1}(\mathbf{r})$	w_3	$\phi^{\mathrm{X(ab)}}_{-\mathbf{K},1\pm 1}(\mathbf{r})$
E'_1	1	1	$\phi^{\mathrm{X(b)}}_{\mathbf{K},1\pm 1}(\mathbf{r})$	1	$\phi^{\mathrm{X(b)}}_{-\mathbf{K},1\pm 1}(\mathbf{r})$
E''_1	- 1	1	$\phi^{\mathrm{X(ab)}}_{\mathbf{K},1\pm 1}(\mathbf{r})$	1	$\phi^{\mathrm{X(ab)}}_{-\mathbf{K},1\pm 1}(\mathbf{r})$
E'_2	1	w_3	$\phi^{\mathrm{X(b)}}_{\mathbf{K},1\pm 1}(\mathbf{r})$	w_3^{-1}	$\phi^{\mathrm{X(b)}}_{-\mathbf{K},1\pm 1}(\mathbf{r})$
E''_2	-1	w_3	$\phi^{\mathrm{X(ab)}}_{\mathbf{K},1\pm 1}(\mathbf{r})$	w_3^{-1}	$\phi^{\mathrm{X(ab)}}_{-\mathbf{K},1\pm 1}(\mathbf{r})$
E'_3	1	w_3^{-1}	$\phi^{\mathrm{X(ab)}}_{\mathbf{K},10}(\mathbf{r})$	w_3	$\phi^{\mathrm{X(ab)}}_{-\mathbf{K},10}(\mathbf{r})$
E''_3	-1	w_3^{-1}	$\phi^{\mathrm{X(b)}}_{\mathbf{K},10}(\mathbf{r})$	w_3	$\phi^{\mathrm{X(b)}}_{-\mathbf{K},10}(\mathbf{r})$

TABLE 5.6: Classification of the Bloch functions built from the atomic orbitals of the X atoms. The phases acquired under the operations C_3 and σ_h are shown.

The conduction band is composed, at the $\mathbf{K}_\pm$ points, predominantly by the d_{z^2} orbitals of the M atoms, plus a smaller contribution from the p_x and p_y orbitals from the X atoms. As we have seen, the Bloch functions are formed from the symmetry-adapted combinations of these functions $\phi^{\mathrm{M}}_{20} \sim d_{z^2}$ and $\phi^{\mathrm{X(b/ab)}}_{1\pm1} \sim p_x \pm ip_y$. The former transforms according to the irreducible representation E'_2 of the D''_{3h} group, acquiring a phase $w_3^{\pm1}$ under the rotation C_3 at $\mathbf{K}_\pm$ (see Tab. 5.5), whereas the latter transform according to the irreps E', E'_1 and E'_2 (bonding) and E'', E''_1 and E''_2 (antibonding) of D''_{3h}, acquiring respectively a phase $w_3^{\mp1}, 1$ and $w_3^{\pm1}$ under C_3 at $\mathbf{K}_\pm$ (see Tab. 5.6). We deduce that the conduction band transforms according to the irrep E'_2, the one that is common to all the relevant orbitals.

The valence band is composed, at the $\mathbf{K}_\pm$ points, predominantly by the $d_{x^2-y^2}$ and d_{xy} orbitals of the M atoms, and a smaller contribution from the p_x and p_y orbitals from the X atoms. As we have seen, the Bloch functions are formed from the symmetry-adapted combinations of these functions $\phi^{\mathrm{M}}_{2\pm2} \sim d_{x^2-y^2} \pm id_{xy}$ and $\phi^{\mathrm{X(b/ab)}}_{1\pm1} \sim p_x \pm ip_y$. The former transform according to the irreps E', E'_1 and E'_3 of D''_{3h}, acquiring respectively a phase $w_3^{\mp1}, 1$ and $w_3^{\pm1}$ under C_3 at $\mathbf{K}_+$ and a phase $w_3^{\pm1}, 1$ and $w_3^{\mp1}$ under C_3 at $\mathbf{K}_-$. The latter, in turn, transform according to the irreps E', E'_1 and E'_2 (bonding) and E'', E''_1 and E''_2 (antibonding) of D''_{3h}, acquiring respectively a phase $w_3^{-1}, 1$ and w_3 under C_3 at $\mathbf{K}_+$ and a phase $w_3, 1$ and w_3^{-1} under C_3 at $\mathbf{K}_-$. Because the atomic orbitals coming from the M atoms are symmetric under $z \to -z$ reflection, we can discard the irreps E'', E''_1 and E''_2. Also, we can discard the irreps E'_2 and E'_3 as the former only accounts for the atomic orbitals of the X atoms, whereas the latter only for those of the M atoms. We are left with the two irreps E' and E'_1 and we identify the correct irrep according to which the valence band transforms as being E'_1 based on the transformation properties of the Bloch functions $\phi^{\mathrm{M}}_{2\pm2}$ and $\phi^{\mathrm{X}}_{1\pm1}$ at $\mathbf{K}_\pm$ under C_3.

5.4 Classification of the operators

5.4.1 Spinless system

Having identified the conduction and valence bands as transofrming, respecively, according to the irreps E'_2 and E'_1, we can build our low-energy theory by considering the space of 4-vectors (E'_2, E'_1) whose entries are the projection of the Bloch wavefunctions on the conduction and valence bands at $\mathbf{K}_\pm$. We can build an effective $\mathbf{k}\cdot\mathbf{p}$ Hamiltonian by considering the possible 16 hermitian matrices acting on this 4-dimensional space, whose reduction in terms of irreducible representations of D_{3h} is deduced by taking the direct product

$$(E'_2, E'_1) \times (E'_2, E'_1) = E'_2 \times E'_2 + E'_1 \times E'_1 + 2E'_1 \times E'_2 \tag{5.31}$$

The irreducible representations of D''_{3h} can be deduced once again by calculating the number of times that each irrep enters the 4-dimensional reducible representation (5.31) by means of formula (B.9), yielding

$$(E'_2, E'_1) \times (E'_2, E'_1) = 2A'_1 + 2A'_2 + 2E' + E'_1 + E'_2 + 2E'_3 \tag{5.32}$$

The space of the matrices acting on these 4-vectors can be built by introducing two sets of mutually commuting Pauli algebras Σ_i and Λ_i, with $i = x, y, z$. The 16 possible operators are generated by considering all products of elements from the two algebras plus the identity. We identify the valley off-diagonal irreps with Λ_x and Λ_y, and the conduction-valence bands off-diagonal irreps with Σ_x and Σ_y. We choose to work in the basis $\psi = (\psi_{c,K_+}, \psi_{v,K_+}, \psi_{v,K_-}, -\psi_{c,K_-})^T$. In this basis, the time reversal operator, that has the effect

of interchanging valleys, reads $T = \Lambda_y \Sigma_y K$, where K represents complex conjugation. With this choice for the basis, it is then clear that all the matrices Σ_i and Λ_i are odd under time reversal:

$$T\Sigma_i T^\dagger = \Sigma_y K \Sigma_i K^\dagger \Sigma_y^\dagger = -\Sigma_i \tag{5.33}$$

$$T\Lambda_i T^\dagger = \Lambda_y K \Sigma_i K^\dagger \Lambda_y^\dagger = -\Lambda_i \tag{5.34}$$

whereas all the products of the kind $\Sigma_i \Lambda_j$ with $i, j = x, y, z$ are time reversal invariant. Therefore the only possible operators that can enter the Hamiltonian in the absence of time-reversal breaking perturbations are products of this kind plus the identity. In order to classify these operators with respect to the irreps of the group D''_{3h}, we have to work out the operatorial form of the elements of the group in this basis (cfr with Tab.s 5.5 and 5.6), obtaining

$$\begin{gathered}
t_{\mathbf{a}_1} = e^{-2\pi i \Lambda_z/3} \qquad t_{\mathbf{a}_2} = e^{2\pi i \Lambda_z/3} \\
C_3 = e^{-2\pi i (\Lambda_z + \Sigma_z)/3} \qquad C_3^2 = e^{2\pi i (\Lambda_z + \Sigma_z)/3} \\
t_{\mathbf{a}_1} C_3 = e^{-2\pi i (\Sigma_z - \Lambda_z)/3} \qquad t_{\mathbf{a}_2} C_3 = e^{-2\pi i \Sigma_z/3} \\
t_{\mathbf{a}_1} C_3^2 = e^{2\pi i \Sigma_z/3} \qquad t_{\mathbf{a}_2} C_3^2 = e^{2\pi i (\Sigma_z - \Lambda_z)/3} \\
\sigma_{v1} = \Sigma_y \Lambda_y \qquad \sigma_{v2} = e^{2\pi i (\Lambda_z + \Sigma_z)/3} \Sigma_y \Lambda_y \qquad \sigma_{v3} = e^{-2\pi i (\Lambda_z + \Sigma_z)/3} \Sigma_y \Lambda_y
\end{gathered} \tag{5.35}$$

In the following, we will make use of the results below:

$$\begin{aligned}
e^{\zeta 2\pi i \sigma_z/3} \sigma_x e^{-\zeta 2\pi i \sigma_z/3} &= \tfrac{1}{2}(-\sigma_x + \zeta\sqrt{3}\sigma_y) \\
e^{\zeta 2\pi i \sigma_z/3} \sigma_y e^{-\zeta 2\pi i \sigma_z/3} &= \tfrac{1}{2}(-\zeta\sqrt{3}\sigma_x - \sigma_y)
\end{aligned} \tag{5.36}$$

where,

$$e^{\zeta 2\pi i \sigma_z/3} = -\frac{1}{2} + \zeta i \sigma_z \frac{\sqrt{3}}{2}, \tag{5.37}$$

$\zeta = \pm 1$, and the σ_i with $i = x, y, z$ are a generic set of matrices satisfying the Pauli matrix algebra. Notice that to see to which irrep a given operator belongs, it suffices to compute the trace associated with just one element for each class, since, by definition, elements within the same class have the same trace. We start by classifying the operators Σ_x, Σ_y and Σ_z. It is clear from the operatorial form of the elements of the group, Eqs. (5.35), that Σ_z trasforms as a scalar whereas (Σ_x, Σ_y) transform as a vector. By applying the elements of the group to (Σ_x, Σ_y), one finds the following characters

$$\chi(t_{\mathbf{a}_i}) = 2 \quad \chi(C_3) = -1 \quad \chi(t_{\mathbf{a}_i} C_3) = -1 \quad \chi(\sigma_{v1}) = 0 \qquad (i = 1, 2) \tag{5.38}$$

By comparing Eq. (5.38) with Tab. 5.2, it follows that $(\Sigma_x, \Sigma_y) \sim E'$. On the other hand, since $C\Sigma_z C^\dagger = \Sigma_z$ for $C = t_{\mathbf{a}_i}, C_3, C_3^2, t_{\mathbf{a}_i} C_3, t_{\mathbf{a}_i} C_3^2$ and $C\Sigma_z C^\dagger = -\Sigma_z$ for $C = \sigma_v$, $\Sigma_z \sim A'_2$. We can proceed in the same way for the operators Λ_x, Λ_y and Λ_z. By applying the elements of the group to (Λ_x, Λ_y), one finds the following characters

$$\chi(t_{\mathbf{a}_1}) = -1 \quad \chi(C_3) = -1 \quad \chi(t_{\mathbf{a}_1} C_3) = -1 \quad \chi(t_{\mathbf{a}_2} C_3) = 2 \quad \chi(\sigma_{v1}) = 0 \tag{5.39}$$

It follows that $(\Lambda_x, \Lambda_y) \sim E'_3$. Since $C\Lambda_z C^\dagger = \Lambda_z$ for $C = t_{\mathbf{a}_i}, C_3, C_3^2, t_{\mathbf{a}_i} C_3, t_{\mathbf{a}_i} C_3^2$ and $C\Lambda_z C^\dagger = -\Lambda_z$ for $C = \sigma_v$, $\Lambda_z \sim A'_2$. Next we consider the product $\Sigma_z \Lambda_z$, that we can classify by noticing that $A'_2 \times A'_2 = A'_1$, thus $\Sigma_z \Lambda_z \sim A'_1$. Also, since $E' \times A'_2 = E'$, we can classify the product of (Σ_x, Σ_y) with Λ_z as transforming according to E'. Specifically,

D''_{3h}	Spinless operators (TR even)	Spinless operators (TR odd)
A'_1	I, $\Sigma_z\Lambda_z$	–
A'_2	–	Σ_z, Λ_z
E'	$(-\Lambda_z\Sigma_y, \Lambda_z\Sigma_x)$	(Σ_x, Σ_y)
E'_1	$(\Sigma_x\Lambda_x + \Sigma_y\Lambda_y, \Sigma_x\Lambda_y - \Sigma_y\Lambda_x)$	–
E'_2	$(-\Sigma_x\Lambda_x + \Sigma_y\Lambda_y, -\Sigma_x\Lambda_y - \Sigma_y\Lambda_x)$	(Λ_x, Λ_y)
E'_3	$(-\Sigma_z\Lambda_y, \Sigma_z\Lambda_x)$	–

TABLE 5.7: Classification of the spinless operators.

the vector that transforms as (Σ_x, Σ_y) is $(-\Lambda_z\Sigma_y, \Lambda_z\Sigma_x)$ as is straightforward to demonstrate by applying the same procedure as above. Analogously, since $E'_3 \times A'_2 = E'_3$, we can classify the product of (Λ_x, Λ_y) with Σ_z as transforming according to E'_3. Specifically, the vector that transforms as (Λ_x, Λ_y) is $(-\Sigma_z\Lambda_y, \Sigma_z\Lambda_x)$. Finally, since $E' \times E'_3 = E'_1 + E'_2$, the vectors containing linear combinations of operators like $\Sigma_i\Lambda_j$ with $i, j = x, y$ transform according to these two irreps. Specifically, the vector $(\Sigma_x\Lambda_x + \Sigma_y\Lambda_y, \Sigma_x\Lambda_y - \Sigma_y\Lambda_x)$ transforms as E'_1 whereas the vector $(-\Sigma_x\Lambda_x + \Sigma_y\Lambda_y, -\Sigma_x\Lambda_y - \Sigma_y\Lambda_x)$ transforms as E'_2. The resulting classification of operators is summarized in Tab. 5.7.

5.4.2 Spinful system

Rigorous treatment of the spin degree of freedom requires to redo our classification of the Bloch wavefunctions according to the irreducible representations of the corresponding double group associated to the original symmetry group D''_{3h}. The new group is obtained by multiplying all the elements of the old group by a new element that represents a rotation by 2π, that is not the same as the identity, since the identity for spinful particles is represented by a rotation by 4π, and considering the union of the old elements with the new elements, what doubles the order of the group. However, this approach can be simplified in the case in which the strength of the spin-orbit coupling is much weaker than the typical energy separation between the bands (governed by crystal fields that are typically of the order of several eV), that is, when the SOC is not strong enough as to invert the order of the 'spinless' bands, and their orbital character is virtually unaltered. This is the case for MX_2 compounds, where the SOC is larger than in graphene but yet smaller than the typical separation of the bands. The way of including the spin degree of freedom in this case is to introduce an additional set of Pauli matrices $\{s_i\}_{i=x,y,z}$ commuting with the $\{\Sigma_i\}_{i=x,y,z}$ and $\{\Lambda_i\}_{i=x,y,z}$ matrices. The transformation rules of these operators are easily determined by considering that spin is an angular momentum operator, that is, it behaves as a pseudo-vector. One can go further by treating on different grounds the in-plane spin components $\mathbf{s}_\parallel = (s_x, s_y)$ and the out-of-plane spin component $s_\perp = s_z$ on account of the fact that MX_2 is a monolayer system with strong in-plane to out-of-plane anisotropy, and as a consequence the $\mathbf{s}_\parallel$ and $s_\perp$ components decouple and can be treated separately: the former will transform accordingly to a pseudo-vectorial irrep (that is, it transforms like a vector under a proper rotation, but gains a sign flip under an improper rotation such as a reflection), whereas the latter belongs to a pseudo-scalar irrep (that is, it changes sign under a parity inversion). $\mathbf{s}_\parallel$ is therefore odd under σ_h whereas $s_\perp$ is

D''_{3h}	Spinful operators (TR even)	Spinful operators (TR odd)
A'_1	$\Sigma_z s_z$, $\Lambda_z s_z$	–
A'_2	–	s_z
A''_1	$\Sigma_x s_x + \Sigma_y s_y$	–
A''_2	$\Sigma_x s_y - \Sigma_y s_x$	–
E'	$(-s_z\Sigma_y, s_z\Sigma_x)$	–
E''	$(s_x\Sigma_z, s_y\Sigma_z)$, $(s_x\Lambda_z, s_y\Lambda_z)$ $(s_y\Sigma_x + s_x\Sigma_y, s_x\Sigma_x - s_y\Sigma_y)$	$(-s_y, s_x)$
E''_1	$(s_y\Lambda_x - s_x\Lambda_y, s_x\Lambda_x + s_y\Lambda_y)$	–
E''_2	$(s_y\Lambda_x + s_x\Lambda_y, -s_x\Lambda_x + s_y\Lambda_y)$	–
E'_3	$(-s_z\Lambda_y, s_z\Lambda_x)$	–

TABLE 5.8: Classification of the spinful operators.

even under σ_h. When the spin degree of freedom is taken into account, the time reversal operator becomes $T = is_y\Lambda_y\Sigma_y K$ (see Appendix A). This allows, when constructing the Hamiltonian, to take into account operators that respect the time-reversal invariance of the problem as products of the kind $\Sigma_i s_j$ and $\Lambda_i s_j$ in addition to those considered in the spinless case. To classify the spinful operators under the irreps of D''_{3h} we have to update the operators in Eq. (5.35) to include their effect on the spin degrees of freedom. The translation operators $t_{\mathbf{a}_{1,2}}$ do not act on the spin, whereas the rotations C_3, C_3^2 and the reflections act as:

$$\begin{gathered} C_3 = e^{\pi i s_z/3} \qquad C_3^2 = e^{-\pi i s_z/3} \\ \sigma_{v1} = s_x \qquad \sigma_{v2} = e^{-\pi i s_z/3} s_x \qquad \sigma_{v3} = e^{\pi i s_z/3} s_x \\ \sigma_h = s_z \end{gathered} \tag{5.40}$$

By applying a procedure analogue to the one employed above, one obtains the classification of these operators shown in Tab. 5.8.

5.5 Hamiltonian of Pristine TMDC's

In order to construct a low-energy Hamiltonian we make an expansion in powers of the 2D momentum $\mathbf{p} = (p_x, p_y)$. This vector transforms as the irrep E'. We can classify accordingly higher powers of the momentum: $p_x^2 + p_y^2 \sim A'_1$, and $(2p_xp_y, p_x^2 - p_y^2) \sim E'$. By considering that (i) odd powers of the momentum are odd under time inversion, whereas even powers are even and that (ii) the Hamiltonian must be invariant under all the operations of the group, that is, it must transform as A'_1, the prescription for generating the Hamiltonian is to take all products between the *isospins* (conduction/valence and valley degrees of freedom) operators acting in the basis $\psi = (\psi_{c,K_+}, \psi_{v,K_+}, \psi_{v,K_-}, -\psi_{c,K_-})^T$ and the momentum operators that belong to the same irrep. In fact, upon taking the direct

D''_{3h}	Momenta	Isospins	Products	TR
A'_1	$p_x^2 + p_y^2$	$I, \Sigma_z\Lambda_z$	$p_x^2 + p_y^2$, $(p_x^2 + p_y^2)\Sigma_z\Lambda_z$	even
E'	(p_x, p_y)	(Σ_x, Σ_y)	$(p_x, p_y)\cdot(\Sigma_x, \Sigma_y)$	even
	(p_x, p_y)	$(-\Lambda_z\Sigma_y, \Lambda_z\Sigma_x)$	$(p_x, p_y)\cdot(-\Lambda_z\Sigma_y, \Lambda_z\Sigma_x)$	odd
	$(2p_xp_y, p_x^2 - p_y^2)$	(Σ_x, Σ_y)	$(2p_xp_y, p_x^2 - p_y^2)\cdot(\Sigma_x, \Sigma_y)$	odd
	$(2p_xp_y, p_x^2 - p_y^2)$	$(-\Lambda_z\Sigma_y, \Lambda_z\Sigma_x)$	$(2p_xp_y, p_x^2 - p_y^2)\cdot(-\Lambda_z\Sigma_y, \Lambda_z\Sigma_x)$	even

TABLE 5.9: Classification of the products between momentum operators and isospins (conduction/valence and valley) operators.

product of an irrep with itself, one always has the identical representation as an output. Therefore, with the double constraint of constructing Hamiltonian terms that belong to A'_1 that are even under time reversal, we end up with a spinless Hamiltonian

$$H_0 = \gamma(\Sigma_x p_x + \Sigma_y p_y) + \frac{\Delta}{2}\Lambda_z\Sigma_z + \frac{\alpha+\beta}{2}p^2 + \frac{\alpha-\beta}{2}p^2\Lambda_z\Sigma_z + \kappa\left[(p_x^2 - p_y^2)\Lambda_z\Sigma_x - 2p_xp_y\Lambda_z\Sigma_y\right] \tag{5.41}$$

The criteria for building the Hamiltonian (5.41) have been summarized in Tab. 5.9. In matrix form, Eq. (5.41) reads

$$H_0 = \begin{pmatrix} \Delta/2 + \alpha p^2 & \gamma p_- + \kappa\xi_+ & 0 & 0 \\ \gamma p_+ + \kappa\xi_- & -\Delta/2 + \beta p^2 & 0 & 0 \\ 0 & 0 & -\Delta/2 + \beta p^2 & \gamma p_- - \kappa\xi_+ \\ 0 & 0 & \gamma p_+ - \kappa\xi_- & \Delta/2 + \alpha p^2 \end{pmatrix} \tag{5.42}$$

We want to project this Hamiltonian on the conduction and valence band respectively, and to do this it is convenient to rearrange our basis vector in the following way:

$$\psi' = \begin{pmatrix} \psi_{c,K} \\ \psi_{c,K'} \\ \psi_{v,K} \\ \psi_{v,K'} \end{pmatrix} = \begin{pmatrix} 1 & 0 & 0 & 0 \\ 0 & 0 & 0 & -1 \\ 0 & 1 & 0 & 0 \\ 0 & 0 & 1 & 0 \end{pmatrix} \begin{pmatrix} \psi_{c,K} \\ \psi_{v,K} \\ \psi_{v,K'} \\ -\psi_{c,K'} \end{pmatrix} = U\psi \tag{5.43}$$

with

$$U = \begin{pmatrix} 1 & 0 & 0 & 0 \\ 0 & 0 & 0 & -1 \\ 0 & 1 & 0 & 0 \\ 0 & 0 & 1 & 0 \end{pmatrix} \tag{5.44}$$

The Hamiltonian H_0 in this new basis is $H'_0 = UH_0U^\dagger$, that is, in matrix form,

$$H'_0 = \begin{pmatrix} \Delta/2 + \alpha p^2 & 0 & \gamma p_- + \kappa\xi_+ & 0 \\ 0 & \Delta/2 + \alpha p^2 & 0 & -\gamma p_+ + \kappa\xi_- \\ \gamma p_+ + \kappa\xi_- & 0 & -\Delta/2 + \beta p^2 & 0 \\ 0 & -\gamma p_- + \kappa\xi_+ & 0 & -\Delta/2 + \beta p^2 \end{pmatrix} \tag{5.45}$$

or, in block form,

$$H_0' = \begin{pmatrix} H_c^{(0)} & V \\ V^\dagger & H_v^{(0)} \end{pmatrix} \tag{5.46}$$

with

$$H_c^{(0)} = (\Delta/2 + \alpha p^2)\mathbb{1}_2, \tag{5.47}$$

$$H_v^{(0)} = (-\Delta/2 + \beta p^2)\mathbb{1}_2 \tag{5.48}$$

and

$$V = \begin{pmatrix} \gamma p_- + \kappa\xi_+ & 0 \\ 0 & -\gamma p_+ + \kappa\xi_- \end{pmatrix} \tag{5.49}$$

Now, we can apply the Lipmann-Schwinger method in order to project the Hamiltonian H' onto a single band (either the conduction or the valence). We block-divide the wavefunction ψ' as

$$\psi' = \begin{pmatrix} \psi_{c,K} \\ \psi_{c,K'} \\ \psi_{v,K} \\ \psi_{v,K'} \end{pmatrix} = \begin{pmatrix} \psi_c \\ \psi_v \end{pmatrix}, \tag{5.50}$$

with

$$\psi_c = \begin{pmatrix} \psi_{c,K} \\ \psi_{c,K'} \end{pmatrix} \qquad \psi_v = \begin{pmatrix} \psi_{v,K} \\ \psi_{v,K'} \end{pmatrix},$$

and consider the eigenvalue equation $H_0'\psi' = \epsilon\psi'$. Explicitly,

$$H_c^{(0)}\psi_c + V\psi_v = \epsilon\psi_c \tag{5.51}$$

$$V^\dagger\psi_c + H_v^{(0)}\psi_v = \epsilon\psi_v \tag{5.52}$$

To project onto the conduction band, one can express ψ_v as a function of ψ_c from the second row, as

$$\psi_v = \left[\epsilon - H_v^{(0)}\right]^{-1} V^\dagger\psi_c$$

and insert it in the first row to obtain an equation for ψ_c:

$$\left[H_c^{(0)} + V\left[\epsilon - H_v^{(0)}\right]^{-1} V^\dagger\right]\psi_c = \epsilon\psi_c \tag{5.53}$$

that we can rewrite as $H_c(\epsilon)\psi_c = \epsilon\psi_c$ where we have defined the Hamiltonian for the conduction band

$$H_c(\epsilon) = H_c^{(0)} + V\left[\epsilon - H_v^{(0)}\right]^{-1} V^\dagger \tag{5.54}$$

An effective Hamiltonian for low concentrations of electrons can be constructed by fixing the energy to be at the bottom of this band, $\epsilon \approx \Delta/2$, whence

$$\tilde{H}_c = H_c^{(0)} + V\left[\Delta/2 - H_v^{(0)}\right]^{-1} V^\dagger \tag{5.55}$$

To lowest order in Δ^{-1}, $\left[\Delta/2 - H_v^{(0)}\right]^{-1} \approx \Delta^{-1}\mathbb{1}_2$, so that, finally

$$\tilde{H}_c = H_c^{(0)} + \Delta^{-1}VV^\dagger \tag{5.56}$$

Explicit calculation of $VV^\dagger$ yields (up to third order in the momentum)

$$VV^\dagger = \gamma^2 p^2 + 2\kappa\gamma p_x(p_x^2 - 3p_y^2)\tau_z$$

so that, finally

$$\tilde{H}_c = \frac{\Delta}{2} + \alpha p^2 + \frac{\gamma^2}{\Delta}p^2 + 2\frac{\kappa\gamma}{\Delta}p_x(p_x^2 - 3p_y^2)\tau_z = \frac{\Delta}{2} + \frac{p^2}{2m_c^*} + \mu_c p_x(p_x^2 - 3p_y^2)\tau_z \quad (5.57)$$

where we have defined

$$m_c^* = \frac{2}{\alpha + \gamma^2/\Delta} \qquad \mu_c = 2\frac{\kappa\gamma}{\Delta}$$

Analogously, one can derive the effective equation for the valence band by solving Eq. (5.51) for ψ_c, obtaining

$$\psi_c = \left[\epsilon - H_c^{(0)}\right]^{-1} V\psi_v$$

and insert it in Eq. (5.52) to obtain a selfconsistent equation for ψ_v:

$$\left[H_v^{(0)} + V^\dagger\left[\epsilon - H_c^{(0)}\right]^{-1} V\right]\psi_v = \epsilon\psi_v \quad (5.58)$$

that again we can rewrite in the form $H_v(\epsilon)\psi_v = \epsilon\psi_v$ where

$$H_v(\epsilon) = H_v^{(0)} + V^\dagger\left[\epsilon - H_c^{(0)}\right]^{-1} V \quad (5.59)$$

An effective Hamiltonian for low concentrations of holes can be defined by fixing the energy to be at the top of this band, $\epsilon \approx -\Delta/2$, whence

$$\tilde{H}_v = H_v^{(0)} + V^\dagger\left[-\Delta/2 - H_c^{(0)}\right]^{-1} V \quad (5.60)$$

To lowest order in Δ^{-1}, $\left[-\Delta/2 - H_c^{(0)}\right]^{-1} \approx -\Delta^{-1}\mathbb{1}_2$, so that

$$\tilde{H}_v = H_v^{(0)} - \Delta^{-1}V^\dagger V \quad (5.61)$$

with

$$V^\dagger V = \gamma^2 p^2 + 2\kappa\gamma p_x(p_x^2 - 3p_y^2)\tau_z$$

so that, finally

$$\tilde{H}_v = -\frac{\Delta}{2} + \beta p^2 - \frac{\gamma^2}{\Delta}p^2 - 2\frac{\kappa\gamma}{\Delta}p_x(p_x^2 - 3p_y^2)\tau_z = -\frac{\Delta}{2} + \frac{p^2}{2m_v^*} + \mu_v p_x(p_x^2 - 3p_y^2)\tau_z \quad (5.62)$$

where we have defined

$$m_v^* = \frac{2}{\beta - \gamma^2/\Delta} \qquad \mu_v = -2\frac{\kappa\gamma}{\Delta}$$

Evidently, once the two bands are considered for separate, one can forget about the offset energies. Also, by applying the above procedure to the spinful part of the Hamiltonian H_s, one is left with

$$H_{c,v} = \frac{p^2}{2m_{c,v}^*} + \mu_{c,v}p_x(p_x^2 - 3p_y^2)\tau_z \quad (5.63)$$

Adding the spin degree of freedom to the above description and sticking to zeroth order in the momentum, it is easy to see that the only spinful terms allowed by symmetry are $\Sigma_z s_z$ and $\Lambda_z s_z$, so that the most general spinful part of the Hamiltonian reads

$$H_0^s = \lambda_1 s_z \Sigma_z + \lambda_2 s_z \Lambda_z \tag{5.64}$$

or, in matrix form

$$H_0^s = s_z \begin{pmatrix} \lambda_1+\lambda_2 & 0 & 0 & 0 \\ 0 & \lambda_2-\lambda_1 & 0 & 0 \\ 0 & 0 & \lambda_1-\lambda_2 & 0 \\ 0 & 0 & 0 & -(\lambda_1+\lambda_2) \end{pmatrix} \tag{5.65}$$

By applying the same procedure as above, we end up with

$$H_{c,v}^s = \lambda_{c,v} s_z \tau_z \tag{5.66}$$

where $\lambda_{c,v} = \lambda_2 \pm \lambda_1$.

5.6 Disorder Potential

We now introduce all types of position-dependent disorder associated to time reversal invariant perturbations that are of zeroth order in the momentum. For the spinless case, we consider all the products $\Sigma_i \Lambda_j$ $(i,j = 0,x,y,z)$ of matrices from our two sets of mutually commuting Pauli algebras that are even under time inversion. This corresponds to neglecting all perturbations associated to external magnetic fields or magnetic impurities. We have seen that the operator for time inversion in this basis reads $T = \Sigma_y \Lambda_y K$ in the spinless case and $T = i s_y \Sigma_y \Lambda_y K$ in the spinful case. When spin-dependent disorder is considered as well, we introduce also products of the kind $\Sigma_i \Lambda_j s_k$ $(i,j,k = 0,x,y,z)$. However, in the basis that we have chosen all odd powers of pauli matrices $\{\Sigma_i\}$, $\{\Lambda_i\}$ and $\{s_i\}$ with $i = x,y,z$ are odd under time-reversal. We are therefore allowed to consider all products of the kind $\Sigma_i \Lambda_j$, $\Sigma_i s_j$ and $\Lambda_i s_j$ with $i,j = x,y,z$, in addition to the identity. We classify these terms according to their structure in valley and spin space.

Spin-independent disorder We discriminate between intravalley and intervalley disorder.

1. Spin-independent intravalley (valley-conserving, vc) disorder. The products of operators for this type of disorder are $\mathbb{1}_4$ and $\Sigma_i \Lambda_z$ with $i = x,y,z$. We notice that the terms of the kind $\Sigma_x \Lambda_z$, $\Sigma_y \Lambda_z$ enter as a valley-dependent gauge-like potential. We therefore have
$$\delta H_{vc}(\mathbf{r}) = U(\mathbf{r}) + M(\mathbf{r}) \Sigma_z \Lambda_z + \boldsymbol{\Sigma} \cdot \mathbf{A}(\mathbf{r})\, \Lambda_z$$

2. Spin-independent intervalley (valley-flipping, vf) disorder. The products of operators for this type of disorder are $\Sigma_i \Lambda_j$ with $i = x,y,z$ and $j = x,y$. We therefore write
$$\delta H_{vf}(\mathbf{r}) = \sum_{\substack{i=x,y,z \\ j=x,y}} V_{ij}(\mathbf{r}) \Sigma_i \Lambda_j$$

In matrix form:

$$\delta H_{vc}(\mathbf{r}) + \delta H_{vf}(\mathbf{r}) =$$

$$\begin{pmatrix} U(\mathbf{r})+M(\mathbf{r}) & A^*(\mathbf{r}) & D^*(\mathbf{r}) & S_-(\mathbf{r})-iR_+(\mathbf{r}) \\ A(\mathbf{r}) & U(\mathbf{r})-M(\mathbf{r}) & S_+(\mathbf{r})+iR_-(\mathbf{r}) & -D^*(\mathbf{r}) \\ D(\mathbf{r}) & S_+(\mathbf{r})-iR_-(\mathbf{r}) & U(\mathbf{r})-M(\mathbf{r}) & -A^*(\mathbf{r}) \\ S_-(\mathbf{r})+iR_+(\mathbf{r}) & -D(\mathbf{r}) & -A(\mathbf{r}) & U(\mathbf{r})+M(\mathbf{r}) \end{pmatrix} \tag{5.67}$$

where we have defined

$$A(\mathbf{r}) = A_x(\mathbf{r}) + iA_y(\mathbf{r})$$
$$D(\mathbf{r}) = V_{zx}(\mathbf{r}) + iV_{zy}(\mathbf{r})$$
$$S_\pm(\mathbf{r}) = V_{xx}(\mathbf{r}) \pm V_{yy}(\mathbf{r})$$
$$R_\pm(\mathbf{r}) = V_{yx}(\mathbf{r}) \pm V_{xy}(\mathbf{r})$$

Spin-dependent disorder We discriminate between spin-conserving (even under σ_h, that we indicate with $\perp$) and spin-flipping (odd under σ_h reflection, that we indicate with $\parallel$) disorder, and between intravalley (vc) and intervalley (vf) disorder.

1. Even spin-dependent intravalley disorder. The products for this type of disorder are $s_z\Lambda_z$ and $s_z\Sigma_i$ with $i = x, y, z$. We have

$$\delta H_{s_\perp, vc}(\mathbf{r}) = V_z^e(\mathbf{r}) s_z \Lambda_z + \sum_{i=x,y,z} U_i^e(\mathbf{r}) s_z \Sigma_i$$

2. Even spin-dependent intervalley disorder. The products for this type of disorder are $s_z\Lambda_i$ with $i = x, y$. We have

$$\delta H_{s_\perp, vf}(\mathbf{r}) = \sum_{i=x,y} V_i^e(\mathbf{r}) s_z \Lambda_i$$

3. Odd spin-dependent intravalley disorder. The products for this type of disorder are $s_j\Lambda_z$ and $s_j\Sigma_i$ with $j = x, y$ and $i = x, y, z$. We have

$$\delta H_{s_\parallel, vc}(\mathbf{r}) = \sum_{j=x,y} V_{jz}^o(\mathbf{r}) s_j \Lambda_z + \sum_{\substack{i=x,y,z \\ j=x,y}} U_{ji}^o(\mathbf{r}) s_j \Sigma_i$$

4. Odd spin-dependent intervalley disorder. The products for this type of disorder are $s_j\Lambda_i$ with $i, j = x, y$. We have

$$\delta H_{s_\parallel, vf}(\mathbf{r}) = \sum_{\substack{i=x,y,z \\ j=x,y}} V_{ji}^o(\mathbf{r}) s_j \Lambda_i$$

In matrix form:

$$\delta H_{s_\perp, vc}(\mathbf{r}) + \delta H_{s_\perp, vf}(\mathbf{r}) =$$
$$\begin{pmatrix} U_z^e(\mathbf{r})+V_z^e(\mathbf{r}) & U_-^e(\mathbf{r}) & V_-^e(\mathbf{r}) & 0 \\ U_+^e(\mathbf{r}) & -U_z^e(\mathbf{r})+V_z^e(\mathbf{r}) & 0 & V_-^e(\mathbf{r}) \\ V_+^e(\mathbf{r}) & 0 & U_z^e(\mathbf{r})-V_z^e(\mathbf{r}) & U_-^e(\mathbf{r}) \\ 0 & V_+^e(\mathbf{r}) & U_+^e(\mathbf{r}) & -U_z^e(\mathbf{r})-V_z^e(\mathbf{r}) \end{pmatrix} s_z \tag{5.68}$$

where

$$U_\pm^e(\mathbf{r}) = U_x^e(\mathbf{r}) \pm iU_y^e(\mathbf{r})$$

and

$$V_\pm^e(\mathbf{r}) = V_x^e(\mathbf{r}) \pm iV_y^e(\mathbf{r})$$

and

$$\delta H_{s_\parallel,vc}(\mathbf{r}) + \delta H_{s_\parallel,vf}(\mathbf{r}) = \sum_{j=x,y} \begin{pmatrix} U^o_{jz}(\mathbf{r}) + V^o_{jz}(\mathbf{r}) & U^o_{j-}(\mathbf{r}) & V^o_{j-}(\mathbf{r}) & 0 \\ U^o_{j+}(\mathbf{r}) & -U^o_{jz}(\mathbf{r}) + V^o_{jz}(\mathbf{r}) & 0 & V^o_{j-}(\mathbf{r}) \\ V^o_{j+}(\mathbf{r}) & 0 & U^o_{jz}(\mathbf{r}) - V^o_{jz}(\mathbf{r}) & U^o_{j-}(\mathbf{r}) \\ 0 & V^o_{j+}(\mathbf{r}) & U^o_{j+}(\mathbf{r}) & -U^o_{jz}(\mathbf{r}) - V^o_{jz}(\mathbf{r}) \end{pmatrix} s_j \tag{5.69}$$

where

$$U^o_{j\pm}(\mathbf{r}) = U^o_{jx}(\mathbf{r}) \pm iU^o_{jy}(\mathbf{r})$$

and

$$V^o_{j\pm}(\mathbf{r}) = V^o_{jx}(\mathbf{r}) \pm iV^o_{jy}(\mathbf{r})$$

The total Hamiltonian, in the original basis and before single-band projection, is therefore

$$H(\mathbf{r}) = H_0 + H_s + \delta H_{vc}(\mathbf{r}) + \delta H_{vf}(\mathbf{r}) + \delta H_{s_\perp,vc}(\mathbf{r}) + \delta H_{s_\perp,vf}(\mathbf{r}) + \delta H_{s_\parallel,vc}(\mathbf{r}) + \delta H_{s_\parallel,vf}(\mathbf{r}) \tag{5.70}$$

In order to obtain the corrections $\delta H_c(\mathbf{r})$ and $\delta H_v(\mathbf{r})$ brought about by time-reversal invariant disorder to the single-band Hamiltonians $\tilde{H}_c$ and $\tilde{H}_v$ derived before, we apply the same procedure indicated in the previous section, first by deriving the Hamiltonian $H'(\mathbf{r}) = UH(\mathbf{r})U^\dagger$ and then by projecting it onto the conduction and valence band sectors, respectively.

5.6.1 Disorder Corrections to the Conduction Band

1. Spin-conserving and valley conserving, $\sim s_0\tau_0$, $s_0\tau_z$, $s_z\tau_z$ and $s_z\tau_0$.

$$\delta\tilde{H}^c_{sc,vc} = u_1(\mathbf{r}) + u_2(\mathbf{r})\, s_z\tau_z + \{\mathbf{p}, \mathbf{u}_3(\mathbf{r})\}\tau_z + \{\mathbf{p}, \mathbf{u}_4(\mathbf{r})\}\, s_z \tag{5.71}$$

   where

$$u_1(\mathbf{r}) = U(\mathbf{r}) + M(\mathbf{r}) + \frac{\gamma}{\Delta}\left[\nabla \times \mathbf{A}(\mathbf{r})\right]_z$$

$$u_2(\mathbf{r}) = U^e_z(\mathbf{r}) + V^e_z(\mathbf{r}) + \frac{\gamma}{\Delta}\left[\nabla \times \mathbf{U}^e(\mathbf{r})\right]_z$$

$$\mathbf{u}_3(\mathbf{r}) = \frac{\gamma}{\Delta}\mathbf{A}(\mathbf{r})$$

$$\mathbf{u}_4(\mathbf{r}) = \frac{\gamma}{\Delta}\mathbf{U}^e(\mathbf{r})$$

   As we see, this correction is divided into one part that is associated with gauge-field-like perturbations ($\sim s_0\tau_z$, $s_z\tau_0$), and one that is not ($\sim s_0\tau_0$, $s_z\tau_z$).

2. Spin-conserving and valley-flipping, $\sim s_0\tau_i$ and $s_z\tau_i$ with $i = x, y$.

$$\delta\tilde{H}^c_{sc,vf} = \mathbf{u}_5(\mathbf{r}) \cdot \boldsymbol{\tau} + \sum_{i=x,y} \{\mathbf{p}, \mathbf{u}^i_6(\mathbf{r})\}\, \tau_i s_z \tag{5.72}$$

   where

$$u_{5,x}(\mathbf{r}) = -(V_{xx}(\mathbf{r}) - V_{yy}(\mathbf{r})) - \frac{\gamma}{\Delta}\left(\partial_x V_{zy}(\mathbf{r}) + \partial_y V_{zx}(\mathbf{r})\right)$$

$$u_{5,y}(\mathbf{r}) = -(V_{yx}(\mathbf{r}) + V_{xy}(\mathbf{r})) - \frac{\gamma}{\Delta}\left(\partial_y V_{zy}(\mathbf{r}) - \partial_x V_{zx}(\mathbf{r})\right)$$

$$u^x_{6,x}(\mathbf{r}) = -\frac{\gamma}{\Delta}V^e_x(\mathbf{r})$$

$$u^{x}_{6,y}(\mathbf{r}) = \frac{\gamma}{\Delta} V^{e}_{y}(\mathbf{r})$$

$$u^{y}_{6,x}(\mathbf{r}) = -\frac{\gamma}{\Delta} V^{e}_{y}(\mathbf{r})$$

$$u^{y}_{6,y}(\mathbf{r}) = -\frac{\gamma}{\Delta} V^{e}_{x}(\mathbf{r})$$

Again, the correction is divided into the one that is associated with gauge-field-like perturbations ($\sim s_z\tau_i$), and the one that is not ($\sim s_0\tau_i$).

3. Spin-flipping and valley-conserving, $\sim s_i\tau_0$ and $s_i\tau_z$, with $i = x, y$.

$$\delta\tilde{H}^{c}_{sf,vc} = \sum_{i=x,y} \{\mathbf{p}, \mathbf{u}^{i}_{7}(\mathbf{r})\}\, s_i + \mathbf{u}_8(\mathbf{r}) \cdot \mathbf{s}\, \tau_z \tag{5.73}$$

where

$$\mathbf{u}^{x}_{7}(\mathbf{r}) = \frac{\gamma}{\Delta} \mathbf{U}^{o}_{x}(\mathbf{r})$$

$$\mathbf{u}^{y}_{7}(\mathbf{r}) = \frac{\gamma}{\Delta} \mathbf{U}^{o}_{y}(\mathbf{r})$$

$$u_{8,i}(\mathbf{r}) = U^{o}_{iz}(\mathbf{r}) + V^{o}_{iz}(\mathbf{r}) + \frac{\gamma}{\Delta} \left[\nabla \times \mathbf{U}^{o}_{i}(\mathbf{r})\right]_z \qquad i = x, y$$

This correction is divided into the one that is associated with gauge-field-like perturbations ($s_i\tau_0$), and the one that is not ($s_i\tau_z$).

4. Spin-flipping and valley-flipping, $\sim s_i\tau_j$, with $i, j = x, y$.

$$\delta\tilde{H}^{c}_{sf,vf} = \sum_{i,j=x,y} \{\mathbf{p}, \mathbf{u}^{ij}_{9}(\mathbf{r})\}\, s_i\tau_j \tag{5.74}$$

$$\mathbf{u}^{xx}_{9,x}(\mathbf{r}) = -\frac{\gamma}{\Delta} V^{o}_{xx}$$

$$\mathbf{u}^{xx}_{9,y}(\mathbf{r}) = -\frac{\gamma}{\Delta} V^{o}_{xy}$$

$$\mathbf{u}^{yx}_{9,x}(\mathbf{r}) = -\frac{\gamma}{\Delta} V^{o}_{yx}$$

$$\mathbf{u}^{yx}_{9,y}(\mathbf{r}) = -\frac{\gamma}{\Delta} V^{o}_{yy}$$

$$\mathbf{u}^{xy}_{9,x}(\mathbf{r}) = -\frac{\gamma}{\Delta} V^{o}_{xy}$$

$$\mathbf{u}^{xy}_{9,y}(\mathbf{r}) = \frac{\gamma}{\Delta} V^{o}_{xx}$$

$$\mathbf{u}^{yy}_{9,x}(\mathbf{r}) = -\frac{\gamma}{\Delta} V^{o}_{yy}$$

$$\mathbf{u}^{yy}_{9,y}(\mathbf{r}) = \frac{\gamma}{\Delta} V^{o}_{yx}$$

This correction is entirelely associated with gauge-field-like perturbations.

5.6.2 Disorder Corrections to the Valence Band

1. Spin-conserving and valley conserving, $\sim s_0\tau_0$, $s_0\tau_z$, $s_z\tau_z$ and $s_z\tau_0$.

$$\delta\tilde{H}^{v}_{sc,vc} = v_1(\mathbf{r}) + v_2(\mathbf{r})\, s_z\tau_z + \{\mathbf{p}, \mathbf{v}_3(\mathbf{r})\}\tau_z + \{\mathbf{p}, \mathbf{v}_4(\mathbf{r})\}\, s_z \tag{5.75}$$

where

$$v_1(\mathbf{r}) = U(\mathbf{r}) - M(\mathbf{r}) + \frac{\gamma}{\Delta}\left[\nabla \times \mathbf{A}(\mathbf{r})\right]_z$$

$$v_2(\mathbf{r}) = -U_z^e(\mathbf{r}) + V_z^e(\mathbf{r}) + \frac{\gamma}{\Delta}\left[\nabla \times \mathbf{U}^e(\mathbf{r})\right]_z$$

$$\mathbf{v}_3(\mathbf{r}) = -\frac{\gamma}{\Delta}\mathbf{A}(\mathbf{r})$$

$$\mathbf{v}_4(\mathbf{r}) = -\frac{\gamma}{\Delta}\mathbf{U}^e(\mathbf{r})$$

As we see, this correction is divided into one part that is associated with gauge-field-like perturbations ($\sim s_0\tau_z, s_z\tau_0$), and one that is not ($\sim s_0\tau_0, s_z\tau_z$).

2. Spin-conserving and valley-flipping, $\sim s_0\tau_i$ and $s_z\tau_i$ with $i = x, y$.

$$\delta\tilde{H}^v_{sc,vf} = \mathbf{v}_5(\mathbf{r}) \cdot \boldsymbol{\tau} + \sum_{i=x,y} \{\mathbf{p}, \mathbf{v}_6^i(\mathbf{r})\}\, \tau_i s_z \tag{5.76}$$

where

$$v_{5,x}(\mathbf{r}) = V_{xx}(\mathbf{r}) + V_{yy}(\mathbf{r}) + \frac{\gamma}{\Delta}\left(\partial_x V_{zy}(\mathbf{r}) - \partial_y V_{zx}(\mathbf{r})\right)$$

$$v_{5,y}(\mathbf{r}) = -(V_{yx}(\mathbf{r}) - V_{xy}(\mathbf{r})) - \frac{\gamma}{\Delta}\left(\partial_y V_{zy}(\mathbf{r}) + \partial_x V_{zx}(\mathbf{r})\right)$$

$$v^x_{6,x}(\mathbf{r}) = -\frac{\gamma}{\Delta}V_x^e(\mathbf{r})$$

$$v^x_{6,y}(\mathbf{r}) = -\frac{\gamma}{\Delta}V_y^e(\mathbf{r})$$

$$v^y_{6,x}(\mathbf{r}) = -\frac{\gamma}{\Delta}V_y^e(\mathbf{r})$$

$$v^y_{6,y}(\mathbf{r}) = \frac{\gamma}{\Delta}V_x^e(\mathbf{r})$$

Again, the correction is divided into the one that is associated with gauge-field-like perturbations ($\sim s_z\tau_i$), and the one that is not ($\sim s_0\tau_i$).

3. Spin-flipping and valley-conserving, $\sim s_i\tau_0$ and $s_i\tau_z$, with $i = x, y$.

$$\delta\tilde{H}^v_{sf,vc} = \sum_{i=x,y} \{\mathbf{p}, \mathbf{v}_7^i(\mathbf{r})\}\, s_i + \mathbf{v}_8(\mathbf{r}) \cdot \mathbf{s}\, \tau_z \tag{5.77}$$

where

$$\mathbf{v}^x_7(\mathbf{r}) = -\frac{\gamma}{\Delta}\mathbf{U}^o_x(\mathbf{r})$$

$$\mathbf{v}^y_7(\mathbf{r}) = -\frac{\gamma}{\Delta}\mathbf{U}^o_y(\mathbf{r})$$

$$v_{8,i}(\mathbf{r}) = -U^o_{iz}(\mathbf{r}) + V^o_{iz}(\mathbf{r}) + \frac{\gamma}{\Delta}\left[\nabla \times \mathbf{U}^o_i(\mathbf{r})\right]_z \qquad i = x, y$$

This correction is divided into the one that is associated with gauge-field-like perturbations ($s_i\tau_0$), and the one that is not ($s_i\tau_z$).

4. Spin-flipping and valley-flipping, $\sim s_i\tau_j$, with $i, j = x, y$.

$$\delta\tilde{H}^v_{sf,vf} = \sum_{i,j=x,y} \{\mathbf{p}, \mathbf{v}_9^{ij}(\mathbf{r})\}\, s_i\tau_j \tag{5.78}$$

$$\mathbf{v}^{xx}_{9,x}(\mathbf{r}) = -\frac{\gamma}{\Delta}V^o_{xx}$$

$$\mathbf{v}_{9,y}^{xx}(\mathbf{r}) = \frac{\gamma}{\Delta} V_{xy}^{o}$$
$$\mathbf{v}_{9,x}^{yx}(\mathbf{r}) = -\frac{\gamma}{\Delta} V_{yx}^{o}$$
$$\mathbf{v}_{9,y}^{yx}(\mathbf{r}) = \frac{\gamma}{\Delta} V_{yy}^{o}$$
$$\mathbf{v}_{9,x}^{xy}(\mathbf{r}) = -\frac{\gamma}{\Delta} V_{xy}^{o}$$
$$\mathbf{v}_{9,y}^{xy}(\mathbf{r}) = -\frac{\gamma}{\Delta} V_{xx}^{o}$$
$$\mathbf{v}_{9,x}^{yy}(\mathbf{r}) = -\frac{\gamma}{\Delta} V_{yy}^{o}$$
$$\mathbf{v}_{9,y}^{yy}(\mathbf{r}) = -\frac{\gamma}{\Delta} V_{yx}^{o}$$

This correction is entirelely associated with gauge-field-like perturbations.

5.7 Discussion and Conclusions

The corrections $w_1(\mathbf{r})$ and $w_2(\mathbf{r})\, s_z \tau_z$ represent intravalley disorder, the former being spin and valley-degenerate and the latter being sensitive to the spin polariztion in each valley. The corrections $\{\mathbf{p}, \mathbf{w}_3(\mathbf{r})\}\tau_z$ and $\{\mathbf{p}, \mathbf{w}_4(\mathbf{r})\}\, s_z$ account for both lattice deformations that preserve the $z \to -z$ symmetry (responsible for a pseudomagnetic field, respectively valley and spin- dependent [314,315]) and the Berry curvature specific for the bands at the corners of the Brillouin zone. The corrections $\mathbf{w}_5(\mathbf{r}) \cdot \boldsymbol{\tau}$ and $\sum_{i=x,y}\{\mathbf{p}, \mathbf{w}_6^i(\mathbf{r})\}\, \tau_i s_z$ account for intervalley disorder ascribable to the presence of defects on the atomic scale that leave the spin-polarization unaltered. The former correction is spin-degenerate, whereas the latter is sensitive to the spin-polarization of the carriers. On the other hand, $\sum_{i=x,y}\{\mathbf{p}, \mathbf{w}_7^i(\mathbf{r})\}\, s_i$ and $\mathbf{w}_8(\mathbf{r}) \cdot \mathbf{s}\, \tau_z$ account for intravalley spin-flipping disorder, that may be induced by deformations that are smooth on the atomic scale and break the $z \to -z$ symmetry, like flexural phonons [300]. Finally, $\sum_{i,j=x,y}\{\mathbf{p}, \mathbf{w}_9^{ij}(\mathbf{r})\}\, s_i \tau_j$ represents intervalley spin-flipping disorder that is associated to the presence of spin-active (though non-magnetic, since time reversal symmetry is preserved) defects on the atomic scale. Following the notation introduced above, $w = u$ in the conduction band and $w = v$ in the valence band. We notice that all the terms that enter as pseudomagnetic gauge fields are momentum dependent and therefore these kind of corrections are absent at the edge of both the conduction and valence bands, where $\mathbf{p} = 0$. One can also notice that in the new basis of conduction and valence band-projected states, the time reversal operator is $T = is_y\tau_x K$, and it is such that $T(s_i\tau_j)T^{-1} = -s_i\tau_j$ for $i, j = x, y$. This implies that disorder of the kind $s_i\tau_j$ with no momentum-dependence is forbidden by the requirement that time-reversal symmetry is preserved, whence such kind of spin and valley flipping disorder is allowed only at finite momentum.

As an interesting application of the disorder potential derived in this chapter, we mention the calculation of the phase-coherent corrections to the conductivity due to quantum interference between time-reversal paired trajectories of carriers calculated in Ref. [56].

Conclusions

In this thesis we have dealt with two of the most thriving topics in contemporary condensed matter physics, namely transport properties and topological hallmarks of two-dimensional systems. Despite their by now long-term presence in the condensed matter community, few-atoms thick systems, among which a key role is played by graphene and transition metal dichalcogenides, have not ceased to be a top-ranking research theme. Strongly overlapping with this field, another privileged spot is occupied by topology, as the Nobel prize awarded in 2016 to Thouless, Haldane and Kosterlitz attests. In most of this thesis we have combined these subjects, obtaining notable results that further prove the high-impact prominence that they still have in both applied and fundamental research. To lay the ground for it, in the first chapter we have provided an overview of the aspects that are more relevant to the topics covered in the rest of the thesis.

The second and third chapters, focusing on graphene materials, make a clear case that the quest for unconventional effects stemming from the linear dispersion of two-dimensional Dirac carriers is far from over. In fact, both the remarkably high anomalous Hall current brought about in a graphene quantum dot by proximity to a magnetic skyrmion (chapter two) and the time reversal-broken quantum spin Hall phase realized by twisted graphene bilayers (chapter three) are distinctive features originating in graphene's far-from-standard electronic structure. The second phenomenon, indeed, requires graphene's unique zero Landau level to split in a nontrivial fashion. This is made possible by the enhanced density of states peculiar to the quantum Hall phase and by the special nature of twisted bilayer graphene's zero Landau level, eightfold degenerate because of an interplay of spin, valley, sublattice and layer degrees of freedom. Combined, these features are responsible for triggering interaction-induced quantum Hall ferromagnetism in the system, that can be further tuned by applying an interlayer bias. The first phenomenon, in turn, is not unique to graphene as the anomalous Hall signal generated by noncoplanar magnetic textures is a well-studied effect that has been known to occur in two-dimensional systems for a long time now. However, this signal is found to be significantly amplified by the resonant low-energy properties of Dirac electrons.

In the fourth chapter we exploit the topological character of the chiral carriers of quantum Hall systems to engineer a phase-coherent state of matter where electrons and holes counterpropagating within a finite distance from each other pair in an unconventional way through a superconducting region separating them. This special crossed electron-hole pairing produces a periodic sign change of the induced gap as a function of the system parameters. This, in turn, makes it possible to engineer a phase difference of π at a domain wall between portions of the system with differing parameters. The mechanism underlying this effect is the well known crossed Andreev reflection that, remarkably, acquires an unconventional twist in the quantum Hall regime on account of the chirality of the carriers. Once again, therefore, it is the low-dimensionality of the platform, together with the topological properties of the carriers, what endows a blend of a few conventional ingredients with a novel and appealing range of phenomena.

In closing, we notice that also the band structure of transition metal dichalcogenides (subject of the fifth chapter) presents a number of unconventional features placing them in a privileged spot, similarly to graphene, although for complementary reasons. In fact,

the two inequivalent valleys act as monopoles for the Berry curvature, as well as independenty controllable degrees of freedom related by time reversal. Moreover, because of the combination of inversion-symmetry breaking and large spin-orbit coupling, the valley flavour and the spin are entangled. All these ingredients make these systems far from standard.

We conclude by commenting on the exciting prospects of current research in the field of low-dimensional topological materials. As we have tried to highlight throughout the thesis, this is extremely fertile ground for the discovery of new physical phenomena and for a deeper understanding of non-trivial electron phases. It is our firm belief that topological two-dimensional materials will deeply affect and enrich our future technologies, and also greatly expand our vocabulary by creating conceptual bridges between seemingly unrelated fields such as topological spaces, non-Abelian anyons, unconventional superconductivity and novel two-dimensional crystals.

Conclusiones

En esta tesis nos centramos en dos de los temás más relevantes dentro de la física de la materia condensada contemporánea, concretamente las propiedades de transporte y los distintivos topológicos de los sistemás bidimensionales. No obstante su presencia ya de largo plazo en la comunidad de la materia condensada, los sistemás de pocos átomos de grosor no han dejado de ser un tema puntero. Entre ellos, grafeno y dicalcogenuros de metales de transición juegan un papel clave. Con un fuerte solape con este campo, otro sitio privilegiado está ocupado por la topología, como el premio Nobel otorgado en 2016 a Thouless, Haldane y Kosterlitz avala. En la mayor parte de esta tesis hemos combinado estos tópicos, obteniendo resultados sorprendentes que demuestran ulteriormente la importancia de alto impacto que todavía tienen tanto en la investigación fundamental como en la aplicada. Para preparar el terreno, en el primer capítulo hemos proveído una perspectiva general sobre algunos de los aspectos que son mas relevantes para los tópicos cubiertos en el resto de la tesis.

El segundo y el tercer capítulo, enfocados en grafeno, evidencian que la búsqueda de efectos no convencionales que resulten de la dispersión lineal de los portadores de Dirac bidimensionales está lejos de su conclusión. Desde luego, tanto la corriente Hall anómala sorprendentemente alta provocada en un punto cuántico de grafeno por proximidad con un skyrmion magnético (capítulo dos) como la fase Hall cuántica de espín con ruptura de simetría de inversión temporal realizada por bicapas de grafeno rotadas (capítulo tres) son características distintivas que tienen su origen en la estructura electrónica extraordinaria de grafeno.

El segundo fenómeno, en efecto, requiere que el nivel cero de Landau que le es exclusivo a grafeno se separe de una manera no trivial. Eso es posible gracias a la alta densidad de estados específica de la fase Hall cuántica y a la naturaleza especial del nivel cero de Landau en bicapas de grafeno rotadas, caracterizado por una degeneración de grado ocho debida a una interacción entre grados de libertad de espín, de valle, de subred y de capa. Estas características, en combinación, son responsables por provocar en el sistema ferromagnetismo cuántico de Hall inducido por interacciones, que puede ser modulado ulteriormente aplicando un voltaje entre las capas. El primer fenómeno, en cambio, no le es específico a grafeno ya que la señal Hall anómala generada por texturas magnéticas no coplanares es un efecto bien estudiado, conocido por ocurrir en sistemás bidimensionales desde hace mucho tiempo. Sin embargo, hemos encontrado que esta señal se ve considerablemente amplificada por las propiedades resonantes de baja energía de los electrones de Dirac.

En el cuarto capítulo explotamos el caracter topológico de los portadores quirales de sistemás cuánticos de Hall para realizar un estado de la materia donde electrones y huecos que se propagan en direcciones opuestas a una distancia finita se aparean de una forma no convencional a través de una región superconductora que los separa. Este apareamiento cruzado especial entre electrones y huecos produce un cambio de signo periódico en el gap inducido en función de los parametros del sistema. Esto, a su vez, permite que se genere una diferencia de fase de π en un muro de dominio entre porciones del sistema caracterizados por parámetros diferentes. El mecanismo subyacente a esta física es la bien conocida reflexión Andreev cruzada que, notablemente, adquiere

un carácter no convencional en el régimen Hall cuántico debido a la quiralidad de los portadores. Una vez más, entonces, la baja dimensionalidad de la plataforma, junto con las propiedades topológicas de los portadores, es lo que le da un alcance novedoso y atractivo a una combinación de pocos ingredientes convencionales.

Para finalizar, notamos que también la estructura de banda de los dicalcogenuros de metales de transición, tema que tratamos en el quinto capítulo, presenta varias características que los colocan en un lugar privilegiado parecido a grafeno, aunque por razones complementarias. En efecto, los dos valles inequivalentes actúan como monopolos para la curvatura Berry, al mismo tiempo que como grados de libertad conectados por inversión temporal que se pueden controlar de forma independiente. Además, debido a la combinación entre ruptura de simetría de inversión espacial y un acoplo espín-órbita grande, los grados de libertad de espín y de valle están enredados. Todos estos ingredientes hacen que estos sistemás estén lejos de ser estandár.

Concluimos comentando sobre las perspectivas fascinantes de la investigación actual en el campo de los materiales topológicos de baja dimensionalidad. Como hemos intentado destacar a lo largo de la tesis, se trata de un terreno extremadamente fértil para descubrir nuevos fenómenos físicos y para entender más profundamente fases electrónicas no triviales. Estamos firmemente convencidos de que los materiales topológicos bidimensionales afectarán y enreciquerán nuestras tecnologías futuras, al mismo tiempo expandiendo nuestro vocabulario a través de la creacion de puentes conceptuales entre campos aparentemente no relacionados como espacios topológicos, anyones no Abelianos, superconductividad no convencional y cristales bidimensionales novedosos.

Appendix A

Time reversal symmetry

The operation of time reversal symmetry consists in reversing the direction of propagation of time, that is changing t to $-t$. In classical mechanics only systems subject to conservative forces are invariant under this operation. To treat quantum system under this operation, one has to distinguish between spinless and spinful systems.

Spinless Particles Given a particle in a static potential with Hamiltonian:

$$H(\mathbf{r},\mathbf{p}) = \frac{\mathbf{p}^2}{2m} + V(\mathbf{r}) \tag{A.1}$$

Since time reversal acts on the time variable, it only affects the velocity, and therefore the momentum, that aquires a negative sign, whereas the position of the particle at time t in the original solution is the same as the position of the particle at time $-t$ in the time-reversed solution:

$$\mathbf{r}(-t) = \mathbf{r}(t) \quad \mathbf{p}(-t) = -\mathbf{p}(t)$$

This can be expressed by introducing a transformation, called time reversal and denoted by T, that has the following property:

$$T\mathbf{r}T^\dagger = \mathbf{r} \quad T\mathbf{p}T^\dagger = -\mathbf{p} \tag{A.2}$$

Considering the time-dependent Schroedinger equation associated to Hamiltonian (A.1):

$$i\frac{\partial}{\partial t}\psi(\mathbf{r},t) = \left[-\frac{\nabla^2}{2m} + V(\mathbf{r})\right]\psi(\mathbf{r},t)$$

if we replace $t \to -t$ we obtain

$$-i\frac{\partial}{\partial t}\psi(\mathbf{r},-t) = \left[-\frac{\nabla^2}{2m} + V(\mathbf{r})\right]\psi(\mathbf{r},-t)$$

where the wave function $\psi(\mathbf{r},-t)$ does not satisfy the same Schroedinger equation as $\psi(\mathbf{r},t)$. However, by taking the complex conjugate of both members in the last equation, we have

$$i\frac{\partial}{\partial t}\psi^*(\mathbf{r},-t) = \left[-\frac{\nabla^2}{2m} + V(\mathbf{r})\right]\psi^*(\mathbf{r},-t)$$

where we see that the function $\psi^*(\mathbf{r},-t)$ satisfies the same equation as $\psi(\mathbf{r},t)$. This implies that for spinless particles the complex conjugation operator plays the role of reversing the direction of propagation of time. Therefore the operator of complex conjugation K has the same effect on $\mathbf{r}$ and $\mathbf{p}$ as the time reversal T:

$$K\mathbf{r}K^\dagger = \mathbf{r} \quad K\mathbf{p}K^\dagger = -\mathbf{p} \tag{A.3}$$

Therefore, for spinless particles the time reversal operator T is proportional to K up to a phase factor, that we can choose to be unity, so that $T = K$ and $T\psi(\mathbf{r}) = \psi^*(\mathbf{r})$. Since the momentum appears quadratically in Hamiltonian (A.1), we have that

$$TH(\mathbf{r}, \mathbf{p})T^\dagger = H(\mathbf{r}, -\mathbf{p}) = H(\mathbf{r}, \mathbf{p})$$

that is to say, the Hamiltonian and the time reversal operator commute (when the Hamiltonian does not depend on odd powers of the momentum, or equivalently, when H is real):

$$[T, H] = 0$$

The time reversal operator is antiunitary (as well as the complex conjugation), meaning that given a vector space L, for any $\phi, \psi \in L$:

$$\langle T\phi | T\psi \rangle = \langle \phi^* | \psi^* \rangle = \langle \phi | \psi \rangle^* = \langle \psi | \phi \rangle$$

and

$$T(a\psi + b\phi) = a^* T\psi + b^* T\phi$$

Spinful Particles For spinful particles, we need to know what is the action of the time reversal operator on the angular momentum. As for the orbital angular momentum, we know that this is given by $\mathbf{L} = \mathbf{r} \times \mathbf{p}$, so it is straightforward to show that

$$T(\mathbf{r} \times \mathbf{p})T^\dagger = -(\mathbf{r} \times \mathbf{p})$$

that is, the time reversal operator and the orbital angular momentum anticommute. The spin operator $\mathbf{s}$, being an angular momentum even if not of orbital origin, anticommutes as well with T, that is

$$T\mathbf{s}T^\dagger = -\mathbf{s} \tag{A.4}$$

In the standard representation in which the projection of the spin operator on the z axis is taken to be diagonal, then the matrices representing s_x and s_z are real, whereas the matrix representing s_y is purely imaginary. Therefore, under the action of complex conjugation, one has

$$Ks_xK^\dagger = s_x \qquad Ks_yK^\dagger = -s_y \qquad Ks_zK^\dagger = s_z \tag{A.5}$$

Therefore, for a particle with spin we need to modify the operator T by introducing a new operator U such that

$$T = UK \rightarrow TK = UK^2 = U$$

and that satisfies eq. (A.4). From the latter equality we deduce that since both T and K are antiunitary, then U must be unitary. Also, we can easily deduce its effect on the position and momentum operators:

$$U\mathbf{r}U^\dagger = (TK)\mathbf{r}(TK)^\dagger = T(K\mathbf{r}K^\dagger)T^\dagger = T\mathbf{r}T^\dagger = \mathbf{r}$$

$$U\mathbf{p}U^\dagger = (TK)\mathbf{p}(TK)^\dagger = T(K\mathbf{p}K^\dagger)T^\dagger = T(-\mathbf{p})T^\dagger = \mathbf{p}$$

implying that U commutes with both. On the other side, its action on the matrices s_x, s_y and s_z representing the spin operators can be calculated, yielding:

$$Us_xU^\dagger = (TK)s_x(TK)^\dagger = T(Ks_xK^\dagger)T^\dagger = Ts_xT^\dagger = -s_x$$

$$Us_yU^\dagger = (TK)s_y(TK)^\dagger = T(Ks_yK^\dagger)T^\dagger = T(-s_y)T^\dagger = s_y$$

$$Us_zU^\dagger = (TK)s_z(TK)^\dagger = T(Ks_zK^\dagger)T^\dagger = Ts_zT^\dagger = -s_z$$

by virtue of eqs. (A.4) and (A.5). Matricially, this reads:

$$U(s_x, s_y, s_z) = (s_x, s_y, s_z)\begin{pmatrix} -1 & 0 & 0 \\ 0 & 1 & 0 \\ 0 & 0 & -1 \end{pmatrix} = (s_x, s_y, s_z)R_y(\pi)$$

where

$$R_y(\phi) = \begin{pmatrix} \cos\phi & 0 & \sin\phi \\ 0 & 1 & 0 \\ -\sin\phi & 0 & \cos\phi \end{pmatrix}$$

Now, since the generator of a transformation of $SO(3)$ corresponding to rotation around an arbitrary axis $\mathbf{u}$ is $I_\mathbf{u} = -\mathbf{L}\cdot\mathbf{u}/|\mathbf{u}|$, the corresponding rotation operator by an arbitrary angle ϕ can be written as

$$R_\mathbf{u}(\phi) = e^{i\phi I_\mathbf{u}} = e^{-i\phi\mathbf{L}\cdot\mathbf{u}/|\mathbf{u}|}$$

Therefore, the operator generating a rotation of π about the y axis can be written as

$$U = e^{-i\pi s_y}$$

and thus

$$T = UK = e^{-i\pi s_y}K$$

If one has a system of n particles having arbitary spins, the time reversal operator can be written as

$$T = e^{-i\pi s_y^1}e^{-i\pi s_y^2}...e^{-i\pi s_y^n}K \tag{A.6}$$

where s_y^j is the spin operator for the j-th particle. It is interesting to notice that all of the operators comprising the above product commute with each other, because all matrices of the kind $e^{-i\pi s_y^j}$ are real (since the operators s_y^j have been chosen to be purely imaginary), and therefore commute with K that does not act on them, and also with each other since they operate on the spin variables of different particles. Therefore the order of the factors in U is unimportant.

Spin-1/2 particles In the case of spin-1/2 particles, $s_i = \sigma_i/2$ for $i = x, y, z$. Therefore

$$T = e^{-i\pi\sigma_y/2}K$$

In order to rewrite the time reversal operator, we notice that we can expand the exponential $e^{i\phi\sigma_y}$ as

$$e^{i\phi\sigma_y} = \cos\phi\sigma_0 + i\sin\phi\sigma_y$$

where we have made use of the fact that $\sigma_y^{2n} = \sigma_0$ and that $\sigma_y^{2n+1} = \sigma_y$. In matricial form:

$$e^{i\phi\sigma_y} = \begin{pmatrix} \cos\phi & \sin\phi \\ -\sin\phi & \cos\phi \end{pmatrix}$$

Thus, for $\phi = -\pi/2$:

$$e^{-i\pi\sigma_y/2} = -i\sigma_y$$

So that finally one has

$$T = -i\sigma_yK$$

Kramer's Theorem By squaring eq. (A.6), one gets

$$T^2 = e^{-2i\pi s_y^1} e^{-2i\pi s_y^2} ... e^{-2i\pi s_y^n}$$

The j-th factor of this product will be equal to $+1$ or -1 depending on whether the spin of the j-th particle s_y^j is an integral or half-odd-integral. Therefore T^2 can be equal to $+1$ or -1 depending on whether the number of particles with half-odd-integral spin is even or odd.

Theorem (Kramer's Theorem)**.** *A system with an odd number of electrons that is invariant under time reversal (that is, such that $T^2 = -1$ and that $[T, H] = 0$) has energy levels that are evenfold degenerate. This degeneracy is known as Kramer's degeneracy.*

Proof. We have seen that if a system has time reversal symmetry, then the Hamiltonian and the time reversal operator commute. This implies that:

$$TH\psi = HT\psi$$

and at the same time

$$TH\psi = TE\psi = ET\psi$$

Consequently

$$H(T\psi) = E(T\psi)$$

Therefore ψ and $T\psi$ are solutions of the same Hamiltonian corresponding to the same eigenenergy E. Let's suppose that ψ is a non-degenerate eigenfunction. Then $T\psi$ must be proportional to ψ: $T\psi = c\psi$. We consider the effect of T^2 on ψ:

$$T^2\psi = T(T\psi) = T(c\psi) = c^* T\psi = c^* c\psi = |c|^2\psi$$

Here, if $T^2 = 1$, it means that $|c|^2 = 1$ and therefore c is a phase factor. However, if $T^2 = -1$, then one should have $|c|^2 = -1$, which is impossible. We deduce that if T squares to -1, then the eigenfunctions of the Hamiltonian must be degenerate and the degeneracy must be at least twofold since ψ and $T\psi$ are independent eigenfunctions of H associated to the same energy E. By further noticing that T^2 commutes with the Hamiltonian, and that $T^2\psi = -\psi$, that is, a multiple of ψ, the net degeneracy must be even. □

Lemma. *In a system with an odd number of electrons that is invariant under time reversal, the functions ψ and $T\psi$ are orthogonal.*

Proof. Consider the product $\langle T^2\psi | T\psi \rangle$:

$$\langle T^2\psi | T\psi \rangle = \langle T(T\psi) | T\psi \rangle = \langle \psi | T\psi \rangle$$

However, it is also true that

$$\langle T^2\psi | T\psi \rangle = -\langle \psi | T\psi \rangle$$

Therefore

$$\langle \psi | T\psi \rangle = -\langle \psi | T\psi \rangle \Rightarrow \langle \psi | T\psi \rangle = 0$$

□

Appendix B

Elements of Group Theory

In this appendix we review some basic concepts of group theory that prove useful for understanding the analysis carried our in the fifth chapter.

B.1 Groups and their Properties

Definition B.1.1 (Group)**.** A group is a set of elements with a binary operation (or group multiplication) defined between them, that satisfy the following properties:

1. Closure. Given any two elements A and B in the group, the product of the multiplication operation between these elements $AB = C$ is itself an element of the group.
2. Associativity. The multiplication is associative, meaning that $A(BC) = (AB)C$
3. Existence of a unit element E. This element is such that for each element A in the group, $AE = EA = A$.
4. Existence of the inverse. For each element A in the group, there exists an element A^{-1} that is itself in the group and such that $AA^{-1} = A^{-1}A = E$.

Definition B.1.2 (Order of a Group)**.** The order of a (finite) group is the number of elements in the group.

Definition B.1.3 (Abelian Group)**.** A group is said to be Abelian or commutative if for each pair of elements A and B in the group holds $AB = BA$.

Definition B.1.4 (Covering Operation)**.** A covering operation of a symmetrical object is any operation (rotation, reflection..) that brings the object into a form that is indistinguishable from its original form.

Definition B.1.5 (Group-multiplication Table)**.** A multiplication table of a group of order g is a $g \times g$ table where each entry is the product of the row element times the column element.

Definition B.1.6 (Homomorphism)**.** An homomorphism is a mapping $f : G \to G'$ of a group G onto another group G' that preserves multiplication. This means that given two elements A and B in G that are mapped by f into two elements $A' = f(A)$ and $B' = f(B)$ in G', then the product element $C = AB$ is mapped onto the product element of the mapped elements $C' = A'B' = f(C)$.

Definition B.1.7 (Isomorphism)**.** An isomorphism is an homomorphism where the mapping is one-to-one. If $AB = C$, this implies that $A'B' = C'$ and viceversa. Two groups with the same multiplication table are isomorphic. If the isomorphism is between two groups G and G' such that $G = G'$, then its is called an automorphism.

Definition B.1.8 (Subgroup)**.** A subgroup of a group G is a subset of G that in itself forms a group.

Definition B.1.9 (Order of an Element)**.** The order of an element A in a group is the least positive integer m such that $A^m = E$.

Definition B.1.10 (Period of an element/Cyclic Group)**.** Given an element A (of order m) in a group, its period is the sequence formed by all its inequivalent powers $A = \{A, A^2, A^3, ..., A^m = E\}$. It is a group in itself and it is called a cyclic group of order m. If it is part of a larger group, then it is called a cyclic subgroup. All cyclic groups are by definition Abelian.

B.1.1 Conjugacy and Classes

Definition B.1.11 (Conjugated Elements)**.** Two elements A and B in a group are said to be conjugated if there is another element X in the group such that $A = XBX^{-1}$ or, equivalently, $B = X^{-1}AX$. This property is a reciprocal property of the two elements.

Theorem B.1.1. *Two elements A and B in a group that are cojugated with a third element C, are conjugated between them.*

Definition B.1.12 (Conjugacy Class)**.** All the elements of a group that are cojugated among themselves form a conjugacy class. The class including the element A_i is formed by all the elements $A_i = \{EA_iE^{-1}, A_2A_iA_2^{-1}, ..., A_gA_iA_g^{-1}\}$ (with g the order of G), some of which might be repetitions. By doing so, one can divide all the elements of the group into different classes.

Note that:

- The identity is always in a class by itself, given that $XEX^{-1} = XX^{-1} = E$ for all X in G.
- All the other classes don't include the identity.
- Abelian groups only admit classes formed by a single element, since $XAX^{-1} = XX^{-1}A = A$.
- If the elements are matrices, then all the elements of a class must have the same trace.

Theorem B.1.2. *If C is a complete class of a group G, then $X^{-1}CX = C$, with $X \in G$.*

Theorem B.1.3. *Any collection C of elements of a group that satisfies the relation $X^{-1}CX = C$ is a complete class or composed of only complete classes.*

Remark. A product of two complete classes satisfies $C_iC_j = X^{-1}C_iXX^{-1}C_jX = X^{-1}C_iC_jX$, meaning that C_iC_j consists of complete classes. Formally, this means that a product of two complete classes can be express as a linear combination of complete classes:

$$C_iC_j = \sum_k c_{ijk}C_k$$

where the coefficients c_{ijk} count the number of times a given complete class C_k appears in the product C_iC_j.

B.1.2 Direct Product Group

Definition B.1.13 (Direct Product Group)**.** Given two groups $A = \{E, A_2, ..., A_a\}$ of order a and $B = \{E, B_2, ..., B_b\}$ of order b, the direct product of A and B, $G = A \times B$ is defined as the group of order $g = ab$ consisting of elements obtained by taking the products of all elements of A with all elements of B

$$G = A \times B = \{E, A_2, ..., A_a\} \times \{E, B_2, ..., B_b\} =$$

$$\{E, B_2, ..., B_b, A_2, A_2B_2, ..., A_2B_b, ..., A_a, A_aB_2, ..., A_aB_b\} =$$

provided that: (1) A and B have no elements in common except the identity E and (2) all the elements of A commute with all elements of B.

Proposition B.1.4. *The direct-product group is a group.*

B.2 Theory of Group Representations

B.2.1 Representations and their Properties

A representation of a group is a collection of concrete mathematical objects that is homomorphic with the original group. We restric our attention to representations that are square matrices with nonzero determinant where the multiplication operation is given by the standard matrix product. By the properties of groups, this means that we associate a square matrix $\Gamma(A)$ to each element of the group $A \in G$, such that:

1. Multiplication is preserved, so that if $AB = C$, then $\Gamma(A)\Gamma(B) = \Gamma(AB) = \Gamma(C)$
2. Multiplication is associative because of the properties of matrices
3. $\Gamma(E) = E$, where $\gamma(E)$ is the identity matrix
4. Since the matrices have nonzero determinant, they can be inveerted

Definition B.2.1 (Representation)**.** A collection of square matrices that satifies the above criteria is said to be a representation of the group G.

Definition B.2.2 (Dimensionality of a Representation)**.** The Dimensionality (or dimension) of a representation is given by the dimension of the square matrices composing the representation.

Action of a Representation Let L_n be an n-dimensional vector space on which the operators of G act and let $\phi_{i=1}^n$ be an orthonormal basis in L_n. The operation of the element A of the group G on one of these basis functions is:

$$A|\phi_i\rangle = \sum_{j=1}^{n} \Gamma_{ij}(A)|\phi_j\rangle \tag{B.1}$$

where $\Gamma(A)_{ji}$ is the matrix representing the group element A in the basis $\phi_{i=1}^n$. By projecting both sides of (B.1) on the function ϕ_k, one has:

$$\langle\phi_k|A|\phi_i\rangle = \sum_{j=1}^{n} \Gamma(A)_{ji}\langle\phi_k|\phi_j\rangle = \sum_{j=1}^{n} \Gamma(A)_{ji}\delta_{jk} = \Gamma_{ik}$$

These matrices, obtained for all the elements of the group, generate all the representations of G.

Theorem B.2.1. *Similarity transformations between representations of the kind* $\Gamma^{(1)}(A) = S^{-1}\Gamma^{(2)}(A)S$ *leave matrix operations unchanged.*

Definition B.2.3 (Equivalent Representations)**.** If two representations are related by a similarity transformation of the kind $\Gamma^{(1)} = S^{-1}\Gamma^{(2)}S$, they are said to be equivalent.

Definition B.2.4 (Irreducible Representations or Irreps)**.** A representation is said to be irreducible if it is possible to express all the matrices comprising the representation in block form by means of the same similarity transformation and with the blocks having the same structure for all the elements of the group.

B.2.2 Great Orthogonality Theorem

Lemma B.2.2. *It is always possible to find an equivalent unitary matrix representation from a given matrix representation of a group by a similarity transformation.*

Lemma B.2.3. *Given two different irreducible representations of a group* $\Gamma^{(1)}(A_i)$ *and* $\Gamma^{(2)}(A_i)$ *of dimensionalities* l_1 *and* l_2 *respectively, if a rectangular matrix* M *exists such that* $M\Gamma^{(1)}(A_i) = \Gamma^{(2)}(A_i)M$*, then:*

1. *If* $l_1 = l_2$*, then* $M = 0$ *or* $\det(M) \neq 0$ *and the matrix* M *is invertible, and therefore the two irreps are equivalent, given that one can be expressed via a similarity transformation with respect to the other:* $\Gamma^{(1)}(A_i) = M^{-1}\Gamma^{(2)}(A_i)M$*.*
2. *If* $l_1 \neq l_2$*, then* $M = 0$*.*

Theorem B.2.4 (Great Orthogonality Theorem)**.** *Considering all the possible representations of a group that are: (i) inequivalent; (ii) irreducible; (iii) unitary, the following equality holds:*

$$\sum_R \Gamma^{(i)}(R)_{\mu\nu}\Gamma^{(j)}(R)_{\alpha\beta} = \frac{g}{l_i}\delta_{ij}\delta_{\mu\alpha}\delta_{\nu\beta} \tag{B.2}$$

where: (i) l_i *is the dimensionality of the i-th representation,* g *is the order of the group and* R *runs over all the elements of the group.*

Theorem B.2.5 (Dimensionality Theorem)**.** *Given a group of order* g *and given all its inequivalent irreducible representations* $\Gamma^{(i)}$ *(each of dimensionality* l_i *and therefore comprising matrices with* l_i^2 *entries each), the following relation holds:*

$$\sum_i l_i^2 = g \tag{B.3}$$

where the sum runs over all the possible inequivalent irreducible representations.

B.2.3 Characters

Given the high degree of arbitrariness of a representation, one is led to look for the invariant properties that characterize all equivalent irreducible representations: since these are related by a similarity transformation, the property that is preserved is their trace: all equivalent irreps have the same trace. Of course each representation has g elements, that is, matrices that represent the g elements of the abstract group, and each matrix has a distinc trace. We therefore define the character of the i-th representation as the sequence of the traces of its g elements: $\left(\chi^{(i)}(E), \chi^{(i)}(A_2), ..., \chi^{(i)}(A_g)\right)$, where

$$\chi^{(i)}(R) = \mathrm{Tr}\,\Gamma^{(i)}(R) = \sum_{\mu=1}^{l_1}\Gamma^{(i)}(R)_{\mu\mu} \tag{B.4}$$

Now, since the elements of a class are all related by conjugacy, then their matrix representations are related by similarity transformations. This means that all the matrices representing elements in a same class have the same traces. Therefore a concise form of specifying the character of a representation os that of listing the traces of one element for each classe instead than of all its elements, given that elements of the same class have the same traces:

$$\left(\chi^{(i)}(E), \chi^{(i)}(A_2), ..., \chi^{(i)}(A_g)\right) \rightarrow \left(\chi^{(i)}(C_1), ..., \chi^{(i)}(C_n)\right)$$

where C_k indicate the k-th class, and $n \leq g$.

Proposition B.2.6 (First Orthogonality Relation for Characters)**.**

$$\sum_{k=1}^{n} \chi^{(i)}(C_k)^* \chi^{(j)}(C_k) N_k = g\delta_{ij} \tag{B.5}$$

Definition B.2.5 (Character Table)**.** The character table is a square matrix whose rows indicate the different irreps and whose columns indicate the classes in which the elements of the group are arranged. Each entry is the trace of the class indicated by the column for a given irreducible representation.

Proposition B.2.7 (Second Orthogonality Relation for Characters)**.**

$$\sum_{i=1}^{h} \chi^{(i)}(C_k)^* \chi^{(j)}(C_{k'}) = \frac{g}{N_k} \delta_{kk'} \tag{B.6}$$

Remark. The first orthogonality relation for characters implies that if one takes the rows of the table and take the vector product multiplying each term of the product by the number of elements in the corresponding class (N_k), they are mutually orthogonal. The second orthogonality theorem, instead, implies that if one takes the columns of the table and take the vector product multiplying each term of the product by the number of elements in the corresponding class, they are mutually orthogonal (basically, same as the first but interchanging rows ad columns).

Rules for Constructing a Character Table

1. The number of irreducible representations is equal to the number of classes.
2. The dimensionalities of the irreducible representations l_i can be deduced by making use of Eq. (B.3). with g the order of the group. There are two further notions that can be employed: (i) There is always a unit element E, that always forms a class by itself, and it is always represented by an identity matrix. Therefore for a given representation of dimensionality l_i, the trace of the matrix that is the representation of E is $\chi^{(i)}(E) = l_i \; \forall \, i$: the character of the class constituted by E is the sequence $(\chi^{(1)}(E) = l_1, \chi^{(2)}(E) = l_2, ...)$ and it always represents the first column of the table. (ii) There is always a one-dimensional representation in which each group element is represented by unity, therefore the first row of the table can always be written as a sequence of 1: $(\chi^{(1)}(C_1) = 1, \chi^{(1)}(C_2) = 1, ...)$.
3. The rows of the table (each referring to a different irrep) must be orthogonal and normalized to g, with a weighing factor given by N_k, the number of elements present in each class. This is mathematically expressed by the first orthogonality relation, Eq. (B.5).

4. The columns of the table (each referring to a different class C_k) must be orthogonal vectors normalized to the factor g/N_k. This is mathematically expressed by the second orthogonality relation, Eq. (B.6).

5. Elements within a row are related by:

$$N_j\chi^{(i)}(C_j)N_k\chi^{(i)}(C_k) = l_i\sum_l c_{jkl}N_l\chi^{(i)}(C_l) \tag{B.7}$$

B.2.4 Decomposition of Reducible Representations

The character of a reducible representation Γ is given by the sum of its constituent irreducible representations $\Gamma^{(i)}$, weighted by the number of times they appear in the reducible representation a_i, that is

$$\chi(R) = \sum_i a_i\chi^{(i)}(R) \tag{B.8}$$

Where a_i is easily determined to be given by

$$a_i = \frac{1}{g}\sum_R \chi(R)\chi^{(i)}(R)^* = \sum_k \chi(C_k)\chi^{(i)}(C_k)^*N_k \tag{B.9}$$

meaning that the number of times that an irreducible representation is present in a reducible one is uniquely determined by the characted of the representation, assuming that the character table is know (and specifically the corresponding row).

B.2.5 Representations in Quantum Mechanics

Transformation of Coordinates and Functions The group that one is typically interested in, in a determined quantum mechanics problem, is the group of symmetry operations (and the operators generating them) that leave the Hamiltonian of the problem invariant. The operators generating these symmetry operations are given by real orthogonal matrices R (such that $U^T = U^{-1}$) that implement a transformation of coordinates $x \to x' = Rx$. Components-wise:

$$x'_i = \sum_j R_{ij}x_j$$

By inverting this relation, one has that

$$x_i = \sum_j R^{-1}_{ij}x'_j = \sum_j R_{ji}x'_j$$

One can introduce a group of operators $\{P_R\}$ that is isomorphic to this group of orthogonal transformations $\{R\}$, but that acts on functions of coordinated in spite of coordinates. The new operators are defined such that the combined application of P_R on a function of the coordinates $f(x)$ and the application of the associated coordinate transformation R must compensate, that is

$$P_R f(Rx) = f(x)$$

Rephrased:

$$f(Rx) = P_R^{-1}f(x) = P_{R^{-1}}f(x)$$

or

$$P_R f(x) = f(R^{-1}x) \tag{B.10}$$

Proposition B.2.8. *The group formed by the operators $\{P_R\}$ is isomorphic with the group of operators $\{R\}$, that is, it is a group and satisfies the multiplication operation $P_R P_S = P_{RS}$.*

Definition B.2.6 (Group of the Schroedinger Equation)**.** The group of the Schroedinger equation is the group formed by all the operators P_R that commute with the Hamiltonian, representing all the coordinate transformations that leave the Hamiltonian invariant. This group is a group because: (i) inverse coordinate transformations exist; (ii) the product of two operators that leave the Hamiltonian invariant must leave the Hamiltonian invariant as the application of the first operator yields the Hamiltonian itself and same goes with the successive application of the second operator.

Proposition B.2.9. *Given an eigenfunction ψ_n of the Hamiltonian H associated to the eigenvalue E_n such that the eigenvalue problem that is satisfied is $H\psi_n = E_n\psi_n$, then $H(P_R\psi_n) = E_n(P_R\psi_n)$ for all the operators P_R associated to operations on the coordinates that leave the Hamiltonian invariant.*

Representations of the Group of the Schroedinger Equation

Given an eigenvalue E_n of an Hamiltonian H, l_n times degenerate, one can choose an l_n-dimensional set of orthonormal eigenfunctions belonging to this eigenvalue. By applying one of the operators P_R that commute with the Hamiltonian on one of these functions, then an eigenfunction belonging to the same eigenvalue E_n is found. This implies that this function can be expressed as a linear combination of the functions of the orthonormal set, that is, the set forms an l_n-dimensional basis for the l_n-dimensional space of the eigenfunctions belonging to E_n. This l_n-dimensional space is a subspace of the whole space of eigenfunctions of H, invariant under all the operations of the group of the Schroedinger equation. Thus, the application of each operator P_R on a function in this subspace is expressible in terms of the application of a matrix $\Gamma^{(n)}(R)$ on all of the basis functions. In matricial form, being $(\psi_1, \psi_2, ..., \psi_{l_n})$ the set of orthonormal basis functions:

$$P_R\psi_i^{(n)} = \sum_{j=1}^{l_n} \Gamma_{ij}^{(n)}(R)\psi_j^{(n)} \tag{B.11}$$

The matrices $\Gamma_{ij}^{(n)}(R)$ form an l_n-dimensional representation of the group of the Schroedinger equation corresponding to the eigenvalue E_n. This representation can be based on each l_n-dimensional set of eigenfunctions belonging to the same eigenvalue. This representation is irreducible because applying an operator of the group of the Schroedinger equation to any eigenfunction, one obtains another eigenfunction degenerate with it. Thus no smaller matrices could be employed to express general transformations.

Proposition B.2.10. *The matrices defined above do form a representation of the Schroedinger equation group, that is $\Gamma(RS) = \Gamma(R)\Gamma(S)$.*

Remark. The set of l_n degenerate eigenfunctions $\{\psi_i\}_{i=1}^{l_n}$ belonging to the eigenvalue E_n form a basis for the irreducible l_n-dimensional representation Γ of the group of the Schroedinger equations.

Proposition B.2.11. *If the set is orthonormal, then the representation is unitary.*

Quantum Numbers

Proposition B.2.12. *Two representations associated with a different choice of basis functions are related by a similarity transformation and therefore are equivalent.*

As a consequence, two representations of the group of the Schroedinger equation belonging to the same eigenvalue but having different basis eigenfunctions are related by a symilarity transformation. This means that, modulo a similarity transformation, the irreducible representation of the Schroedinger equation associated to a given eigenvalue is unique. Each set of eigenfunctions can uniquely be classified according to the irreducible representation to which it belongs, that is the representation for which those eigenfunctions form a basis. When one choses a representation, then each eigenfunction can be specified even more precisely by giving the row index within the representation. This corresponds to defining the quantum number of the problem: the index of the representation plus the index of the row within that representation corresponding to a given function. The degeneracy of the quantum number is the dimensionality of the representation.

Abelian and Cyclic Groups In Abelian groups all elements stand in a class on their own, and thefeore there are as many classes (each comprising a single elements) as elements in the group. Same goes for representations. Owing to the rule (B.3), this means that all the representations are unidimensional and therefore are given by complex numbers. As a consequence, if the symmetry group of a given Hamiltonian is Abelian, this means that the Hamiltonian admits no degeneracies of its eigenvalues. Cyclic groups are Abelian and therefore they admit only one-dimensional representations. Since a cyclic group of order g comprises the elements $\{E, A, A^2, ..., A^g = E\}$, then if the complex number that is the representation of A is $\Gamma(A) = r$, then $\Gamma(A^n) = \Gamma(A)^n = r^n$. For the periodicity of the group, one has that $r^g = 1$, satisfied by $r = e^{2\pi i n/g}$. A way of fomalizing this is to define the n-th one-dimensional representations of a cyclic group of order g as $\Gamma^{(p)} = e^{2\pi i n/g}$.

2D Rotation Group and Conservation of Angular Momentum If we consider rotations by an arbitrary angle about an axis of a system with full rotational symmetry, then there are infinite elements in the group (group of infinite order) of its symmetry operations (that is, rotations of all angles). Also, this group is Abelian and therefore the representations are merely numbers. If we indicate the angles of rotation by ϕ the multiplication property of the group must enforce the identity $\Gamma(\phi_1)\Gamma(\phi_2) = \Gamma(\phi_1 + \phi_2)$ that can be satisfied by an exponential relation:

$$\Gamma(-\phi) = e^{im\phi} \quad m = 0, \pm 1, \pm 2, ...$$

where the restriction of the values of m stems from the fact that $\Gamma(\phi = 2\pi) = 1$. Now, if one considers a function $\psi_m(r, \theta, \phi)$ and rotates it by ϕ_0, one gets that:

$$\psi_m(r, \theta, \phi - \phi_0) = P_{\phi_0}\psi_m(r, \theta, \phi) = \Gamma^{(m)}(\phi_0)\psi_m(r, \theta, \phi) = e^{-im\phi_0}\psi_m(r, \theta, \phi)$$

that is, it depends on the angle ϕ via the factor $e^{im\phi}$. This tells us that an eigenfunction of an Hamiltonian that is invariant under rotations about an axis (in other words: whose symmetry group is the group of rotations about an axis) has a dependence on the angle of rotation about that axis of the kind $\psi_m(r, \theta, \phi) = f(r, \theta)e^{im\phi}$, that is a consequence of the fact that the angular momentum about that axis of symmetry is conserved and has as a consequence the existence of a good quantum number m.

B.2.6 Basis Functions for Irreps

If the irreducible representations with which we have to deal have a dimensionality larger than one, then two labels (or indices) are needed in order to identify the basis functions: (i) the index j of the representation (there is an irreducible representation for each eigenvalue of the Hamiltonian); (ii) the row κ of the representation to which the function belongs. We denote the basis function belonging to the κ-th row of the j-the representation as $\varphi_\kappa^{(j)}$. All the other functions of the basis, $\{\varphi_\lambda^{(j)}\}_{\lambda=1}^{l_j-1}$ are called the partners of this function. As we know from before, the result of operating with one of the symmetry operators of the group of the Schroedinger equation on this function, yields a linear combination of the very operator plus all of its partners with coefficients given by the irreducible representation that has a basis those functions:

$$P_R\varphi_\kappa^{(j)} = \sum_{\lambda=1}^{l_j} \Gamma_{\kappa\lambda}^{(j)}(R)\varphi_\lambda^{(j)} \tag{B.12}$$

If we now apply the operator $\Gamma_{\mu\nu}^{(i)}(R)^*$ and sum over R both sides of this equation, we get:

$$\sum_R P_R\Gamma_{\mu\nu}^{(i)}(R)^*\varphi_\kappa^{(j)} = \frac{g}{l_i}\delta_{\mu\kappa}\delta_{ij}\varphi_\nu^{(j)}$$

Therefore, we can define a *transfer operator* as

$$P_{\mu\nu}^{(i)} = \frac{l_i}{g}\sum_R P_R\Gamma_{\mu\nu}^{(i)}(R)^* \tag{B.13}$$

where the effect of applying this operator on the basis function belonging to the κ-th row of the j-th representation is

$$P_{\mu\nu}^{(i)}\varphi_\kappa^{(j)} = \delta_{\mu\kappa}\delta_{ij}\varphi_\nu^{(j)} \tag{B.14}$$

this is nonzero only when $i = j$ and $\mu = \kappa$, that is, this operation returns non-zero only if the operator $P_{\mu\nu}^{(i)}$ is applied on the μ-th row of the i-th representation, and in this case it yields $\varphi_\nu^{(i)}$:

$$P_{\mu\nu}^{(i)}\varphi_\mu^{(i)} = \varphi_\nu^{(i)} \tag{B.15}$$

Remark. Since $P_{\mu\mu}^{(i)}$ is a linear operator, this results tell us that any given combination of two or more functions belonging to the same row (say, the μ-th) of different but equivalent representations (that is, related by a similarity transformation) like $f_\mu^{(i)} = \alpha\varphi_\mu^{(i)} + \beta\psi_\mu^{(i)}$, will itself be a function belonging to the μ-th row of the i-th representation.

Theorem B.2.13. *Given c irreps $\Gamma^{(1)}, \Gamma^{(2)}, ..., \Gamma^{(c)}$ of a group of operators $P_R = \{P_E, P_{A_2}, ..., P_{A_g}\}$ then any function defined in the space operated by these operators F is expressible as the sum*

$$F = \sum_{j=1}^{c}\sum_{\kappa=1}^{l_j}\varphi_\kappa^{(j)}$$

where $\varphi_\kappa^{(j)}$ is a function that belongs to the κ-th row of the j-th irrep.

As a consequence, summing both sides of Eq. (B.14) with $\nu = \mu$ over j and κ, one gets:

$$P^{(i)}_{\mu\mu} \sum_{j,\kappa} \varphi^{(j)}_{\kappa} = \sum_{j,\kappa} \delta_{\mu\kappa}\delta_{ij}\varphi^{(j)}_{\mu}$$

that is:

$$P^{(i)}_{\mu\mu} F = \varphi^{(i)}_{\mu} \tag{B.16}$$

This makes $P^{(i)}_{\mu\mu}$ a projection operator that projects out of *any* function F the part of it that belongs to the μ-th row of the j-th representation.

Basis Function Generating Machine Given any representation, we have now all the ingredients to generate a set of basis functions. Given a generic function F, we project out one function $\varphi^{(j)}_{\mu}$ by means of $P^{(i)}_{\mu\mu}$. Then, the use of the transfer operator $P^{(i)}_{\lambda\mu}$ allows to generate all the vectors of the basis that are partners of this vector.

Theorem B.2.14. *Two functions that belong to different irreps of different rows of the same irrep are orthogonal.*

If instead of knowing the entire representation of a given group, we only have the character table, we still can know something about the basis of the representation. This can be seen by taking the definition of the transfer operator for $\mu = \nu$ and summing over μ. One obtains

$$P^{(i)} = \sum_{\mu=1}^{l_i} P^{(i)}_{\mu\mu} = \sum_{R} P_R \chi^{(i)}(R)^* \tag{B.17}$$

where $\chi^{(i)}_{\mu}(R)^*$ are the characters of the representation. Here one can repeat argumentations analogous to those presented previously, and see that:

$$P^{(i)}\varphi^{(i)} = \varphi^{(i)}$$

meaning that any function expressible as a combination of only functions belonging to a given representation is an eigenfunction of the operator $P^{(i)}$ with eigenvalue 1, and

$$P^{(i)} F = \varphi^{(i)} \tag{B.18}$$

telling us that the operator $P^{(i)}$ has the effect of projecting out of a generic function F the component that belongs to the i-th representation.

B.2.7 Direct Products and Representations

Proposition B.2.15. *Given two representations a and b of a same group G, the matrices that are obtained as the direct product of these two representations form a representation of G.*

Proposition B.2.16. *The basis of the direct product of two irreducible representations is given by all the products of the basis functions of the constituent irreducible representations. The Hilbert space space spanned by these basis functions is the direct product of the Hilbert spaces spanned by the original basis functions.*

Proposition B.2.17. *The representation built as the direct product of the representations of two commuting groups H and G is a representation of the direct product group $K = H \times G$.*

Proposition B.2.18. *If the two representations $\Gamma^{(h)}$ or $\Gamma^{(g)}$ of H and G are irreducible, then their direct product is an irreducible representations of the direct product group.*

Proposition B.2.19. *All irreducible representations of the direct product group H are direct products of an irreducible representation of H and one of G.*

Proposition B.2.20. *The character of any direct-product representation is the product of the characters of the component representations.*

B.3 Crystallographic Symmetries

The geometrical symmetry transformations of a crystal are of three types: (i) translations, (ii) rotations, reflections and inversions and (iii) combinations of the above.

B.3.1 Point Groups and Space Groups

The transformations of type (ii) are also called point symmetry operations, and they have the property of leaving at least one point undisplaced. The set of such symmetry transformations for a crystal define its so called *point group*. The group of transformations that include the point group of a system, plus itstranslational symmetry, defines instead its *space group*. The only n-fold rotations (that is, rotations by an angle $2\pi/n$ around an axis passing through a lattice point) consistent with translational symmetries are those with $n = 1, 2, 3, 4, 6$. This allows for the existence of 32 point groups. If one chooses as the origin of the cartesian coordinates the point which is invariant under the point group, then the latter only contains:

- rotations about axes passing through the origin
- reflections in planes passing through the origin
- inversion, that is a rotation followed by a reflection or viceversa (also called improper rotation)

The full symmetry group of the crystal Hamiltonian is the space group to which the crystal belongs. The reciprocal lattice has the same point group symmetry as the direct lattice. According to the Bloch theorem, the Hamiltonian eigenfunctions have definite translational properties determined by a wave vector $\mathbf{k}$ and the values of an eigenfunction at equivalent points in different unit cells are related by a phase factor:

$$\psi(\mathbf{r} + \mathbf{t}) = e^{i\mathbf{k}\cdot\mathbf{r}}\psi(\mathbf{r}) \tag{B.19}$$

This tells us that every value of $\mathbf{k}$ gives an irreducible representation of the translational group. Now, since $\mathbf{k}' = \mathbf{k} + \mathbf{G}$, all the points of the reciprocal lattice that are related to $\mathbf{k}$ by a primitive reciprocal vector $\mathbf{G}$ correspond to the same irreducible representation of the translational group. In order to characterize each irrep univoquely by a single $\mathbf{k}$, we choose a unit cell in the reciprocal lattice and from the set of all the equivalent $\mathbf{k} + \mathbf{G}$ points we single out the one that lives within that unit cell (the Wigner-Seitz cell or first Brillouin zone of the crystal). The cell thus chosen has the full point group symmetry of the lattice. The group of the Schroedinger equation is the space group to which the system belongs. The electronic energy levels and their degeneracies are thus determined by the irreps of the space group.

Star Group of the Wave Vector Given a wave vector $\mathbf{k}$, if we apply on t all the transformations of the point group G, of order g, in general we obtain g wave vectors, of which only $q \leq g$ are distinct. The set of these q vectors is the star group of $\mathbf{k}$. If $q = g$, then we have a general vector $\mathbf{k}$, otherwise if $q < g$, this means that $\mathbf{k}$ must be on a line of symmetry (in two dimensions) of the Brillouin zone.

Group of the Wave Vector The set of elements $\{B\}$ of the point group G that leave the wave vector unchanged modulo a vector $\mathbf{G}$:

$$B\mathbf{k} = \mathbf{k} + \mathbf{G}$$

forms a group, that is called the *group of the wave vector K*, and it is a subgroup of G. For a $\mathbf{k}$ that is a special point of symmetry, the order of K, k, is larger than one, and specifically it satisfies the following equality

$$g = k \times q$$

All the irreps of a space group can be obtained from those of the group K of the wave vector $\mathbf{k}$ and letting it run throughout the Brillouin zone.

Compatibility relations In general there is more degeneracy at special points than on lines of symmetry, and more on the lines of symmetry than at a generic point $\mathbf{k}$ where the degeneracy is completely lifted. As a consequence when one moves away from one point of higher to one of lower symmetry an irrep at the former point will split into the direct sum of different irreps, where the reduction can be obtained by inspecting the character tables of the two different groups of the wave vector at the two different points.

List of Publications

The research performed during the development of this thesis has led to the following publications:

1. Spin-valley relaxation and quantum transport regimes in two-dimensional transition-metal dichalcogenides.
   H. Ochoa, F. Finocchiaro, F. Guinea and V. I. Fal'ko,
   Physical Review B **90**, 235429 (2014)

2. Quantum spin Hall effect in twisted bilayer graphene.
   F. Finocchiaro, F. Guinea and P. San-Jose,
   2D Materials **4**, 025027 (2017)

3. Electrical detection of individual skyrmions in graphene devices.
   F. Finocchiaro, J. L. Lado and J. Fernanded-Rossier,
   Physical Review B **96**, 155422 (2017)

4. Topological π junctions from crossed Andreev reflection in the quantum Hall regime.
   F. Finocchiaro, F. Guinea and P. San-Jose,
   Physical Review Letters **120**, 116801 (2018)

Bibliography

[1] A. H. Castro Neto et al. "The electronic properties of graphene". In: *Reviews of Modern Physics* 81.1 (2009), p. 109162.

[2] A. K. Geim and I. V. Grigorieva. "Van der Waals heterostructures". In: *Nature* 499 (2013), p. 419.

[3] Rafael Roldan et al. "Theory of 2D crystals: graphene and beyond". In: *Chemical Society Reviews* 46.15 (2017), p. 43874399.

[4] Riccardo Frisenda et al. "Recent progress in the assembly of nanodevices and van der Waals heterostructures by deterministic placement of 2D materials". In: *Chemical Society Reviews* 47.1 (2018), p. 5368.

[5] K. S. Novoselov et al. "Electric Field Effect in Atomically Thin Carbon Films". In: *Science* 306.5696 (2004), p. 666.

[6] C.L. Kane and E.J. Mele. "Quantum spin Hall effect in graphene". In: *Phys. Rev. Lett.* 95.22 (2005), p. 226801.

[7] Hongki Min et al. "Intrinsic and Rashba spin-orbit interactions in graphene sheets". In: *Physical Review B* 74.16 (2006), p. 165310.

[8] Jason Alicea and Matthew P. A. Fisher. "Graphene integer quantum Hall effect in the ferromagnetic and paramagnetic regimes". In: *Phys. Rev. B* 74 (7 2006), p. 075422.

[9] V. P. Gusynin et al. "Excitonic gap, phase transition, and quantum Hall effect in graphene". In: *Phys. Rev. B* 74 (19 2006), p. 195429.

[10] Kentaro Nomura and Allan H. MacDonald. "Quantum Hall Ferromagnetism in Graphene". In: *Phys. Rev. Lett.* 96 (25 2006), p. 256602.

[11] Zhenhua Qiao et al. "Quantum anomalous Hall effect in graphene from Rashba and exchange effects". In: *Phys. Rev. B* 82 (16 2010), p. 161414.

[12] Maxim Kharitonov. "Phase diagram for the $\nu = 0$ quantum Hall state in monolayer graphene". In: *Phys. Rev. B* 85 (15 2012), p. 155439.

[13] K. S. Novoselov et al. "Two-dimensional gas of massless Dirac fermions in graphene". In: *Nature* 438 (2005), p. 197.

[14] A. K. Geim and K. S. Novoselov. "The rise of graphene". In: *Nature Materials* 6 (2007), p. 183.

[15] Melinda Y. Han et al. "Energy Band-Gap Engineering of Graphene Nanoribbons". In: *Physical Review Letters* 98.20 (2007), p. 206805.

[16] D. C. Elias et al. "Dirac cones reshaped by interaction effects in suspended graphene". In: *Nature Physics* 7 (2011), p. 701.

[17] R. R. Nair et al. "Spin-half paramagnetism in graphene induced by point defects". In: *Nature Physics* 8 (2012), p. 199.

[18] L. A. Ponomarenko et al. "Cloning of Dirac fermions in graphene superlattices". In: *Nature* 497 (2013), p. 594.

[19] R. V. Gorbachev et al. “Detecting topological currents in graphene superlattices”. In: *Science* 346.6208 (2014), p. 448.

[20] P. San-Jose et al. “Majorana Zero Modes in Graphene”. In: *Phys. Rev. X* 5 (4 2015), p. 041042.

[21] Yuanbo Zhang et al. “Experimental observation of the quantum Hall effect and Berry’s phase in graphene”. In: *Nature* 438.7065 (2005), p. 201204.

[22] Y. Zhang et al. “Landau-Level Splitting in Graphene in High Magnetic Fields”. In: *Phys. Rev. Lett.* 96 (13 2006), p. 136806.

[23] K. S. Novoselov et al. “Room-Temperature Quantum Hall Effect in Graphene”. In: *Science* 315.5817 (2007), p. 1379.

[24] Y. W. Tan et al. “Measurement of Scattering Rate and Minimum Conductivity in Graphene”. In: *Physical Review Letters* 99.24 (2007), p. 246803.

[25] Z. Q. Li et al. “Dirac charge dynamics in graphene by infrared spectroscopy”. In: *Nature Physics* 4 (2008), p. 532.

[26] Andrea F. Young and Philip Kim. “Quantum interference and Klein tunnelling in graphene heterojunctions”. In: *Nature Physics* 5 (2009), p. 222.

[27] Kirill I. Bolotin et al. “Observation of the fractional quantum Hall effect in graphene”. In: *Nature* 462 (2009), p. 196.

[28] Young Jae Song et al. “High-resolution tunnelling spectroscopy of a graphene quartet”. In: *Nature* 467.7312 (2010), p. 185189.

[29] J. M. B. Lopes dos Santos, N. M. R. Peres, and A. H. Castro Neto. “Graphene Bilayer with a Twist: Electronic Structure”. In: *Phys. Rev. Lett.* 99.25 (2007), p. 256802.

[30] Yuanbo Zhang et al. “Direct observation of a widely tunable bandgap in bilayer graphene”. In: *Nature* 459 (2009), p. 820.

[31] L. A. Ponomarenko et al. “Tunable metal–insulator transition in double-layer graphene heterostructures”. In: *Nature Physics* 7 (2011), p. 958.

[32] R. Bistritzer and A. H. MacDonald. “Moiré butterflies in twisted bilayer graphene”. In: *Phys. Rev. B* 84 (3 2011), p. 035440.

[33] Edward McCann and Mikito Koshino. “The electronic properties of bilayer graphene”. In: *Reports on Progress in Physics* 76.5 (2013), p. 056503.

[34] M. T. Greenaway et al. “Resonant tunnelling between the chiral Landau states of twisted graphene lattices”. In: *Nature Physics* 11 (2015), p. 1057.

[35] Long Ju et al. “Topological valley transport at bilayer graphene domain walls”. In: *Nature* 520 (2015), p. 650.

[36] A. V. Rozhkov et al. “Electronic properties of graphene-based bilayer systems”. In: *Physics Reports* 648 (2016), p. 1104.

[37] F Finocchiaro, F Guinea, and P San-Jose. “Quantum spin Hall effect in twisted bilayer graphene”. In: *2D Materials* 4.2 (2017), p. 025027.

[38] Kin Fai Mak et al. “Atomically Thin MoS_2: A New Direct-Gap Semiconductor”. In: *Physical Review Letters* 105.13 (2010), p. 136805.

[39] Qing Hua Wang et al. “Electronics and optoelectronics of two-dimensional transition metal dichalcogenides”. In: *Nature Nanotechnology* 7 (2012), p. 699.

[40] Ting Cao et al. “Valley-selective circular dichroism of monolayer molybdenum disulphide”. In: *Nature Communications* 3 (2012), p. 887.

[41] Kin Fai Mak et al. "Control of valley polarization in monolayer MoS_2 by optical helicity". In: *Nature Nanotechnology* 7 (2012), p. 494.

[42] Hualing Zeng et al. "Valley polarization in MoS_2 monolayers by optical pumping". In: *Nature Nanotechnology* 7 (2012), p. 490.

[43] E. Cappelluti et al. "Tight-binding model and direct-gap/indirect-gap transition in single-layer and multilayer MoS_2". In: *Physical Review B* 88.7 (2013), p. 075409.

[44] R. A. Gordon et al. "Structures of exfoliated single layers of WS_2, MoS_2, and $MoSe_2$ in aqueous suspension". In: *Physical Review B* 65.12 (2002), p. 125407.

[45] V. Zólyomi, N. D. Drummond, and V. I. Fal'ko. "Band structure and optical transitions in atomic layers of hexagonal gallium chalcogenides". In: *Physical Review B* 87.19 (2013), p. 195403.

[46] Gui-Bin Liu et al. "Three-band tight-binding model for monolayers of group-VIB transition metal dichalcogenides". In: *Physical Review B* 88.8 (2013), p. 085433.

[47] Hideaki Takayanagi, Tatsushi Akazaki, and Junsaku Nitta. "Observation of Maximum Supercurrent Quantization in a Superconducting Quantum Point Contact". In: *Phys. Rev. Lett.* 75 (19 1995), p. 35333536.

[48] T. Bauch et al. "Correlated quantization of supercurrent and conductance in a superconducting quantum point contact". In: *Phys. Rev. B* 71 (17 2005), p. 174502.

[49] J. Shabani et al. "Two-dimensional epitaxial superconductor-semiconductor heterostructures: A platform for topological superconducting networks". In: *Phys. Rev. B* 93 (15 2016), p. 155402.

[50] M. Kjaergaard et al. "Quantized conductance doubling and hard gap in a two-dimensional semiconductor-superconductor heterostructure". In: *Nat Commun* 7 (2016), p. 12841.

[51] H. J. Suominen et al. "Zero-Energy Modes from Coalescing Andreev States in a Two-Dimensional Semiconductor-Superconductor Hybrid Platform". In: *Physical Review Letters* 119.17 (2017), p. 176805.

[52] H. J. Suominen et al. "Anomalous Fraunhofer interference in epitaxial superconductor-semiconductor Josephson junctions". In: *Phys. Rev. B* 95 (3 2017), p. 035307.

[53] M. Kjaergaard et al. "Transparent Semiconductor-Superconductor Interface and Induced Gap in an Epitaxial Heterostructure Josephson Junction". In: *Physical Review Applied* 7.3 (2017), p. 034029.

[54] Andor Kormányos et al. "Monolayer MoS_2: Trigonal warping, the Γ valley, and spin-orbit coupling effects". In: *Physical Review B* 88.4 (2013), p. 045416.

[55] Habib Rostami, Ali G. Moghaddam, and Reza Asgari. "Effective lattice Hamiltonian for monolayer MoS_2: Tailoring electronic structure with perpendicular electric and magnetic fields". In: *Physical Review B* 88.8 (2013), p. 085440.

[56] Hector Ochoa et al. "Spin-valley relaxation and quantum transport regimes in two-dimensional transition-metal dichalcogenides". In: *Physical Review B* 90.23 (2014), p. 235429.

[57] Xiaodong Xu et al. "Spin and pseudospins in layered transition metal dichalcogenides". In: *Nature Physics* 10 (2014), p. 343.

[58] Di Xiao et al. "Coupled Spin and Valley Physics in Monolayers of MoS_2 and Other Group-VI Dichalcogenides". In: *Physical Review Letters* 108.19 (2012), p. 196802.

[59] V. L. Ginzburg and L. D. Landau. "On the Theory of superconductivity". In: *Zh. Eksp. Teor. Fiz.* 20 (1950), pp. 1064–1082.

[60] Edward Witten. "Topological quantum field theory". In: *Comm. Math. Phys.* 117.3 (1988), p. 353386.

[61] X. G. Wen. "Topological Orders in Rigid States". In: *International Journal of Modern Physics B* 04.02 (1990), p. 239271.

[62] Xiao-Gang Wen. *Quantum Field Theory of Many-body Systems*. Oxford University Press, 2004.

[63] F. H. Croom. *Pinciples of Topology*. Saunders College Publishing, 1989.

[64] Xiao-Liang Qi and Shou-Cheng Zhang. "Topological insulators and superconductors". In: *Reviews of Modern Physics* 83.4 (2011), p. 10571110.

[65] Martin R. Zirnbauer. "Riemannian symmetric superspaces and their origin in random-matrix theory". In: *Journal of Mathematical Physics* 37.10 (1996), p. 49865018.

[66] Alexander Altland and Martin R. Zirnbauer. "Nonstandard symmetry classes in mesoscopic normal-superconducting hybrid structures". In: *Physical Review B* 55.2 (1997), p. 11421161.

[67] Shinsei Ryu et al. "Topological insulators and superconductors: tenfold way and dimensional hierarchy". In: *New Journal of Physics* 12.6 (2010), p. 065010.

[68] M. V. Berry. "Quantal phase factors accompanying adiabatic changes". In: *Proceedings of the Royal Society of A* 392.1802 (1984), p. 45.

[69] Raffaele Resta. "Manifestations of Berry's phase in molecules and condensed matter". In: *Journal of Physics: Condensed Matter* 12.9 (2000), R107.

[70] Di Xiao, Ming-Che Chang, and Qian Niu. "Berry phase effects on electronic properties". In: *Rev. Mod. Phys.* 82 (3 2010), p. 19592007.

[71] B. Andrei. Bernevig and Taylor L. Hughes. *Topological Insulators and Topological Superconductors*. Princeton University Press, 2013.

[72] K. v. Klitzing, G. Dorda, and M. Pepper. "New Method for High-Accuracy Determination of the Fine-Structure Constant Based on Quantized Hall Resistance". In: *Physical Review Letters* 45.6 (1980), p. 494497.

[73] B. Andrei Bernevig, Taylor L. Hughes, and Shou-Cheng Zhang. "Quantum Spin Hall Effect and Topological Phase Transition in HgTe Quantum Wells". In: *Science* 314.5806 (2006), p. 1757.

[74] Markus König et al. "Quantum Spin Hall Insulator State in HgTe Quantum Wells". In: *Science* 318.5851 (2007), p. 766.

[75] Haijun Zhang et al. "Topological insulators in Bi_2Se_3, Bi_2Te_3 and Sb_2Te_3 with a single Dirac cone on the surface". In: *Nature Physics* 5 (2009), p. 438.

[76] Y. Xia et al. "Observation of a large-gap topological-insulator class with a single Dirac cone on the surface". In: *Nature Physics* 5 (2009), p. 398.

[77] Y. L. Chen et al. "Experimental Realization of a Three-Dimensional Topological Insulator, Bi_2Te_3". In: *Science* 325.5937 (2009), p. 178.

[78] D. Hsieh et al. "Observation of Unconventional Quantum Spin Textures in Topological Insulators". In: *Science* 323.5916 (2009), p. 919.

[79] J. L. Lado and J. Fernández-Rossier. "Quantum anomalous Hall effect in graphene coupled to skyrmions". In: *Phys. Rev. B* 92 (11 2015), p. 115433.

[80] Keita Hamamoto, Motohiko Ezawa, and Naoto Nagaosa. "Quantized topological Hall effect in skyrmion crystal". In: *Physical Review B* 92.11 (2015), p. 115417.

[81] F. D. M. Haldane. "Model for a Quantum Hall Effect without Landau Levels: Condensed-Matter Realization of the "Parity Anomaly"". In: *Physical Review Letters* 61.18 (1988), p. 20152018.

[82] Naoto Nagaosa et al. "Anomalous Hall effect". In: *Reviews of Modern Physics* 82.2 (2010), p. 15391592.

[83] Naoto Nagaosa and Yoshinori Tokura. "Topological properties and dynamics of magnetic skyrmions". In: *Nat Nano* 8.12 (2013), p. 899911.

[84] F. Finocchiaro, J. L. Lado, and J. Fernandez-Rossier. "Electrical detection of individual skyrmions in graphene devices". In: *Physical Review B* 96.15 (2017), p. 155422.

[85] Masatoshi Sato and Yoichi Ando. "Topological superconductors: a review". In: *Reports on Progress in Physics* 80.7 (2017), p. 076501.

[86] Jason Alicea. "New directions in the pursuit of Majorana fermions in solid state systems". In: *Reports on Progress in Physics* 75.7 (2012), p. 076501.

[87] E. Hall. "On a New Action of the Magnet on Electric Currents". In: *Amer. J. Math.* 2 (1879), p. 287.

[88] R. Landauer. "Spatial Variation of Currents and Fields Due to Localized Scatterers in Metallic Conduction". In: *IBM Journal of Research and Development* 1.3 (1957), p. 223231.

[89] A. F. Young et al. "Tunable symmetry breaking and helical edge transport in a graphene quantum spin Hall state". In: *Nature* 505.7484 (2014), p. 528532.

[90] Daniel Huertas-Hernando, F. Guinea, and Arne Brataas. "Spin-orbit coupling in curved graphene, fullerenes, nanotubes, and nanotube caps". In: *Physical Review B* 74.15 (2006), p. 155426.

[91] Javier D. Sanchez-Yamagishi et al. "Helical edge states and fractional quantum Hall effect in a graphene electron–hole bilayer". In: *Nature Nanotechnology* 12 (2016), p. 118.

[92] Karsten Flensberg. "Non-Abelian Operations on Majorana Fermions via Single-Charge Control". In: *Phys. Rev. Lett.* 106 (9 2011), p. 090503.

[93] Niklas Romming et al. "Writing and Deleting Single Magnetic Skyrmions". In: *Science* 341.6146 (2013), p. 636.

[94] Jens Brede et al. "Long-range magnetic coupling between nanoscale organic–metal hybrids mediated by a nanoskyrmion lattice". In: *Nature Nanotechnology* 9 (2014), p. 1018.

[95] Niklas Romming et al. "Field-Dependent Size and Shape of Single Magnetic Skyrmions". In: *Phys. Rev. Lett.* 114 (17 2015), p. 177203.

[96] S. Mühlbauer et al. "Skyrmion Lattice in a Chiral Magnet". In: *Science* 323.5916 (2009), p. 915919.

[97] X. Z. Yu et al. "Real-space observation of a two-dimensional skyrmion crystal". In: *Nature* 465.7300 (2010), p. 901904.

[98] X. Z. Yu et al. "Near room-temperature formation of a skyrmion crystal in thin-films of the helimagnet FeGe". In: *Nature Materials* 10 (2010), p. 106.

[99] W. Münzer et al. "Skyrmion lattice in the doped semiconductor $Fe_{1-x}Co_xSi$". In: *Phys. Rev. B* 81 (4 2010), p. 041203.

[100] Y Tokunaga et al. "A new class of chiral materials hosting magnetic skyrmions beyond room temperature". In: *Nature communications* 6 (2015).

[101] T. Adams et al. "Long-Wavelength Helimagnetic Order and Skyrmion Lattice Phase in Cu_2OSeO_3". In: *Physical Review Letters* 108.23 (2012), p. 237204.

[102] Shinichiro Seki et al. "Observation of skyrmions in a multiferroic material". In: *Science* 336.6078 (2012), p. 198201.

[103] M. C. Langner et al. "Coupled Skyrmion Sublattices in Cu_2OSeO_3". In: *Phys. Rev. Lett.* 112 (16 2014), p. 167202.

[104] SL Zhang et al. "Imaging and manipulation of skyrmion lattice domains in Cu_2OSeO_3". In: *Applied Physics Letters* 109.19 (2016), p. 192406.

[105] Xiuzhen Yu et al. "Magnetic stripes and skyrmions with helicity reversals". In: *Proceedings of the National Academy of Sciences* 109.23 (2012), p. 8856.

[106] Christian Pfleiderer. "Magnetic order: Surfaces get hairy". In: *Nat Phys* 7.9 (2011), p. 673674.

[107] Stefan Heinze et al. "Spontaneous atomic-scale magnetic skyrmion lattice in two dimensions". In: *Nat Phys* 7.9 (2011), p. 713718.

[108] Yuliya Dovzhenko et al. "Imaging the Spin Texture of a Skyrmion Under Ambient Conditions Using an Atomic-Sized Sensor". In: *arXiv:1611.00673* (2016).

[109] Y. S. Lin, P. J. Grundy, and E. A. Giess. "Bubble domains in magnetostatically coupled garnet films". In: *Applied Physics Letters* 23.8 (1973), p. 485487.

[110] T. Garel and S. Doniach. "Phase transitions with spontaneous modulation-the dipolar Ising ferromagnet". In: *Physical Review B* 26.1 (1982), p. 325329.

[111] I. Dzyaloshinsky. "A thermodynamic theory of "weak"ferromagnetism of antiferromagnetics". In: *Journal of Physics and Chemistry of Solids* 4.4 (1958), p. 241255.

[112] Tôru Moriya. "Anisotropic Superexchange Interaction and Weak Ferromagnetism". In: *Physical Review* 120.1 (1960), p. 9198.

[113] Tsuyoshi Okubo, Sungki Chung, and Hikaru Kawamura. "Multiple-q States and the Skyrmion Lattice of the Triangular-Lattice Heisenberg Antiferromagnet under Magnetic Fields". In: *Physical Review Letters* 108.1 (2012), p. 017206.

[114] XZ Yu et al. "Skyrmion flow near room temperature in an ultralow current density". In: *Nature communications* 3 (2012), p. 988.

[115] J Sampaio et al. "Nucleation, stability and current-induced motion of isolated magnetic skyrmions in nanostructures". In: *Nature nanotechnology* 8.11 (2013), p. 839844.

[116] R. Tomasello et al. "A strategy for the design of skyrmion racetrack memories". In: *Scientific Reports* 4 (2014), p. 6784.

[117] Stuart SP Parkin, Masamitsu Hayashi, and Luc Thomas. "Magnetic domain-wall racetrack memory". In: *Science* 320.5873 (2008), p. 190194.

[118] F. Jonietz et al. "Spin Transfer Torques in MnSi at Ultralow Current Densities". In: *Science* 330.6011 (2010), p. 1648.

[119] Jinwu Ye et al. "Berry Phase Theory of the Anomalous Hall Effect: Application to Colossal Magnetoresistance Manganites". In: *Physical Review Letters* 83.18 (1999), p. 37373740.

[120] Y. Lyanda-Geller et al. "Charge transport in manganites: Hopping conduction, the anomalous Hall effect, and universal scaling". In: *Physical Review B* 63.18 (2001), p. 184426.

[121] Gen Tatara and Hikaru Kawamura. "Chirality-driven anomalous Hall effect in weak coupling regime". In: *Journal of the Physical Society of Japan* 71.11 (2002), p. 26132616.

[122] A. A. Thiele. "Steady-State Motion of Magnetic Domains". In: *Physical Review Letters* 30.6 (1973), p. 230233.

[123] Jiadong Zang et al. "Dynamics of Skyrmion Crystals in Metallic Thin Films". In: *Physical Review Letters* 107.13 (2011), p. 136804.

[124] Karin Everschor-Sitte and Matthias Sitte. "Real-space Berry phases: Skyrmion soccer (invited)". In: *Journal of Applied Physics* 115.17 (2014), p. 172602.

[125] Kai Litzius et al. "Skyrmion Hall effect revealed by direct time-resolved X-ray microscopy". In: *Nature Physics* 13 (2016), p. 170.

[126] Wanjun Jiang et al. "Direct observation of the skyrmion Hall effect". In: *Nature Physics* 13 (2016), p. 162.

[127] Gen Yin et al. "Topological spin Hall effect resulting from magnetic skyrmions". In: *Physical Review B* 92.2 (2015), p. 024411.

[128] Luca Banszerus et al. "Ballistic transport exceeding 28 μm in CVD grown graphene". In: *Nano letters* 16.2 (2016), p. 13871391.

[129] Nils M Freitag et al. "Electrostatically confined monolayer graphene quantum dots with orbital and valley splittings". In: *Nano Letters* 16.9 (2016), p. 57985805.

[130] M Ben Shalom et al. "Quantum oscillations of the critical current and high-field superconducting proximity in ballistic graphene". In: *Nature Physics* 12.4 (2016), p. 318322.

[131] A. Candini et al. "Hysteresis loops of magnetoconductance in graphene devices". In: *Phys. Rev. B* 83 (12 2011), p. 121401.

[132] Andrea Candini et al. "Graphene Spintronic Devices with Molecular Nanomagnets". In: *Nano Letters* 11.7 (2011), p. 26342639.

[133] J. W. González, F. Delgado, and J. Fernández-Rossier. "Graphene single-electron transistor as a spin sensor for magnetic adsorbates". In: *Phys. Rev. B* 87 (8 2013), p. 085433.

[134] Börge Göbel et al. "Unconventional topological Hall effect in skyrmion crystals caused by the topology of the lattice". In: *Physical Review B* 95.9 (2017), p. 094413.

[135] E. Hall. "On the "Rotational Coefficient" in nickel and cobalt". In: *Phil. Mag.* 12 (1881), p. 157.

[136] Alpheus W. Smith. "The Variation of the Hall Effect in Metals with Change of Temperature". In: *Physical Review (Series I)* 30.1 (1910), p. 134.

[137] Emerson M. Pugh and Norman Rostoker. "Hall Effect in Ferromagnetic Materials". In: *Reviews of Modern Physics* 25.1 (1953), p. 151157.

[138] Yasufumi Araki and Kentaro Nomura. "Skyrmion-induced anomalous Hall conductivity on topological insulator surfaces". In: *Physical Review B* 96.16 (2017), p. 165303.

[139] Z. H. Liu et al. "Transition from Anomalous Hall Effect to Topological Hall Effect in Hexagonal Non-Collinear Magnet Mn3Ga". In: *Scientific Reports* 7.1 (2017), p. 515.

[140] G E Volovik. "Linear momentum in ferromagnets". In: *Journal of Physics C: Solid State Physics* 20.7 (1987), p. L83.

[141] Shufeng Zhang and Steven S. L. Zhang. "Generalization of the Landau-Lifshitz-Gilbert Equation for Conducting Ferromagnets". In: *Physical Review Letters* 102.8 (2009), p. 086601.

[142] MP Lopez Sancho et al. "Highly convergent schemes for the calculation of bulk and surface Green functions". In: *Journal of Physics F: Metal Physics* 15.4 (1985), p. 851.

[143] Peng Wei et al. "Strong interfacial exchange field in the graphene/EuS heterostructure". In: *Nature materials* (2016).

[144] H. X. Yang et al. "Proximity Effects Induced in Graphene by Magnetic Insulators: First-Principles Calculations on Spin Filtering and Exchange-Splitting Gaps". In: *Phys. Rev. Lett.* 110 (4 2013), p. 046603.

[145] Zhenhua Qiao et al. "Quantum Anomalous Hall Effect in Graphene Proximity Coupled to an Antiferromagnetic Insulator". In: *Physical Review Letters* 112.11 (2014), p. 116404.

[146] Zhiyong Wang et al. "Proximity-Induced Ferromagnetism in Graphene Revealed by the Anomalous Hall Effect". In: *Phys. Rev. Lett.* 114 (1 2015), p. 016603.

[147] Karin Everschor et al. "Rotating skyrmion lattices by spin torques and field or temperature gradients". In: *Physical Review B* 86.5 (2012), p. 054432.

[148] Kentaro Nomura and A. H. MacDonald. "Quantum Transport of Massless Dirac Fermions". In: *Physical Review Letters* 98.7 (2007), p. 076602.

[149] L Schmidt et al. "Symmetry breaking in spin spirals and skyrmions by in-plane and canted magnetic fields". In: *New Journal of Physics* 18.7 (2016), p. 075007.

[150] Alexander Tzalenchuk et al. "Towards a quantum resistance standard based on epitaxial graphene". In: *Nature nanotechnology* 5.3 (2010), p. 186189.

[151] Beat Jeckelmann and Blaise Jeanneret. "The quantum Hall effect as an electrical resistance standard". In: *Reports on Progress in Physics* 64.12 (2001), p. 1603.

[152] Roland Wiesendanger. "Nanoscale magnetic skyrmions in metallic films and multilayers: a new twist for spintronics". In: *Nature Reviews Materials* 1 (2016), p. 16044.

[153] O. A. Pankratov, S. V. Pakhomov, and B. A. Volkov. "Supersymmetry in heterojunctions: Band-inverting contact on the basis of $Pb_{1-x}Sn_xTe$ and $Hg_{1-x}Cd_xTe$". In: *Solid State Communications* 61.2 (1987), p. 9396.

[154] Liang Fu and C. L. Kane. "Superconducting Proximity Effect and Majorana Fermions at the Surface of a Topological Insulator". In: *Phys. Rev. Lett.* 100 (9 2008), p. 096407.

[155] Yugui Yao et al. "Spin-orbit gap of graphene: First-principles calculations". In: *Physical Review B* 75.4 (2007), p. 041401.

[156] V. E. Calado et al. "Ballistic Josephson junctions in edge-contacted graphene". In: *Nature Nanotechnology* 10 (2015), p. 761.

[157] M. Ben Shalom et al. "Quantum oscillations of the critical current and high-field superconducting proximity in ballistic graphene". In: *Nature Physics* 12 (2015), p. 318.

[158] E. J. Mele. "Commensuration and interlayer coherence in twisted bilayer graphene". In: *Physical Review B* 81.16 (2010), p. 161405.

[159] I. Brihuega et al. "Unraveling the Intrinsic and Robust Nature of van Hove Singularities in Twisted Bilayer Graphene by Scanning Tunneling Microscopy and Theoretical Analysis". In: *Physical Review Letters* 109.19 (2012), p. 196802.

[160] J. M. B. Lopes dos Santos, N. M. R. Peres, and A. H. Castro Neto. "Continuum model of the twisted graphene bilayer". In: *Phys. Rev. B* 86 (15 2012), p. 155449.

[161] Pilkyung Moon and Mikito Koshino. "Optical absorption in twisted bilayer graphene". In: *Phys. Rev. B* 87 (20 2013), p. 205404.

[162] A. O. Sboychakov et al. "Electronic spectrum of twisted bilayer graphene". In: *Physical Review B* 92.7 (2015), p. 075402.

[163] Rafi Bistritzer and Allan H. MacDonald. "Moiré bands in twisted double-layer graphene". In: *PNAS* 108.30 (2011), pp. 12233–12237.

[164] G. Trambly de Laissardière, D. Mayou, and L. Magaud. "Localization of Dirac Electrons in Rotated Graphene Bilayers". In: *Nano Letters* 10.3 (2010), p. 804808.

[165] E. Suárez Morell et al. "Flat bands in slightly twisted bilayer graphene: Tight-binding calculations". In: *Physical Review B* 82.12 (2010), p. 121407.

[166] G. Trambly de Laissardière, D. Mayou, and L. Magaud. "Numerical studies of confined states in rotated bilayers of graphene". In: *Physical Review B* 86.12 (2012), p. 125413.

[167] W. Landgraf et al. "Electronic structure of twisted graphene flakes". In: *Physical Review B* 87.7 (2013), p. 075433.

[168] S. Shallcross, S. Sharma, and O. Pankratov. "Emergent momentum scale, localization, and van Hove singularities in the graphene twist bilayer". In: *Physical Review B* 87.24 (2013), p. 245403.

[169] Lan Meng et al. "Single-layer behavior and slow carrier density dynamic of twisted graphene bilayer". In: *Applied Physics Letters* 100.9 (2012), p. 091601.

[170] Wei Yan et al. "Angle-Dependent van Hove Singularities in a Slightly Twisted Graphene Bilayer". In: *Physical Review Letters* 109.12 (2012), p. 126801.

[171] M. Sprinkle et al. "First Direct Observation of a Nearly Ideal Graphene Band Structure". In: *Physical Review Letters* 103.22 (2009), p. 226803.

[172] J. Hicks et al. "Symmetry breaking in commensurate graphene rotational stacking: Comparison of theory and experiment". In: *Physical Review B* 83.20 (2011), p. 205403.

[173] Taisuke Ohta et al. "Evidence for Interlayer Coupling and Moiré Periodic Potentials in Twisted Bilayer Graphene". In: *Physical Review Letters* 109.18 (2012), p. 186807.

[174] Zhenhua Ni et al. "Reduction of Fermi velocity in folded graphene observed by resonance Raman spectroscopy". In: *Physical Review B* 77.23 (2008), p. 235403.

[175] P. Poncharal et al. "Raman spectra of misoriented bilayer graphene". In: *Physical Review B* 78.11 (2008), p. 113407.

[176] A. Righi et al. "Graphene Moiré patterns observed by umklapp double-resonance Raman scattering". In: *Physical Review B* 84.24 (2011), p. 241409.

[177] Robin W. Havener et al. "Angle-Resolved Raman Imaging of Interlayer Rotations and Interactions in Twisted Bilayer Graphene". In: *Nano Letters* 12.6 (2012), p. 31623167.

[178] P. San-Jose, J. González, and F. Guinea. "Non-Abelian Gauge Potentials in Graphene Bilayers". In: *Physical Review Letters* 108.21 (2012), p. 216802.

[179] Long-Jing Yin et al. "Experimental evidence for non-Abelian gauge potentials in twisted graphene bilayers". In: *Physical Review B* 92.8 (2015), p. 081406.

[180] Z. Jiang et al. "Quantum Hall States near the Charge-Neutral Dirac Point in Graphene". In: *Phys. Rev. Lett.* 99 (10 2007), p. 106802.

[181] Y. Zhao et al. "Symmetry Breaking in the Zero-Energy Landau Level in Bilayer Graphene". In: *Physical Review Letters* 104.6 (2010), p. 066801.

[182] A. F. Young et al. "Spin and valley quantum Hall ferromagnetism in graphene". In: *Nature Physics* 8 (2012), p. 550.

[183] L. Brey and H. A. Fertig. "Edge states and the quantized Hall effect in graphene". In: *Phys. Rev. B* 73.19 (2006), p. 195408.

[184] Dmitry A. Abanin, Patrick A. Lee, and Leonid S. Levitov. "Spin-Filtered Edge States and Quantum Hall Effect in Graphene". In: *Phys. Rev. Lett.* 96 (17 2006), p. 176803.

[185] M. O. Goerbig, R. Moessner. "Electron interactions in graphene in a strong magnetic field". In: *Phys. Rev. B* 74 (16 2006), p. 161407.

[186] Jean-Noël Fuchs and Pascal Lederer. "Spontaneous Parity Breaking of Graphene in the Quantum Hall Regime". In: *Phys. Rev. Lett.* 98 (1 2007), p. 016803.

[187] Igor F. Herbut. "SO(3) symmetry between Néel and ferromagnetic order parameters for graphene in a magnetic field". In: *Phys. Rev. B* 76 (8 2007), p. 085432.

[188] Igor F. Herbut. "Theory of integer quantum Hall effect in graphene". In: *Physical Review B* 75.16 (2007), p. 165411.

[189] J. Jung and A. H. MacDonald. "Theory of the magnetic-field-induced insulator in neutral graphene sheets". In: *Phys. Rev. B* 80 (23 2009), p. 235417.

[190] M. O. Goerbig. "Electronic properties of graphene in a strong magnetic field". In: *Reviews of Modern Physics* 83.4 (2011), p. 11931243.

[191] Maxim Kharitonov. "Edge excitations of the canted antiferromagnetic phase of the $\nu = 0$ quantum Hall state in graphene: A simplified analysis". In: *Phys. Rev. B* 86 (7 2012), p. 075450.

[192] J. L. Lado and J. Fernández-Rossier. "Noncollinear magnetic phases and edge states in graphene quantum Hall bars". In: *Phys. Rev. B* 90 (16 2014), p. 165429.

[193] T. O. Wehling et al. "Strength of Effective Coulomb Interactions in Graphene and Graphite". In: *Phys. Rev. Lett.* 106 (23 2011), p. 236805.

[194] S. Sorella and E. Tosatti. "Semi-Metal-Insulator Transition of the Hubbard Model in the Honeycomb Lattice". In: *EPL (Europhysics Letters)* 19.8 (1992), p. 699.

[195] R. de Gail et al. "Topologically protected zero modes in twisted bilayer graphene". In: *Physical Review B* 84.4 (2011), p. 045436.

[196] Min-Young Choi, Young-Hwan Hyun, and Yoonbai Kim. "Angle dependence of the Landau level spectrum in twisted bilayer graphene". In: *Physical Review B* 84.19 (2011), p. 195437.

[197] Pilkyung Moon and Mikito Koshino. "Energy spectrum and quantum Hall effect in twisted bilayer graphene". In: *Physical Review B* 85.19 (2012), p. 195458.

[198] Javier D. Sanchez-Yamagishi et al. "Quantum Hall Effect, Screening, and Layer-Polarized Insulating States in Twisted Bilayer Graphene". In: *Physical Review Letters* 108.7 (2012), p. 076601.

[199] B. Hunt et al. "Massive Dirac Fermions and Hofstadter Butterfly in a van der Waals Heterostructure". In: *Science* 340.6139 (2013), p. 1427.

[200] Douglas R. Hofstadter. "Energy levels and wave functions of Bloch electrons in rational and irrational magnetic fields". In: *Physical Review B* 14.6 (1976), p. 22392249.

[201] Luis A. Gonzalez-Arraga et al. "Electrically Controllable Magnetism in Twisted Bilayer Graphene". In: *Physical Review Letters* 119.10 (2017), p. 107201.

[202] M. T. Deng et al. "Anomalous Zero-Bias Conductance Peak in a Nb–InSb Nanowire–Nb Hybrid Device". In: *Nano Letters* 12.12 (2012), pp. 6414–6419.

[203] J. R. Williams et al. "Unconventional Josephson Effect in Hybrid Superconductor-Topological Insulator Devices". In: *Phys. Rev. Lett.* 109 (5 2012), p. 056803.

[204] V. Mourik et al. "Signatures of Majorana Fermions in Hybrid Superconductor-Semiconductor Nanowire Devices". In: *Science* 336.6084 (2012), p. 10031007.

[205] Leonid P. Rokhinson, Xinyu Liu, and Jacek K. Furdyna. "The fractional a.c. Josephson effect in a semiconductor-superconductor nanowire as a signature of Majorana particles". In: *Nat Phys* 8.11 (2012), p. 795799.

[206] Anindya Das et al. "Zero-bias peaks and splitting in an Al-InAs nanowire topological superconductor as a signature of Majorana fermions". In: *Nat Phys* 8.12 (2012), p. 887895.

[207] A. D. K. Finck et al. "Anomalous Modulation of a Zero-Bias Peak in a Hybrid Nanowire-Superconductor Device". In: *Phys. Rev. Lett.* 110 (12 2013), p. 126406.

[208] Stevan Nadj-Perge et al. "Observation of Majorana fermions in ferromagnetic atomic chains on a superconductor". In: *Science* 346.6209 (2014), p. 602607.

[209] Michael Ruby et al. "End States and Subgap Structure in Proximity-Coupled Chains of Magnetic Adatoms". In: *Phys. Rev. Lett.* 115 (19 2015), p. 197204.

[210] S. M. Albrecht et al. "Exponential protection of zero modes in Majorana islands". In: *Nature* 531.7593 (2016), p. 206209.

[211] M. T. Deng et al. "Majorana bound state in a coupled quantum-dot hybrid-nanowire system". In: *Science* 354.6319 (2016), p. 15571562.

[212] C. Nayak et al. "Non-Abelian anyons and topological quantum computation". In: *Rev. Mod. Phys.* 80.3 (2008), p. 10831159.

[213] Roman M. Lutchyn, Jay D. Sau, and S. Das Sarma. "Majorana Fermions and a Topological Phase Transition in Semiconductor-Superconductor Heterostructures". In: *Phys. Rev. Lett.* 105.7 (2010), p. 077001.

[214] Yuval Oreg, Gil Refael, and Felix von Oppen. "Helical Liquids and Majorana Bound States in Quantum Wires". In: *Phys. Rev. Lett.* 105 (17 2010), p. 177002.

[215] D. A. Ivanov. "Non-Abelian Statistics of Half-Quantum Vortices in p-Wave Superconductors". In: *Phys. Rev. Lett.* 86 (2 2001), p. 268271.

[216] Parsa Bonderson, Michael Freedman, and Chetan Nayak. "Measurement–Only Topological Quantum Computation". In: *Phys. Rev. Lett.* 101 (1 2008), p. 010501.

[217] B van Heck et al. "Coulomb-assisted braiding of Majorana fermions in a Josephson junction array". In: *New Journal of Physics* 14.3 (2012), p. 035019.

[218] Martin Leijnse and Karsten Flensberg. "Introduction to topological superconductivity and Majorana fermions". In: *Semiconductor Science and Technology* 27.12 (2012), p. 124003.

[219] Parsa Bonderson. "Measurement–only topological quantum computation via tunable interactions". In: *Phys. Rev. B* 87 (3 2013), p. 035113.

[220] Sagar Vijay and Liang Fu. "Teleportation-based quantum information processing with Majorana zero modes". In: *Phys. Rev. B* 94 (23 2016), p. 235446.

[221] Torsten Karzig et al. "Scalable designs for quasiparticle-poisoning-protected topological quantum computation with Majorana zero modes". In: *Phys. Rev. B* 95 (23 2017), p. 235305.

[222] Kaveh Gharavi, Darryl Hoving, and Jonathan Baugh. "Readout of Majorana parity states using a quantum dot". In: *Phys. Rev. B* 94 (15 2016), p. 155417.

[223] Silas Hoffman et al. "Universal quantum computation with hybrid spin-Majorana qubits". In: *Phys. Rev. B* 94 (4 2016), p. 045316.

[224] David Aasen et al. "Milestones Toward Majorana-Based Quantum Computing". In: *Phys. Rev. X* 6 (3 2016), p. 031016.

[225] Sergey Bravyi and Alexei Kitaev. "Universal quantum computation with ideal Clifford gates and noisy ancillas". In: *Physical Review A* 71.2 (2005), p. 022316.

[226] Sergey Bravyi. "Universal quantum computation with the $\nu = 5/2$ fractional quantum Hall state". In: *Physical Review A* 73.4 (2006), p. 042313.

[227] Michael Freedman, Chetan Nayak, and Kevin Walker. "Towards universal topological quantum computation in the $\nu = 5/2$ fractional quantum Hall state". In: *Physical Review B* 73.24 (2006), p. 245307.

[228] David J. Clarke and Kirill Shtengel. "Improved phase-gate reliability in systems with neutral Ising anyons". In: *Physical Review B* 82.18 (2010), p. 180519.

[229] F Hassler et al. "Anyonic interferometry without anyons: how a flux qubit can read out a topological qubit". In: *New Journal of Physics* 12.12 (2010), p. 125002.

[230] Parsa Bonderson et al. "Implementing Arbitrary Phase Gates with Ising Anyons". In: *Physical Review Letters* 104.18 (2010), p. 180505.

[231] Parsa Bonderson and Roman M. Lutchyn. "Topological Quantum Buses: Coherent Quantum Information Transfer between Topological and Conventional Qubits". In: *Physical Review Letters* 106.13 (2011), p. 130505.

[232] Liang Jiang, Charles L. Kane, and John Preskill. "Interface between Topological and Superconducting Qubits". In: *Physical Review Letters* 106.13 (2011), p. 130504.

[233] F Hassler, A R Akhmerov, and C W J Beenakker. "The top-transmon: a hybrid superconducting qubit for parity-protected quantum computation". In: *New Journal of Physics* 13.9 (2011), p. 095004.

[234] Gil-Ho Lee et al. "Inducing superconducting correlation in quantum Hall edge states". In: *Nat Phys* 13.7 (2017), p. 693698.

[235] M F Goffman et al. "Conduction channels of an InAs-Al nanowire Josephson weak link". In: *New Journal of Physics* 19.9 (2017), p. 092002.

[236] P. G. De Gennes. *Superconductivity of Metals and Alloys*. CRC Press, 1966.

[237] Walther Meissner and Robert Ochsenfeld. "Ein neuer Effekt bei eintritt der Supraleitfahigkeit". In: *Naturwiss* 21.787-788 (1933).

[238] A. F. Andreev. "Thermal conductivity of the intermediate state of superconductors". In: *Sov. Phys. JETP* 19 (1964), p. 1228.

[239] G. E. Blonder, M. Tinkham, and T. M. Klapwijk. "Transition from metallic to tunneling regimes in superconducting microconstrictions: Excess current, charge imbalance, and supercurrent conversion". In: *Physical Review B* 25.7 (1982), p. 45154532.

[240] H. Hoppe, U. Zülicke, and Gerd Schön. "Andreev Reflection in Strong Magnetic Fields". In: *Phys. Rev. Lett.* 84 (8 2000), p. 18041807.

[241] David J. Clarke, Jason Alicea, and Kirill Shtengel. "Exotic non-Abelian anyons from conventional fractional quantum Hall states". In: *Nature Communications* 4 (2013), p. 1348.

[242] Zhe Hou et al. "Crossed Andreev effects in two-dimensional quantum Hall systems". In: *Physical Review B* 94.6 (2016), p. 064516.

[243] Netanel H. Lindner et al. "Fractionalizing Majorana Fermions: Non-Abelian Statistics on the Edges of Abelian Quantum Hall States". In: *Physical Review X* 2.4 (2012), p. 041002.

[244] Meng Cheng. "Superconducting proximity effect on the edge of fractional topological insulators". In: *Physical Review B* 86.19 (2012), p. 195126.

[245] Abolhassan Vaezi. "Fractional topological superconductor with fractionalized Majorana fermions". In: *Physical Review B* 87.3 (2013), p. 035132.

[246] Jason Alicea and Paul Fendley. "Topological Phases with Parafermions: Theory and Blueprints". In: *Annual Review of Condensed Matter Physics* 7.1 (2016), p. 119139.

[247] F. Amet et al. "Supercurrent in the quantum Hall regime". In: *Science* 352.6288 (2016), p. 966.

[248] Roger S. K. Mong et al. "Fibonacci anyons and charge density order in the 12/5 and 13/5 quantum Hall plateaus". In: *Physical Review B* 95.11 (2017), p. 115136.

[249] Ettore Majorana. "Teoria simmetrica dell'elettrone e del positrone". In: *Il Nuovo Cimento* 14.4 (1937), pp. 171–84.

[250] Ramon Aguado. "Majorana quasiparticles in condensed matter". In: *Riv. Nuovo Cimento* 40.11 (2017), pp. 523–593.

[251] David P. DiVincenzo. "The Physical Implementation of Quantum Computation". In: *Fortschritte der Physik* 48 (2000), pp. 771–783.

[252] M. Nielsen and I. Chuang. *Quantum Computation and Quantum Information*. Cambridge University Press, 2010.

[253] Gregory Moore and Nicholas Read. "Nonabelions in the fractional quantum hall effect". In: *Nuclear Physics B* 360.2 (1991), p. 362396.

[254] M. Dolev et al. "Observation of a quarter of an electron charge at the $\nu = 5/2$ quantum Hall state". In: *Nature* 452 (2008), p. 829.

[255] Iuliana P. Radu et al. "Quasi-Particle Properties from Tunneling in the $\nu = 5/2$ Fractional Quantum Hall State". In: *Science* 320.5878 (2008), p. 899.

[256] Aveek Bid et al. "Observation of neutral modes in the fractional quantum Hall regime". In: *Nature* 466 (2010), p. 585.

[257] N. Read and Dmitry Green. "Paired states of fermions in two dimensions with breaking of parity and time-reversal symmetries and the fractional quantum Hall effect". In: *Physical Review B* 61.15 (2000), p. 1026710297.

[258] Xiao-Liang Qi, Taylor L. Hughes, and Shou-Cheng Zhang. "Chiral topological superconductor from the quantum Hall state". In: *Phys. Rev. B* 82 (18 2010), p. 184516.

[259] A Yu Kitaev. "Unpaired Majorana fermions in quantum wires". In: *Physics-Uspekhi* 44.10S (2001), p. 131.

[260] Jason Alicea et al. "Non-Abelian statistics and topological quantum information processing in 1D wire networks". In: *Nat Phys* 7.5 (2011), p. 412417.

[261] Falko Pientka et al. "Topological Superconductivity in a Planar Josephson Junction". In: *Phys. Rev. X* 7 (2 2017), p. 021032.

[262] Michael Hell, Martin Leijnse, and Karsten Flensberg. "Two-Dimensional Platform for Networks of Majorana Bound States". In: *Phys. Rev. Lett.* 118 (10 2017), p. 107701.

[263] Anna Keselman et al. "Inducing Time-Reversal-Invariant Topological Superconductivity and Fermion Parity Pumping in Quantum Wires". In: *Physical Review Letters* 111.11 (2013), p. 116402.

[264] Jelena Klinovaja and Daniel Loss. "Time-reversal invariant parafermions in interacting Rashba nanowires". In: *Phys. Rev. B* 90 (4 2014), p. 045118.

[265] Jelena Klinovaja, Amir Yacoby, and Daniel Loss. "Kramers pairs of Majorana fermions and parafermions in fractional topological insulators". In: *Phys. Rev. B* 90 (15 2014), p. 155447.

[266] Erikas Gaidamauskas, Jens Paaske, and Karsten Flensberg. "Majorana Bound States in Two-Channel Time-Reversal-Symmetric Nanowire Systems". In: *Physical Review Letters* 112.12 (2014), p. 126402.

[267] Constantin Schrade et al. "Proximity-Induced π Josephson Junctions in Topological Insulators and Kramers Pairs of Majorana Fermions". In: *Physical Review Letters* 115.23 (2015), p. 237001.

[268] T. M. Klapwijk. "Proximity Effect From an Andreev Perspective". In: *Journal of Superconductivity* 17.5 (2004), p. 593611.

[269] G. Falci, D. Feinberg, and F. W. J. Hekking. "Correlated tunneling into a superconductor in a multiprobe hybrid structure". In: *Europhys. Lett.* 54.2 (Apr. 2001), p. 255261.

[270] D. Beckmann, H. B. Weber, and H. v. Löhneysen. "Evidence for Crossed Andreev Reflection in Superconductor-Ferromagnet Hybrid Structures". In: *Physical Review Letters* 93.19 (2004), p. 197003.

[271] R. Mélin and D. Feinberg. "Sign of the crossed conductances at a ferromagnet/superconductor/ferromagnet double interface". In: *Physical Review B* 70.17 (2004), p. 174509.

[272] S. Russo et al. "Experimental Observation of Bias-Dependent Nonlocal Andreev Reflection". In: *Physical Review Letters* 95.2 (2005), p. 027002.

[273] David J. Clarke, Jason Alicea, and Kirill Shtengel. "Exotic circuit elements from zero-modes in hybrid superconductor–quantum-Hall systems". In: *Nature Physics* 10 (2014), p. 877.

[274] Prada, E. and Sols, F. "Entangled electron current through finite size normal-superconductor tunneling structures". In: *Eur. Phys. J. B* 40.4 (2004), pp. 379–396.

[275] Sergej Konschuh, Martin Gmitra, and Jaroslav Fabian. "Tight-binding theory of the spin-orbit coupling in graphene". In: *Physical Review B* 82.24 (2010), p. 245412.

[276] B. D. Josephson. "Possible new effects in superconductive tunnelling". In: *Physics Letters* 1.7 (1962), p. 251253.

[277] John Bardeen et al. "Structure of Vortex Lines in Pure Superconductors". In: *Physical Review* 187.2 (1969), p. 556569.

[278] W. Kirk and P. Reed. "Nanostructures and Mesoscopic Systems". In: *Academic Press* (1992).

[279] Daniel Litinski et al. "Combining Topological Hardware and Topological Software: Color-Code Quantum Computing with Topological Superconductor Networks". In: *Physical Review X* 7.3 (2017), p. 031048.

[280] Christopher Reeg, Jelena Klinovaja, and Daniel Loss. "Destructive interference of direct and crossed Andreev pairing in a system of two nanowires coupled via an *s*-wave superconductor". In: *Phys. Rev. B* 96 (8 2017), p. 081301.

[281] Constantin Schrade et al. "Low-field topological threshold in Majorana double nanowires". In: *Phys. Rev. B* 96 (3 2017), p. 035306.

[282] S. Baba et al. "Gate tunable parallel double quantum dots in InAs double-nanowire devices". In: *arXiv:1703.03559* (2017).

[283] B. Radisavljevic et al. "Single-layer MoS2 transistors". In: *Nature Nanotechnology* 6 (2011), p. 147.

[284] Dattatray J. Late et al. "Hysteresis in Single-Layer MoS2 Field Effect Transistors". In: *ACS Nano* 6.6 (2012), p. 56355641.

[285] Hui Fang et al. "High-Performance Single Layered WSe2 p-FETs with Chemically Doped Contacts". In: *Nano Letters* 12.7 (2012), p. 37883792.

[286] Branimir Radisavljevic and Andras Kis. "Mobility engineering and a metal–insulator transition in monolayer MoS2". In: *Nature Materials* 12 (2013), p. 815.

[287] Dmitry Ovchinnikov et al. "Electrical Transport Properties of Single-Layer WS2". In: *ACS Nano* 8.8 (2014), p. 81748181.

[288] L. Britnell et al. "Strong Light-Matter Interactions in Heterostructures of Atomically Thin Films". In: *Science* 340.6138 (2013), p. 1311.

[289] Andreas Pospischil, Marco M. Furchi, and Thomas Mueller. "Solar-energy conversion and light emission in an atomic monolayer p–n diode". In: *Nature Nanotechnology* 9 (2014), p. 257.

[290] Jason S. Ross et al. "Electrically tunable excitonic light-emitting diodes based on monolayer WSe2 p–n junctions". In: *Nature Nanotechnology* 9 (2014), p. 268.

[291] Britton W. H. Baugher et al. "Optoelectronic devices based on electrically tunable p–n diodes in a monolayer dichalcogenide". In: *Nature Nanotechnology* 9 (2014), p. 262.

[292] Wanxiang Feng et al. "Intrinsic spin Hall effect in monolayers of group-VI dichalcogenides: A first-principles study". In: *Physical Review B* 86.16 (2012), p. 165108.

[293] K. F. Mak et al. "The valley Hall effect in MoS_2 transistors". In: *Science* 344.6191 (2014), p. 1489.

[294] Yilei Li et al. "Valley Splitting and Polarization by the Zeeman Effect in Monolayer $MoSe_2$". In: *Physical Review Letters* 113.26 (2014), p. 266804.

[295] Ajit Srivastava et al. "Valley Zeeman effect in elementary optical excitations of monolayer WSe2". In: *Nature Physics* 11 (2015), p. 141.

[296] G. Aivazian et al. “Magnetic control of valley pseudospin in monolayer WSe2”. In: *Nature Physics* 11 (2015), p. 148.

[297] V. V. Enaldiev. “Edge states and spin-valley edge photocurrent in transition metal dichalcogenide monolayers”. In: *Physical Review B* 96.23 (2017), p. 235429.

[298] G Széchenyi, L Chirolli, and A Pályi. “Impurity-assisted electric control of spin-valley qubits in monolayer MoS 2”. In: *2D Materials* 5.3 (2018), p. 035004.

[299] Z. Y. Zhu, Y. C. Cheng, and U. Schwingenschlögl. “Giant spin-orbit-induced spin splitting in two-dimensional transition-metal dichalcogenide semiconductors”. In: *Physical Review B* 84.15 (2011), p. 153402.

[300] H. Ochoa, F. Guinea, and V. I. Fal’ko. “Spin memory and spin-lattice relaxation in two-dimensional hexagonal crystals”. In: *Physical Review B* 88.19 (2013), p. 195417.

[301] Kristen Kaasbjerg et al. “Symmetry-forbidden intervalley scattering by atomic defects in monolayer transition-metal dichalcogenides”. In: *Physical Review B* 96.24 (2017), p. 241411.

[302] H. Ochoa and R. Roldán. “Spin-orbit-mediated spin relaxation in monolayer MoS_2”. In: *Physical Review B* 87.24 (2013), p. 245421.

[303] I. L. Aleiner and K. B. Efetov. “Effect of Disorder on Transport in Graphene”. In: *Physical Review Letters* 97.23 (2006), p. 236801.

[304] E. McCann et al. “Weak-Localization Magnetoresistance and Valley Symmetry in Graphene”. In: *Physical Review Letters* 97.14 (2006), p. 146805.

[305] D. M. Basko. “Resonant low-energy electron scattering on short-range impurities in graphene”. In: *Physical Review B* 78.11 (2008), p. 115432.

[306] D. M. Basko. “Theory of resonant multiphonon Raman scattering in graphene”. In: *Physical Review B* 78.12 (2008), p. 125418.

[307] Fernando de Juan. “Non-Abelian gauge fields and quadratic band touching in molecular graphene”. In: *Physical Review B* 87.12 (2013), p. 125419.

[308] Aires Ferreira et al. “Extrinsic Spin Hall Effect Induced by Resonant Skew Scattering in Graphene”. In: *Physical Review Letters* 112.6 (2014), p. 066601.

[309] Chunli Huang, Y. D. Chong, and Miguel A. Cazalilla. “Anomalous Nonlocal Resistance and Spin-Charge Conversion Mechanisms in Two-Dimensional Metals”. In: *Physical Review Letters* 119.13 (2017), p. 136804.

[310] Chunli Huang, Mirco Milletarì, and Miguel A. Cazalilla. “Spin-charge conversion in disordered two-dimensional electron gases lacking inversion symmetry”. In: *Physical Review B* 96.20 (Nov. 2017), pp. 205305–.

[311] Susanne Irmer et al. “Resonant scattering due to adatoms in graphene: Top, bridge, and hollow positions”. In: *Physical Review B* 97.7 (2018), p. 075417.

[312] H. Katzke, P. Tolédano, and W. Depmeier. “Phase transitions between polytypes and intralayer superstructures in transition metal dichalcogenides”. In: *Physical Review B* 69.13 (2004), p. 134111.

[313] Z. M. Wang. MoS_2*: Materials, Physics, and Devices*. Springer, 2013.

[314] S. V. Iordanskii and A. E. Koshelev. “Dislocations and localization effects in multivalley conductors”. In: *JETP Letters* (1985).

[315] A. F. Morpurgo and F. Guinea. “Intervalley Scattering, Long-Range Disorder, and Effective Time-Reversal Symmetry Breaking in Graphene”. In: *Physical Review Letters* 97.19 (2006), p. 196804.